Laser-induced breakdown spectroscopy for planetary research: Analysis of salts and frozen salt solutions under Martian conditions

vorgelegt von

Dipl.-Phys.
Susanne Schröder
aus Nürnberg

Von der Fakultät II - Mathematik und Naturwissenschaften
der Technischen Universität Berlin
zur Erlangung des akademischen Grades

Doktor der Naturwissenschaften
- Dr. rer. nat. -

genehmigte Dissertation

Promotionsausschuss:

Vorsitzender: Prof. Dr. rer. nat. Mario Dähne
Gutachter: Prof. Dr. rer. nat. Heinz-Wilhelm Hübers
Gutachter: Dr. rer. nat. Jörg Fritz

Tag der wissenschaftlichen Aussprache: 29. August 2012

Berlin 2013

D83

On the surface of Mars, the Sun is about half the size as seen from Earth. The nights are colder than Antarctica has ever been, and even summer days are freezing. The atmosphere is so thin, that it would boil our blood from the smallest wound, and the air consists of deadly amounts of carbon dioxide. There is no life, there is no running water and there is no shelter to escape the Sun's ultraviolet radiation that sterilizes everything left to the Red Planet's surface. The whole planet is a large, dead desert.

And yet, after Earth, it is the most hospitable place for humans in the Solar System!

Mars, meaning the God of War, has two tiny moons, Phobos and Deimos. The Greek names mean fear and terror. This illustrates the planet well as a place for humans to go. And still we will go. Eventually, we will step our feet to the Red Planet. Because we must.

But first come the robots!

Matti Anttila, 2005

Abstract

The research presented in this thesis addresses laser-induced breakdown spectroscopy (LIBS) and its potential for in-situ investigations of geological samples for planetary science. The focus of this work was on the ability of LIBS to detect and identify various salts and frozen salt solutions under Martian atmospheric conditions by utilizing different multivariate analysis (MVA) methods.

LIBS is an emission spectroscopy technique and permits rapid multi-elemental analysis both qualitatively and quantitatively. It relies on ablating and evaporating material from the target by focusing radiation from a pulsed laser onto the sample surface. The generated plasma is analyzed spectroscopically and information about the elemental composition is obtained from specific atomic or ionic transitions and the associated emanating photons, which result in characteristic spectral lines. For the geochemical investigation of extraterrestrial surfaces LIBS has been suggested as a powerful analytical tool and is part of the payload on NASA's rover MSL (Mars Science Laboratory), which will reach Mars in August 2012. This is the first time that LIBS will be used for planetary science.

In this work, salts, which are considered relevant for Martian geochemistry were investigated, including sulfates, chlorides, and perchlorates. The salts were investigated in their pure form, mixed with Martian analogue soil and in frozen salt solutions under simulated Martian atmospheric conditions. In general, the emission lines of metals are detectable with LIBS with high signal-to-noise ratios, which facilitates a relatively straightforward identification of the type of the cation. However, due to weak excitation of the high-energy levels required for efficient radiative transitions of both sulfur and chlorine ions, their emission lines are typically weak and hardly detectable, in particular in the LIBS spectra of the ices. This considerably complicates differentiation between salts with the same type of cation. The focus in this study was on the capability of different MVA techniques applied to LIBS data to discriminate between salts with cations of the same kind in frozen salt solutions. The influence of different gating parameters for time-resolved detection of the plasma were studied for analyzing salts and frozen salt solutions and parameters best suited for the LIBS analysis of ices were determined. The applied MVA methods differed in suitability in terms of discriminating between the various salts. The most important emission lines for successful discrimination were identified for the LIBS spectra and spectral features such as line profiles, shifts, and the influence of background radiation were investigated. Partial least squares discriminant analysis (PLS-DA), which is a special form of PLS regression using a binary matrix that comprises information on the sample classes for compiling a prediction model, was found to be best suited for the purpose of identification of a test set in the case of the frozen salt solutions, but also for the other sample sets. LIBS spectra of salts with the same cation in frozen salt solution could be identified within the scope of the prediction model, although there were no chlorine and sulfur lines detectable. This was achieved on the basis of emission line intensities and line profiles of other lines available in the LIBS spectra.

The results of this work demonstrate that LIBS is a suitable analytical technique for the investigation of salts and frozen salt solutions under Martian atmospheric conditions. With appropriate prediction models, salts in different matrices, such as in frozen salt solutions, can be identified. These results are not only important for the application of LIBS for the analysis of salts and frozen salt solutions on Mars, but also in view of possible future missions to the icy satellites of the gas giants in our Solar System like Europa and Enceladus.

Kurzfassung

Die vorliegende Dissertation beschäftigt sich mit dem Einsatz der laserinduzierten Plasmaspektroskopie (LIBS, engl. Laser-induced Breakdown Spectroscopy) in der Planetenforschung zur in-situ Analyse von geologischen Proben. Der Schwerpunkt liegt hierbei auf der Detektion und Identifizierung von Salzen und gefrorenen Salzwasserlösungen unter marsähnlichen Umgebungsbedingungen und unter Anwendung verschiedener multivariater Analysemethoden.

LIBS stellt eine Variante der optischen Atomemissionsspektroskopie dar und erlaubt die simultane und schnelle Analyse von vielen Elementen. Hierzu wird mit einem gepulsten Laser Probenmaterial abgelöst, atomisiert und ionisiert. Die elementspezifische Strahlung des entstandenen Plasmas wird zur qualitativen als auch quantitativen Bestimmung der Elemente in der Probe spektroskopisch analysiert. LIBS ist eine leistungsstarke Analysetechnik, welche für die geochemische Untersuchung planetarer Oberflächen mehrfach für verschiedene Missionen vorschlagen wurde. Das erste LIBS Instrument für den Einsatz in der Planetenforschung befindet sich derzeit auf dem Rover MSL (engl. Mars Science Laboratory) der NASA auf dem Weg zum Mars, wo er im August 2012 landen wird.

In dieser Arbeit wurde eine experimentelle Studie an einer Auswahl von Salzen durchgeführt, die für die geochemischen Vorgänge auf der Marsoberfläche von besonderer Bedeutung sind. Unter simulierten marsähnlichen Bedingungen wurden Sulfate, Chloride und Perchlorate mit LIBS sowohl pur als auch gemischt mit marsanalogem Gestein sowie in gefrorenen Salzwasserlösungen untersucht. LIBS erlaubt eine einfache Identifizierung der Kationen der untersuchten Salze anhand ihrer intensiven Emissionslinien. Die Detektion von Chlor und Schwefel ist jedoch wegen der deutlich höheren Anregungsenergien im Vergleich zu den Metallen stark erschwert bzw. im Fall der Salzeise nicht möglich. Aus diesem Grund stand die Frage im Mittelpunkt, ob mit LIBS und multivariaten Analysemethoden zwischen Salzen unterschieden werden kann, die das gleiche Kation haben. Zu diesem Zweck wurden im Rahmen dieser Arbeit geeignete Messparameter für die optimierte zeitaufgelöste Detektion der LIBS Spektren der Salzeise ermittelt. Mit den verschiedenen auf die LIBS Daten angewandten multivariaten Analysemethoden konnten die Spektren unterschiedlich gut ausgewertet und unterschieden werden. Die für die Unterscheidung der Proben wichtigen Spektrallinien wurden identifiziert und die spektralen Eigenschaften wie Linienprofile, Linienverschiebungen und Untergrundstrahlung der verschiedenen Proben aufgezeigt. Die PLS-DA (engl. Partial Least Squares Discriminant Analysis) stellte sich als am besten für die Identifikation von Testspektren gefrorener Salzwasserlösungen als auch für die der anderen Probensets geeignet heraus. Die PLS-DA ist eine Art der PLS Regression, welche die in binärer Form vorliegende Information über die verschiedenen Salzgruppen bei der Erstellung des Vorhersagemodels miteinbezieht. LIBS Spektren von Salzen mit dem gleichen Kation im Wassereis können somit trotz nicht detektierbarer Chlor- und Schwefellinien auf Grund der Linienintensitäten und -profile anderer im Spektrum vorkommenden Emissionslinien unterschieden und damit identifiziert werden.

Die Ergebnisse dieser Arbeit zeigen, dass LIBS eine geeignete Analysetechnik zur Untersuchung von Salzen und Salzeisen unter marsähnlichen Bedingungen darstellt und mit geeigneten Modellen Salze in verschiedenen Proben wie in Salzwassereis identifiziert werden können. Diese Ergebnisse sind nicht nur relevant für den Einsatz von LIBS zur Analyse von Salzen und Salzeisen für Missionen zum Mars, sondern können auch im Hinblick auf mögliche Missionen zu den Eismonden unseres Sonnensystems wie Europa und Enceladus herangezogen werden.

Contents

1 Introduction

Mars has been and still is a target of particular interest for planetary exploration. In relatively close proximity to Earth Mars resembles our own planet more than it might appear from a first sight. Although the Martian surface is a cold, dry and desert environment with a thin atmosphere, where liquid water is unstable and strong oxidizing conditions occur. Nevertheless, Mars is the most Earth-like planet we know of to date and also the celestial body with the most hospitable climate and surface conditions for humans. Apart from the main motivations for its exploration, such as comprehending its formation and evolution up to the present state also with regard to possible analogies to the evolution and destiny of Earth, Mars is of particular interest in the context of past or present extraterrestrial life. Past environmental conditions seem to have been different from what is observed today and there is comprehensive evidence, that at some points in time conditions were such that water was able to flow on the Martian surface at least temporarily [Carr, 2012]. Together with volcanic activity these conditions resemble conditions that were present on early Earth and might have allowed primitive, bacteria-like life to evolve. The search for evidence of past or present life on Mars has long since been in the focus of robotic exploration of our neighbor planet [Rapp, 2008].

The detection of salts on Mars is of particular interest as they are, for instance, considered in the context of possibly still existing liquid brines. Salts can significantly depress the eutectic point of brines to temperatures much below the freezing point of water, which in its pure form is not stable at the Martian surface under today's atmospheric conditions. Salts could stabilize liquid water on Mars at least temporarily, giving rise to potentially habitable zones at least on small scales. Furthermore, salt is a good preserver of organic matter and some of the oldest terrestrial life forms have been found in salts, e.g. [Davila et al., 2010]. Hydrated minerals, such as sulfates and chlorides, have been found to be present in the Martian soil by orbiting spacecraft and in situ investigations [Gendrin et al., 2005], [Osterloo et al., 2008], [Rieder et al., 2004], [Squyres et al., 2004], [Wray et al., 2009]. They can form through the evaporation of liquid water from a salt-water solution or other processes involving more or less water and are considered representative of aqueous depositional environments on Mars. Thus, these minerals indicate different aqueous alteration and can, beyond that, provide insight about the physical and chemical settings of different locations and past environmental conditions [Bell, 2008]. By this means, estimations on the amount of liquid water present at the surface of Mars in the course of its history can be obtained, also in a global view. Another reason to have a close look at the salts on Mars is a current imbalance in the detection of salts with respect to the presence of widespread alteration minerals [Milliken et al., 2009]. Hence, the detection of salts is not only important in the context of habitability of early or present Mars but also interesting from a geologic point of view. Although there were times when Mars hosted diverse aqueous environments with conditions that allowed liquid water to flow over the surface at least temporarily [Carr, 2012], Mars appears as a cold and dry place today. The majority of water today is stored in the cryosphere as near-surface ground ice widespread in permafrost soil in the high-latitude and polar regions and as water ice in the permanent northern and southern polar caps. At its landing site inside the arctic circle on Mars the Phoenix lander uncovered a table of subsurface water ice at a depth of 5 to 18 centimeters [Smith et al., 2009]. There, anions of perchlorates and chlorides were reported to be found in Martian soil at the Phoenix lander site [Hecht et al., 2009].

In this work, laser-induced breakdown spectroscopy (LIBS) was addressed as an analytical technique for the in-situ investigation of geological samples for planetary research. LIBS works by firing a brief, intense laser pulse at the sample surface whereby material is ablated and vaporized. The plasma emission is captured and analyzed. Unique spectral features due to the elements in the sample allow for a multi-elemental analysis both qualitatively and quantitatively. LIBS requires little to no sample preparation and one of the main advantages of LIBS is its utility for investigating samples in-situ and remotely. Only optical access to the target is required. This makes LIBS an excellent technique in particular for the investigation of targets which are difficult to access. The advantages of LIBS in view of the geochemical analysis of extraterrestrial surfaces have led to several proposed missions [Cremers, 2007] and finally a selection of LIBS as part of the payload on NASA's rover MSL (Mars Science Laboratory), which will reach the Martian surface in August 2012 [Maurice et al., 2012], [Wiens et al., 2012].

Laser-induced breakdown spectroscopy has been investigated and is under development for more than 40 years [Cremers and Radziemski, 2006b]. However, up to now LIBS has only been applied to Earth-based purposes. Laboratory set-ups were heavy and requested high power in comparison to the typically small payloads for robotic missions to extraterrestrial planets, which are associated with restrictions on size, weight and energy. On the one hand, components became smaller and lightweight with time, and small and low-power instruments are proposed for landers or rovers to explore the surfaces of Mars, the Moon or asteroids [Pavlov et al., 2012], [Rauschenbach et al., 2010]. Moreover, with NASA's Mars Science Laboratory (MSL) a major mission was realized which was able to offer enough resources for a not miniaturized LIBS system for stand-off analyses. With the ChemCam instrument on board MSL the LIBS technique will be applied for the first time for in-situ analysis on a planetary mission.

Since LIBS is capable of doing rapid analysis at distances of up to several meters and beyond that reaching even to hazardous terrains, cliffs, and inside cracks and crevices, the scientific return of robots for planetary exploration will be greatly increased. Weathering layers and dust can be removed with preceding pulses in order to reveal the true composition beneath. While quantitative analysis with LIBS is relatively straightforward and elements including in particular the light elements H, Li, Be, B, C, N, and O can be detected simultaneously, quantitative analysis, i.e. determination of the relative abundances of the elements in the sample, requires careful and elaborate calibration techniques. In order to optimize the scientific return of missions with LIBS, i.e. to best obtain the chemical composition of rock, soil and frozen samples qualitative and quantitative analytical methods have been developed and improved for LIBS data in the past. One valuable attempt to compensate for matrix effects and other factors that influence the plasma's composition and properties and therefore the LIBS spectra are multivariate analysis (MVA) methods. In particular for sample classification and quantitative analysis of geological samples with LIBS a great number of studies was performed and MVA techniques for LIBS data were tested, improved and further developed by multiple authors, e.g. [Anderson et al., 2011], [Clegg et al., 2009], [Gottfried et al., 2009b], [Labbé et al., 2008], [Lasue et al., 2011], [Sirven et al., 2007]. In comparison to univariate data analysis, where only one statistical variable is considered at a time, MVA is based on multivariate statistics, taking into account multiple variables, i.e. spectral lines for LIBS. Redundant spectral information is combined and the relevant information is unveiled. The typically large and complex LIBS data sets are reduced by means of extracting the important information from the spectra.

The aim of this work was to test the feasibility of LIBS for detecting and identifying various salts and frozen salt solutions under Martian atmospheric conditions by utilizing different multivariate analysis (MVA) methods. Several salts covering the potential Martian salts deposits and are considered relevant for Martian geochemistry were analyzed with LIBS under simulated Martian atmospheric conditions, including sulfates, chlorides and perchlorates. The salts were investigated in their pure form, mixed with Martian analogue soil, and in frozen salt solutions in a dedicated chamber under

simulated Martian atmospheric conditions. The most important spectral features for discrimination were identified for the LIBS spectra of the different salt comprising samples applying Principal Component Analysis (PCA). Moreover, Soft independent modeling of class analogy (SIMCA) and PLS-DA models were built, tested and optimized with regard to discriminating between the salts in the different samples with focus on the ices. In a following step frozen salt solutions with "unknown" salts were predictively identified by means of the models.

Outline and content overview

The work is structured as follows: In Chapter 2, our neighbor planet Mars is presented and a rough overview is provided of what is known about Mars today. In Chapter 3, LIBS is described, explaining the principle and fundamentals of this method. An overview of the main parameters is given which can be used to describe and characterize the plasma. The advantages, disadvantages, and applications of LIBS are presented with the focus on its utilization for planetary in-situ exploration. Three MVA methods are presented in Chapter 4, namely PCA, SIMCA, and a special form of PLS-regression, called PLS-DA, which were applied to the LIBS data in the following chapters. Chapter 5 covers the laboratory setup as well as the investigated materials and sample preparation techniques. Chapter 6 contains a study on the influence of different gating parameters for analyzing salts and frozen salt solutions with time-resolved LIBS. Parameters best suited for the LIBS analysis of ices under Martian atmospheric conditions are determined. Moreover, the feasibility of a low energy laser for the analysis of salts and frozen salt solutions is investigated. In Chapter 7, a set of eight salts comprising four chlorides and four sulfates with the same type of cation are analyzed with LIBS. Different multivariate methods are used to investigate the ability to distinguish between the LIBS spectra of chloride and sulfate salts both in their pure form and in ices. The potential of LIBS for identifying two ferric salts (iron(III) sulfate and iron(III) chloride) with MVA methods is investigated for pure salts and the salts in frozen salt solutions in Chapter 8. In Chapter 9 perchlorates and chlorides are addressed. The focus is on the question of whether, by applying LIBS and the MVA methods, perchlorates can be distinguished from chlorides with metal atoms of the same kind (here sodium and magnesium) in Martian analogue soil and in frozen salt solutions. A brief study addressing the potential of LIBS for the identification of biological material in Martian analogue soil is presented in Chapter 10. Finally, in Chapter 11 the main results and conclusions are summarized.

2 Exploration of planetary surfaces - focus on Mars

One of the major goals of space exploration is to better understand the origin and evolution of the Solar System and, beyond that, to learn about the origin and evolution of life, its conditions and habitability. Revealing the physical and chemical processes that shape and alter a planet not only helps us to understand its past, but also to become capable of predicting the future of solar system bodies, including our own planet Earth and placing it in context. Observational research for planetary analysis involves space exploration with robotic missions for remote sensing and also in-situ analysis. With time, the measurements get more accurate, the maps more resolved, and the study of planetary science shifts from physics to geology. During the history of space exploration various techniques were deployed for planetary geology, the majority of them based on spectroscopic methods. For remote analysis thermal emission spectroscopy is frequently deployed, providing information of the mineralogy of rocks and soils due to characteristic emission and absorption features in the spectra. Reflectance spectroscopy is another passive method, which is based on the detection of the sunlight reflected from rocks and soils, giving information about mineralogy and occasionally about the elements, too. It is utilized both, remotely and in-situ. For landers or rovers on planetary missions methods such as x-ray fluorescence (XRF) spectrometry, alpha-proton x-ray spectrometry (APXS), and mössbauer spectrometry were applied for in-situ elemental analysis, e.g. [Brückner et al., 2003], [Clark et al., 1977], [Klingelhöfer et al., 2002], [Rieder et al., 2004]. These methods provided useful data, however, their main limitation was the time required to approach a target or to retrieve it [Cremers, 2007].

LIBS is an active detection method where a laser is utilized to ablate and excite material of the target of interest, forming a little plasma, which is then analyzed [Cremers and Radziemski, 2006a]. So far, LIBS was not applied for planetary science but promises to greatly increase scientific return from new missions, as explained in detail in Chapter 3. With the ChemCam instrument on NASA's rover Mars Science Laboratory (MSL) arriving on Mars in August 2012, the LIBS technique will be applied for the first time on a planetary mission [Maurice et al., 2012], [Wiens et al., 2012]. Additionally other missions are proposed, for instance for Venus [Arp et al., 2004a], [Lambert et al., 2010] or the Moon [Lasue et al., 2012], [Mezzacappa et al., 2010], [Shu et al., 2007]. As this thesis focuses on LIBS applications on the Martian surface, Earth's outer neighbor will be presented in detail in the following section.

Mars - The red planet

Our neighbor planet Mars is the most Earth-like planet we know of to date and it has fascinated humankind for centuries. Apart from the main motivations for its exploration, such as comprehending its formation and evolution up to the present state and also with regard to possible analogies to the evolution and destiny of our own planet, Mars is of particular interest when it comes to the discussion on whether bearing life is a unique property of the Earth. The question of whether life might have formed on Mars and persisted up to the present is one of the major scientific topics in Mars science and subject of intense debate and ongoing investigation. The following overview of information about Mars is collected from [Barlow, 2008], [Bell, 2008], and [Carr, 2006] if not indicated otherwise.

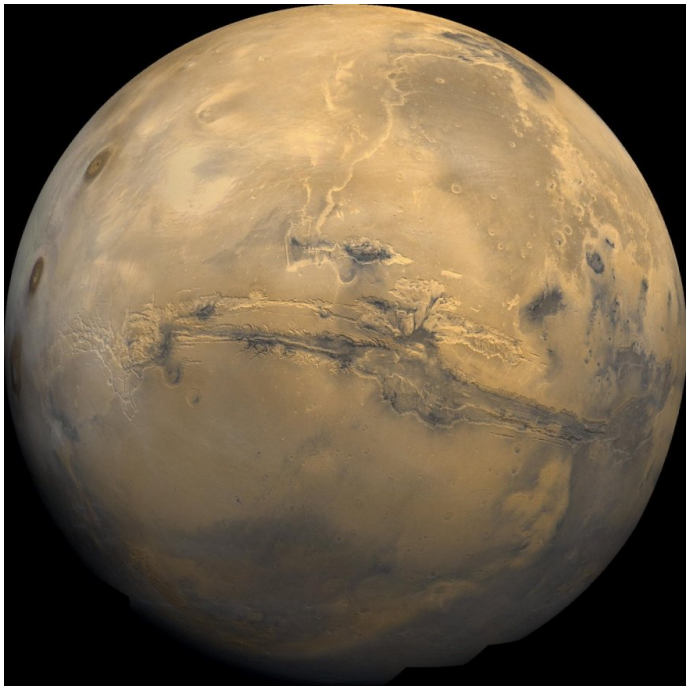

Figure 2.1: *Global view of Mars, Viking 1 Orbiter mosaic (NASA).*

Physical and orbital properties of Mars

Mars is a so called terrestrial planet and is Earth's direct neighbor being the fourth planet of the solar system and the last of the so called inner planets. At an average distance of 2.279×10^8 km from the Sun Mars' orbit is inclined 1.851° to the ecliptic plane. The orbit of Mars is distinctly eccentric with an eccentricity of 0.934 resulting in an orbital period of about 687 days with a mean orbital velocity of 24.13 km/s. Like Earth, Mars rotates counterclockwise as seen from above the ecliptic. With an equatorial radius of approximately 3396 km, which is about half that of Earth, Mars is notably smaller than our own planet. Moreover, Mars is about one-tenth the mass of the Earth having a smaller ferric core and lower general density in addition. Two small irregularly shaped moons accompany Mars, called Phobos and Deimos, which are presumably captured asteroids. Both satellites have circular orbits near the equator and consist of a carbonaceous chondrite composition. Their dark surfaces reflect only about 5% of the sunlight. Mars has a solid surface, a thin atmosphere and two ice-covered polar caps. With 24 hours 39 minutes and 35.2 seconds a Martian day (sol) has a similar duration to an Earth day. Another similarity to Earth are four seasons due to Mars' rotation axis being tipped approximately 30° from the perpendicular to its orbit. A summary of the major astronomical and physical parameters of Mars is provided in Table 2.1. In Fig. 2.1 a picture of Mars is shown which is a global mosaic obtained from Viking 1 Orbiter images.

Instead of months, a Martian year is subdivided due to the areocentric longitude of the Sun (L_S), an equivalent for Mars's position with respect to the Sun. Spring in the northern hemisphere starts at $L_S = 0°$ (first day of autumn in the southern hemisphere), northern hemisphere summer starts at $L_S = 90°$, the autumn at $L_S = 180°$, and northern winter occurs at $L_S = 270°$. Due to Mars' high orbital eccentricity, the seasons on Mars differ in length and intensity. Mars is at perihelion with a minimum distance to the Sun of 1.381 AU at the time of southern summer. Increased incoming sunlight in this position leads to a hotter but shorter summer in the southern hemisphere in comparison

to the summer in the north and, on the contrary to an extended and far colder southern winter as well. In the northern hemisphere spring lasts for 199.6 Earth days, summer for 181.7 Earth days, autumn is 145.6 Earth days long and northern winter lasts 160.1 Earth days.

Eccentricity, obliquity, and inclination vary with time due to gravitational interactions with other planets, particularly Jupiter, and thus all of these parameters suffered from strong fluctuations during Mars' evolution. Among these, obliquity is thought to have the most influence on the climate, being subject to possibly very large variations (between 15° and 35°) and particularly effecting the polar regions. Enhanced incoming solar flux and permanent illumination in polar summer time with high obliquity lead to high sublimation rates of ice. Moreover this is accompanied with deep penetration of large annual thermal wave. Both effects could have led to a redistribution of Mars' water deposits, as water ice might have been driven from the poles and accumulated at low to mid latitudes.

Properties of Mars	
Radius	3396.2 km
Mass	$6.4185 \cdot 10^{23}$ kg
Mean density	$3.933 \frac{g}{cm^3}$
Surface area	$144 \cdot 10^6$km
Gravitation at surface	$3.711 \frac{m}{s^2}$
Mean atmospheric pressure at surface	663 Pa
Average temperature	210 K
Lowest temperature	130 K
Highest temperature	290 K
Mean distance to the sun	$227.94 \cdot 10^6$ km (1.52 AU)
Duration of a Martian day (SOL)	24°39′35.2″
Duration of a year in Martian days	669 Martian solar days
Inclination	1.85°
Declination	52.89°
Obliquity relative to orbital plane	25.19°

Table 2.1: *Overview astronomical and physical parameters of Mars.*

Global structure and topography

Mars exhibits a global dichotomy in its crustal structure between the heavily cratered ancient terrains in the southern highlands and the younger, smooth northern lowlands, which are relatively devoid of craters. The origin of this dichotomy is still not known and subject of ongoing discussion. Possible explanations are (1) the single impact hypothesis with a mega-impact, which - if true - resulted in Borealis Basin being the largest impact crater in the Solar System, (2) an endogenic origin theory, where plate tectonic processes could have shaped asymmetrically the Martian surface, or (3) multiple impact events. While most of the units in the northern hemisphere are at elevations much below the

reference surface (due to the lack of a sea level defined artificially on the basis of an equipotential surface with an average radius at the equator of 3396 km), the southern terrains are mostly above the reference, with a total difference in elevation by 1 to 3 km. The southern hemisphere harbors two huge impact basins called Hellas and Argyre. The depressed floor of Hellas constitutes the largest negative topographic feature on Mars being 8.2 km below the rim. On the other hand, the highest elevation on Mars is the Tharsis volcanic region covering much of the western hemisphere of Mars with several enormous volcanoes. One of them is Olympus Mons, which with a height of about 21 km and a base 600 km in diameter, is the largest volcano in the Solar System. Another outstanding feature is Valles Marineris, a gigantic tectonic rift valley in the east of Tharsis. The rift is 4000 km long, up to 600 km wide and in some areas 8 km deep. In the northern hemisphere, vast, mixed sedimentary and volcanic plains are found. Apart from the Tharsis bulge another volcanic province in the northern hemisphere is Elysium Planitia consisting of three main volcanoes: Elysium Mons, Hecates Tholus, and Albor Tholus.

The hemispheres additionally differ in composition, age and thickness of the crust. Topographic and gravity data suggest a maximum thickness of the Martian crust of about 58 km in the southern hemisphere and thinner depths around 32 km in the north, however, with regional variations [Neumann et al., 2004], [Wieczorek and Zuber, 2004]. Also, there is a difference in the surface roughness between the smooth sedimentary plains in the northern hemisphere in comparison to rougher terrains in the southern hemisphere as a result of the multiple craters.

Like Earth, Mars has permanent polar caps, however they differ from those on Earth in that they contain both, frozen carbon dioxide and water ice. Due to the currently asymmetric climate conditions across the hemispheres of Mars, the polar regions are differently influenced by seasonal variations. The small northern icecap is about one-eighth the size of the southern icecap and grows slightly during northern winter as a result of carbon dioxide precipitating as frost when temperatures fall to the frost point of CO_2 at 148 K. Sublimation in summer causes the upper CO_2 layer to disappear, exposing the northern residual permanent frozen water icecap. At the bigger south polar icecap the carbon dioxide layer does not completely sublime during southern hemisphere's summer and only in some places areas of water ice are exposed. Due to the longer and much colder winter carbon dioxide condensation and sublimation during a Martian year is much greater in the south and the growth and dissipation of the southern polar cap strongly influences and controls the seasonally changing atmospheric pressure on Mars. During a season the elevation can change up to heights of two meters. The ice caps are surrounded by sequences of thick, layered deposits of interbedded ice and dust.

Martian evolution

Mars has undergone differentiation which resulted in a crust consisting of silicates, a mantle, and a dense core. The core is FeS-rich and has a radius of ca. 1300-1700 km. After core formation, Mars presumably had an active magnetic dynamo for a short time, which is indicated by various remnant magnetic anomalies in the crust. However, the lack of a structured global magnetic field at present times suggests that presently there is either a wholly liquid core or a partially liquid core, where both fail to produce any convection or magnetic field. Since the loss of its geodynamo producing the magnetic field, Mars is unprotected from the solar flux, which strips volatiles from the fragile atmosphere. Mars is thought to have once possessed a much denser atmosphere with carbon dioxide, sulfur oxides, water, and other volatiles emanating from intense outgassing processes caused by volcanic activity and impacts. The composition of the mantle is primarily olivine ($(Mg,Fe)_2SiO_4$) and spinel (the high pressure polymorph of olivine) in a depths ranging from ca. 1700-2100 km [Zuber, 2001]. The presence of volcanic and tectonic features such as shield volcanoes, lava flows and vast volcanic plains, suggest that Mars has been and may still be seismically active. In general, the dynamic forces shaping the surface of a planetary body after the formation of a crust are represented by geological processes

linked to (1) the crust, lithosphere, and interior (e.g. tectonics, volcanism) (2) the atmosphere (e.g. eolian), and (3) the hydrosphere (e.g. fluvial). All these processes have formed the Martian surface to a variable extent at different times. Today, wind is the most active process modifying the Martian surface and enormous dust storms are common occurrences, some of them being over a mile high. Also the results of external interaction can be seen, i.e. impact cratering processes. For Mars, three major time periods have been defined by the number of meteorite impact craters on the ground surface. These are, from the oldest to the youngest: Noachian (about 4.6-3.7 Ga before present), Hesperian (about 3.6-3.1 Ga before present), and the most recent period called the Amazonian starting before 3.1 Ga and extending to the present day. It is suggested, that conditions on Mars changed from neutral-to-alkaline in early history to sulfurous acidic conditions in a later area due to waning aqueous activity. While the first conditions correlate, for instance, with the formation of phyllosilicates as a dominant weathering product, the latter is accompanied with the production of sulfates.

Martian geology and in-situ investigations

The composition of the Martian crust was revealed through orbiting spacecrafts with remote sensing observations, the analysis of Martian meteorites (SNC), and moreover in situ investigations of the surface by landers. The majority of information was obtained through various types of spectroscopic methods as mentioned above. Elements detected on Mars include silicon, oxygen, iron, magnesium, aluminum, calcium, and potassium. To a lesser extent, titanium, chromium, manganese, sulfur,

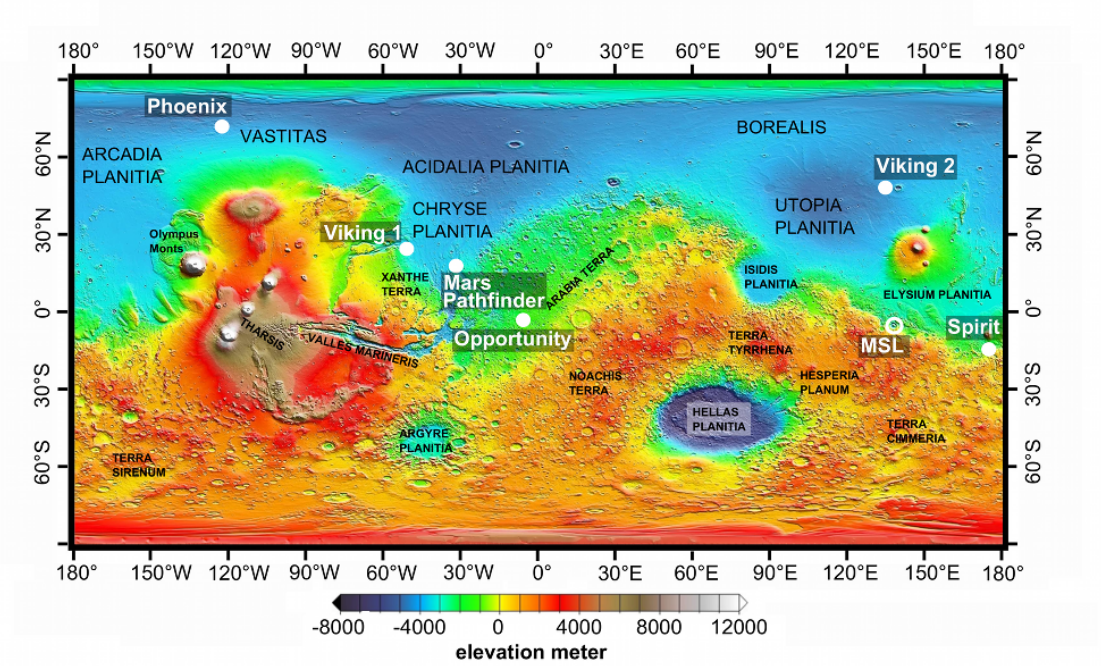

Figure 2.2: *Topographic shaded relief map of Mars based on data obtained with the Mars Orbiter Laser Altimeter (MOLA) on board NASA's Mars Global Surveyor [Smith et al., 2001] with major surface features labeled. Indicated are six landing sites of successful landing missions on Mars (filled points) and the Gale Crater (circle) where MSL will land in August 2012.*

phosphorus, sodium, potassium, and chlorine are abundant as well as some trace elements. Moreover, there is hydrogen bound in water in form of ice or stored in hydrated minerals. Carbon is present bound in carbon dioxide in the atmosphere, seasonally as dry ice at the poles, and also in an unknown amount in carbonates.

The reddish-orange color of the Martian surface is a result of a deep covering dust layer made up of oxidized iron bearing minerals iron(III) oxide and the iron(III) oxide-hydroxide mineral goethite. However, there are slight variations and a range in color is observed, which is caused by both, different composition and locally varying grain size. While brighter regions are mostly a result of dust deposits, the darker regions are generally correlated with basaltic-rich materials with the minerals olivine, pyroxene, and plagioclase feldspar. The Martian surface is primarily composed of mostly unaltered or only weakly altered basaltic rocks and sand, however, with extensive altered minerals in local environments. Weathered basalt seems to be correlated with higher latitudes due to conditions that allow ice to be stable at these locations [Wyatt et al., 2004]. The southern hemisphere is dominated by plagioclase, pyroxene, and a minor amount of olivine pointing to a basaltic composition [Poulet et al., 2009]. The northern hemisphere was once thought to be made up of andesitic materials such as plagioclase, feldspar, and volcanic glasses [Bandfield et al., 2000] [McSween et al., 2003] however more likely is a basaltic composition affected by weathering [McSween et al., 2009].

Both landers of NASA's Viking program, which were the first spacecrafts to successfully land on the Martian surface in 1976, carried an x-ray fluorescence (XRF) spectrometer for geochemical analysis. With these, loose soil could be analyzed for major elements heavier than Na. The Viking 1 lander set down in Chryse Planitia and XRF analyses suggested a basaltic composition with a large amount of sulfur. Measurements of Viking 2, which landed in Utopia Planitia, resulted in a similar composition suggesting that these soils are not of local origin but are mobile materials that have been redistributed over the surface of Mars. This conclusion has been moderated later on when global mapping such as with the gamma-ray spectrometer onboard the Odyssey orbiter provided information of locally varying chemical compositions of the surface [Newsome et al., 2007].

In 1997 Mars Pathfinder, the first rover on Mars, set down in Chryse Planitia about 800 km southeast of the Viking landing site. It was able to move within 10-15 m from its landing site and traveled a total distance of about 100 m in its three months of operation. For geochemical analysis the Mars Pathfinder included an alpha-proton x-ray spectrometer (APXS) and a navigation camera, moreover a stereo camera and a meteorology package. The covering dust layer was found to have a similar composition than at the landing sites of the two Viking spacecrafts, again with a significant fraction of sulfur (6-8 % SO_3). Analysis of the covered, unaltered rocks was corrected by taking into account the sulfur content. The rocks were found to have andesitic composition. In comparison to the Martian meteorites, these rocks contained more silicon, but less magnesium and iron [Brückner et al., 2003].

Seven years after Mars Pathfinder, the two Mars Exploration Rovers (MERs) reached the Martian surface in 2004. Both rovers carried identical instruments: a panorama camera (Pancam), a minature thermal emission spectrometer (Mini-TES) for the analysis of minerals in soil and rocks, a microscopic imager (MI) with a resolution of 30 μm/pixel, an APXS for geochemical analysis, and a Mössbauer Spectrometer to investigate the mineralogy of iron-bearing rocks and soils. A rock abrasion tool (RAT) allowed for grinding away dust and weathered surface coatings and to expose rock interiors. The MERs were sent to sites which might hold evidence of water activity in the past. Spirit (MER-A) landed inside the 160 km Gusev impact crater, where once a lake could have existed. However, only little evidence for ancient water was found and instead of lacustrine deposits the soil was found to contain only slightly altered basaltic rocks, containing the minerals pyroxene, olivine, plagioclase, and magnetite. Spirit also investigated rocks in the Columbia Hills traveling a distance of approximately 2.6 km. There, the rocks were very different from those of the plains and also different from one another, varying in texture and composition. They were altered to a different degree due to aqueous

fluids and were enriched in phosphorus, sulfur, chlorine, and bromine. Moreover, oxidized and hydrated minerals were found including goethite, which only forms in the presence of water. The Spirit rover was active until 2010 after becoming stuck in late 2009 and stopping communication in 2010.

Opportunity (MER-B) was sent to Meridiani Planum due to the region containing abundant hematite at the surface, a mineral which often forms in a water-rich environment. It landed in the small 20 m crater Eagle and also investigated a crater named Endurance in a distance of 800 m. Sedimentary rocks at Eagle crater were reported to be composed of fine-grained siliciclastic materials derived from weathering of basaltic rocks, sulfate minerals such as magnesium sulfate and jarosite, and hematite [Squyres et al., 2004]. Hematite-rich spherules were found dispersed throughout the outcrop [Klingelhöfer et al., 2004].

The Phoenix lander was sent to a region above Mars' arctic circle and set down in 2008 on the partially eroded ejecta blanket approximately 20 km from the 0.5-0.75 billion year old Heimdal crater [Smith et al., 2009]. One of the primary scientific goals was to verify the presence of subsurface ice. Moreover, the aim was to understand the history of the water at the landing site and to investigate the hability. For this purpose the payload included a Thermal and Evolved Gas Analyzer (TEGA), an optical and an atomic force microscope, a Thermal and Electrical Conductivity Probe (TECP), a robotic arm with a camera, a Stereoscopic Surface Imager (SSI), an atmospheric/weather station (MET), and four identical Wet Chemistry Laboratory (WCL) cells. In a nearby polygon, a shallow ice table was uncovered by the robotic arm at a depth of 5 to 18 cm. The soil was alkaline with a pH = 7.7 and $CaCO_3$ was found, together with aqueous minerals and salts such as chlorides and perchlorates [Kounaves et al., 2010], [Hecht et al., 2009].

Atmosphere, surface pressure and temperatures

The Martian atmosphere today is very thin with an average value of 663 Pa, comparable to Earth's atmospheric pressure at an altitude of approximately 35 km above sealevel. Like that of Venus, the Martian atmosphere is composed largely of carbon dioxide (95.32 %) and nitrogen (2.7 %) with less than 1 % oxygen. Atmospheric water accounts for only 0.03 %. A detailed overview of the Martian atmospheric composition is given in Table 2.2. Due to the southern terrains being higher in elevation and pressure varying significantly with height, the atmospheric pressure in the southern hemisphere is correspondingly lower. At the deepest point at Hellas a pressure of 1.4 kPa is obtained, whereas at the summit of Olympus Mons it is merely 70 Pa.

As a result of the polar caps sublimating and condensating during a Martian year, the atmospheric pressure is subject to variations. UV radiation from the sun leads to reactions that permanently transform CO_2 into oxygen (O_2) and carbon monoxide (CO). Due to the low pressure, there is no greenhouse effect on Mars but the atmosphere is thick enough to support thin water ice clouds. Mars' dry atmosphere holds at least a little bit of dust at all times, with the amount of dust being raised at times by more or less extended whirlwinds, called dust devils. Surface winds on Mars can reach up to 40 m/s.

Mars is a place of extremes. In polar winter the temperatures can fall to a low of 130 K ($-140°$C), but can reach up to 290 K (20°C) in Martian summer. The wide range of surface temperatures is mostly a result of the low capacity of the dry and thin atmosphere, which is neither capable of absorbing radiation nor of storing it.

Water on Mars

Liquid water is unstable at the present surface conditions on Mars with a low surface pressure in conjunction with temperatures ranging from approximately 130 K to 290 K. However, there is comprehensive evidence pointing to conditions different from the dry and cold planet that is observed

Composition of the Martian atmosphere	
Carbon dioxide CO_2	95.32 Vol%
Nitrogen N_2	2.70 Vol%
Argon Ar	1.60 Vol%
Oxygen O_2	0.13 Vol%
Carbon monoxide CO	0.08 Vol%
Water H_2O	0.03 Vol%
Neon Ne	2.50 ppm
Krypton Kr	0.30 ppm
Xenon Xe	0.08 ppm
Ozone O_3	0.04-0.2 ppm

Table 2.2: *Martian atmospheric composition.*

today. Geological structures such as branching valleys similar to terrestrial river valleys have been found on the surface of Mars [Carr, 2012]. Presumably, Mars passed through different episodes involving water during its history and at least temporarily water could flow on its surface.

Evidence for water on Mars was obtained by various Mars-orbiting satellites and in situ measurements by landing robots of several missions such as Mars Global Surveyor, Mars Odyssey, Mars Express, the Viking lander, Pathfinder, the Mars Exploration Rovers Spirit and Opportunity, and the Phoenix lander. The observations provide strong evidence that water has played an important role on Mars for a relatively long time in the past indicating the possibility of a once warmer and wetter climate, e.g. [Chevrier and Mathe, 2007]. However, an alternative explanation for at least some alteration signatures are highly acidic solutions with a small amount of water involved and not necessarily hot temperatures [Berger et al., 2009]. A dramatic climate change is thought to have appeared at the end of the Noachian. But there are also signs for more recent water activity. For instance, gullies presumably carved by water or water-filled debris were found over sand dunes which are thought to be only a few billion years old [Carr, 2012]. Also, sediments in craters were found, suggesting former crater lakes.

The majority of Martian water observed so far is stored in the cryosphere as near-surface ground ice widespread in permafrost soil in the high-latitude and polar regions and as water ice in the permanent northern and southern polar caps. Hydrogen was detected in the first meter in polar regions [Boynton et al., 2002], [Feldman et al., 2002]. Although its form is still uncertain, the data indicates the presence of a subsurface layer including ice, which constitutes about 35 wt.%. Theoretical models and geomorphological observations support the idea of ground ice. Moreover, groundwater is believed to reside in even deeper regions below the cryosphere [Clifford et al., 2010]. Calculations considering new estimates of the Martian geothermal heat flow suggest a thickness of the cryosphere of 0 - 9 km in the equatorial region, which increases to approximately 10 - 22 km at the poles. The thickness depends on the ground water freezing temperature and, thus, on the availability of salts. As mentioned before, at its landing site inside the arctic circle on Mars the Phoenix lander uncovered a table of subsurface water ice at a depth of 5 to 18 centimeters [Smith et al., 2009]. Water has also been detected in the form of water vapor in the atmosphere and ice clouds [Jakosky and Mellon, 2004], [Levrard et al., 2004], and bound in hydrated minerals, or adsorbed in soil and rocks, constituting a global inventory of near-surface water. The atmosphere, polar caps and near-surface regolith interact and water is exchanged between the reservoirs on different timescales due to transportation by

wind, diffusion into and out of the surface, condensation, sublimation and adsorption. Under certain circumstances liquid water may exist at least temporarily in the sub-surface, for instance as the result of premelting as interfacial water, or as result of greenhouse melting in the form of sub-surface melt water [Dash et al., 2006], [Möhlmann, 2010].

Water-altered minerals and hydrated clays have been found on Mars at different locations such as at Meridiani Planum, Valles Marineris and the Noachian terrains by spectroscopic instruments on orbiters and also in situ by rovers as mentioned above [Bibring et al., 2005], [Murchie et al., 2009], [Poulet et al., 2005]. It was found that phyllosilicate and sulfate bearing terrains, located widely separated in areas of Noachian-aged material, were hydrated above average, which could indicate a spatially extensive chemical alteration by water-rock interaction in the early history of Mars [Milliken et al., 2007].

Salts on Mars

Salts are another important component of the Martian soil and of particular interest in view of geochemical processes. Many salts lower the freezing point of the solution, which suppresses evaporation rates and could therefore stabilize the liquid water on Mars, at least temporarily [Brass, 1980], [Kargel, 1991], [Knauth and Burt, 2002], [Möhlmann and Thomson, 2011]. Due to their potential for significantly depressing the eutectic points of salts they are discussed in the context of possibly existing liquid saline water on Mars, possibly providing habitable conditions supporting life on small scales.

Various kinds of salts have been detected, including sulfates, chlorides and perchlorates. They indicate different aqueous alteration and can provide insight about the physical and chemical settings of different locations and past environmental conditions [Bell, 2008]. For instance, on Earth chlorides usually occur in alkaline environments whereas on Mars they are predicted to form from acid fluids derived from basaltic weathering [Osterloo et al., 2008]. Sulfate minerals can form for instance by evaporation of water or by weathering of basalts by means of acidic sulfate-rich fluids, wherefore not neccessarily discrete bodies of water are required.

At the Viking, Pathfinder, and Mars Exploration Rovers's landing sites sulfates were discovered in the surface material [Clark et al., 1982], [Foley et al., 2003], [Moore, 2004]. Examples are magnesium sulfate and jarosite (KFe_3 $+3(OH)_6(SO_4)_2$) at Meridiani Planum [Squyres et al., 2004] and sulfates containing iron, magnesium, and calcium in soils in Gusev Crater [Campbell et al., 2008] [Johnson et al., 2007]. With hyperspectral data obtained by the Mars Express OMEGA instrument kieserite ($MgSO_4 \times H_2O$), gypsum ($CaSO_4 \times 2H_2O$), and polyhydrated sulfates were identified at numerous sites e.g. [Gendrin et al., 2005]. Moreover, Mg-, Fe-, and Ca-sulfate deposits were detected on the basis of data obtained from OMEGA and CRISM among others in the northern region of Valles Marineris e.g. [Bishop et al., 2009], [Le Deit et al., 2008], [Wendt et al., 2011]. Gypsum was found in the circum-polar dune field and the North Polar Cap [Massé et al., 2010]. Chlorides, too, are present on Mars; however, they are much less abundant than sulfates. Chloride bearing salts have been found globally widespread in deposits in the ancient highlands in the southern Martian hemisphere with Mars Odyssey THEMIS data [Osterloo et al., 2008]. The discovery of perchlorates at the phoenix landing site was reported by [Hecht et al., 2009] together with the detection of the predominant occurrence of Mg^{2+} and Na^{+} cations in the soil. Moreover, [Massé et al., 2010] found spectral signatures consistent with perchlorates in the polar and circum-polar sediments. An imbalance in the detection of salts with respect to the presence of widespread alteration minerals was found by [Milliken et al., 2009].

Extant life?

The search for evidence of existing or extinct life on another celestial body of our solar system is of great interest and for a long time included in the aims of robotic missions to Mars [Rapp, 2008]. Habitability is closely related to liquid water, which is considered to be a key condition for life as we know it from Earth. However, liquid water is unstable at the low surface pressure in conjunction with temperatures ranging from 130 K to 290 K. So far no evidence for life on Mars has been found. However, Mars is the celestial body with the most hospitable climate in our solar system and the possibility that at one time it might have hosted some form of life remains plausible.

3 Laser-induced breakdown spectroscopy (LIBS)

Laser-induced breakdown spectroscopy (LIBS) - sometimes also obsoletely termed laser-induced plasma spectroscopy and then abbreviated with LIPS - is an atomic emission technique that allows rapid multi-elemental sample analysis both, quantitatively and qualitatively. LIBS is considered as quasi-non-destructive and its most important advantage is probably its utility for investigating samples in-situ and remotely. Only optical access to the target is required and without the need for sample preparation. This makes LIBS an excellent technique in particular for the investigation of targets which are difficult to access and led to its selection for the payload of NASA's Mars Science Laboratory (MSL) rover Curiosity, which will reach Mars in August 2012.

This chapter deals with the principle and fundamentals of LIBS. Parameters influencing and affecting the processes of ablation, plasma formation, and emission are described. An overview of the main parameters is given which can be used to describe and characterize the plasma. The advantages, disadvantages, and applications of LIBS are presented with the focus on its utilization for planetary in-situ exploration in the last section of this chapter.

3.1 LIBS principle and basics

Laser-induced breakdown spectroscopy is a powerful analytical, however, a comparatively simple optical diagnostic technique. It is a special type of atom emission spectroscopy (AES) where a pulsed laser is utilized to generate a plasma, e.g. [Cremers and Radziemski, 2006b]. By focusing the radiation of the laser onto a small area at the sample to be analyzed a small amount of material is ablated locally from the target and evaporated. Different matrices such as solid, liquid, and gaseous substances can be examined in this way. Sufficient irradiance (i.e. $> 10^9$ W/cm^2 depending on the state of the aggregate and being highest for gases) enables the generation of a typically transient and weakly ionized plasma, which consists of atoms and ions in electronically excited states as well as free electrons and simple molecules. The plasma light emission is collected and spectrally analyzed. Information about the investigated sample is obtained on basis of the characteristic emission lines in the spectra, more precisely their position (wavelength), intensity, and intensity ratios. Basic line identification and hereby determination of the atomic constituents of the sample can be done as well as more complex analysis, where relative concentrations or absolute masses are calculated.

Plasma creation and temporal evolution

Although LIBS by itself is a relatively straightforward and simple method, plasma formation and evolution are very complicated. The processes including laser-matter interaction, the breakdown, and plasma formation are all complex and depend on multiple parameters, including the characteristics of the substance to be analyzed, the composition and pressure of the ambient atmosphere, and the laser parameters, e.g. [Yalcin et al., 1999]. Most commonly lasers with pulse durations in the lower ns-range are used, however, there are also applications with ps- or fs-lasers for which the processes of mass ablation and plasma evolution differ remarkably [Amoruso et al., 2006], [Angel et al., 2001],

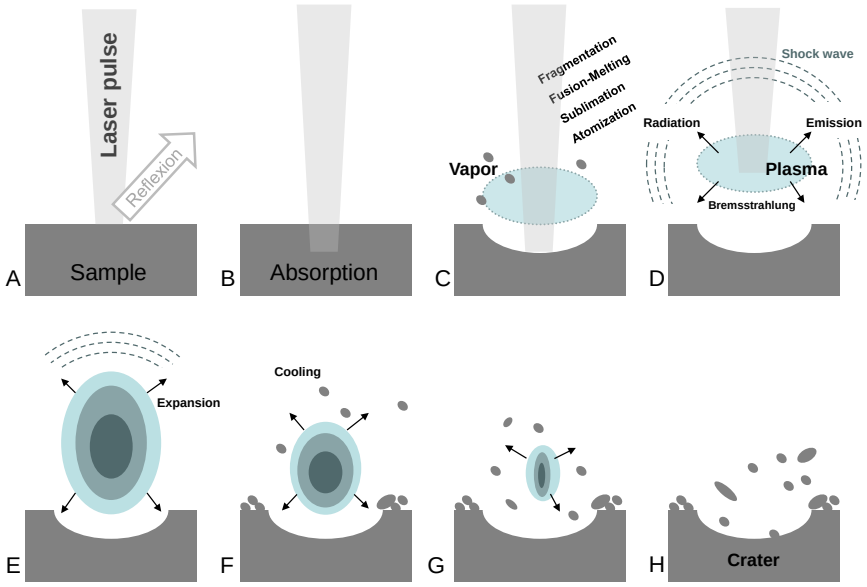

Figure 3.1: *Schematic sequence of the main processes during laser-induced plasma formation on a solid surface using a nanosecond laser pulse, based on [Vadillo and Laserna, 2004]. While the incoming laser radiation is partly reflected (A) the remaining part is absorbed by the material and converted into heat (B). The sample is vaporized and a small amount of material is ablated (C). The high pressure vapor absorbs energy from the further incoming laser pulse which leads to ionization, plasma formation and the creation of a shock wave (D). The plasma then expands; the ions and atoms decay to lower energy levels accompanied by the emission of radiation (E). After the laser pulse has ended the plume's expansion velocity decreases and the plasma cools (F), followed finally by plasma extinction (G). The ablated material falls back down and is deposited in and around the crater (H).*

[Kaiser et al., 2000], [Russo et al., 2004]. What is described in the following are the main processes for a plasma initiated on a solid surface with a several ns lasting laser pulse with an infrared wavelength under earth atmospheric conditions. Different conditions in particular in view of applications in space science will be addressed thereafter. In Fig. 3.1 the processes occurring during laser-induced plasma formation are summarized and depicted in chronological order.

Ablation, vaporization and breakdown

When the high-power laser pulse reaches the surface of a soil during the first moments of interaction the laser energy is coupled into the material where it is absorbed. After local heating, thermal surface melting and laser-induced ablation of the upper micrometers of the sample the removed substance is atomized. A few free electrons are generated, which serve as initial receptors of optical energy. They are accelerated gaining more and more energy by the still present electric field of the laser beam by means of inverse bremsstrahlung i.e. transfer of the photons' energy to the free electrons with the involvement of a third neutral particle, namely an atom. These high energetic electrons then collide with atoms of the high pressure vapor, causing additional ions and free electrons, which also absorb

energy of the incident laser radiation. Avalanche occurs when a critical value of the electron density in the order of 10^{18} cm^{-3} is exceeded, followed by plasma formation, e.g. [Miziolek et al., 2007]. Another mechanism to initiate breakdown is multi-photon ionization where the sum of the energy of the simultaneously absorbed photons has to compensate for the ionization potential. The probability of releasing electrons by multi-photon absorption decreases with the number of photons necessary for that process. Therefore, this is favored for shorter wavelength, i.e. higher photon energies. Moreover, multi-photon ionization takes place in low pressure environments where the particle density is too small to enable collision-based cascade ionization.

Expansion and emission

After the breakdown, the plasma expands in all directions giving rise to a shock wave propagating at supersonic speed with the accompanying sound. The plasma is interacting with the still incoming laser radiation, including further atomization of still present molecules in the vapor but also additional thermal and photochemical excitation takes place. Expansion is greatest towards the incoming laser radiation, where most of the optical energy enters the plasma. On the other side, further mass ablation by the laser can be prevented given high enough power densities by an optically dense plasma absorbing the infrared laser photons before they can reach the surface of the soil (plasma shielding). The decisive parameter is the plasma resonant frequency ν_e given by [Fußmann, 2005]

$$\nu_e = \frac{1}{2\pi}\sqrt{\frac{n_e e^2}{\varepsilon_0 m_e}} \tag{3.1}$$

which is a function of the electron number density n_e and the constant values of the electron mass m_e, electron charge e, and the electric constant $\varepsilon_0 = 8.854 \times 10^{-12}$ Fm^{-1}. For laser frequencies up to the plasma frequency the electrons in the plasma are able to follow the oscillations due to the electromagnetic radiation of the laser and the photons are absorbed, which is the case mostly for NIR and IR wavelengths. Radiation from a laser with a smaller wavelength (i.e. higher frequency) can penetrate the plasma considerably deeper right up to the sample surface since absorption varies as the square of the wavelength. For excitation with radiation in the UV therefore, lower pulse energies are sufficient for inducing a plasma. Moreover, deeper craters are obtained for UV excitation due to higher mass ablation. Further information on the laser-wavelength dependence of mass ablation can be found for instance in [Fabbro et al., 1982]. For a NIR laser, despite plasma shielding, additional material can still be removed by thermal interaction of the plasma with the targets surface.

Due to collisions with the ambient gas, expansion slows down. The plasma is cooled by self absorption (quenching) and starts to decay. In the cooling plasma energy is released both, through radiation and conduction. Relaxation and both, chemical and radiative recombination occur, resulting in the formation of neutral atoms and simple molecules. Shortly after plasma initiation the plasma emission is dominated by continuum emission due to interaction of ions with electrons and absorption of free electrons: bremsstrahlung and recombination. Bremsstrahlung is produced when a charged particle, here an electron, is decelerated in the coulomb field of another charged particle in the plasma, typically an atomic nucleus or ion. Kinetic energy of the moving electron is converted to the energy of the radiated photon, which is a free-free transition and results in a continuous spectrum. Recombination is another process leading to uncharacteristic radiation. It is a free-bound transition, where a free electron is captured to a bound level of an ion and a photon is emitted spontaneously. This process becomes more probable for small velocity differences of the electron and the ion. After a few hundred nanoseconds relaxation occurs and the highly excited species decay to lower energy levels giving rise to narrow emission lines in the spectra (bound-bound transition). These atomic or ionic transitions are definite and the concomitant characteristic photons transmit the relevant information on the el-

emental composition of the plasma. When relaxation starts, characteristic emission is dominated by those of the ions due to the high degree of ionization. Over time this shifts to a domination of atomic emission lines, followed by the formation of simple molecules associated with specific lines in the final moments before plasma extinction. In Fig. 3.2 the processes and transitions during plasma evolution in an atomic picture are shown. While the laser is still interacting with the plasma the uncharacteristic continuum radiation exceeds characteristic emission arising from electron transitions in the atomic or ionic shells by far. However, recombination and bremsstrahlung abate much faster than the element-specific emission (several hundred ns vs. some μs) and can be excluded from detection for improved spectra as explained in the next section. In a typical LIBS spectrum tens to hundreds of characteristic spectral lines are received, ranging from vacuum ultra-violet (VUV) to near infrared (NIR) wavelengths.

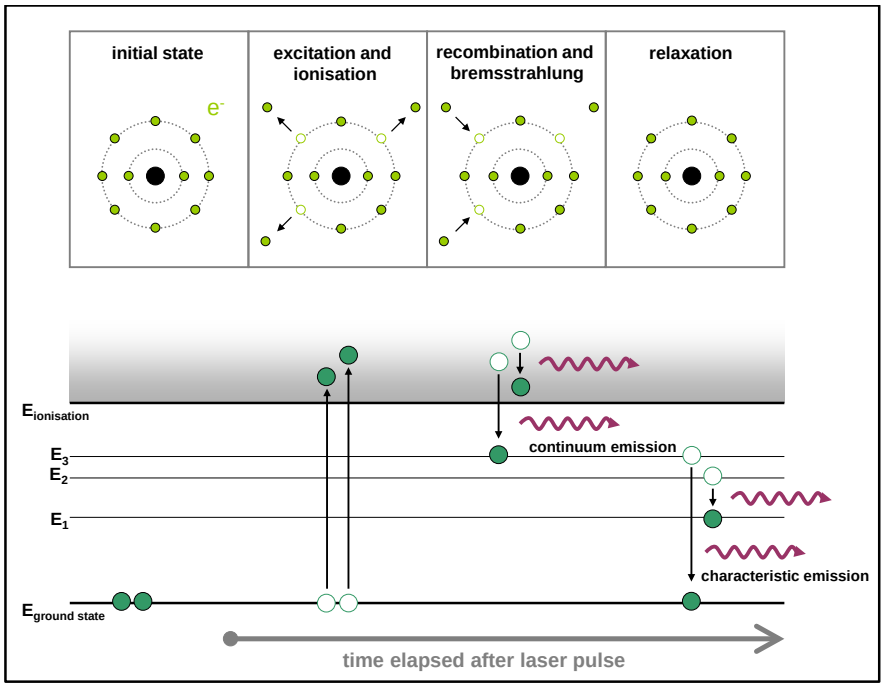

Figure 3.2: *Sketch of the processes on an atomic level during the evolution of a laser-induced plasma, based on [Rauschenbach, 2009]. After excitation and ionization the plasma is cooling. In the early post-laser-pulse-regime bremsstrahlung due to free-free transitions in the field of an atom prevails along with recombination (free-bound transitions). Both processes result in continuous emission. Later on bound-bound transitions in the atom and ion shells occur, giving rise to characteristic emission which can be used for elemental analysis.*

A crater is left, where the laser has hit the target surface. Usually the crater is bigger than the laser spot size, depending on the material's thermal conductivity and the pressure of the surrounding atmosphere. Ablation depends on the sample properties such as the density and melting point of the material. Generally, for substances with lower melting points a bigger portion of material is ablated compared to samples with higher melting points. Moreover, materials with higher density such as metals or glasses are ablated more efficiently than powders. Opacity of the substance to be analyzed is of relevance, too. On a sample that is highly transparent for the laser radiation the photons penetrate into the target. Energy is not efficiently released at the sample surface which impedes

plasma initiation.

In a low pressure environment significantly more mass is ablated due to the plasma quickly expanding and, therefore, lowering plasma densities and resulting in less shielding of the surface, e.g. [Knight et al., 2000], [Peter and Noll, 2007]. Additionally, the plasma's properties and dynamics such as expansion velocity and plasma life time depend on the ambient conditions. In an environment with low pressure the plasma expands much faster than under high pressure conditions, thus, resulting in shorter plasma life times. Typically, plasma life times last from several tens of microseconds to a few milliseconds.

Moreover, in low pressure environments higher stages of ionization are obtained for the same laser intensity on the sample [Cremers and Radziemski, 2006b]. At pressures below approximately 100 Pa only low intensities of the emission lines are observed due to the fast plasma expansion times associated with a plasma of low density and reduced collisional excitation. However, studies such as those by [Knight et al., 2000], [Sallé et al., 2005] have shown that strongest emission signals are obtained for pressures ranging from 1 kPa to 10 kPa, cf. Fig. 3.6. The spectral line intensities are increased due to more material being ablated and excited in comparison to a laser-induced plasma under normal (Earth) atmospheric conditions, where increased plasma shielding occurs as mentioned above. The effects of a Martian-like environment for the laser-induced plasma will be discussed in detail in the last section of this chapter.

Emission lines resulting from constituents of the surrounding gas can appear in the LIBS spectra in addition to those from the elements constituting the sample. This is a problem for instance for the application of LIBS on Mars in which case it is highly complicated to distinguish the signal from carbonous samples from that due to CO_2 in the Martian atmosphere. For applications on Earth a similar problem is faced when oxygen or nitrogen contents in a sample are intended to be observed. Here, if realizable, vacuum conditions or an atmosphere consisting of a noble gas (commonly Argon or Helium) are favorable. The noble gas atmosphere leads to an extended plasma life time and an enhanced sensitivity of the analysis. While in an argon atmosphere excitation is usually enhanced, helium or oxygen were found to suppress excitation. The pressure and composition of the ambient gas also have effect on the line intensities, their widths and in some cases also on their relative intensities by reason of occurring near-resonant collisions.

The plasma emission is affected by the ambient conditions as well as the transmission of the plasma light, which reaches the spectrometer after traversing the optical path through the ambient gas. For applications where emission lines in the VUV-range are of interest, an atmosphere comprising oxygen has to be avoided because of its absorption below 200 nm. Here, too, it is necessary to work under vacuum conditions or with an inert gas.

Advantages, disadvantages, and applications

LIBS is an unique technique that demonstrated several advantages in comparison to other analytical techniques for elemental analysis. It is sensitive to major, minor and trace elements including in particular the light elements H, Li, Be, B, C, N, and O, and enables their simultaneous detection. LIBS is a very fast technique allowing for real-time analysis since plasma creation and its detection last only a few seconds. Moreover, LIBS has an advantage over several other techniques, where mechanical preparation of the sample is required, such as milling or grinding, or other time-consuming sample pretreatment. By contrast, LIBS requires only little or no sample preparation at all. Thin covering layers, coatings, dust or superficial contaminants can be ablated and penetrated with preceding laser pulses. This can be done in order to clean the surface from a composition, which may not be representative of the underlying bulk material. However, also depths profiling can be done, where layer by layer is ablated and investigated. By this means, LIBS is not only capable of spatially-resolved analysis

(< 1 mm) but also of depth-resolved measurements. Nonetheless, LIBS is considered nondestructive due to only small amounts being removed by each shot in the range of some nanograms. Another advantage of LIBS is that targets, which are difficult to access or from which a distance has to be kept to avoid for instance a hazard to health, can be investigated remotely.

LIBS has been used for a wide variety of applications ranging from geochemical analysis e.g. [Gottfried et al., 2009b], [Harmon et al., 2009], [Lucia and Gottfried, 2011], [Tucker et al., 2010] to analysis of steel, e.g. [Peter et al., 2003] to the analysis in hazardous environments such as for radioactive material e.g. [Sirven et al., 2009]. Explosives were investigated by [De Lucia et al., 2008], [Gottfried et al., 2009a]. LIBS includes even applications for the investigation of biological material, e.g. [Diedrich et al., 2007], [Multari et al., 2012], [Rehse et al., 2012]. The listed applications are by far not complete and are also constantly growing. A comprehensive summary of LIBS research and applications can be found e.g. in [Miziolek et al., 2007]. Although solids, liquids, and gases can be investigated with LIBS, the majority of applications deals with the investigation of solids.

Coupled with a Raman spectrometer, supplementary molecular information on the sample can be obtained, enabling simultaneous multi-elemental and molecular micro-analysis, e.g. [Hoehse et al., 2009]. Raman spectroscopy identifies molecules from vibrational spectra and allows fast online and in-situ analysis without extended sample preparation. A combination of both techniques is furthermore suggested for the purpose of planetary surface exploration on Mars, e.g. [Dreyer et al., 2007]. Another beneficial combination is obtained by bringing together LIBS and laser-induced fluorescence (LIF), e.g. [Hilbk-Kortenbruck et al., 2001].

On the other hand the main drawback of LIBS includes the low reproducibility of the method, which results from multiple factors such as variations in the laser energy or differing laser-matter interaction due to the complex physical and chemical processes involved. Typically, a relative standard deviation (%RSD) for LIBS spectra is found to reach up to 10%. Matrix-effects of heterogeneous samples additionally complicate analysis. Self-absorption of spectral lines may occur due to high densities in the plasma, leading to a saturation effect on the emission lines and preventing successful quantitative analysis. The small size of the laser spot, cited as an advantage above, could be interpreted as a disadvantage, too, when compared to other analysis techniques such as APXS, where an average composition over a larger area is obtained.

3.2 Plasma physics and analysis

A plasma is defined as a distinct state of matter similar to a gas but composed of a certain amount of charged particles such as free electrons and ions. It behaves differently from other states of matter due to the charged particles it consists of, which interact strongly and in a collective way to electromagnetic fields. This applies to externally imposed fields as well as to electric and magnetic fields caused by the plasma itself through local heterogeneities in charge distribution and currents resulting from differing motions of electrons and ions. Thus, although the particles in the plasma are unbound they can not move unaffected by the fields they themselves and the other particles are generating. These collective effects are also used to define the plasma, requiring a certain minimum distance between the charged particles that enables interaction with a large number of particles simultaneously. The Debye screening length λ_D is the scale over which the usual Coulomb field is deleted exponentially by the polarization of the plasma, i.e. the plasma beyond this distance is essentially shielded from the effects of a charge. For an electron this reads [Fußmann, 2005]:

$$\lambda_D = \sqrt{\frac{\varepsilon_0 k_B T_e}{n_e e^2}}. \tag{3.2}$$

It is a function of temperature and the number density n of the plasma where ε is the electric constant and $k_B = 8.617 \times 10^{-5}$ eV/K is the Boltzmann constant. Increasing temperature leads to an increase in the shielding lengths whereas an increased number of shielding particles is more effective and thus reduces the Debye length. For a plasma the Debye screening length is short in comparison to the spatial extent L of the plasma $\lambda_D \ll L$ (typically in the order of several nm in comparison to a few mm), which means that interactions between the particles are an issue only in very small volumina. A plasma can be characterized by its degree of ionization, which gives the ratio of electrons to other particles in the plasma. A LIBS plasma usually falls into the category of a weakly ionized plasma with less than 10% ionization [Cremers and Radziemski, 2006a].

Overall, the plasma is electrically quasi-neutral meaning that there are equal numbers of negative and positive charge carriers which compensate for each other on macroscopic length-scales:

$$\frac{n_e - \sum_i Z_i n_i}{n_e} = \varepsilon \ll 1 \tag{3.3}$$

where n is the number density of each species. The sum is extended over all ions with charge number Z_i. Deviations from neutrality can occur on small length scales given by the Debye lengths of the plasma as stated above.

In a plasma several processes occur such as inelastic collisions, where kinetic energy is transferred to internal energy and vice versa. The most important reactions between atom, ions, electrons, and photons are listed below [Fußmann, 2005]:

$$A^{+Z} + \gamma \rightleftharpoons A^{+Z+1} + e \qquad \text{(photoionization / radiative recombination)} \tag{3.4}$$

$$A^{+Z} + e \rightleftharpoons A^{+Z+1} + e + e \qquad \text{(collisional ionization / three-body recombination)} \tag{3.5}$$

$$A^{+Z} + e \rightleftharpoons \left(A^{+Z}\right)^* + e \qquad \text{(collisional excitation / deexciation)} \tag{3.6}$$

$$A^{+Z} + \gamma \rightleftharpoons \left(A^{+Z}\right)^* \qquad \text{(photon absorption / spontaneous radiative decay)} \tag{3.7}$$

$$A^{+Z} + e + \gamma \rightleftharpoons A^{+Z} + e^* \qquad \text{(photon absorption / bremsstrahlung)} \tag{3.8}$$

The first two reactions, Eq. (3.4) & Eq. (3.5), describe the main mechanisms for ionization as explained in the previous paragraph. Radiative recombination arises from a free-bound transition and leads to uncharacteristic, continuous photons. Also, in the last two reactions photons are emitted

which result in spectral lines for the spontaneous radiative decay (bound-bound transition), Eq. (3.7), and in a continuous spectrum for photons due to bremsstrahlung, Eq. (3.8). In case of complete thermodynamic equilibrium (CTE) every reaction proceeds equally to its reciprocal process and the plasma can be fully described by five thermodynamical variables: temperature T, volume V, pressure p, entropy S, internal energy U, and chemical potential μ. A complete thermal equilibrium is characterized by a single temperature, i.e. the temperature is the same for all species, including electrons as well as heavy particles (atoms and ions). Additionally, for CTE it is required that the photons, i.e. the radiative temperature is coupled. The temperature is of particular importance as it determines, together with the atomic energy levels and ionization energies, the following values and distributions [Fußmann, 2005]:

Population density: The ratio of the population densities of two discrete energy states E_k and E_i for an atom or ion species follows a *Boltzmann-distribution*

$$\frac{n_k}{n_i} = \frac{g_k}{g_i} \times e^{\frac{-(E_k - E_i)}{k_B T_e}} \tag{3.9}$$

with g_k and g_i being the degeneracy parameters of the states k and i, the electron temperature T_e, and the Boltzmann constant k_B.

Number density distribution of ionization stages: The ratio of population densities for two consecutive ionization levels of one species is given by the *Saha-Eggert-Equation*:

$$\frac{n_{z+1} n_e}{n_z} = \frac{g_{z+1}}{g_z} \times \frac{2(2\pi m_e k_B T_e)^{3/2}}{h^3} \times e^{-\frac{E_{z+1} - E_z}{k_B T_e}} \tag{3.10}$$

where n_e is the plasma electron density, n_{z+1} and n_z are number densities of the ionic species, $h = 6.626 \times 10^{-34}$ Js is Planck's constant, and $(E_{z+1} - E_z)$ the ionization energy which is necessary to remove another electron. This equation describes the degree of ionization of a (weakly ionized) plasma as a function of the temperature, density, and ionization energies for a single atomic species. In a LIBS plasma usually no higher excitation states than singly ionized are obtained.

Velocity distribution: The *Maxwell-Boltzmann distribution* describes the particle speeds of the different species in the plasma as a function of the temperature and the mass of the particle m_a:

$$f_a(\vec{r}, \vec{v}) = n_a(\vec{r}) \left(\frac{m_a}{1\pi k_B T_a} \right)^{3/2} e^{-\frac{-m_a v^2}{2 k_B T_a}}. \tag{3.11}$$

Radiation intensity: The energy (frequency) distribution function of the photons in the plasma is determined by Bose-Einstein statistics. For CTE this leads to a continuous emission spectrum (black-body radiation), which is isotropic and unpolarized, described by the *Kirchhoff-Planck-function*:

$$I_\nu = \frac{2h\nu^3}{c^2} \frac{1}{e^{\frac{h\nu}{k_B T}} - 1} \qquad \text{or with} \quad c = \lambda\nu: \qquad I_\lambda = \frac{2hc^2}{\lambda^5} \frac{1}{e^{\frac{hc}{k_B T \lambda}} - 1}. \tag{3.12}$$

Radiated power: The integrated total radiation density is given by the Stefan-Boltzmann-law:

$$F = \int_0^\infty \int_0^{\pi/2} (I_\nu \cos\theta) 2\pi \sin\theta \, d\theta \, d\nu = \sigma T^4 \tag{3.13}$$

with the constant $\sigma = 2\pi^5 k_B^4 / (15 c^2 h^3) = 5.67 \cdot \mathrm{W}/(m^2 \mathrm{K}^4)$.

Complete thermal equilibrium conditions of a plasma can be approached, for instance in the interior of stars, but are not met for the whole system of a laser-induced plasma, where diffusion and interactions with the environment result in energy losses. What could be obtained, however, is a local thermodynamic equilibrium (LTE) which applies only for a certain subset of particles in a small region of the system. In the first instance due to different masses the various species in the plasma equilibrate separately. In a typical LIBS plasma the electron collisions with atoms and ions are more important than radiative processes and radiation temperature is decoupled. Given high enough electron densities, the electron collision rates determine the population distribution of excited states and mainly cause energy transfer approaching an equal temperature for the electrons, ions, and atoms for small regions in the plasma. The critical electron density which has to be reached for LTE is given by the McWhirter criterion[1] [Griem, 1997]:

$$n_e \geq 1.6 \cdot 10^{12} \sqrt{T_e} (E_k - E_i)^3. \tag{3.14}$$

The difference $(E_k - E_i)$ is the highest energy transition for the plasma species. Provided that LTE conditions are fulfilled the Maxwell, Boltzmann, and Saha-Eggert functions are applicable as given in Eq. (3.9-3.11), while in general Eq. (3.12) & Eq. (3.13) for the radiation become unusable. For LTE the plasma can be described by the plasma electron temperature T_e and the electron density n_e. Conversely, these values can be derived from the spectral data.

Plasma temperature

One approach to obtain the plasma temperature is compiling a so-called Boltzmann-plot where relative line intensities of at least two emission lines of the same element are connected to population densities associated with the temperature. Two methods to obtain the plasma temperature in this way are presented in brief here, further information can be found e.g. in [Tognoni et al., 2006].

For an optically thin plasma the total spectrally integrated line intensity due to a transition from level i to a lower level j in units of $\mathrm{Wm^{-3}sr^{-1}}$ is given by [Cremers and Radziemski, 2006a]:

$$I_{ij} = \frac{1}{4\pi} \frac{hc}{\lambda_{ij}} A_{ij} n_i g_i. \tag{3.15}$$

Here, λ_{ij} is the wavelength of the emitted photon, A_{ij} is the Einstein transition probability per unit time, n_i is the population density, and g_i is the degeneracy parameter of the upper level i. Under the assumption that LTE is provided and neglecting self-absorption, the emission line intensities are related to the population of the corresponding energy levels, which in turn are determined by the Boltzmann distribution, cf. Eq. (3.9):

$$n_i = \frac{g_i n}{Z(T)} \times e^{\frac{-E_i}{k_B T_e}}. \tag{3.16}$$

$Z(T)$ is the internal partition function determined by the temperature and expressed as a statistical sum over all states i with energies E_i and the related degeneracy parameters:

$$Z(T) = \Sigma_i g_i e^{-\frac{E_i}{k_B T_e}}. \tag{3.17}$$

- **Two-line method:** When the intensity ratio of two emission lines of the same element and in the same ionization stage is calculated by combination of Eq. 3.15 and Eq. 3.16, the common

[1] It should be noted, that this is a necessary, however, not a sufficient condition to insure LTE but typically holds for a LIBS plasma during the first stages of its lifetime.

constants drop out of the term:

$$\frac{I_{ij}}{I_{kl}} = \frac{g_i A_{ij} \lambda_{kl}}{g_k A_{kl} \lambda_{ij}} \times e^{\frac{E_k - E_i}{k_B T_e}}. \tag{3.18}$$

Applying a logarithm on Eq. 3.18 a linearization is achieved, resulting in

$$\ln \frac{I_{ij} g_k A_{kl} \lambda_{ij}}{I_{kl} g_i A_{ij} \lambda_{kl}} = \frac{E_k - E_i}{k_B T_e}. \tag{3.19}$$

For two emission lines for which A_{ij}, g_i, E_k, and E_i are known, the plasma temperature can then be obtained from the slope $1/(k_B T)$ of the straight line. However, it is not easy to obtain exact relative intensities for the emission lines and the data bases of transition probabilities and degeneracies contain high uncertainties. Multiple transitions should therefore be analyzed in order to obtain a reliable value of the temperature. Appropriate lines of the same species should be selected within close proximity of each other in the spectrum to reduce differences in the spectral response, but on the other hand with different excitation energies to compensate for small fluctuations in emission intensity and to facilitate the definition of the slope of the line.

- **Boltzmann-plot:** Another way to obtain the temperature due to emission line intensities but not being limited to transitions of one ionization stage only is utilizing Eq. 3.18 again with the Boltzmann-equation Eq. 3.16 and logarithmizing:

$$\ln\left(\frac{I_{ij}}{g_i A_{ij}}\right) = \ln\left(\frac{n}{Z(T)}\right) - \frac{E_i}{k_B T_e}. \tag{3.20}$$

Several emission lines from different excitation states of the same species are analyzed simultaneously and are plotted together due to Eq. (3.20) in a Boltzmann-plot. A linear regression is computed for this data and the plasma temperature is obtained from the slope. Thus, the temperature determining the population distribution can be calculated from the relative intensities of several emission lines, whereas knowledge of the population density or degeneracy parameters is not needed. Using multiple emission lines at the same time is an advantage compared to the two-line method presented before in view of the difficulties already mentioned and a more precise value of the plasma temperature can be obtained. An example of a multi-line Boltzmann-plot for a $Fe_2(SO_4)_3$ pressed sample is shown in Fig. 3.3 (right). Here, a set of iron lines in the spectral region ranging from 350 nm to 440 nm was used as indicated in Fig. 3.3 (left). Improvement can be obtained in some cases by correcting for the wavelength response of the system, background correction, or utilizing the integral area of the spectral lines instead of their amplitudes. For comparison, laser-induced plasmas can reach temperatures of up to tens of thousands of degrees shortly after plasma initiation given irradiances of 10^9 to 10^{11} W/cm^2.

Other methods for the determination of the plasma temperature are, for instance based on the ratio of line intensity to continuum intensity, which is applicable for an early stage of the plasma lifetime. Moreover, the Saha ionization and Boltzmann excitation distributions can be used to calculate plasma temperature in case the electron density is known.

Emission lines: shapes, widths and shifts

The emission lines do not only depend on the temperature but are affected also by other plasma parameters and processes. Line widths are related to both, the plasma temperature and the electron density. Moreover, the shapes and shifts of the emission lines can give information on broadening mechanisms.

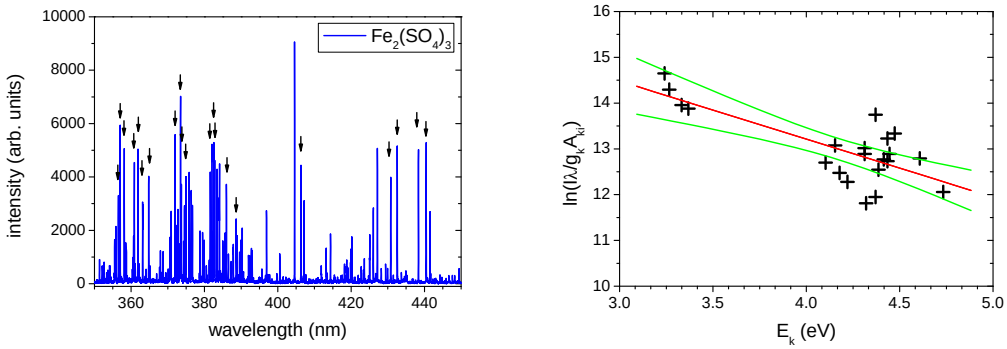

Figure 3.3: *LIBS spectrum of a pressed $Fe_2(SO_4)_3$ salt sample obtained under Martian atmospheric conditions with a delay time of 500 ns and an integration time of 5 µs (left). Indicated are the selected iron lines used for the Boltzmann-plot (right). From the slope of the linear fit (red line) a temperature of $T = 9145 \pm 1810$ K is obtained. The comparatively big error is a result of the widespread data points mainly due to the long integration time, which leads to a mean value for the temperature with regard to both, time and space. Shown are also the 95% confidence level of the linear regression in green.*

Natural broadening: A transition of an electron from one discrete level n_k to a lower level n_i in the atomic shell results in the emission of a photon with the corresponding discrete energy

$$E_\gamma = h\nu_{ki} = \Delta E = E_k - E_i. \tag{3.21}$$

However, the energy is not perfectly defined and even for a free atom, which does not interact with its environment, there is a finite line width as a consequence of the fourier transform limit and the Heisenberg uncertainty principle

$$\Delta E \Delta t \geq \frac{\hbar}{2}. \tag{3.22}$$

Accordingly, a fundamental limit on the precision is set, with which an excited energy state is determined due to its finite lifetime. This uncertainty of energy states translates into an uncertainty of frequency for the emitted photons:

$$\Delta\nu = \frac{\Delta E}{h} = \frac{1}{4\pi\tau} \tag{3.23}$$

The mean lifetime τ of an optical transition is in the order of 10^{-8} to 10^{-9} s which leads to a natural broadening of the line with widths of about 10^{-5} to 10^{-6} nm. The natural broadening effect is homogeneous and results in a Lorentzian profile [Singh and Thakur, 2007]:

$$I(\nu_N) = \frac{I_0 \left(\frac{\gamma}{4\pi}\right)^2}{(\nu - \nu_0)^2 + \left(\frac{\gamma}{4\pi}\right)^2} \tag{3.24}$$

Here, I_0 is the intensity at the center of the line profile ν_0, γ is the radiation damping constant, and $\gamma/2\pi$ is the full width at half maximum (FWHM). Natural broadening is almost always small in comparison to other effects on the spectral line width and can therefore be neglected in the majority of cases.

Doppler broadening: A broadening mechanism virtually always present in a plasma arises from random thermal motions of the particles. Due to the velocity distribution of the atoms emitting

radiation, a red- or blue-shift in the photon's wavelengths is caused by the Doppler effect. Different velocities of the atoms relative to the observer result in different shifts, which collectively lead to a broadening of the line, called Doppler broadening. The Doppler broadening is a heterogeneous effect and depends on the frequency ν_0 of the spectral line but also on the mass M of the emitting atom or ion, and the velocity determined by the plasma temperature T through a Maxwell-Boltzmann distribution, cf. Eq. (3.11). With increasing temperature of the plasma the velocity distribution becomes wider, giving rise to a broader spectral emission line. The resulting emission line profile has a Gaussian profile with a FWHM given by [Hahn and Omenetto, 2010]

$$\Delta\lambda_D = \frac{2\lambda_0}{c}\sqrt{\frac{k_B T \ln 2}{M}} = 7.16 \times 10^{-7}\lambda_0\sqrt{\frac{T}{M}}. \tag{3.25}$$

The line shape is mainly influenced near its center. In comparison to the speed of light, the atomic speeds are relatively small, which leads to a comparatively small effect on the frequency in the order of 10^{-2} to 10^{-3} nm. However, this is considerably bigger by two to three orders of magnitude in comparison to the natural broadening, which for that reason can usually be neglected. In a plasma with low electron densities, broadening due to the Doppler effect is usually the dominant mechanism.

Pressure broadening: There are several mechanisms, which lead to a broadening of the spectral lines due to interaction of the radiating atoms and ions with other neighboring particles of the plasma, hence, disturbing the emitted photons' frequencies and causing a phase shift. For instance, broadening occurs as a consequence of the van-der-Waals forces between a neutral particle emitting a photon and other neutral particles of the plasma. This is an effect predominant in a plasma with a low degree of ionization. Moreover, resonance broadening (self-broadening) takes place, where two identical species interact. An emitted photon can be absorbed by another atom or ion of the same kind or may induce the emission of another photon of the same frequency. The natural lifetime of an energy state is decreased by this induced absorption and emission, which leads to a resonance broadening of the spectral lines, but unshifted.

In a plasma with a higher degree of ionization Stark broadening occurs, which is due to an emitting particle being perturbed by the electric field of close-by charged particles. The energy levels of the radiating atom or ion are split and shifted by the interacting Coulomb-field

$$\vec{E}_C = \frac{e}{4\pi\varepsilon_0 r^2}\cdot\hat{\vec{r}}. \tag{3.26}$$

The first-order Stark-effect causes a shift in energy linear in the applied field strength ($\sim E$ and $\sim 1/r^2$), called linear Stark effect, and exists for hydrogen and hydrogen-like ions only. Here, the energy levels split up symmetrically, which leads to a symmetrically broadened and unshifted line. For non-hydrogenic species the quadratic Stark effect applies ($\sim E^2$ and $\sim 1/r^4$), causing an asymmetric broadening and also a red-shift, which is the same for electrons and ions [Gornushkin et al., 1999]. The line width due to the quadratic Stark broadening is given by [Tognoni et al., 2006]

$$\Delta\lambda_S = 2w\left(\frac{n_e}{10^{16}}\right) + 3.5A\left(\frac{n_e}{10^{16}}\right)^{1/4}\left[1 - BN_D^{-1/3}\right]w\left(\frac{n_e}{10^{16}}\right). \tag{3.27}$$

Here, w is the electron impact parameter, A is the ion broadening parameter, B is a coefficient with values of 1.2 or 0.75 for ionic or neutral lines, respectively, and N_D is the number of particles in a sphere where the radius equals the Debye length (cf. Eq. (3.2)). Electron interaction is considered in the first term on the right side whereas the second term allows for ion interaction and is negligible for typical LIBS conditions. Thus, broadening due to the Stark effect in a LIBS plasma is given approximately by

$$\Delta\lambda_S \approx 2w \left(\frac{n_e}{10^{16}}\right). \tag{3.28}$$

Values of w can be found e.g. in [Griem, 1974]. If the Stark effect is the dominant line broadening effect in the plasma and other effects can be neglected, from a measured line width and with Eq. (3.28) the electron density can be calculated. Of all the pressure broadening effects the Stark effect in a plasma usually dominates resonance and van-der-Waals broadening.

In a typical LIBS plasma the main contributions to the line widths are a result of both, the Stark effect and the Doppler effect. The Stark effect dominates for high electron densities, such as those found during the early stages of plasma lifetime. Later on when the plasma cools and electron densities decrease, the Doppler effect becomes more important. Both effects do not only vary on a temporal scale but also spatially within the plasma. Also, lines of different species are differently affected due to the transition and the species' relative abundance in the plasma. When both effects take place and none can be neglected, the line profiles are superimposed. The combination of the Doppler broadening, which is described by a Gaussian function, and the Stark effect, given by a Lorentz function, yields a so-called Voigt profile. Given high enough resolution of the LIBS spectra the spectral line profiles can be deconvoluted and the Gaussian and Lorentzian component can be separated. Moreover, a broadening due to the instrument (determined by the parameters of the spectrometer and camera) should be taken into account and has to be deconvoluted prior to further analysis.

An emission line which is dramatically broadened by the Stark effect is the most intense hydrogen line H_α at 656.285 nm. It has been frequently used for determining the electron density in a LIBS plasma [Hahn and Omenetto, 2010] since the linear Stark effect applies. This allows for a simple calculation and yields more accurate results than the quadratic Stark effect [Singh and Thakur, 2007]. However, self-absorption is likely to occur, which strongly distorts the spectral line shape. A more favorable choice is H_β at 486.133 nm, which has a high enough intensity but with a reduced chance for self-absorption.

Optimizing LIBS data acquisition

Typically the emission from multiple laser-induced plasmas is accumulated or averaged in order to obtain higher signal-to-noise ratios (SNR) of the emission lines and to increase accuracy and precision of the analysis. By averaging several spectra, partly substantial shot-to-shot variations in the plasma characteristics and statistical fluctuations are compensated. Moreover, in case of small spatial variations and irregularities in the composition of the sample a mean spectrum can be obtained, which represents an average of the bulk material. A not representative surface layer can be removed by preceding laser pulses as previously mentioned.

The continuum radiation caused by bremsstrahlung and recombination during the first several hundred nanoseconds after plasma formation contributes no information about the elemental composition and can prevent the detection of weak lines in the spectra. Commonly time-resolved detection of the plasma emission where recording starts after a certain time delay in order to exclude the strong continuum radiation from detection considerably improves SNR of the spectral lines. Another effect of dismissing the emission of the first instants of the plasma are sharper emission lines due to a reduced density in the post-laser-pulse regime and therefore less spectral-line broadening as a result of the Stark effect. A sketch of the chronology of time-resolved plasma detection for LIBS is shown in Fig. 3.4. The time delay t_d is defined as the time between the laser trigger signal and the camera trigger signal which starts observation of the plasma emission. It has to be optimized, additionally taking into account the emission lines of fast decaying ions, whose signal might be lost at some point. An optimal delay time highly depends on the sample characteristics, its elements and matrix. The so called gate time t_g is the time period over which the light is recorded and has to be tuned as

well. Both gating parameters have to be chosen in order to maximize SNR of the emission line to be analyzed. If multiple elements are of interest, which usually require more or less different gating parameters for maximum SNR, a compromise has to be made. Parameters best suited for the LIBS analysis of frozen salt solutions are determined in Chapter 6.

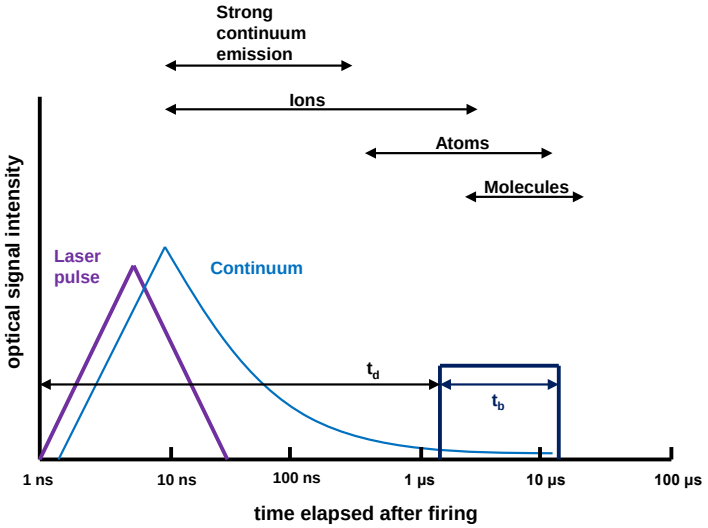

Figure 3.4: *Shown is schematically the temporal history of a laser-induced plasma (laser wavelength 1064 nm, pulse duration 5 - 10 ns) in air at 101 kPa and subsequent time-resolved detection, adapted from [Cremers and Radziemski, 2006a]. After plasma initiation the emission is dominated by continuum radiation which can be partially excluded from detection by not starting detection until a certain time delay t_d. Also the detector gating window is shown, which is the time duration t_g in which the plasma emission is recorded.*

3.3 Hardware and instruments

Generally, a LIBS system consists of a high-energy pulsed laser source, an optical system that focuses the laser radiation on the target sample and optics constituting the plasma light collecting system, such as lenses, mirrors or fiber optic. Moreover, a spectrometer with a dispersive element causing a spatial separation of the plasma emission due to different wavelengths and a detector to record it. A computer is usually used to control and synchronize the trigger of both, the laser and the spectrometer. The hardware used for this study is presented in detail in Chapter 5.

3.4 LIBS for space applications

As an analytical technique LIBS is particularly well-suited for its application in planetary science. Maybe the most outstanding advantage of LIBS is its ability to investigate soil and rocks at distances of up to several meters requiring optical access only. Stand-off elemental analysis can thus be done with a high power laser which is focused onto a target of interest near the instrument. This is a big advantage in comparison to other methods deployed for geochemical analysis on planetary missions, which require physical contact with the sample for its investigation. Most techniques require the sample of interest to be closely approached or even placed inside the instrument, which is a time- and energy-consuming activity. In some cases additionally time-consuming and complex sample preparation is required. Given limited time (and energy) on a planetary mission and additionally being restricted by the accessability of multiple targets, only a small number of samples can be analyzed. For LIBS the only requirement is that the target to be analyzed needs to be within a certain radius and in direct line-of-sight, in this way enabling the analysis of physically hard to reach and inaccessible targets. This can be done in an in-situ or close-range scenario but also at stand-off distances up to 80 m meters with nanosecond (ns) pulses and even further with femtosecond (fs) laser pulses [Cremers, 2007]. Dust or weathering layers can be removed and also analyzed if required [Sharma et al., 2007]. As already mentioned, LIBS is capable of depth profile analysis, which was shown for the purpose of extraterrestrial exploration e.g. by [Cousin et al., 2009], [Rauschenbach et al., 2010].

LIBS was soon considered a powerful analytical technique for the in-situ geochemical investigation of extraterrestrial surfaces and has been evaluated for application in planetary science in a number of studies, e.g. [Brennetot et al., 2003], [Colao et al., 2004], [Del Bianco et al., 2006], [Sallé et al., 2005], [Rauschenbach et al., 2008]. In an early study the effects of different pressures were investigated as mentioned before by [Knight et al., 2000]. The visual appearance, i.e. the size and brightness of the laser-induced plasma plume highly depends on the ambient pressure, as can be seen in Fig. 3.5 [Cremers, 2007]. At normal (Earth) atmospheric pressure, a small and bright spherical plasma about 2-3 mm in height is obtained, confined by the ambient pressure. Under Mars conditions ($\approx$ 930 Pa) a much enhanced laser spark is observed due to the lower pressure permitting plasma expansion into a larger volume. Most of the emission results from the central region of the plume slightly above the surface. When the pressure is further reduced, the spatial distribution of the emitting species

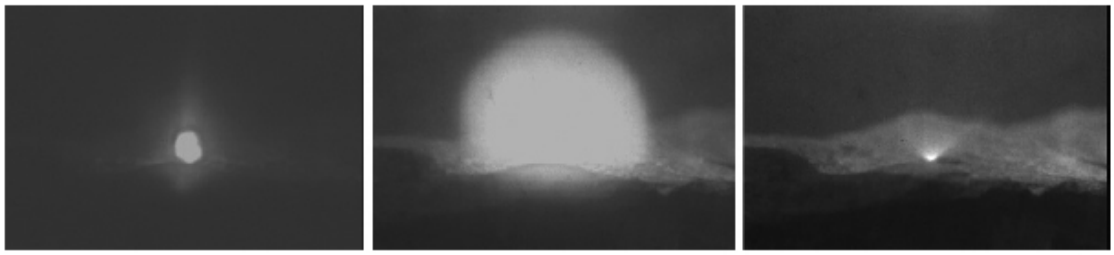

Figure 3.5: *Shown are three individual laser-induced plasmas formed on basalt rock at different pressures (left: 78 kPa (terrestrial, Los Alamos atmospheric pressure), center: 930 Pa (Mars), right: 0.016 Pa (airless bodies) recorded with an ICCD. A gain was chosen which yielded an enhancement of the intensity of the images by a factor of 7. Gating delay and width were 2 µs and 80 ms, respectively. For Earth atmospheric conditions the plasma is a small sphere confined by the surrounding pressure. For Martian atmospheric conditions (930 Pa) the plasma volume increases whereas for further reduced pressures simulating airless bodies merely a small cone-shaped plasma is observed, which quickly decays. Adopted from [Cremers, 2007].*

significantly decreases in size to a small cone-shaped region just above the target surface. The different appearances of the plasma can be explained as a result of mainly two processes [Cremers, 2007]. First, as previously mentioned in Section 3.1, a varying amount of mass is ablated depending on the efficiency of plasma shielding, which in turn is a function of pressure. At high pressure, mass ablation is reduced by the dense plasma attenuating still incoming laser radiation. Second, with decreasing ambient pressure the plasma expansion increases, resulting in lower electron densities and a reduced collisional excitation accompanied by reduced plasma emission. Martian atmospheric pressure is almost optimal for LIBS observations, as more material is ablated in comparison to Earth atmospheric conditions, which more than compensates for intensity losses due to decreased pressure. At even lower pressures the amount of ablated mass remains constant, however, the plasma expands rapidly and decreasing collisions rates result in a significantly decreased signal. Emission line intensities of four elements as a function of pressure are shown in Fig. 3.6. As can be seen, the line intensities are maximal for pressures ranging from 1 kPa to 10 kPa.

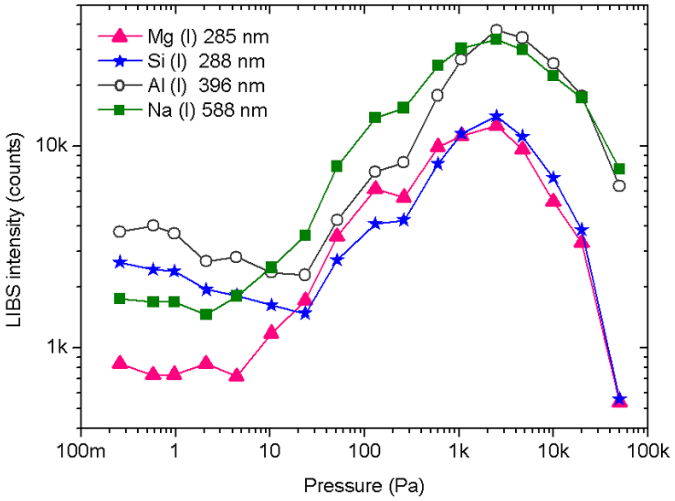

Figure 3.6: *Emission line intensities of four elements obtained from a basaltic sample as a function of pressure [Pavlov et al., 2012]. A low energy laser was utilized with a pulse energy of 1.88 mJ corresponding to an irradiance on the sample of approximately 96 MW/mm^2.*

The advantages of LIBS have also been acknowledged by NASA and together with a remote micro-imager (RMI) a standoff LIBS system called ChemCam is part of the payload on the Mars Science Laboratory (MSL) Curiosity rover. MSL is currently on its way to Mars [Wiens et al., 2011a], [Wiens et al., 2011b]. It was launched in November 2011 and will arrive on Mars in August 2012 in the Gale Crater, cf. Fig. 2.2. The landing site was chosen from a total of 50 proposed targets considering [Anderson, 2012] [Grant et al., 2011]

- the capability to characterize the geology,
- the likelihood of finding a present or in former times habitable environment,
- the preservation potential of the depositional setting,
- the ability to judge the biological potential of the deposits.

In combination with engineering considerations and after a selection process proceeding over 6 years and including several landing site workshops, finally Gale Crater was chosen and was announced as the MSL landing site in July 2011. ChemCam will utilize an infrared (wavelength 1067 nm) Nd:KGW laser with a spot size of 200-500 μm, a pulse duration of 5 ns, 1-10 Hz repetition rate, and a pulse energy of ca. 14 mJ to ablate material of targets within a distance of 7 m to the rover [Maurice et al., 2012]. The ChemCam instrument will take measurements independently and carry out analysis of targets beyond the reach of the other instruments on board of MSL. Furthermore, it will be used in a supportive way for strategic planning, contributing information for decisions about further investigation of potentially interesting and accessible targets with other techniques, which require further approaches, additional energy and time. This is the first time that a LIBS instrument will be applied for in-situ analysis on a planetary mission.

Due to the ChemCam instrument including LIBS, multiple recent studies focused on the application of LIBS on the Martian surface and concentrated on stand-off analysis with ChemCam-like set-ups e.g. [Anderson et al., 2011], [Sallé et al., 2007], [Tucker et al., 2011]. Strategies for data acquisition were developed and tested, and analysis procedures optimized in order to improve reliability. Moreover, calibration was done for geological material [Fabre et al., 2011], [Lanza et al., 2010] and data bases were built [Cousin et al., 2011].

Chlorine and sulfur are two important elements in Martian geochemistry, however, known to be difficult to detect with LIBS due to high excitation energies ($\geq$ 10 eV). This applies above all for LIBS measurements in ambient conditions, e.g. [Gaft et al., 2009]. Martian atmospheric conditions facilitate the detection of chlorine and sulfur which was shown e.g. with a ChemCam parameters replicating instrument by [Dyar et al., 2011] or earlier for two different LIBS setups by [Sallé et al., 2004]. Plasma emission in the vacuum ultraviolet (VUV) spectral region ranging from 100-200 nm was investigated under Martian atmospheric conditions [Radziemski et al., 2005] in a close-up setup. The effects of laser energy and delay time were examined and among other elements also sulfur and chlorine were detected. Also, the effect of the CO_2 in the ambient gas was investigated with regard to the detection of carbon in soil. [Arp et al., 2004b] investigated water ice and water ice/soil mixtures with LIBS for a possible application to Mars polar exploration. At short and intermediate stand-off distances LIBS spectra of several kinds of samples with water ice were acquired in a CO_2 atmosphere at 700 Pa. LIBS for rocks, soil and ices at subzero temperatures in a Martian environment was moreover investigated by [Lazic et al., 2007].

Research is also performed on the application of LIBS for bodies with thin or no atmosphere like for missions to asteroids [Ishibashi et al., 2011], [Pavlov et al., 2012] and lunar exploration ($\approx$ 0.05 Pa) [Lasue et al., 2012], [Mezzacappa et al., 2010]. Applying LIBS in high pressure environments such as on Venus ($\approx$ 9200 kPa) [Arp et al., 2004a], [Lambert et al., 2010] is considered as well. Together with temperatures in excess of 700 K these conditions are significantly challenging for spacecraft design. Here, a fast technique is needed for a rapid analysis of chemical data due to expected operational lifetimes of surface instrumentation in the order of only two hours in total. While the temperature should pose no problem to the analytical capabilities of the LIBS spark, the high pressure has strong influence on the laser-induced plasma and significant emission line broadening and self-absorption appears in the LIBS spectra [Arp et al., 2004a].

4 Multivariate data analysis methods

LIBS is known to suffer from so-called matrix effects i.e. chemical and physical properties of the sample influencing the intensity of the emission lines of a specific element. The so-called physical matrix effects are due to physical properties of the sample such as specific heat, thermal conductivity, absorption, or soil grain size. These properties mainly influence the process of ablation and therefore the amount and the composition of ablated material [Cremers and Radziemski, 2006b]. In some cases these effects can be corrected for by building ratios of emission lines with another element of known or constant concentration. On the other hand, the emission signal of one element can be affected by the presence and abundance of an interfering signal from another element of the matrix, called a chemical matrix effect. All matrix effects complicate quantitative analysis, where the intensity of an emission line should correlate with the element's abundance at best linearly.

A traditional approach for quantitative analysis is calibration with a set of standards i.e. reference materials with a matching or at least similar matrix. The composition of unknown samples is then predicted by means of univariate linear regression. However, insufficient comparability of the reference matrix and also varying characteristics of the plasma from shot to shot can inhibit a suitable calibration. Moreover, the use of lines which are affected by self-absorption can make a quantification difficult or impossible.

Different approaches to overcome these matrix effects have been developed and applied in the past, one of them being multivariate data analysis (MVA) methods. In particular for sample classification and quantitative analysis of geological samples with LIBS a great number of studies was performed and MVA techniques for LIBS data were tested, improved and further developed by multiple authors [Anderson et al., 2011], [Clegg et al., 2009], [Gottfried et al., 2009b], [Labbé et al., 2008], [Lasue et al., 2011], [Ollila et al., 2012], [Sirven et al., 2007], [Tucker et al., 2010]. In comparison to univariate data analysis, where only one statistical variable is considered at a time, MVA is based on multivariate statistics, taking into account multiple variables, i.e. spectral lines for LIBS. Redundant spectral information is combined and the relevant information is unveiled. The typically large and complex LIBS data sets are reduced by means of extracting the important information from the spectra.

The following sections present an overview of three MVA methods applied in this work, further detail can be found e.g. in [Esbensen, 2010], [Kessler, 2007].

4.1 Principal component analysis (PCA)

PCA is one of the most frequently utilized methods for pattern recognition of latent structures in data sets of high dimension. It is an unsupervised technique i.e. initial information about classes or composition of the samples in the data matrix is not involved.

The initial $(m \times n)$ data matrix $\mathbf{X}$, where m is the number of variables, i.e. wavelength channels and n the number of spectra, is transferred into two smaller matrices, a so-called scores matrix $\mathbf{T}$ $(a \times n)$ and the loadings $\mathbf{P}$ $(m \times a)$, as illustrated in Fig. 4.1. A smaller number $(< m)$ of uncorrelated variables is determined, which are linear combinations of the initial variables in the multidimensional data matrix but still provide the main information. So-called principal components (PCs) constitute the axes of a new basis and are found by calculating the eigenvectors and corresponding eigenvalues.

Every eigenvalue together with the related eigenvector constitute a factor (PC) which is stored in the columns of the loadings matrix. The loadings matrix **P** thus contains the systematic variation in the data matrix **X**. Their weighting is stored in the score matrix **T**, which provides the coordinates for every object (spectrum) with respect to the newly defined PCs. The matrix **E** contains the spectral residues, which are obtained as the difference of original and reconstructed spectra.

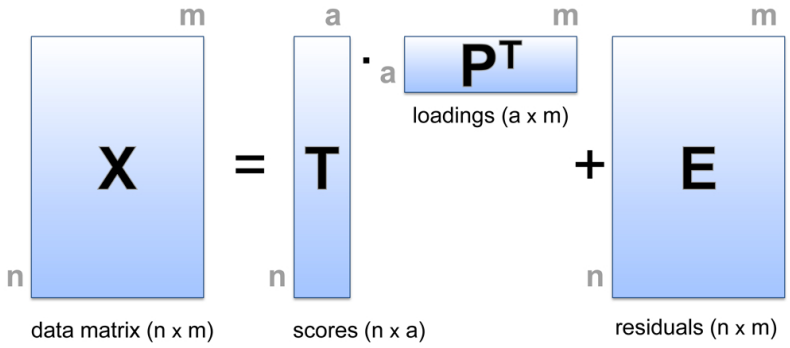

Figure 4.1: *With principal component analysis (PCA) the ($m \times n$) data matrix* **X** *(m = number of wavelength channels, n = number of spectra) is decomposed into a part that contains the relevant information (scores and loadings matrices) and a part that includes what remains (spectral residues* **E***), which is mainly noise. Adapted from [Kessler, 2007].*

Mathematically, for PCA an eigenvalue problem has to be solved and a linear transformation to a newly defined orthogonal basis is performed taking into account the greatest variance in the data. The data matrix **X** is mean centered for this purpose, meaning that a mean value is calculated for every column (variable) which is then subtracted from every original value in the column. In this way the mean value is excluded from the first PC. The general PCA-model reads

$$\mathbf{X} = \mathbf{T}\mathbf{P}^{\top} + \mathbf{E} \tag{4.1}$$

which can be written as

$$x_{nm} = x_{\text{mean},m} + \sum_{a=1}^{A} t_{na} p_{ma} + e_{nm(A)} \tag{4.2}$$

for the case that mean centering has been done in a previous step. Here:

$x_{\text{mean},m}$ = mean value of the m-th column
t_{na} = score for n-th object (spectrum) and a-th principal component
p_{ma} = loading for m-th variable and a-th principal component
$e_{nm(A)}$ = residual error for A principal components.

The PC model is a linear additive model where step by step PCs are added containing additional information. The first PC accounts for the maximal amount of variance in the data and all variables it correlates with are included. The second PC accounts for the maximal remaining variance and is orthogonal to the first PC and thus uncorrelated. Every subsequent PC is another orthogonal solution which contains the largest amount of variation in the data set that was not included in the previously defined PCs. The dimension of the originally large and complex data set is thus reduced, but contains the relevant information in a compact form. For the PCA the The Unscrambler software

[CAMO, 2012], which was utilized in this study, employs the Non-linear Iterative Partial Least Squares (NIPALS) algorithm to determine the eigenvectors. This algorithm was developed by Herman Wold [Wold, 1966] and can be used for the iterative calculation of the PCs, one component at a time and one after another. NIPALS is based on a numerical approach with an approximation procedure to find the first A eigenvalues of the covariance matrix obtained from the data matrix. An initial random solution is improved stepwise until a predefined error level is undercut. In summary this reads [Esbensen, 2010], [Kessler, 2007]:

1. First, the data matrix $\mathbf{X}$ is centered and optionally scaled appropriately, the index is initialized: $f = 1$; $\mathbf{X}_f = \mathbf{X}$.

2. The algorithm starts with an initial proxy score vector $\mathbf{t}_f$, for which it is advantageous to choose the column with the largest variance.

3. The corresponding loading vector $\mathbf{p}_f$ is calculated for iteration step f by projecting the data vectors of the $\mathbf{X}$ onto this score vector:

$$\mathbf{p'}_f = \frac{\mathbf{X}_f^T \mathbf{t}_f}{|\mathbf{t}_f^T \mathbf{t}_f|}. \tag{4.3}$$

4. The loading vector $\mathbf{p'}_f$ is normalized to length 1, giving $\mathbf{p}_f$.

5. A new corresponding score vector $\mathbf{t}_f$ is calculated by projecting the matrix $\mathbf{X}_f$ onto the new loading vector $\mathbf{p}_f$:

$$\mathbf{t}_f = \frac{\mathbf{X}_f \mathbf{p}_f}{|\mathbf{p}_f^T \mathbf{p}_f|}. \tag{4.4}$$

6. In order to check for the convergence of the iterative process, the eigenvalue of the new score vector $\mathbf{t}_f$ is compared to the previous one:

$$d = \tau_{\text{f-1}} - \tau_{\text{f}}. \tag{4.5}$$

   If the difference d is larger than a predefined threshold (e.g. 10^{-6}) the process continues with step 3.

7. In case the convergence criterion is fulfilled, the estimated PCA component (which is the product of the scores and the loadings) is removed from the data matrix $\mathbf{X}_f$:

$$\mathbf{X}_{f+1} = \mathbf{X}_f - \mathbf{t}_f \mathbf{p}_f^T. \tag{4.6}$$

8. The index is increased by 1 ($f = f + 1$) and the next principal component is calculated restarting with step 2.

The steps 2 to 8 are repeated until either all possible PCs are calculated (maximum number of PCs = total number of variables m in the data matrix), a previously determined number of PCs is obtained and/or a demanded amount of total variance is explained. The NIPALS algorithm is frequently applied for data where the number of required PCs is much less than the possible number m, which is usually the case for spectral data.

One of the main aims of PCA is data reduction by means of combining multiple features (variables) by the use of principal components and to describe the objects with them. PCA is commonly utilized for data exploration in order to reveal hidden patterns, structures, and major trends. Similarities and differences can be found and variables responsible for these are unveiled. However, it should be noted that PCA is not optimized for class separability.

4.2 Soft independent modeling of class analogy (SIMCA)

An application of PCA is SIMCA, a supervised technique, where the class membership of the samples is known in advance and utilized for building a model [Esbensen, 2010]. SIMCA is applied for pattern recognition and classification of unknown samples by comparing them to a group of similar samples and assigning them to the class to which they show maximal similarity. Instead of performing a PCA for all of the data, the data set is subdivided corresponding to class affiliation. The classes are centered and scaled independently and a separate PCA model is built for each of those classes. A sufficient number of PCs is considered, which account for most of the variation within the local group and is determined by cross-validation. For cross-validation, segments of the data are omitted from the data matrix and a PCA is performed with the remaining training set. The excluded data are used as validation set and are predicted in comparison to the actual values. The procedure is repeated until every element of the data has been kept out at least once and the PCA model with minimum prediction error is retained. For the total number of PCs included for the model two aspects should be considered [Kessler, 2007]: First, the number of PCs has to be chosen in order to sufficiently describe the data. Second, with too many PCs the model can become over-determined and higher PCs include randomly distributed noise (over-fitting). The optimal number of PCs can be determined by the validation. The prediction error of a model is a combination of the model error (i.e. calibration error) and the estimation error, which is a result of the calibration model describing random variations. The model error decreases with an increasing number of PCs included in the model, whereas the estimation error increases, although less strongly. A minimum prediction error thus indicates the best suitable number of PCs, which should be included in the model. When all classes are modeled, the samples with unknown class membership are assigned to a class by projecting them into each subspace and comparing the distance. Minimal distance to a class is interpreted as highest probability of class membership.

With SIMCA the common properties of the classes are modeled, which was shown to be a suitable approach for the prediction of classes with big differences. However, for data sets of classes, which are very similar, SIMCA experiences difficulties in distinguishing among them as discussed later on in Chapter 7.

4.3 Partial least squares (PLS) regression

PLS regression - sometimes also called "Projection to Latent Structures" - is a supervised statistical method, which considers both, the data matrix $\mathbf{X}$ and the structure of a response matrix $\mathbf{Y}$ to determine principal components for the data matrix. The goal is to predict a set of dependent variables (=responses) from a set of independent variables (=data, predictors). A PCA is performed for both matrices, which are then connected. The underlying model is

$$\mathbf{X} = \mathbf{T}\mathbf{P}^T + \mathbf{E} \tag{4.7}$$

$$\mathbf{Y} = \mathbf{U}\mathbf{Q}^T + \mathbf{F} \tag{4.8}$$

which is depicted schematically in Fig. 4.2. Here, $\mathbf{X}$ is again the data matrix (predictor variables), $\mathbf{Y}$ contains the response variables, $\mathbf{T}$ and $\mathbf{P}$ are scores and loadings of the data matrix, respectively, and $\mathbf{U}$ and $\mathbf{Q}$ represent scores and loadings of the $\mathbf{Y}$ matrix. $\mathbf{E}$ and $\mathbf{F}$ are the matrices of residuals. The $\mathbf{W}$ matrix is of the same dimension as the loadings matrix $\mathbf{P}$ and connects $\mathbf{X}$ to $\mathbf{Y}$ with loading weights vectors. They contain the information about how each x-variable relates to a variation in $\mathbf{Y}$.

For PLS one, or several dependent variables (PLS1 or PLS2, respectively) are taken into account, which could be, for instance elemental composition or simply class membership. The PLS2 NIPALS algorithm used in the Unscrambler software includes the following steps [Esbensen, 2010], [Kessler, 2007]:

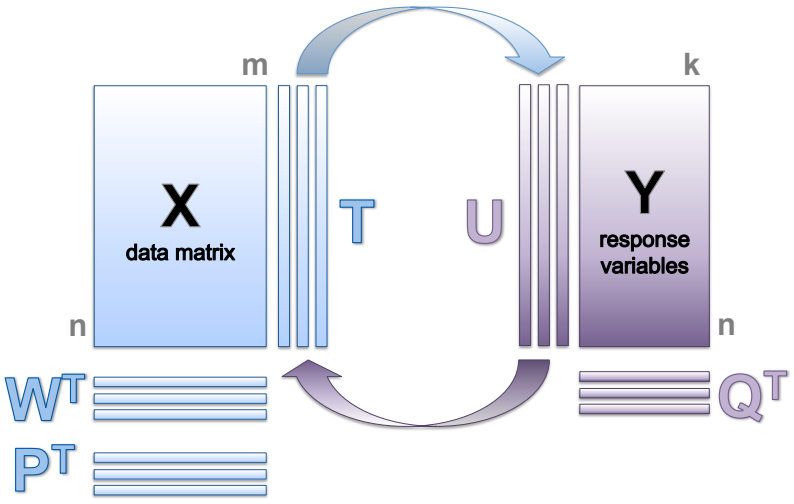

Figure 4.2: *Schematic overview of the partial least squares (PLS) regression and the two matrices involved. PLS actively connects* $\mathbf{X}$ *and* $\mathbf{Y}$ *creating score vectors by maximizing the covariance between both. Adopted from [Kessler, 2007].*

1. Both matrices, $\mathbf{X}$ and $\mathbf{Y}$ are centered and scaled appropriately, the index f is initialized: $f = 1$; $\mathbf{X}_f = \mathbf{X}$; $\mathbf{Y}_f = \mathbf{Y}$.

2. An initial proxy score vector $\mathbf{u}$ is chosen, expediently the column vector of $\mathbf{Y}$ with the largest value $\mathbf{u}_f = \max|\mathbf{Y}_i|$.

3. The weighted loadings $\mathbf{w}_f$ for $\mathbf{X}_f$ are found by solving

$$\mathbf{X}_f = \mathbf{u}_f \mathbf{w}_f^T + \mathbf{E} \tag{4.9}$$

   by means of a least squares procedure. The solution reads

$$\mathbf{w}_f = \frac{\mathbf{X}_f^T \mathbf{u}_f}{\sqrt{(\mathbf{X}_f^T \mathbf{u}_f)(\mathbf{X}_f^T \mathbf{u}_f)^T}} \tag{4.10}$$

   where $\mathbf{w}_f$ is normalized to a length of one.

4. The appropriate scores for every object are calculated with a least squares procedure solving

$$\mathbf{X}_f = \mathbf{t}_f \mathbf{w}_f^T + \mathbf{E} \tag{4.11}$$

   which yields $\mathbf{t}_f = \mathbf{X}_f \mathbf{w}_f$.

5. For the now known scores $\mathbf{t}_f$ the appropriate loadings $\mathbf{p}_f$ are calculated:

$$\mathbf{X}_f = \mathbf{t}_f \mathbf{p}_f^T + \mathbf{E} \tag{4.12}$$

   which yields $\mathbf{p}_f = \mathbf{X}_f^T \mathbf{t}_f / (\mathbf{t}_f^T \mathbf{t}_f)$.

6. Information is then transfered from the X-variable space to the Y-variable space by performing a regression of the scores $\mathbf{t}_f$, which were obtained in step 4:

$$\mathbf{Y}_f = \mathbf{t}_f \mathbf{q}_f + \mathbf{F}. \tag{4.13}$$

This yields $\mathbf{q}_f = \mathbf{t}_f^T \mathbf{Y}_f / (\mathbf{t}_f)^T \mathbf{t}_f$.

7. Convergence is tested by comparing the newly obtained scores $\mathbf{t}_f$ with those of the previous iteration $\mathbf{t}_{f-1}$ (in case of the first iteration they are compared to the $\mathbf{u}_f$ vector). If the scores differ more than a certain amount (typically in the order of 10^{-6}) the current $\mathbf{u}$-scores have to be updated with the $\mathbf{q}$-loadings:

8.
$$\mathbf{Y}_f = \mathbf{u}_f \mathbf{q}_f^T + \mathbf{F} \tag{4.14}$$

which yields $\mathbf{u}_f = \mathbf{Y}_f \mathbf{q}_f / (\mathbf{q}_f^T \mathbf{q}_f)$. The $\mathbf{t}_f$-scores are replaced by the newly found $\mathbf{u}_f$-vector and the process continues with step 3.

9. In case convergence was achieved, the fth-component is subtracted from both, the $\mathbf{X}$ and the $\mathbf{Y}$ matrix, called deflation:

$$\mathbf{X}_{f+1} = \mathbf{X}_f - \mathbf{t}_f \mathbf{p}_f^T \qquad \text{and} \qquad \mathbf{Y}_{f+1} = \mathbf{Y}_f - \mathbf{t}_f \mathbf{q}_f^T. \tag{4.15}$$

Using the $\mathbf{p}$-vectors instead of the $\mathbf{w}$-vectors for updating $\mathbf{X}$ allows for the desired orthogonality for the $\mathbf{t}$-vectors.

10. The index is increased by 1 ($f = f+1$) and the next PLS-component is calculated restarting with step 4. This is repeated until a predefined total number f_{max} of PLS-components is obtained.

11. What remains of $\mathbf{X}$ and $\mathbf{Y}$ after subtraction of the information included in the model is stored in $\mathbf{E}$ and $\mathbf{F}$, respectively, and constitute the remaining variance: $\mathbf{E} = \mathbf{X}_{\text{fmax}+1}$ and $\mathbf{F} = \mathbf{Y}_{\text{fmax}+1}$.

12. As a last step, the regression coefficients for the x-variables are calculated, which results in a regression coefficient matrix $\mathbf{R}$ with the dimension of $n \times k$:

$$\mathbf{B} = \mathbf{W} \left(\mathbf{P}^T \mathbf{W} \right)^{-1} \mathbf{Q}^T \tag{4.16}$$

which includes a regression vector $\mathbf{b}_k$ for every column k of the $\mathbf{Y}$ matrix. Moreover, $\mathbf{b}_0 = \overline{\mathbf{y}}^T - \overline{\mathbf{x}}^T \mathbf{B}$.

The PLS components are referred to as latent variables (LVs).

Partial least squares discriminant analysis (PLS-DA)

In this work Partial Least Squares Discriminant Analysis (PLS-DA), which focuses on class separation revealing and utilizing the features in the data relevant for classification, was applied to LIBS data. PLS-DA is a classical PLS regression where the response variable matrix $\mathbf{Y}$ is binary. A $\mathbf{Y}$ matrix of dependent variables is built, comprising the information of class affiliation in an encoded, binary form by using artificial variables, e.g. 1 for the members of a certain class and 0 for non-members. LVs are then derived which maximize the covariance between the measured variables and the response variables by taking into account the spectral variance as well as the information about class membership as explained above. In comparison to the PCs, the derived LVs better describe the variation that affects the response variable alteration. Large variations in the data which do not affect the response variables are disregarded. The relevant measured variables for classification are identified.

5 LIBS for planetary surface exploration - experimental set-up and samples

As stated in Chapter 3, both pressure and composition of the ambient atmosphere have great influence on the laser-induced plasma, its characteristics and therefore its emission and the resulting LIBS spectra. In order to test the performance and suitability of LIBS for different applications in planetary science, similar atmospheric conditions have to be simulated experimentally. The experimental work presented in this thesis was done in the laboratory at the German Aerospace Center (Deutsches Zentrum für Luft- und Raumfahrt e.V., DLR) at Berlin Adlershof. An overview of the hardware is given in this chapter. Moreover, an overview of the samples that were analyzed is given and the sample preparation procedure is described.

5.1 Laboratory setup

The laboratory LIBS setup at DLR Berlin was constructed specially for the purpose of testing and developing LIBS for applications in planetary science. The setup allows for exchange and coupling of different components to the already existing system. Thus, prototypes and single components can be tested. During the time of taking measurements at the DLR Berlin for this thesis, the laboratory setup was composed of two different infrared lasers and an echelle spectrometer with intensified charge-coupled device (ICCD) with two available wavelength ranges. The setup is combined with a dedicated simulation chamber for the simulation of planetary conditions. A sketch of the setup can be seen in Fig. 5.1 and an overview of the components is provided in Table 5.1.

Laser

The first laser (henceforth referred to as "Inlite laser") used during this work was a Q-switched Nd:YAG laser (Continuum, model Inlite II-20) operating at its fundamental wavelength of 1064 nm with 10 Hz repetition rate, 8-10 ns pulse duration, and a maximum pulse energy of 220 mJ. The energy of the laser can be varied by a set of grey filters, resulting in transmissions ranging from 0.4 to 70.5% by different combinations. Throughout the studies presented in this work, the laser was usually reduced to 35 mJ in order to simulate energies that were sufficient for the analysis of frozen salt solutions and might be available for an instrument for planetary exploration. The laser beam is directed through a lens system with an effective focal length of 410 mm almost vertical (5° offset) onto the sample. The focussed beam diameter ($1/e^2$) at the sample surface is about 300 μm. For the case of reducing the energy of the laser to 35 mJ this results in an irradiance of ≈ 50 MW/mm^2 at the sample surface. A LIBS control unit in combination with the software Sophi provided by LTB Lasertechnik Berlin are used to synchronize the laboratory laser with the camera. The internal clock generator in the LIBS control unit triggers the flash lamp of the laser with a chosen frequency.

The second laser utilized was a low-energy passively Q-switched Nd:YLF laser from neoLASE GmbH, Hannover, Germany, henceforth referred to as "neoLASE laser". The laser operates at its fundamental wavelength of 1053 nm with a pulse duration of 3-5 ns and a variable repetition rate of 1 to 50 Hz. The maximum pulse energy of the laser is 5 mJ. By means of a Brewster plate and a

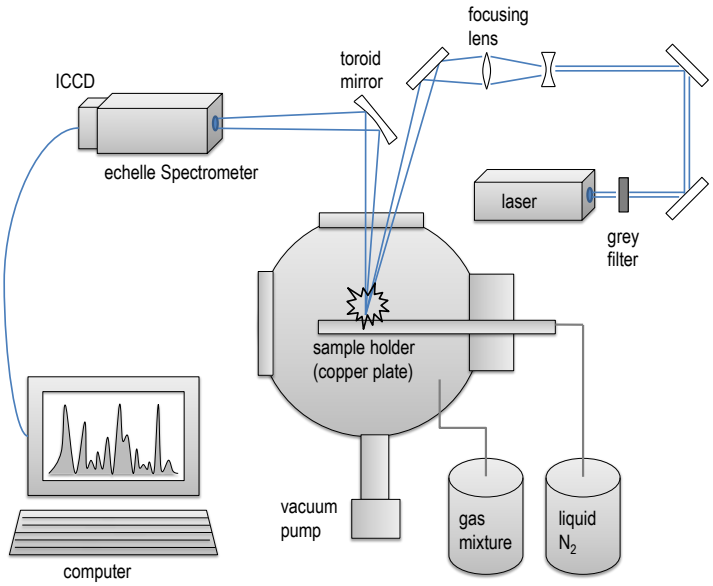

Figure 5.1: *Sketch of the LIBS setup at DLR Berlin. Radiation of the laser is focused onto the sample surface from above. Plasma emission is collected with a toroid mirror and focused onto the entrance slit of an echelle spectrometer. In the simulation chamber, pressure, atmospheric composition, and temperature of the sample holder can be adjusted.*

rotating half wave plate the output pulse energy can be controlled. Due to losses in the focussing optics and at the window of the simulation chamber the maximum energy on the sample surface is reduced to 2.7 mJ. A picture of its interior and a sketch of the optical setup is shown in Fig. 5.2. This laser has been developed in order to explore the application spectrum of a miniaturized LIBS system for planetary exploration, like for the Raman-LIBS-Spectrometer (RLS) which was once planned to be a part of the instrumentation payload onboard ESA's ExoMars mission. The neoLASE is provided by courtesy of the Institut für Planetologie (IfP) of the Westfälische Wilhelms-Universität Münster. It resembles laser parameters of a miniaturized space flight instrument in terms of pulse energy and pulse width, however, not concerning its size and weight. With a laser spot diameter ($1/e^2$) of about 150 μm an irradiance of $\approx$ 50 MW/mm^2 is obtained at the sample surface. Working with this laser the camera is triggered optically with a photo-sensitive diode.

Simulation chamber

In a dedicated simulation chamber with a volume of approximately 5000 cm^3 planetary atmospheric conditions can be imitated by choosing the appropriate pressure, temperature and atmospheric composition. In the simulation chamber the sample to be analyzed is placed on the sample holder that can be moved automatically in x, y and z directions by stepper motors. The sample holder previously had to be moved manually. During the work of this thesis the step motor was installed and coupled to the software, that also controls camera and spectrometer. The manufacturer provided software allows for an user-friendly programming of scripts written in Pascal syntax for automatically scanning the sample, taking measurements, and saving the data files. On the sample holder a positioning device can be attached, holding a total of six pressed samples at one time. Moreover, small copper cups can

Components	Manufacturer	Properties	
Laser			
(1)	Continuum	material and wavelength:	Nd:YAG, 1064 nm
	Model Inlite I-20	pulse energy:	10-220 mJ
		pulse duration:	10 ns
		repetition rate:	10 Hz
(2)	neoLASE GmbH	material and wavelength:	Nd:YLF, 1053 nm
		pulse energy:	0.1-5 mJ
		pulse duration:	3-5 ns
		repetition rate:	1-50 Hz
Spectrometer	LTB Lasertechnik Berlin	wavelength range:	191-372 nm
	Aryelle Butterfly		281-900 nm
		spectral resolution:	14-96 pm
		spectral accuracy:	<3-20 pm
		dimensions (LxWxH):	(450x280x240) mm
Detector	Andor	image area:	13.3x13.3 mm
	ICCD-camera		1024x1024 pixel
		wavelength calibration:	Hg
		weight	
		spectrometer incl. detector:	20 kg
Simulation chamber	LTB Lasertechnik Berlin / BesTec	pressure range:	0.1 Pa - 10 kPa
		temperature range:	145 K to 232 K
		composition of the gas:	CO_2 95.32 Vol%
			N_2 2.70 Vol%
			Ar 1.60 Vol%
			O_2 0.13 Vol%

Table 5.1: *Overview of the components of the laboratory LIBS setup at DLR Berlin.*

be attached. The sample holder can be cooled by feeding liquid nitrogen into the mounting. A heating system in the copper-made sample holder allows for setting the temperature at any value above the one of liquid nitrogen. The temperature of the sample holder can be measured by a thermocouple type C (tungsten/rhenium).

In the chamber constant pressures ranging from 0.1 Pa to 10 kPa can be adjusted. For the simulation of a Martian-like atmosphere an appropriate gas mixture composed of 95.55 %vol. CO_2, 2.7 %vol. N_2, 1.6 %vol. Ar, and 0.15 %vol. O_2 at a pressure of 600-700 Pa was filled into the chamber after evacuation. In order to prevent alteration and contamination of the Martian conditions by ablated and sublimated material during a LIBS data acquisition, a constant flow of the gas mixture through the chamber was kept during the measurement. A camera for video monitoring provides an enlarged view of the sample surface, simultaneous surveillance of the plasma generation and emission, and afterwards inspection of the laser-induced craters. Both video camera and laser have the same focal plane.

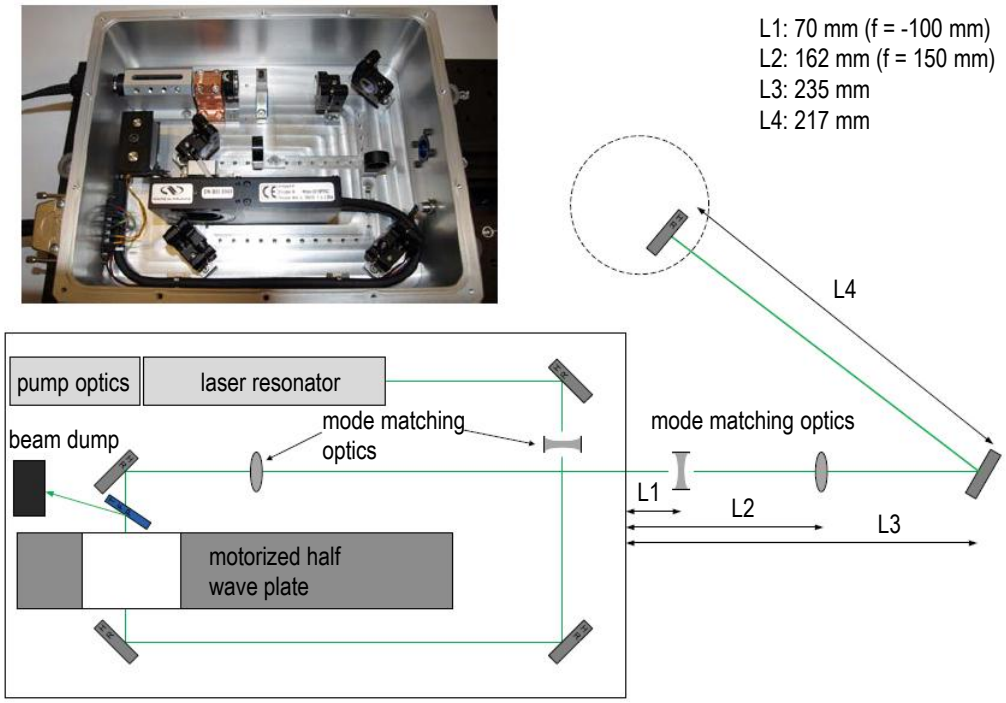

Figure 5.2: *Optical set-up for the low-energy Nd:YLF laser neoLASE. This laser resembles laser parameters of a miniaturized space flight instrument in terms of pulse energy and pulse width, however, not concerning its size and weight.*

Spectrometer

A toroid mirror above the simulation chamber reflects part of the plasma emission onto the entrance slit of an echelle spectrometer (LTB Lasertechnik Berlin, Aryelle Butterfly). This spectrometer consists of two spectrographs sharing one detector, see Fig. 5.4. Hence, two different wavelength ranges can be recorded: 191-372 nm (VUV/UV) and 281-900 nm (Vis/NIR), respectively. The wavelength range of interest is selected prior to data acquisition; it can be utilized only one range at a time. While plasma generation takes place in the simulation chamber, the optical path collecting plasma emission is mainly outside and under Earth atmospheric conditions. This should be considered with regard to possible absorption in the VUV spectral range.

For LIBS, as for other atomic spectroscopy methods, a broad wavelength range is of interest, starting in the VUV and ending in the NIR, which results from electron transitions in the atom shells. Generally, for analysis of the plasma emission a wavelength selective component is required. Separation of wavelength can be achieved by means of filter, prisms, or diffraction gratings, where the latter are commonly utilized nowadays. The aim of covering a wide wavelength range for multielement detection is usually achieved only at the expense of high spectral resolution in order to resolve individual emission lines and vice versa. An example is the conventional Czerny-Turner-spectrometer in combination with a charge-coupled device (CCD), which provides high spectral resolution but only in a restricted range of the spectrum. In contrast, with an echelle spectrometer and exploiting the two dimensions of a CCD, a broad continuous wavelength coverage can be obtained simultaneously. In an echelle spectrometer two

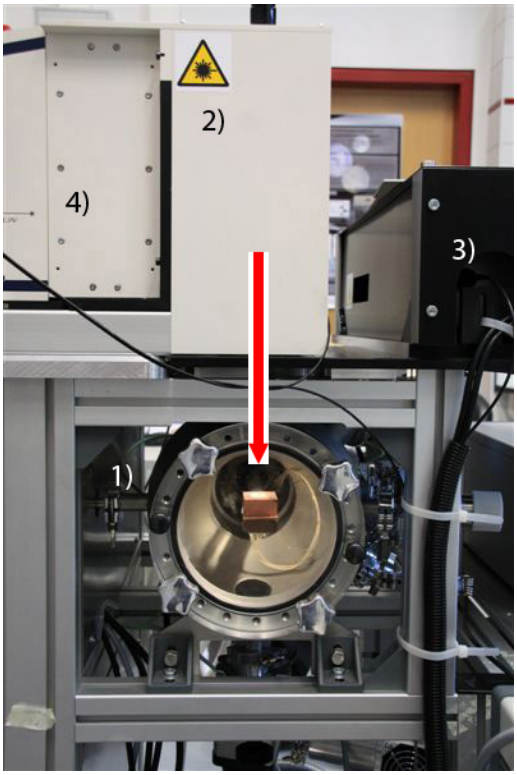

Figure 5.3: *LIBS set-up at the Institute of Planetary Research, DLR Berlin. Shown are 1) the simulation chamber, 2) the box covering the optical path of the Inlite laser, 3) the box covering the optical path of the neoLASE laser, and 4) the echelle spectrometer. Indicated is the laser beam in red.*

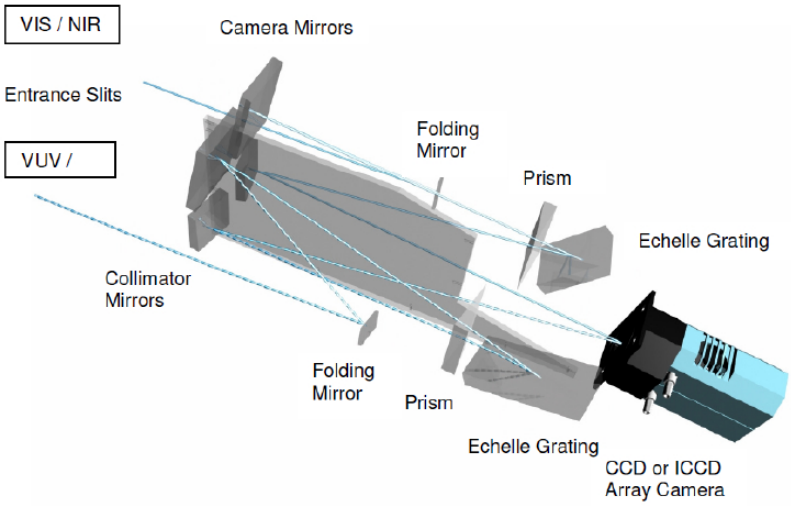

Figure 5.4: *With the Aryelle Butterfly echelle spectrometer two wavelength ranges can be measured due to two spectrographs sharing one detector (ICCD): 191-372 nm (VUV/UV) and 281-900 nm (Vis/NIR).*

dispersive elements are utilized, an echelle grating and an additional dispersive element such as another grating or a prism. The principle of an echelle grating is pictured in Fig. 5.5 (right) in comparison to a conventional reflection grating, called an echelette (left). On an echelette the incident radiation is reflected on the longer groove facet and constructive interference leads to a central zero order

of maximum intensity. Successive higher orders appear at angles determined by the wavelength and grating density, well separated for lower orders and becoming closer with increasing number of order. The so-called blaze angle defines the wavelength for which maximum grating efficiency is obtained. In contrast, on an echelle grating incoming radiation is reflected on the short, steep groove facet [Palmer and Loewen, 2005]. Here, the much higher blaze angle ($\approx$ 65-75° in comparison to 10-40° for conventional gratings) is optimized for multiple overlapping high diffraction orders, which have to be separated afterwards. The wavelength interval observed for a certain order, called free spectral range, can become very narrow for high diffraction orders [Palmer and Loewen, 2005]. Multiplication with the linear dispersion, which too, is high for an echelle used in high orders, results in an usable spectral range between two consecutive diffraction orders. In each free spectral range the maximum efficiency is reached in the central region for wavelengths corresponding to the blaze angle. However, efficiency strongly decreases towards the edges of the range due to angles different from the blaze angle.

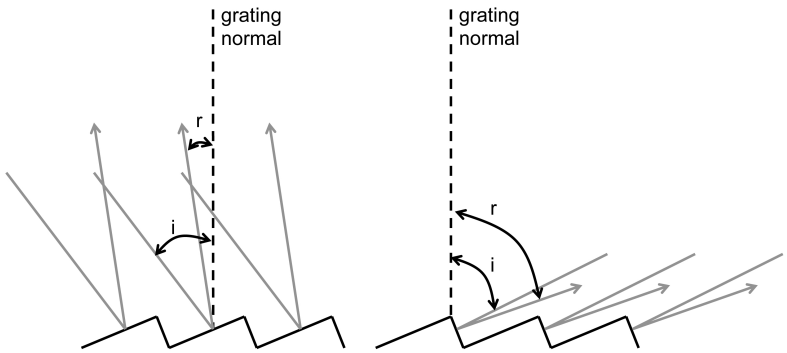

Figure 5.5: *Shown is the geometry of an echelette grating (left) in comparison to the geometry of an echelle grating (right). While for the first the longer groove facet is used for diffraction, on an echelle grating the shorter groove facet is irradiated. The utilization at high angles in high diffraction orders leads to high efficiency and high dispersion, which can be exploited for building high-resolution instruments.*

As cross dispersion element, in the echelle spectrometer used in the laboratory setup a prism mounted perpendicular to the echelle grating separates the overlapping orders. A two-dimensional image is obtained, well matching to CCD arrays, and enabling the simultaneous recording of a large quantity of spectroscopic data. It contains as many slightly overlapping wavelength ranges as orders detected. The individual spectra are combined, overlapping ranges are excluded, and a broadband and highly resolved spectrum is obtained. The spectral resolution depends on the wavelength and is 14-96 pm with a precision of 3-20 pm.

The spectrometer is equipped with a time-gated ICCD camera (Andor iStar) with an image area of 13.3x13.3 mm and 1024x1024 pixel. For an intensified CCD a micro channel plate (MCP) is used to amplify the intensity of the image and to increase sensitivity. The narrow channels provide distortionless imaging with high spatial resolution by preventing the electron cascades from spreading out. The voltage applied across both ends of the MCP controls the amplification and can reach values of up to 10^4. Moreover, the MCP can be used as an optical shutter as it can be switched on and off on a ns scale, thus, allowing for time-resolved detection of the plasma light.

Calibration is done with an incorporated Hg-lamp, which is coupled into the spectrometer with a fibre optic. A desktop computer controls the pulsed laser as well as the gating and amplification of the ICCD and the data acquisition.

5.2 Samples and sample preparation

Different salts have been found on Mars as mentioned in Chapter 2 and are of particular interest in the context of Martian geochemistry, possibly existing liquid brines on Mars and moreover in the context of habitable conditions supporting life.

Different samples with several salts were investigated with LIBS in this study. An overview of the samples is given here:

- Four sulfates and four chlorides with cations of the same kind: $CaCl_2$, $CaSO_4$, KCl, K_2SO_4, $MgCl_2$, $MgSO_4$, NaCl, Na_2SO_4. These salts were investigated as pure salt pellets and as frozen salt solution applying three MVA methods as described in Chapter 7.
- Two ferric salts: iron(III) sulfate hydrate ($Fe_2(SO_4)_3 \cdot x\, H_2O$) and iron(III) chloride hexahydrate $FeCl_3 \cdot 6\, H_2O$. Both were analyzed as pure pressed sample and as a frozen salt solution applying MVA methods with focus on PLS-DA as described in Chapter 8.
- Two chlorides and two perchlorates with cations of the same kind: $Mg(ClO_4)_2$, $NaClO_4$, $MgCl_2$, and NaCl were investigated first in a mix with Martian analogue soil and second as a frozen salt solution with focus with PCA (Chapter 9).
- Martian analogue soil with micro bacterial content which grew in a NaCl solution, see Chapter 10.

Pressed salt samples

The salts for analysis were purchased and 1 g of every salt was pressed at 3760 kg/cm^2 for 15 min. Pellets were obtained with a diameter of 13 mm. A subset of pressed salt samples is shown in Fig. 5.6. The salt pellets differ in color and degree of transparency, spanning a range from white to yellow and opaque to slightly transparent.

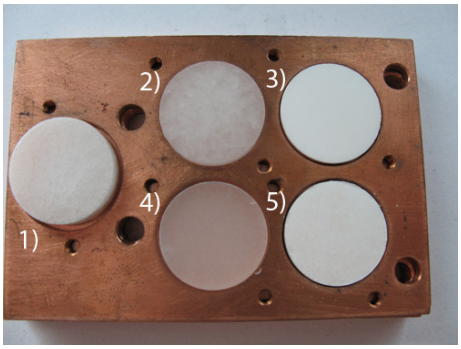

Figure 5.6: *Pressed salt samples of 1) NaCl, 2) $MgCl_2$, 3) Na_2SO_4, 4) KCl, and 5) $MgSO_4$ with a diameter of 13 mm.*

Frozen salt solutions

All salts were investigated as frozen salt solutions, too, and great effort was made to produce similar ice samples with smooth surfaces. First tests of sample preparation were done with sodium chloride (NaCl) in deionized water. For the salt solution a salt content of 2 wt.% was chosen which is well

below the eutectic mixture of sodium chloride and water with an eutectic point of 252 K and 23.3 wt.% (cf. binary phase diagrams provided in Fig. 7.1). By comparison, seawater on Earth typically has a salt content of about 3.5 wt.%.

All ice samples were prepared in little copper cups with an inner diameter of 2.5 cm (see Fig. 5.7) which were filled with 8 ml of the frozen salt solution. Freezing the salt solution resulted in ice with multiple bubbles of trapped air, which were also detectable in the LIBS spectra obtained under simulated Martian atmospheric conditions on the basis of nitrogen emission lines, e.g. N(II)at 399.5 nm. In order to avoid the inclusions of air the salt solution was degassed before freezing. Evacuation to pressures down to 10 Pa for 10 min almost completely prevented the formation of the bubbles with trapped air. Moreover, the nitrogen disappeared from the LIBS spectra of the frozen salt solution taken under simulated Martian conditions.

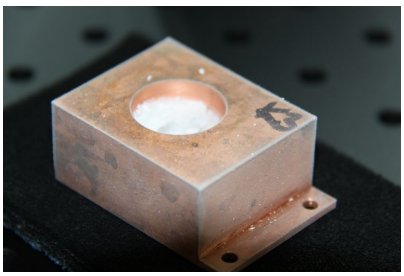

Figure 5.7: *Frozen salt solution with 2 % of the appropriate salt in copper containers with an inner diameter of 2.5 cm.*

In order to obtain ice with smooth surfaces different procedures of freezing the salt solution were tried. Growing a homogeneous salt-ice-lattice would require an eutectic mixture and a controlled freezing process starting in one bottom edge of the copper container and slowly growing from the initial starting point (seed crystal), which is a problem for water since the density of ice is smaller than the density of the liquid. In binary systems (e.g. salt and water) the freezing process is complex and involves many physical effects [Viskanta et al., 1997]. Phase transformation does not take place at a discrete temperature as for single component systems, but over a temperature range. Below the eutectic temperature the solid consists of pure ice and salts or crystal hydrates [Yatsenko and Chudotvortsev, 2002]. For the case of a binary H_2O-NaCl system this means:

$$\text{solution} \longrightarrow \text{ice} + \text{hydrohalite}$$

As growing a perfect ice with a binary component system was not realizable within this project and since perfect, homogeneous ices are not required for the LIBS studies as analogue material, the sample preparation focused on the production of relatively smooth surfaces. Details about the complex sequences during a freezing process of aqueous solutions containing solutes such as sodium chloride can be found in the above mentioned publications or e.g. in [Vrbka and Jungwirth, 2005]. Moreover, effects of supercooling were not studied in this work, which would have gone beyond the scope of this thesis.

Freezing the salt solution in a laboratory freezer from room temperature to the minimum temperature available of 233 K, see Fig. 5.8 for the temperature profile of the cooling device, resulted in uneven surfaces. An irregularly shaped central peak on the frozen surface developed during the freezing process. This can be explained by the freezing process starting at the edge of the small copper container and from the surface of the solution and, moreover, the expanding volume of the substance during solidification. The volume in the central region below the already frozen surface which is the last to freeze, expands and displaces the ice surface above. This happens uncontrolled

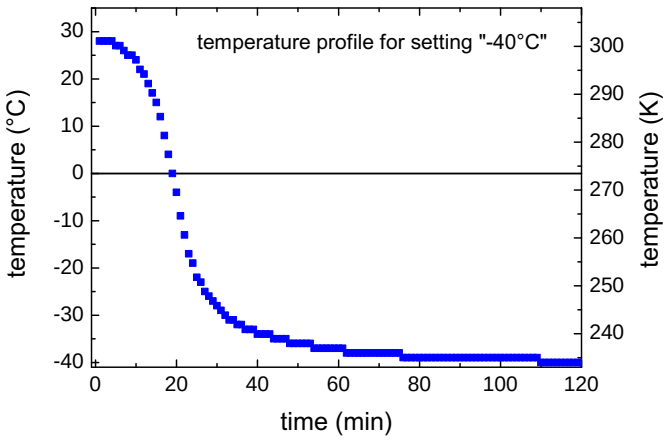

Figure 5.8: *Temperature profile of laboratory freezer for the setting to cool to -40° C (233 K).*

due to the steep decline in temperature of the laboratory freezer and the thermal capacity of the salt solution, which prevents as fast a temperature reduction of the solution. Presumably there is a high temperature gradient within the salt solution, cold at the edges with contact to the copper container and much warmer in the central region.

Another test was done freezing the frozen salt solution in the copper cup in a bath of liquid nitrogen, which resulted in similar irregularly shaped surfaces with the central rise. Here, the freezing process took place on a timescale of some tens of seconds, starting at the edge from different positions, continued with a total freezing of the surface and ended with the formation of the central rise. In some cases the surface in the central region broke up and still liquid water flew over the surface were it solidified as an additional surface layer.

The ices were finally prepared by cooling the salt solution stepwise and slowly (ca. -10 K/hour) in the laboratory freezer, thus giving time for the temperature of the copper container and the temperature of the salt solution to adjust to the interior temperature of the freezer. This approach yielded comparatively smooth surfaces of the ices with only slightly deformed central region on the ice. The frozen salt solution was cooled to a temperature of 277 K as a first step, to 263 K as a second step, which is still above the eutectic temperature of 252 K of NaCl, and in further steps of -10 K down to 233 K.

For a two component system such as NaCl in water the species which has a concentration below the concentration of a eutectic mixture (with 2 wt.% typically the salt) is rejected during the freezing process while the other component (water) solidifies [Viskanta et al., 1997], [Vrbka and Jungwirth, 2005]. Liquid and solid coexist and the remaining liquid solution becomes more concentrated. At the eutectic point two solid phases develop simultaneously. This results in a heterogeneous distribution of the concentration of salt in the frozen salt solution. The volume that is the last to freeze thus has the maximum concentration.

The frozen salt solutions with other salts were prepared also with 2 wt.% of the appropriate salt in deionized water, degassed, and cooled stepwise to 233 K as explained above. For the four sulfates investigated in Chapter 7 eutectic temperature is reached after step 2 with 263 K, for calcium sulfate already earlier at 282 K, cf. Fig. 7.1. In this subset of eight salts the chlorides in water solution feature lower eutectic temperatures than the sulfates. Potassium chloride has the highest eutectic

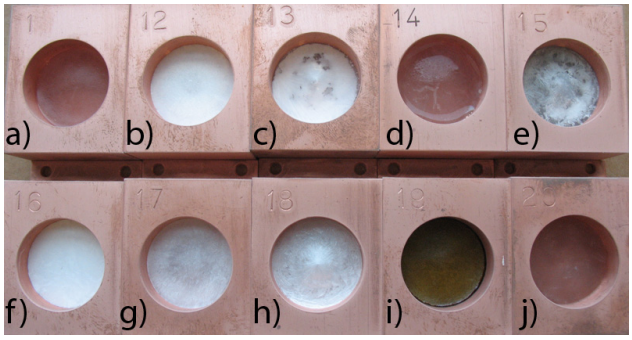

Figure 5.9: *Subset of frozen salt solutions in copper container with an inner diameter of 2.5 cm. The salts displayed here are: a) $CaCl_2$, b) KCl, c) $MgSO_4$, d) $MgCl_2$, e) $Fe_2(SO_4)_3$, f) NaCl, g) NaJ, h) Na_2SO_4, i) $FeCl_3$, j) LiCl. NaJ and LiCl were not further investigated in this study.*

temperature among the chlorides with a value of 262 K, whereas calcium chloride is the last to freeze at a temperature of 223 K and was still partly liquid after cooling in the freezer. A subset of salts in ices as prepared during this work is shown in Fig. 5.9. The ices occur in different consistencies, opacities and show slight variations in color and surface pattern. Further information on the frozen salt solutions analyzed is given in the corresponding chapters.

For the LIBS data acquisition the frozen salt solutions were cooled further down to 198 K by feeding liquid nitrogen into the mounting of the sample stage and adjusting the temperature to a constant value with controlled counter heating. This temperature was chosen with regard to the temperatures typical for regions on Mars, were ice near the surface is available. At the Phoenix landing site the temperature was measured with the Thermal and Electrical Conductivity Probe (TECP) on board the lander and a maximum temperature of 253.4 K during arctic summer was reached whereas the coldest temperature recorded was 175.3 K [Canadian Space Agency, 2010]. In Fig. 5.10 the minimum daily atmospheric temperature is shown. For the temperature of the frozen salt solutions investigated in this study a relatively low temperature of 198 K was chosen. This temperature is well below an average temperature for Mars of approximately 210 K [Williams, 2010] but still quite common also for other regions such as at the Viking 1 lander site with a diurnal temperature ranging from 184 K to 242 K [Kiefer et al., 1977].

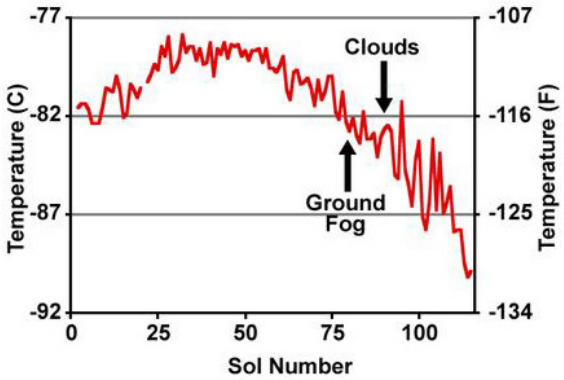

Figure 5.10: *The minimum daily atmospheric temperature as measured by NASA's Phoenix Lander at its landing site above Mars' arctic circle. Image taken from [NASA, 2008].*

6 Investigating salts and frozen salt solutions with LIBS

Apart from spectral emission lines required for further analysis, the plasma emission is made up of uncharacteristic continuum radiation due to bremsstrahlung and recombination as explained in Chapter 3. Emission lines of low intensity of minor or trace elements are superimposed by this continuum emission and can disappear in the background and noise, thus, evading detection. Because of the continuum radiation decaying on a shorter timescale than the emission lines, with time-resolved detection of the plasma this background can be excluded, allowing for better SNR of the spectral lines. LIBS instruments for the use in planetary science presumably will not implement time-resolved detection due to limited mass and energy available. However, since in particular the plasma emission of frozen solutions is accompanied by strong background radiation, the effects of gated LIBS analysis were investigated. In the first part of this chapter the influence of different gating parameters were studied for analyzing salts and frozen salt solutions and parameters best suited for the LIBS analysis of ices were determined. The second part briefly deals with the lens to sample distance and variations of the sample surface with respect to the focal plane of the laser. In the third part of this chapter the feasibility of a low energy laser for the investigation of salts and frozen salt solutions was studied.

6.1 Optimizing gating parameters for time-resolved LIBS

All measurements for optimization were performed with a frozen NaCl solution with 2 wt.% of the salt, which was prepared as explained in detail in the previous chapter. Under simulated Martian atmospheric conditions and a sample temperature of 198 K, 20 laser-induced plasmas were accumulated using the Inlite laser. The laser energy was reduced to 35 mJ by grey filters. The gain was set to 80, which results in an amplification by a factor of approximately eight counts per photoelectron. Three measurements with the same gating parameters at different positions on the sample were averaged to compensate for the typically large fluctuations in the LIBS spectra between different measurements of the ices. A dark background spectrum measured prior to each measurement was subtracted from the raw data to account for fixed pattern noise and counts due to thermal dark current.

Time delay for plasma detection

First, the temporal evolution of the plasma emission was investigated in terms of both, background radiation and emission line intensities by varying the time delay for plasma detection. A constant detection time (gate) of 1 μs was chosen while the delay time for the start of plasma emission recording was varied in steps of 100 ns up to 1 μs and in steps of 200 ns from 1 μs to 2 μs. A minimum delay of the system due to signal processing of the trigger and the time until the camera actually responds was measured to be 40 ns and can not be shortened. Thus, a measurement performed with a nominally delay time of 0 ns and indicated as such corresponds to a true delay of 40 ns.

The temporal evolution of a LIBS spectrum of a frozen NaCl water solution under simulated Martian atmospheric conditions for delay times up to 600 ns is shown in Fig. 6.1. In the top row the whole

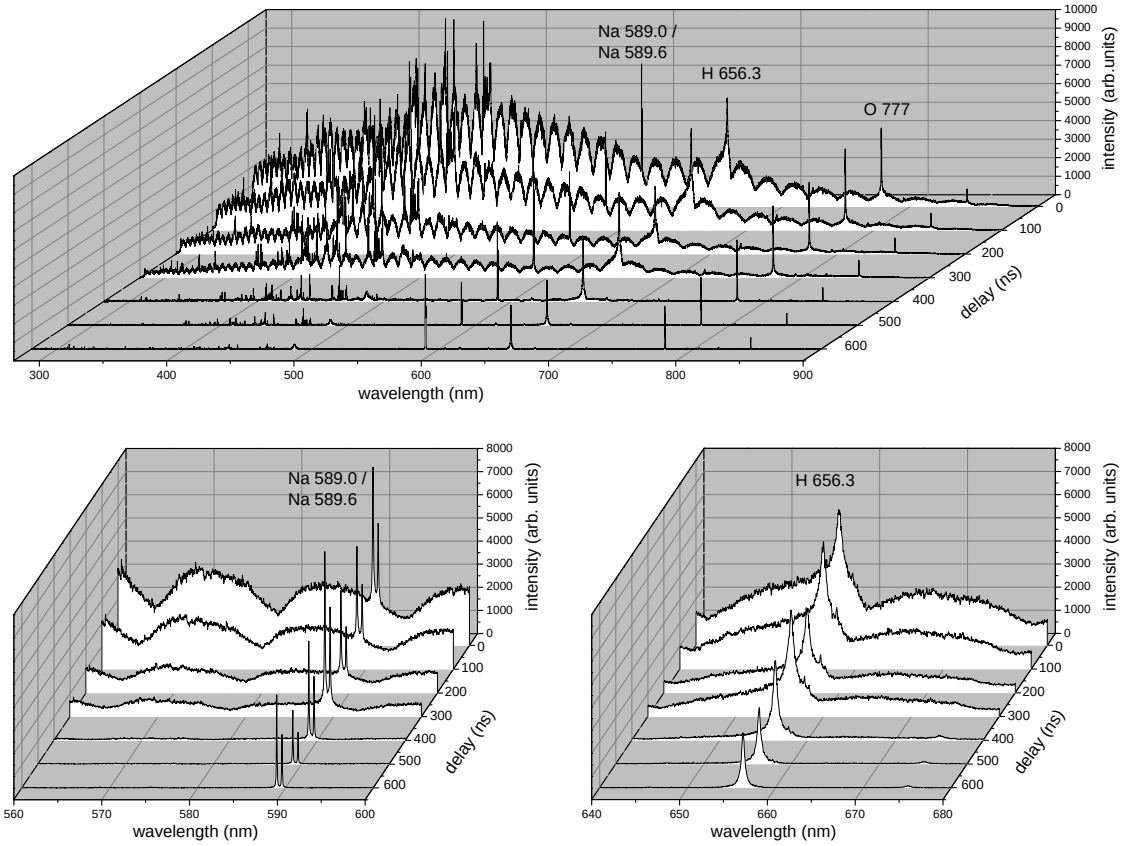

Figure 6.1: *LIBS spectra of NaCl frozen salt solution with increasing delay time obtained under simulated Martian atmospheric conditions. In the early time after plasma inition the spectra are dominated by continuous background emission. The whole Vis/NIR spectral range is shown (top) as well as enlarged regions of the strongly broadened hydrogen line (bottom left) and the intense sodium doublet (bottom right).*

LIBS spectrum can be seen in the Vis/NIR range for increasing delay times. Due to the dominant background radiation in the early phases of the plasma evolution the individual echelle orders become clearly visible. Two spectral regions are displayed enlarged in the bottom of Fig. 6.1. In the bottom left plot the spectral region from 560 to 600 nm is shown, which includes the intense sodium doublet at 589.0 nm and 589.6 nm, which is a result of the transition from the 3p (with total angular momentum of j=3/2 and j=1/2, respectively) to the 3s levels. The sodium line at 589.0 nm has twice the intensity of the second line, see also Table 7.2 for further information. Moreover, lines of hydrogen (strongly broadened, see Fig. 6.1 bottom right) and oxygen are clearly recognizable in the spectra from the first moments on and are lasting during the first two μs. As can be seen, plasma emission of the frozen salt solution is dominated by continuous emission during the first 400 ns which can be almost totally excluded when starting detection not until after 500 ns. The spectral line intensities are most intense in the early phase of plasma emission and decrease with time as expected.

In Fig. 6.2 the emission line intensities are shown for the most intense lines in the spectrum of the frozen NaCl solution: Na(I) 589.0 nm, Na(I) 589.6 nm, O(I) 777.2 nm, O(I) 844.6 nm, and H(I) 656.3 nm. The oxygen line at 777.2 nm belongs to a triplet, which can be resolved in the LIBS spectra due the high-resolution echelle spectrometer. The temporal evolution of the chlorine

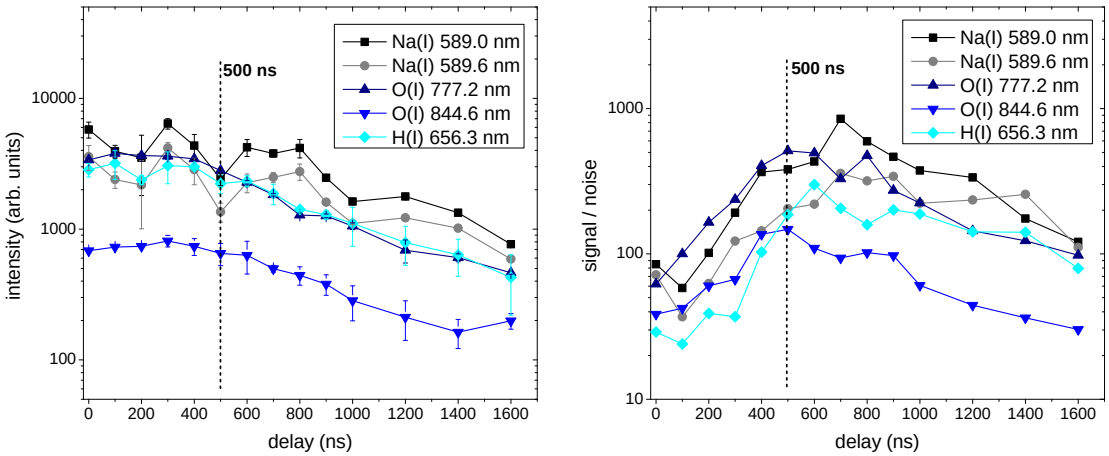

Figure 6.2: *Temporal evolution of the intensity of the five most intense emission lines in the LIBS spectrum of a frozen salt solution obtained under simulated Martian atmospheric conditions (left). The SNRs as a function of time show maximum values between 500 to 800 ns, depending on the element (right).*

lines could not be investigated with the spectra of the frozen salt solutions as the chlorine lines there were found to be too weak and not distinguishable from background and noise. The line intensities depicted in Fig. 6.2 (left) correspond to the amplitudes of the emission lines and were obtained from a Lorentzian fit; underlying background emission was allowed for with an additive offset. The error bars correspond to the uncertainty of the amplitude obtained from the fit. The effect of the typically high variations between two consecutive LIBS measurements when scanning over the surface of a frozen salt solution can be seen in the shape of the curve in Fig. 6.2. However, the general trend, i.e. the decrease of line intensity with time can be recognized from the plots. In close proximity to every line a spectral range without peak and of equal width to the corresponding line was chosen to obtain a related value for the noise, considering also the edges of echelle orders in the spectrum. The value for the noise is defined as the standard deviation in this range. Signal-to-noise ratios (SNRs) are presented in Fig. 6.2 (right). As can be seen from this plot a maximum of SNR is obtained for delay times of 400 to 500 ns in case of oxygen and a little later with delay times of 600 to 800 ns for sodium and hydrogen.

In Fig. 6.3 a mean noise value is shown as a function of delay time, together with a value representative for the intensity of the background radiation, which corresponds to the mean value of a peak-free interval close to the sodium lines. As mentioned above, the continuum radiation dominates the early stages of plasma evolution, but rapidly decays after approximately 400 ns for the laser-induced plasma on a frozen NaCl solution. The noise declines, too, by one order of magnitude during the first 500 ns and remains approximately constant afterwards.

Marked in all three figures is the delay time of 500 ns that was finally chosen for further analysis. It is a compromise considering absolute intensity of the emission lines, their SNR and the superimposed background emission. This decision is supported by investigating the emission line intensities and SNRs of chlorine as a function of delay time for a pressed NaCl sample, see Fig. 6.4. The chlorine lines were considered and the gating parameters were optimized for their detection representatively for both, chlorine and sulfur lines, which were of thematic priority in this study. The most intense chlorine lines emanating from singly charged ions were found to be Cl(II) at 479.4 nm and Cl(II) at 481.0 nm. The most intense chlorine line resulting from a transition in neutral chlorine atoms was

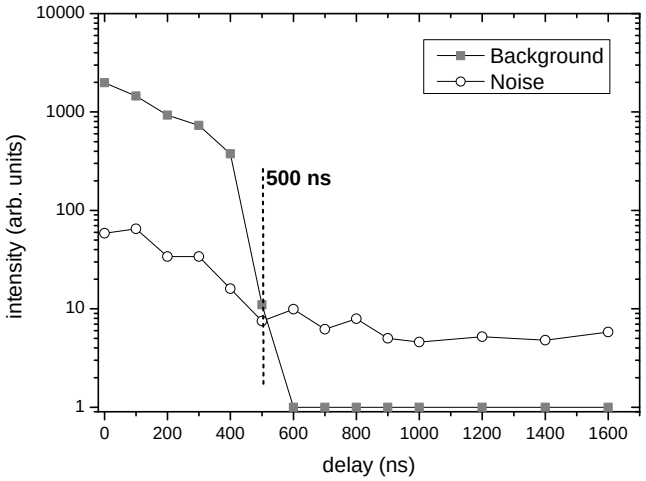

Figure 6.3: *Temporal evolution of background (uncharacteristic continuum emission) and noise for LIBS spectra of a frozen NaCl solution under Martian atmospheric conditions. Background emission can be excluded from detection for delay times higher than 500 ns.*

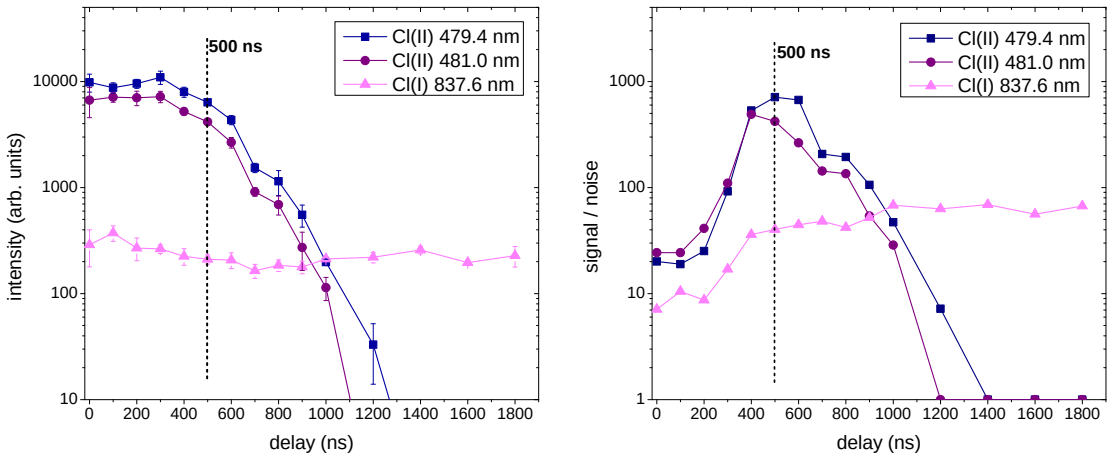

Figure 6.4: *Temporal evolution of the intensity of chlorine lines in the LIBS spectra of a pressed NaCl sample under simulated Martian atmospheric conditions (left). The lines of the ions decay on a much faster time scale than the chlorine line emanating from a neutral atom. The latter is detected with low intensity due to the quantum efficiency of the camera strongly decreasing for wavelengths longer than 800 nm. The SNRs of the spectral lines of the ions reach maximum values for 400 to 500 ns, whereas the SNR for Cl(I) increases and remains constant for long delay times (right).*

found to be Cl(I) at 837.6 nm. As can be seen from Fig. 6.4 (left), the chlorine lines from the ions strongly decrease after delay times of about 400 ns and cannot be distinguished from noise after more than about 1.2 μs after plasma initiation. In contrast, the spectral line from the neutral chlorine atom is detected with lower intensity (due to the quantum efficiency of the camera strongly decreasing for

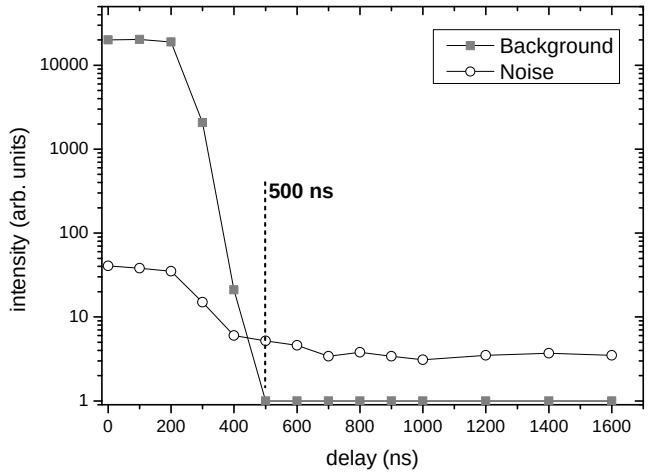

Figure 6.5: *Temporal evolution of background emission and noise for LIBS spectra of a pressed NaCl sample under Martian atmospheric conditions. Background emission strongly decreases for times longer than 300 ns after plasma inition.*

wavelengths above 800 nm) but remains almost constant up to long delay times. The SNRs of the lines of both ions reach maximum values for 400 to 500 ns whereas the SNR for the chlorine lines of the neutral atom increases for delay times up to 1 μs and remains constant afterwards.

In Fig. 6.5 noise and background are depicted as a function of time in the case of the pressed NaCl sample. The continuous background here decays on a faster timescale in comparison to the LIBS spectra obtained from the frozen salt solution. Here, the background emission strongly decreases after 300 ns and is excluded entirely for delay times of 500 ns and more. The noise shows similar behavior to the case of the frozen salt solution and decreases by one order of magnitude within the first 500 to 600 ns after plasma inition. For higher delay times the noise remains approximately constant.

Time duration (gate) for plasma detection

The second parameter investigated and optimized for the analysis of frozen salt solutions with time-resolved LIBS was the gate time, i.e. the time period over which plasma light is detected after each delay time. A delay time of 500 ns was chosen for the reasons already stated and the gate time was varied in steps of 200 ns up to 1 μs and in increasingly larger steps to a maximum investigated gate time of 20 μs. In Fig. 6.6 (left) the line intensities of the same five elements as analyzed before are shown as a function of gating time. In general the absolute intensities of all spectral lines increase for increasing gate times up to approximately 3 μs and remain constant for even longer times. Here again the effects of high variability in the data can be seen. The SNRs (Fig. 6.6, right) increase for gate times from 200 ns to about 5 μs and appear to obtain stable values for gate widths larger than that. The noise, too, is depicted in this figure and approximately constant values are obtained when disregarding the general fluctuations of the LIBS data. For further measurements utilizing the Inlite laser a gate of 5 μs was chosen as indicated in the plots.

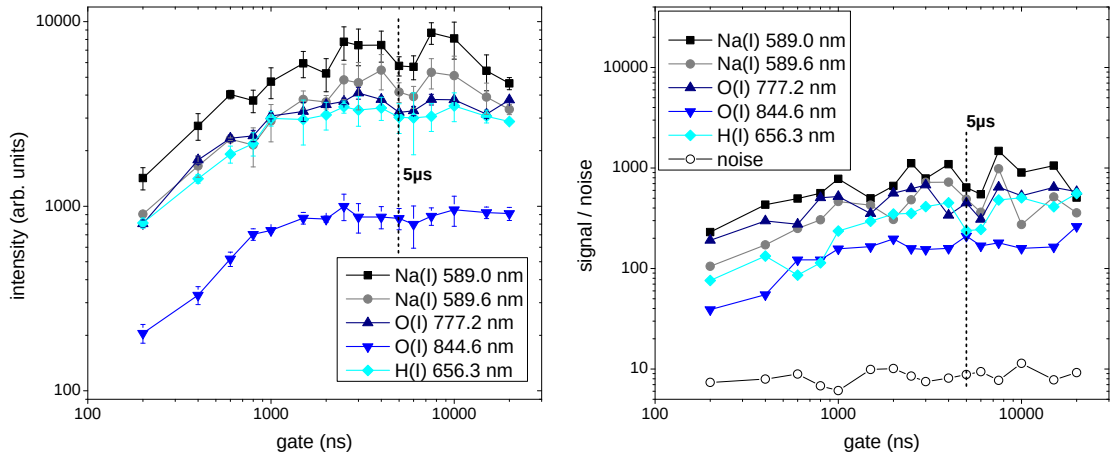

Figure 6.6: *Emission line intensities (left) and SNRs with noise (right) as a function of gate time with constant delay time of 500 ns for a frozen NaCl solution obtained under simulated Martian atmospheric conditions.*

6.2 Focussing lens-to-sample distance and depth profile analysis

Although the samples of the frozen salt solution were carefully prepared with emphasis placed on obtaining flat surfaces, the icy surfaces still slightly varied in height. Moreover, ice is ablated easily with the first shots of a LIBS measurement and the distance between the focussing lens and the sample surface as well as the sample surface with respect to the focal plane of the laser vary during a LIBS measurement with several shots. Deviation of this distance from the focal length can affect the process of ablation and plasma formation and accordingly the emission line intensities. In a weakly ionizable gas a breakdown can occur unintendedly above the sample surface. The Martian atmosphere mainly consists of CO_2 with an ionization potential of 13.7 eV, which therefore facilitates accidental breakdown of the gas. Ablated particles present in the beam path slightly above the sample surface additionally facilitate a breakdown of the gas. In avoidance of a breakdown above the sample surface, a shorter focussing lens-to-sample distance can be chosen. On the contrary, an enhanced laser-spot is obtained when deviating from the focal plane position, which results in a reduced irradiance on the sample surface. The optimal distance between the sample surface and the focussing lens for maximum plasma emission has to be determined.

The distance between the sample surface and the focussing lens was varied in order to study the effect on the emission line intensities in the LIBS spectra of frozen salt solutions for distances deviating from the focal length. Frozen NaCl solution was investigated under Martian atmospheric conditions with the optimized gating parameters, i.e. a delay time of 500 ns and a gate time of 5 μs. The position of the sample was altered by moving the vertically adjustable sample holder. This was done in steps of 1 mm from -6 mm to +5 mm with respect to the focal plane of the laser. In Fig. 6.7 the emission line intensities and SNRs with varying focussing lens-to-sample distance i.e. sample surface position with respect to focal plane position are shown. Negative values on the abscissa correspond to a focal plane position of the laser below the sample surface. As can be seen from these plots, the emission line intensities as well as the SNRs are only marginally affected by the focal plane position with respect to the samples surface in the range investigated.

In order to investigate the effects of the laser drilling into the ice and thus, lowering the sample surface with respect to the laser's focal plane, a kind of depth profiling was performed. LIBS spectra

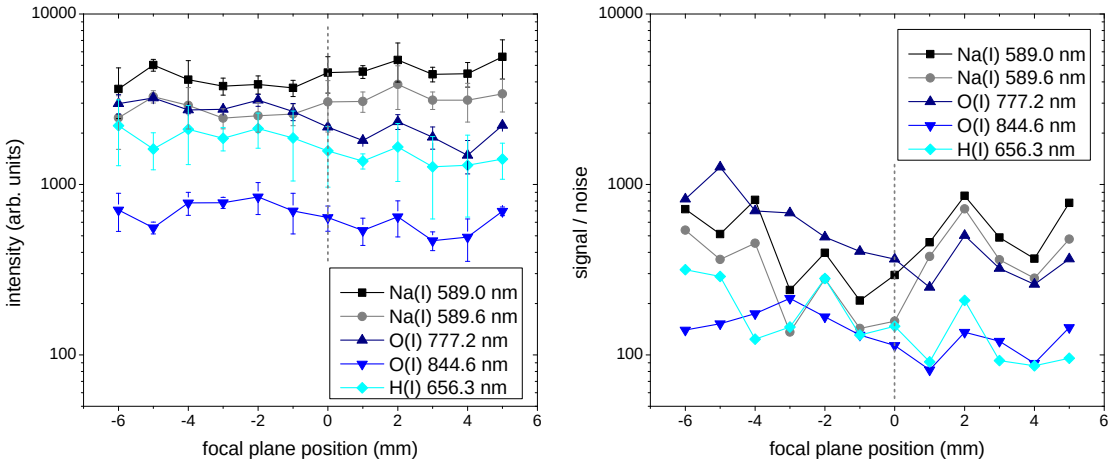

Figure 6.7: *Emission line intensities (left) and SNRs (right) with varying focussing lens-to-sample distance i.e. sample surface with respect to focal plane position. Negative values on the abscissa correspond to a focal plane position of the laser below the sample surface. The measurements were performed with a frozen NaCl solution under simulated Martian conditions.*

obtained from a single laser-induced plasma were recorded by sampling the same position on the ice several times. As an effect was not well deducible due to high fluctuations, poor quality LIBS spectra, and low SNRs, the depth profile analysis was repeated accumulating the emission of three laser-induced plasmas each and probing the same position 10 times. Thus, a total of 30 laser-induced plasmas was generated at the same position and in doing so drilling deeper into the ice with every shot. This measurement was repeated five times at different positions on the sample. The emission line intensities of five spectra were averaged and are shown in Fig. 6.8; the error bars in the plots correspond to the standard deviation. In Fig. 6.8 (left) the emission line intensities of the sodium lines are depicted, which obtain maximum values in the first spectrum, i.e. with the first three laser-induced plasmas recorded. In the spectra obtained thereafter, the emission line intensities of sodium remained approximately constant. The line intensities of hydrogen and oxygen (Fig. 6.8, center) slightly decrease when drilling into the frozen salt solution. The intensities of the chlorine lines dropped after the first three shots (first value) to a level almost undistinguishable from background and noise, see Fig. 6.8 (right). Negative values can occur as a result of the subtraction of the dark current spectrum. The decrease in line intensity of the elements of the salt in the ice, while on the other hand the emission lines of hydrogen and oxygen are less affected, can be explained as a result of a thin surface layer made up of NaCl. This layer develops when the ice is exposed to simulated Martian atmospheric conditions and water molecules of the ice sublimate, leaving behind the sodium chloride.

In general, the standard deviation of the sodium, oxygen, and hydrogen emission lines was found to increase when drilling deeper into the ice. A possible explanation might be, that after several ablation processes the plasma is spatially confined in the developing crater and interacts with the inside walls. Presumably, melting occurs at the crater rim and inside wall, and liquid water flows towards the bottom of the crater and resolidifies. Plasma confinement, interaction with the crater walls, and the resulting irregularly deformed crater profile lead to high variability in the ablation process and formation of following laser-induced plasmas in terms such as occurrence, orientation, and shape. This results in high fluctuations in the spectra and thus, enlarged error bars. Another aspect, which

should be considered is that plasma emission in the crater is inhibited from detection to a certain amount.

These results show, that the spectra obtained from the first laser-induced plasmas feature the most intense lines of the components of the salt due to the thin salt layer, while subsequent spectra represent the underlying frozen salt solution. Moreover, later detected spectra of laser-induced plasmas in the developing crater are subject to larger fluctuations. For the measurements as well as for the LIBS analysis presented in the next chapters, emission of a total of 20 laser-induced plasmas was accumulated without exclusion of the first spectra.

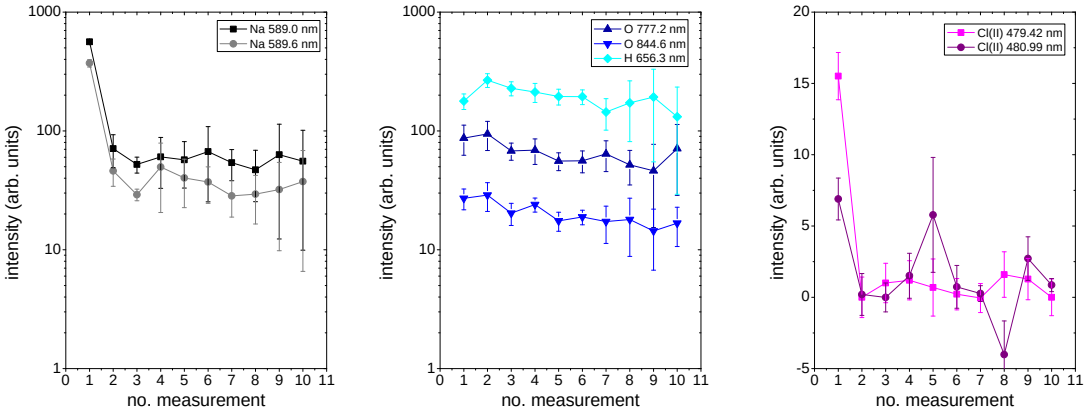

Figure 6.8: *Depth profiling for frozen NaCl solution. Three laser-induced plasmas are accumulated each. The same position was probed 10 times.*

Summary

In this section a set of parameters was investigated and determined to obtain optimized LIBS spectra of salts and frozen salt solutions under simulated Martian atmospheric conditions using the set-up as previously described. An overview of the parameters and the standard procedure used for data acquisition in this work is given here:

- The plasma emission was recorded time-resolved with a delay time of 500 ns.
- A gate time of 5 μs was chosen for plasma detection.
- Spectra were intensified with a factor of ca. eight counts per photoelectron.
- A total of 20 laser-induced plasmas was accumulated for each spectrum
- No preceding cleaning shots were performed.
- A dark current spectrum recorded with equal parameters in terms of gate time and gain was measured prior to each measurement and subtracted from the plasma spectrum.

6.3 Investigating salts and frozen salt solutions with a low-energy laser

The low-energy laser neoLASE was tested for its suitability to detect the salts both in their pure form and in frozen salt solutions. Studies similar and analogously to the investigations presented in the last section were carried out and parameters best suited for the identification of the ices were determined. However, even optimized LIBS spectra of the frozen salt solutions obtained by utilizing the neoLASE laser were found to be of only poor quality. Since the further work of this thesis focussed on spectra of ices obtained by employing the Inlite laser, the studies with the neoLASE laser are not discussed in the same detail and only a brief overview of the results is presented here.

With the neoLASE laser a maximum energy of 2.7 mJ can be obtained at the sample surface in a spot diameter of approximately 150 μm. This results in an irradiance in the same order of magnitude compared to the Inlite laser. In Fig. 6.9 typical spectra of four chlorides and four sulfates with the same cation (calcium, magnesium, potassium, and sodium) as pure pressed samples are shown, which were obtained with the neoLASE laser. The spectra obtained from the frozen salt solutions are presented in Fig. 6.10. All measurements were performed under Martian atmospheric conditions. In the case of the frozen salt solutions, the sample holder was cooled to a temperature of 198 K by feeding liquid nitrogen into the mounting. The emission of a total of 50 laser-induced plasmas was accumulated for one spectrum. The gating parameters used here were a nominal delay time of 0 ns and a detection gate time of 5 μs. The delay time was chosen as a result of the emission line intensities in the spectra decreasing significantly for higher delay times. Emission signals of the lines are indistinguishable from noise for delay times longer than 400-500 ns when generating the plasma with the neoLASE laser under Martian atmospheric conditions. Also, the SNRs obtained maximum values for the smallest delay time possible due to almost no background radiation present in the early phase of the plasma evolution. In order to amplify the poor spectra obtained from the frozen salt solution a relatively high gain was chosen (also for the spectra of the salts to provide comparable conditions), resulting in an amplification factor of 200 per initial photo electron.

In the spectra of the pressed salts the most intense lines are those of the cations in the salts, i.e. calcium, magnesium, potassium, and sodium. Moreover, oxygen and hydrogen can be detected. Sulfur and chlorine lines were not detected with the low energy laser in this study.

The spectra of the frozen salt solutions are of poor quality. For solidly frozen and opaque ices such as sodium chloride in water, the metal lines are detectable with good SNRs. On the other hand, on more transparent or mushy ice samples, the generation of the plasma frequently failed. Due to the high gain of the amplifier also noise is amplified and multiple spikes appear in the spectra.

Although the irradiance obtained with the low energy neoLASE laser is in the same order of magnitude in comparison to the irradiance provided by the Inlite laser, the plasma characteristics in terms of temporal evolution, background and characteristic emission significantly differ. Emission lines of sulfur and chlorine were not detectable in the spectra of the pure pressed salt samples and the generation of a suitable plasma for the analysis of the frozen salt solutions was not obtained. A possible explanation might be an insufficiently focussed laser beam at the sample surface which could be improved by inserting beam expanding optics in front of the focussing lens for the neoLASE laser. The studies presented in the following sections were performed with the Inlite laser.

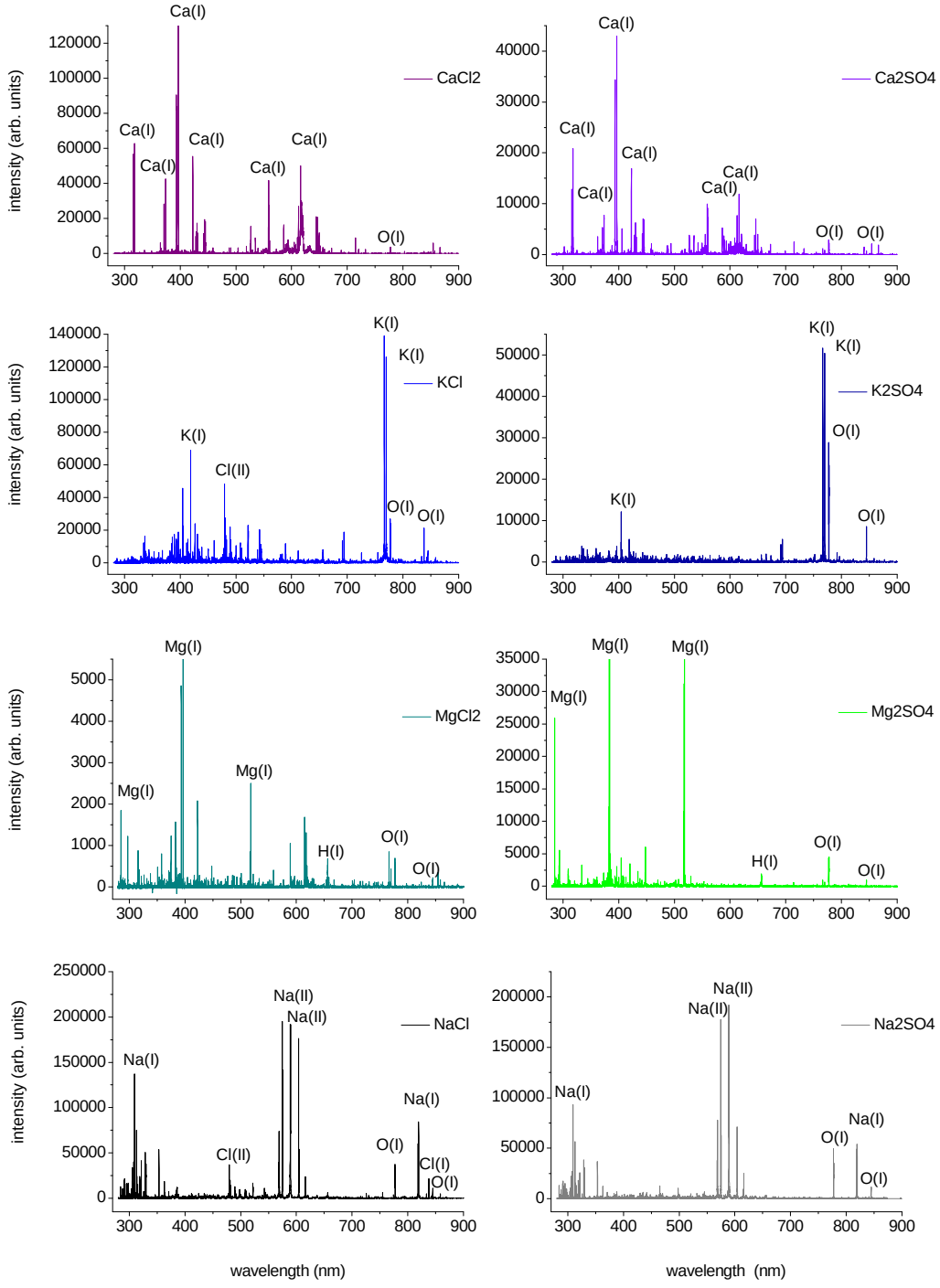

Figure 6.9: *LIBS spectra of eight pure pressed salts obtained with a low energy laser in the Vis/NIR region. Clearly visible are the emission lines of the metals dominating the spectra. Oxygen and hydrogen can be detected as well as chlorine.*

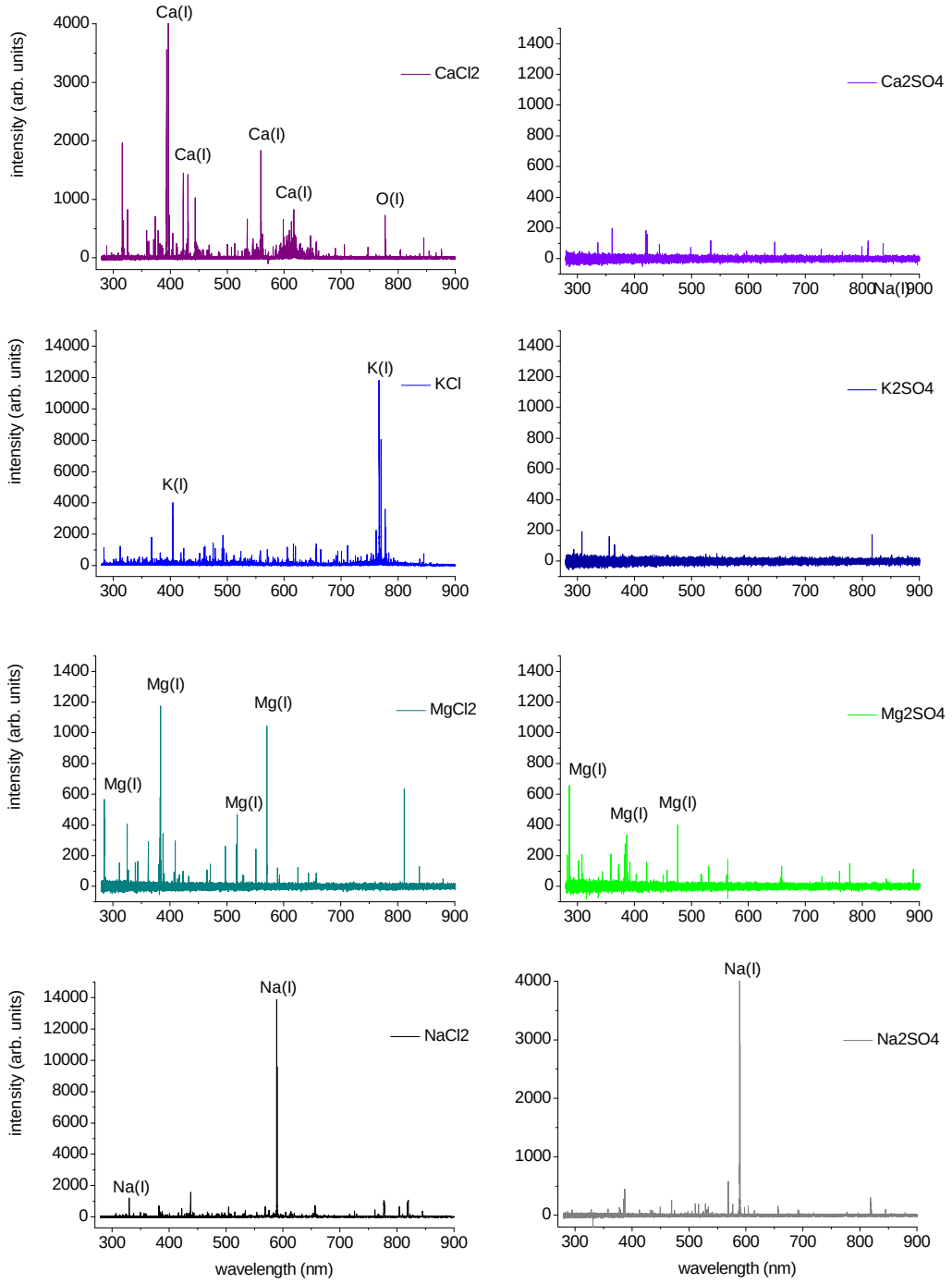

Figure 6.10: *LIBS spectra of eight frozen salt solutions obtained with a low energy laser in the Vis/NIR region. The emission lines of the most intense metals are visible in some of the spectra. Due to the high gain used in this study, noise is amplified, too, and multiple lines due to fluctuations are found in the data.*

7 Investigation of sulfates and chlorides in frozen salt solutions applying MVA methods [1]

Sulfur and chlorine are elements important in the context of Martian geochemistry as discussed in detail previously. However, the detection of chlorine and sulfur with LIBS is known to be a challenging task due to their high excitation energies $\geq$ 10 eV. For applications under terrestrial atmospheric conditions usually sulfur and chlorine emission lines in the vacuum UV range or in the NIR are chosen, e.g. [Gaft et al., 2009], [Peter et al., 2003], [Radivojevic et al., 2004], [Weritz et al., 2005], [Weritz et al., 2007]. A suitable chlorine line Cl(I) at 837.6 nm can be detected with the set-up used in this study, too. However, the quantum efficiency of the utilized camera strongly decreases in the NIR and strong lines of neutral sulfur atoms at 921.3 nm, 922.8 nm, and 923.8 nm are not detectable with this set-up. Martian atmospheric conditions are an advantage for the detection of sulfur and chlorine in the visible wavelength range, and several emission lines due to transitions in ions were found to be detectable with LIBS [Sallé et al., 2004], [Dyar et al., 2011]. While in this study several emission lines of both, sulfur and chlorine, can be detected with good SNRs in the visible range of spectra of the pressed salt samples, their detection in spectra obtained from frozen salt solutions is very difficult.

The aim of this study is to evaluate the ability of LIBS to detect and identify different salts in frozen salt water solutions under Martian atmospheric conditions by applying MVA methods. The focus was on discriminating between sulfates and chlorides with cations of the same kind. In general, the emission lines of metals are detectable with LIBS with high signal-to-noise ratios (SNR), facilitating a relatively straightforward identification of the type of the cation. However, due to weak excitation of the high-energy levels required for efficient radiative transitions of both, sulfur and chlorine ions, their emission lines are typically weak and hardly detectable in particular in the LIBS spectra of the ices, which considerably complicates differentiation between salts with the same cation. The most important parameters for discrimination are identified for the LIBS spectra of the pure pressed salts as well as for the frozen salt solutions applying PCA. Moreover, SIMCA and PLS-DA models were built, tested and optimized for both, the pure salts and the frozen salt solutions. In a following step frozen salt solutions with "unknown" salts were predictively identified by means of the models.

In this study a suite of eight salts ($CaCl_2$, $CaSO_4$, KCl, K_2SO_4, $MgCl_2$, $MgSO_4$, NaCl, Na_2SO_4) was analyzed with LIBS in two different ways: first, as pure salt pellets, and second in frozen salt solutions. The majority of the selected salts were chosen due to their relevance to Mars, as they have either been found on its surface or they are of prime interest in the context of brine formation on Mars. Moreover, salts which have not yet been found on Mars were added to the selection in order to complete pairs of a sulfate and a chloride with metal ions of the same kind. The focus was on the capability of the MVA techniques for LIBS data to discriminate between the sulfates and chlorides with cations of the same kind. With PCA both data sets were analyzed with the aim of

[1] Major parts of this section are submitted for publication in the journal Icarus: S. Schröder, S.G. Pavlov, I. Rauschenbach, E.K. Jessberger, and H.-W. Hübers, Detection and identification of salts and frozen salt solutions combining laser-induced breakdown spectroscopy and multivariate analysis methods: A study for future Martian exploration.

separating the spectra of the ices into groups and revealing the most important lines in the spectra for discrimination and identification of the type of salt. PCA performance is improved by selecting the most relevant lines with emphasis on the sulfur and chlorine lines and additionally averaging the spectra before analysis. Moreover, a subsequent local PCA (i.e. with a subset of data) can improve the discrimination ability for a sulfate and a chloride with the same type of cation. SIMCA and PLS-DA were performed for both data sets. While SIMCA worked well for the pressed salt samples, its application to the spectra of the frozen salt solutions was not successful. It was found that a local PLS-DA of the LIBS spectra of salts with the same cation is capable of distinguishing sulfate and chloride.

Samples and experimental

The salts for analysis were purchased, the chemical and physical data are listed in Table 7.1. The binary phase diagrams of the salt with water are shown in Fig. 7.1. For the first test series eight pellets consisting of the pure salt were produced by pressing 1 g of the chlorides and sulfates at 3760 kg/cm^2 into pellets with a diameter of 13 mm. Salt solutions with 2 wt.% of the appropriate salt were prepared with deionized water as described in detain in Chapter 5.2. The salt solutions feature the same value of mass fraction of the appropriate salt; however, they differ when converting the value of 2 wt.% to molar concentration due to the different molar masses of the various salts.

The molar concentration of the prepared salt solutions ranges from about 0.08 mol/l ($MgSO_4$) to 0.34 mol/l (NaCl). The ices occur in different consistencies, opacities and show slight variations in color and surface pattern, cf. Fig. 5.9. $MgCl_2$ and $CaCl_2$, which are the salts with the lowest eutectic temperature investigated in this study, remained only partly frozen with a mushy consistency at a temperature of 233 K at normal pressure. Also under simulated Martian atmospheric conditions and at a temperature of 198 K these solutions did not entirely solidify, which resulted in lower quality LIBS spectra.

Measurements of the pressed salt samples were performed at room temperature (295 K). In the case of data recording of the frozen samples only a single sample at a time can be placed in the simulation chamber and analyzed with LIBS. The copper container with the ices was placed on the sample stage and cooled down to a temperature of 198$\pm$2 K by feeding liquid nitrogen into the mounting and controlled heating. The temperature was measured with a thermocouple type C (W/Re), which was placed in contact with the copper-made sample holder. The temperature was kept constant throughout the measurement.

For all measurements the ICCD gain was set to 80. A 5 μs gate was used and a gate delay of 500 ns was chosen, which are the optimized gating parameters as obtained from Section 6.1. Except for the gain, for which a comparatively high value was chosen but still within the linear regime of the camera, these parameters were found by maximizing the signal-to-noise ratio for the majority of frozen salt solutions. Important emission lines in this study are those of chlorine and sulfur, which here are mostly due to ionic transitions and decay on short time scales. On the other hand there is much continuum emission, especially in the spectra of the frozen salt solutions during the first 500 ns after plasma initiation. The optimal parameter combination is not identical for all the different kinds of salt pellets and frozen salt solutions investigated in this study since, in particular the ices featured color variations, but more importantly differed in consistency and opacity due to their diverse eutectic behaviors. Thus, a compromise was chosen when setting the parameters. For each spectrum the emission of 20 laser-induced plasmas was accumulated to increase SNR and 8 spots per sample were probed by moving the sample holder with the fixed sample on it after every 20 laser pulses.

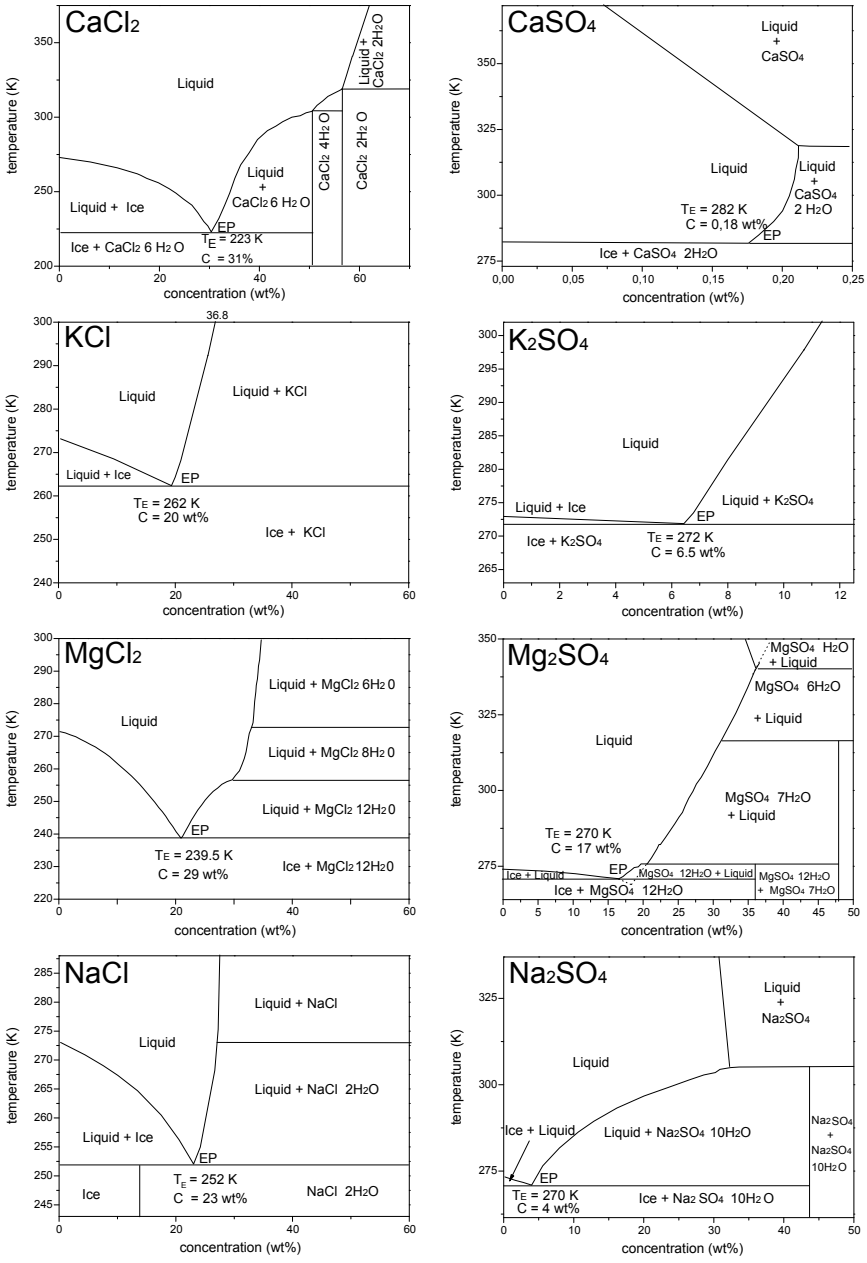

Figure 7.1: *Phase diagrams for the eight salts investigated in this study. Adopted from [Kargel, 1991] ($CaCl_2$, K_2SO_4, $MgSO_4$, Na_2SO_4), [Brady, 2009] (KCl), [Altheide et al., 2009] ($MgCl_2$), and [Viskanta et al., 1997] (NaCl).*

Salt	Eutectic temp. (K)	Conc. (wt.%)	Substance used in this study		Mineral	Molar mass (g/mol)
$CaCl_2$	223	31.0	Calcium chloride dihydrate	$CaCl_2$ x 2 H_2O	Sinjarite	147.01
$CaSO_4$	282	0.2	Calcium sulfate dihydrate	$CaSO_4$ x 2 H_2O	Gypsum	172.17
KCl	262	20.0	Potassium chloride	KCl	Sylvite	74.55
K_2SO_4	272	6.5	Potassium sulfate	K_2SO_4	Arcanite	174.26
$MgCl_2$	240	29.0	Magnesium chloride hexahydrate	$MgCl_2$ x 6 H_2O	Bischofite	203.30
$MgSO_4$	270	17.0	Magnesium sulfate heptahydrate	$MgSO_4$ x 7 H_2O	Epsomite	246.47
NaCl	252	23.0	Sodium chloride	NaCl	Halite	58.44
Na_2SO_4	270	4.0	Sodium sulfate	Na_2SO_4	Thenardite	142.04

Table 7.1: *Overview of salts investigated in this study with chemical information.*

Data processing

The LIBS spectra obtained in this study contain 32476 wavelength channels (bins) in a wavelength range starting at 279 nm in the UVB and extending into the NIR to 900 nm. In this range tens to hundreds of emission lines resulting from specific atomic or ionic transitions of most of the elements composing the plasma appear in a typical LIBS spectrum. Additionally, lines from newly formed simple molecular fragments appear in the spectra of certain substances. All spectra (2 x 64) were assembled and stored into a single data file, which was then further processed employing the commercial software The Unscrambler (CAMO Software AS). To account for pulse-to-pulse variations in the laser energy all spectra were normalized by dividing each spectrum by its average, accomplishing an equal area under the curve for each spectrum:

$$\mathbf{X}_{\text{norm}}(n, m) = \frac{\mathbf{X}(n, m)}{\overline{\mathbf{X}}(n, \bullet)}, \tag{7.1}$$

where $\overline{\mathbf{X}}(n, \bullet)$ denotes the mean value of the n-th row vector in the data matrix [CAMO, 2012]. The influence of continuous background emission from bremsstrahlung and recombination is to a large extent determined by the gating parameters (delay and integration time) as discussed in detail in the previous chapter. However, for some samples it is still apparent in the spectra, uncovering the typical sensitivity loss towards the sides in every order of the echelle spectrum for angles different from the blaze angle. This dependence of sensitivity on the angle of each order translates into a sensitivity dependence on the wavelength in the spectrum. Together with the gradient of the quantum efficiency of the camera for different wavelengths and other parameters affecting the sensitivity in particular ranges of the resulting spectrum (geometrical configuration, absorption,...) this leads to an inherent apparatus function of the LIBS instrument. A background is usually determined mathematically with an algorithm that does not take into account the orders of the echelle spectrum and varies from spectrum to spectrum. A subtraction of this calculated background thus distorts the characteristic shape of the underlying apparatus function. It was purposely chosen to do no further data pre-processing other than normalization. Since the underlying background structure contains inherent features for this set-up and is similar for all the spectra recorded in this study it will therefore drop out as a common feature in the multivariate data analysis. Beyond that the extent of the remaining continuum background might include information about the sample in that it depends on the material properties and should therefore be useful for discrimination and identification of different samples.

The LIBS spectra were analyzed employing the MVA methods PCA, SIMCA and PLS-DA using the commercial software The Unscrambler as explained in Chapter 4. To reduce computing time for the multivariate analysis the LIBS spectra were rebinned with a factor of 5, i.e. 5 bins were accumulated

each, resulting in 6496 columns, which is the number of variables entering the analysis. The rebinning had no appreciable effect on the outcome of the MVA and is discussed in the next section.

Results and discussion

LIBS spectra and general characteristics

In order to achieve information on the most relevant lines in the spectra, also with regard to the following MVA, a first investigation was done with the LIBS data obtained from the pressed salt pellets. Typical spectra are shown in Fig. 7.2. The alkali metal and alkaline earth metals (Ca, K, Mg, Na) are clearly detectable as they appear with high SNR ranging from 400 (potassium) to more than 4000 (calcium) and dominate the LIBS spectra. For each salt there are several lines of the respective metal available in the spectral range and discrimination between salts with different cations is easily achieved. Spectral lines of chlorine and sulfur, however, are difficult to observe in the spectral range covered by the spectrometer. Inducing the plasma under Martian conditions i.e. in a low pressure environment, has an advantage for the detection of sulfur and chlorine lines in that ionic lines occur, which are usually suppressed in air at atmospheric conditions of about 1 bar [Sallé et al., 2004]. In this study chlorine is best observed in the spectral region from 476 nm to 545 nm where several ionic chlorine lines appear. The most intense chlorine line is Cl(II) at 479.4 nm with a SNR of up to 500 for KCl and NaCl in the LIBS spectra of the pressed salts. Also multiple atomic lines are found between 725 nm and 860 nm with Cl(I) at 837.6 nm being the most intense line in this region with a SNR of about 250 (KCl, NaCl). The spectra of $CaCl_2$ and $MgCl_2$ provide less intense chlorine lines with maximum SNR of approximately 50. For sulfur the most intense lines were found in the spectral region from 542 nm to 567 nm in agreement with sulfur emission lines reported previously [Sallé et al., 2004], [Dyar et al., 2011]. About ten ionic lines can be found there including S(II) at 545.4 nm with maximum SNR of almost 100 in the case of Na_2SO_4 and K_2SO_4, whereas the chlorine lines in the spectra of $CaSO_4$ and $MgSO_4$ feature SNR of roughly half the value. An overview of the spectral lines relevant for the analysis and focused on in this study is shown in Table 7.2.

In comparison, the overall intensity of the LIBS spectra obtained from the frozen salt solutions is highly reduced, Fig 7.3. The emission line intensities of the metals are generally reduced to 10-50% with line widths of about half the values compared to the data from the pressed salts, an overview can be seen in Fig. 7.4. The sulfur and chlorine lines lose even more and only the most intense of them can be found in a couple of spectra; the majority disappears in the noise. In general, the chlorine lines in the ice spectra can be observed still better than the sulfur lines. In the case of the LIBS spectra of salts with cations of the same kind it is very difficult to distinguish between the spectra of chlorides and those of sulfates by visual inspection only, due to the weak sulfur and chlorine lines and the spectra's overall similarity. All ice spectra show strong emission lines from hydrogen (H(I) 656.3 nm, H(I) 486.1 nm and H(I) 434.0 nm) and oxygen (triplet O(I) 777.2 nm, O(I) 777.4 nm, O(I) 777.5 nm and O(I) 844.6 nm). While in the spectra of the frozen chlorides in water the intensity of the oxygen triplet in the 777 nm region hardly changed when compared to the spectra of the pure salts. In the data acquired from the frozen sulfates the intensities of these lines were found to decrease. There is additional oxygen present due to the H_2O ice, but the hydrogen suppresses high plasma temperatures, which leads to a reduction of the emission line intensities of oxygen.

In Fig. 7.5 and Fig. 7.6 a comparison of the spectrum of a pure salt and its frozen salt solution is shown illustrating the variation in intensity of several lines in four selected wavelength ranges using the examples of NaCl and Na_2SO_4. Here, the distinct decrease in the intensity of the ionic chlorine lines is obvious, whereas the intensity of the hydrogen line at 486.1 nm increases. In the LIBS spectra

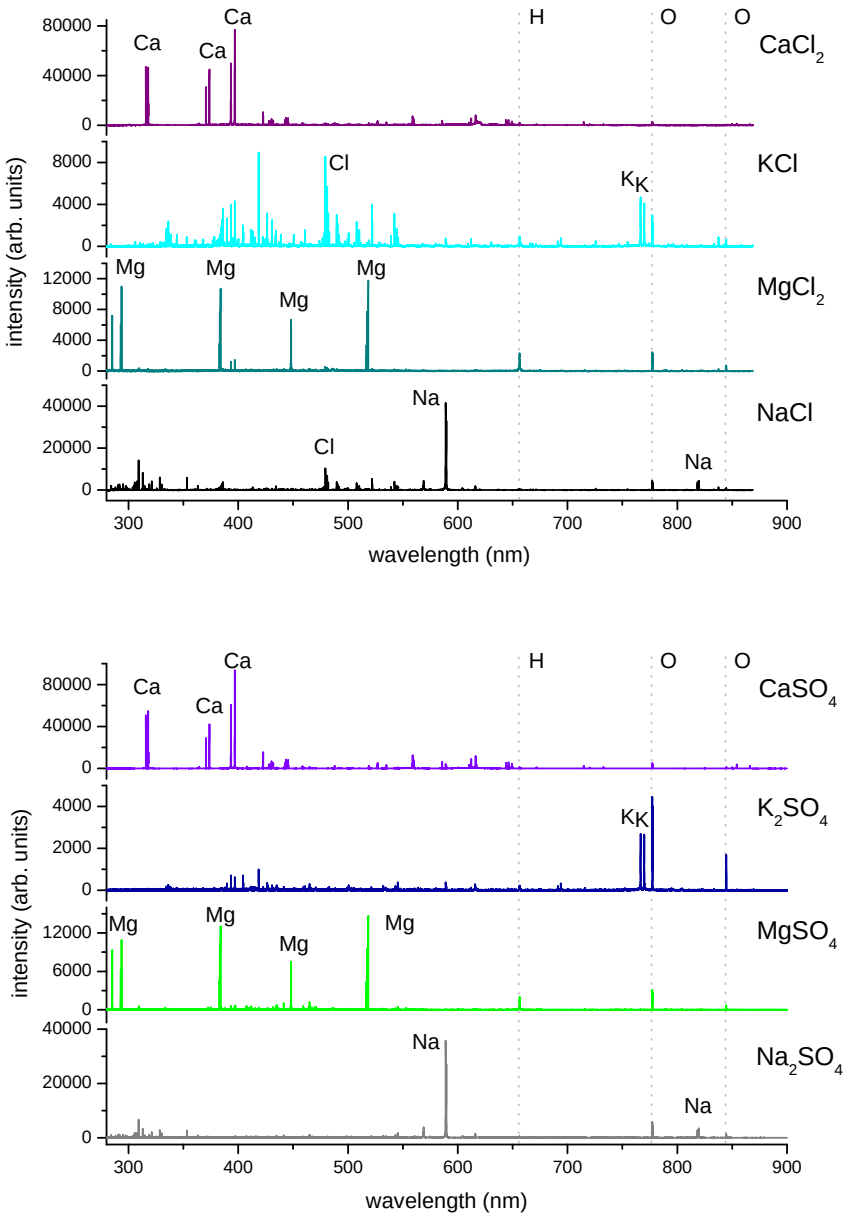

Figure 7.2: *Broadband LIBS spectra of eight pressed salt samples, four chlorides (top) and four sulfates (bottom) with the same cation each, obtained by accumulating the plasma emission generated by 20 laser pulses each. The cations account for the most intense emission lines in the spectra.*

acquired at different positions on the sample the intensities of the emission lines are subject to partly large variations, although nominally identical conditions were provided. This applies in particular to the spectra of the ices. The key reason here is the heterogeneity of the salt distributed in the frozen sample and, thus, small spatial variations in composition. The coupling efficiency of the laser highly

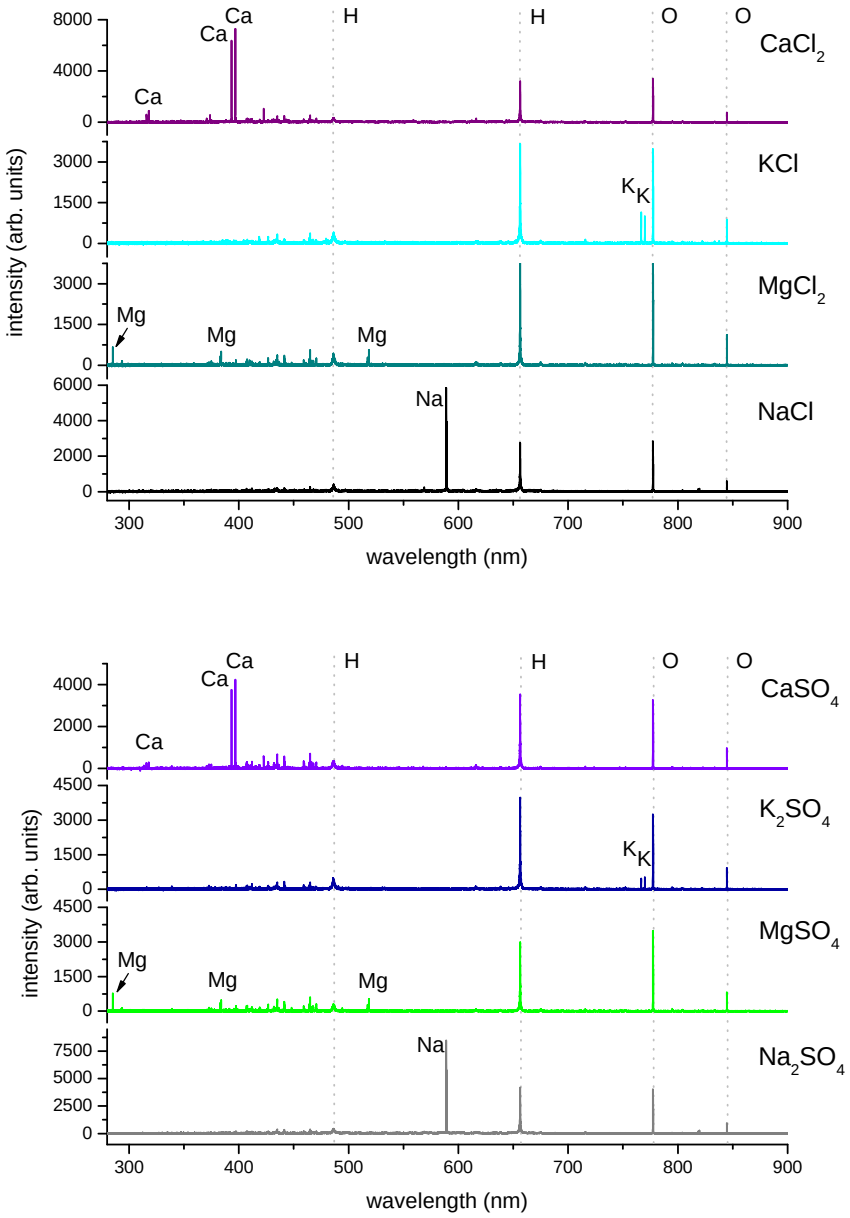

Figure 7.3: *Broadband LIBS spectra of the chlorides (top) and sulfates (bottom) in a frozen salt water solution. The most intense spectral lines are due to hydrogen and oxygen. The metals significantly loose in intensity but are still detectable in the spectra.*

depends on the opacity of the ice and as expected positions, with visible small salt spots resulted in much better spectra than those obtained from more diaphanous positions. For comparison, radiation with a wavelength of 1064 nm has a penetration depth of several cm in pure hexagonal ice [Warren and Brandt, 2008]. In addition, part of the laser energy is reflected from the ice to a greater

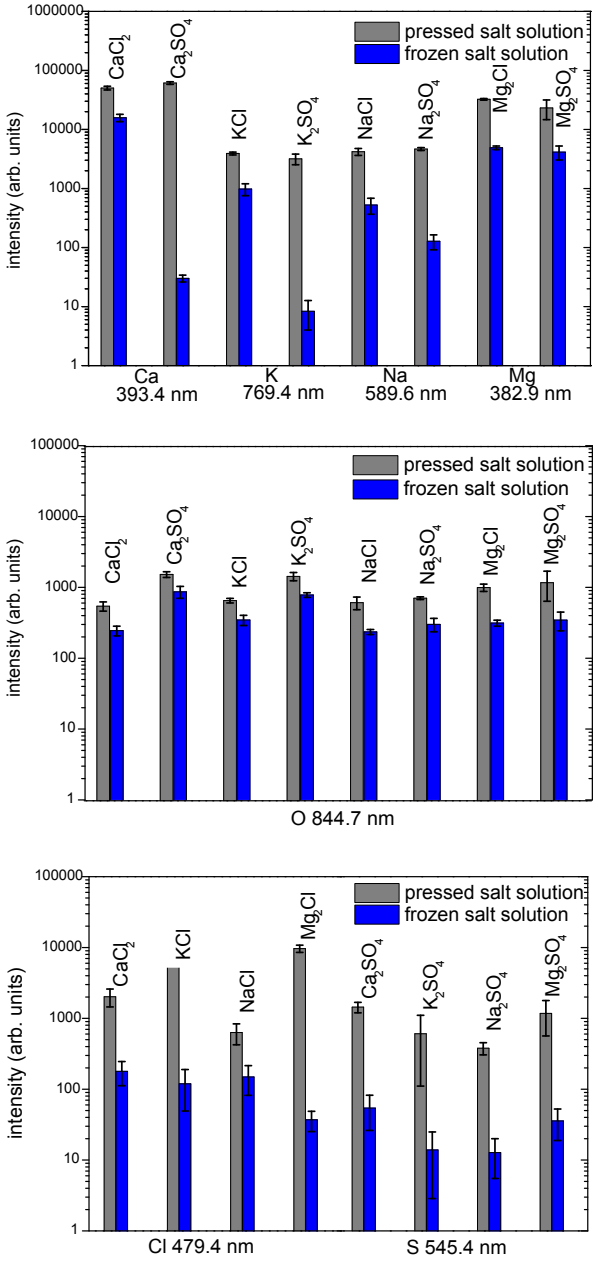

Figure 7.4: *Comparison of line intensities in the LIBS spectra of the pure salt pellets (grey) and the frozen salt solutions (blue) for selected metal lines (top), oxygen (middle), and chlorine and sulfur (bottom).*

or lesser extent and cannot contribute to the ablation process resulting in an overall reduced intensity of the spectrum. In the most unfavorable case the generation of a plasma fails. Surface irregularities can influence the plasma expansion and, hence, additionally affect the detectable plasma emission together with the line intensities. LIBS is known to suffer from matrix effects i.e. chemical and

physical properties of the sample influencing the plasma composition and properties and, thus, the emission line intensities in the spectra. This is a problem most notably for quantitative analysis where calibration usually depends on a (linear) correlation of the abundance of an element in the sample to the corresponding emission line intensity in the spectrum, but is also relevant for identification or discrimination of materials with similar content. To overcome the partly large fluctuations in the LIBS spectra of the ices and to determine other characteristics that may help to distinguish the chlorides from the sulfates since there are only weak lines available in the spectra, PCA was applied to the LIBS data.

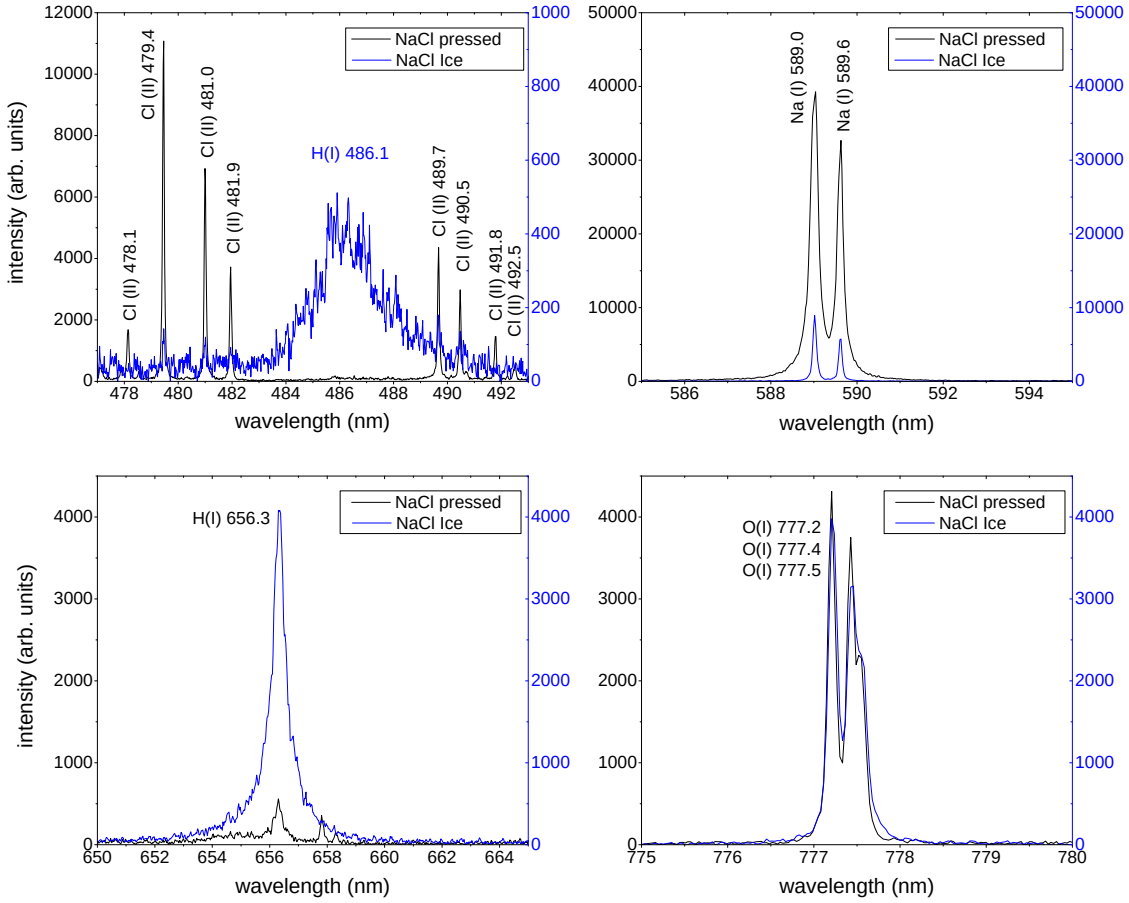

Figure 7.5: *Enlarged view of important emission lines in the LIBS spectra of NaCl as a pure salt sample (black) in comparison to those obtained from the frozen salt solution (blue). The intensities of the sodium and chlorine lines are strongly reduced in the ice spectra, whereas the hydrogen emission is significantly increasing. The line intensities of oxygen remain roughly unchanged.*

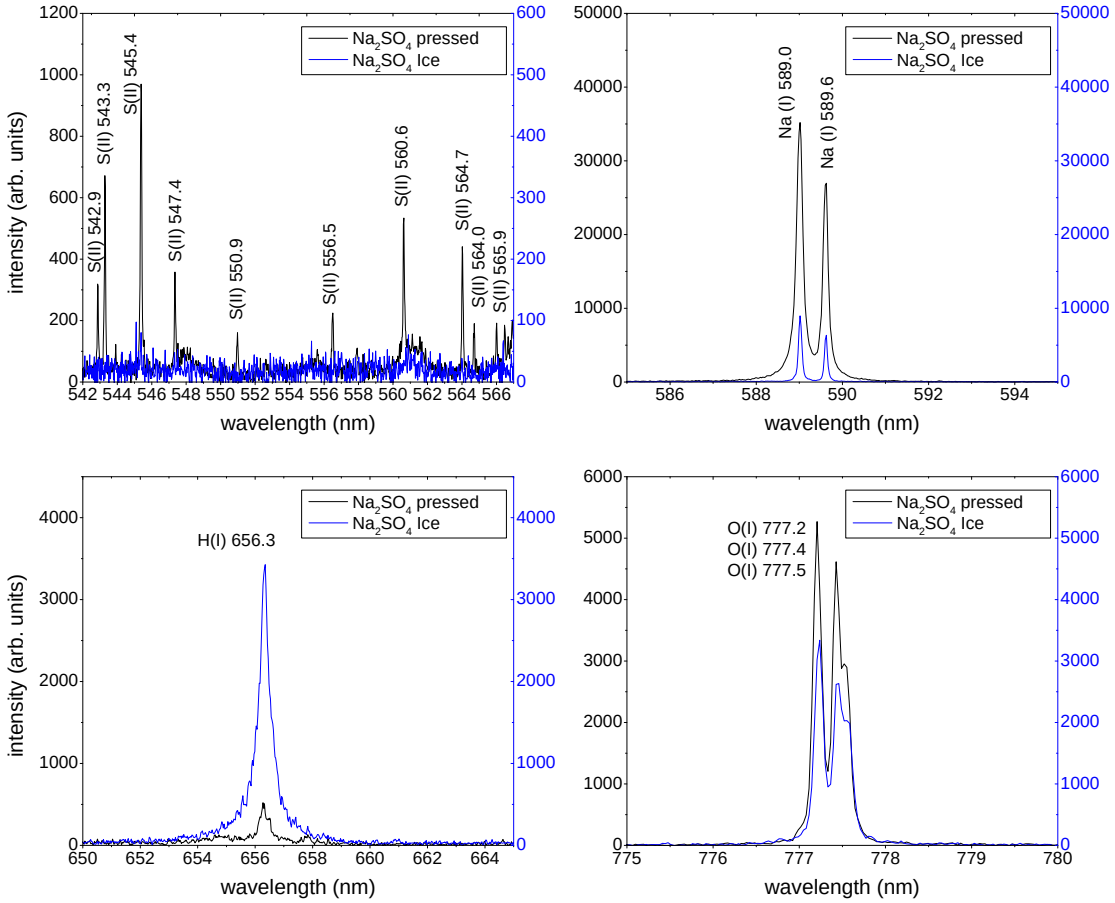

Figure 7.6: *Comparison of LIBS spectra of Na_2SO_4 pressed and as frozen salt solution (blue). The weak sulfur lines obtained from the pressed salt are not detectable in the case of the frozen salt solution. A strong emission of hydrogen is detected and the oxygen line intensities are slightly reduced in most of the spectra of the frozen salt solutions.*

Species	Wavelength (nm)	Configurations	Term	$E_i(\mathrm{cm}^{-1})$ - $E_k(\mathrm{cm}^{-1})$
Mg(I)	293.68	3s3p - 2s6s	$^1P^0$ - ^2S	21 850.41 - 55 891.80
Ca(II)	315.92	$3p^6$4p - $3p^6$4d	$^2P^0$ - ^2D	25 191.51 - 56 839.25
Ca(II)	317.95	$3p^6$4p - $3p^6$4d	$^2P^0$ - ^2D	25 414.40 - 56 858.46
Mg(I)	383.16	3s3p - 3s15d	$^1P^0$ - ^1D	35 051.26 - 61 142.1
Mg(I)	383.86	2s2p - 3s3d	$^1P^0$ - ^3D	21 911.18 - 47 957.03
Cl(II)	385.09	$2s^22p^1(^4S^0)$4p - $3s^23p^1(^4S^0)$4d	^5P - $^5D^0$	128 663.57 - 154 623.57
Cl(II)	386.09	$2s^22p^1(^4S^0)$4p - $3s^23p^1(^4S^0)$4d	^5P - $^5D^0$	128 730.82 - 154 624.66
K(II)	389.76	$3p^5$4s - $3p^5$4p	$^1P^0$ - ^1D	162 502.7 - 188 150.3
Ca(II)	393.36	$3p^6$4s - $3p^6$4p	^2S - $^2P^0$	0 - 25 414.40
Ca(II)	396.86	$3p^6$4s - $3p^6$4p	^2S - $^2P^0$	0 - 25 191.51
K(II)	418.63	$3p^5$4s - $3p^5$4p	$^1P^0$ - ^1D	162 502.7 - 186 383.8
Mg(II)	448.08	$2p^6$3d - $2p^6$4f	^2D - $^2P^0$	71 490.19 - 93 799.75
Cl(II)	479.46	$2s^22p^1(^4S^0)$4p - $3s^23p^1(^4S^0)$4d	$^5S^0$ - ^5P	107 879.66 - 128 730.82
Cl(II)	481.09	$2s^22p^1(^4S^0)$4p - $3s^23p^1(^4S^0)$4d	$^5S^0$ - ^5P	107 879.66 - 128 663.57
Cl(II)	481.91	$3s^23p^3(^4S^0)$4s - $3s^23p3(^4S^0)$4p	$^5S^0$ - ^5P	107 879.66 - 128 622.99
Cl(II)	489.67	$3s^23p^3(^2D^0)$4s - $3s^23p3(^4D^0)$4p	$^3D^0$ - ^3F	126 784.37 - 147 200.24
Mg(I)	518.33	3s3p - 3s4s	$^1P^0$ - ^1S	21 911.18 - 41 197.40
Cl(II)	521.78	$2s^22p^1(^4S^2)$4p - $3s^23p^1(^4S^0)$4d	$^1S^0$ - ^1P	112 609.36 - 131 768.66
Cl(II)	539.19	$3s^23p^3(^2D^0)$4s - $3s^23p^3(^2D^0)$4p	$^1D^0$ - ^1F	129 066.96 - 147 607.37
Cl(II)	542.31	$2s^22p^1(^4S^2)$4p - $3s^23p^1(^4S^0)$4d	^5P - $^5D^0$	110 296.84 - 128 730.82
S(II)	542.86	$3s^23p^1(^3P)$4s - $3s^23p^2(^3P)$4p	^4P - $^4D^0$	109 560.69 - 127 976.34
S(II)	543.19	$3s^23p^1(^3P)$4s - $3s^23p^2(^3P)$4p	^4P - $^4D^0$	109 831.59 - 128 233.20
Cl(II)	544.40	$3s^23p^1(^4S^0)$3d - $3s^23p^1(^4S^0)$4p	$^5D^0$ - ^5P	110 297.72 - 128 663.57
S(II)	545.38	$3s^23p^2(^3P)$4s - $3s^23p^2(^3P)$4p	^4P - $^4D^0$	110 268.60 - 128 599.16
Cl(II)	545.71	$3s^23p^1(^4S^0)$3d - $3s^23p^1(^4S^0)$4p	$^5D^0$ - ^5P	110 303.12 - 128 622.99
S(II)	547.35	$3s^23p^2(^3P)$4s - $3s^23p^2(^3P)$4p	^4P - $^4D^0$	109 560.69 - 127 825.08
S(II)	556.49	$3s^23p^2(^3P)$4s - $3s^23p^2(^3P)$4p	^4P - $^4D^0$	110 268.60 - 128 233.20
S(II)	560.58	$3s^23p^2(^3P)$3d - $3s^23p^2(^3P)$4p	^4F - $^4D^0$	110 766.56 - 128 599.16
S(II)	563.93	$3s^23p^2(^3P)$4s - $3s^23p^2(^3P)$4p	^2P - $^2D^0$	113 461.54 - 131 187.19
S(II)	564.03	$3s^23p^2(^3P)$3d - $3s^23p^2(^3P)$4p	^4F - $^4D^0$	110 508.71 - 128 233.20
S(II)	564.72	$3s^23p^2(^3P)$4s - $3s^23p^2(^3P)$4p	^2P - $^2D^0$	112 937.57 - 130 641.11
S(II)	565.99	$3s^23p^2(^3P)$4s - $3s^23p^2(^3P)$4p	^4F - $^4D^0$	110 313.40 - 127 976.34
Na(I)	588.97	$2p^6$3s - $2p^6$3p	^2S - $^2P^0$	0 - 16 973.37
Na(I)	589.56	$2p^6$3s - $2p^6$3p	^2S - $^2P^0$	0 - 16 956.17
H(I)	656.30	3p - 3d	$^2P^0$ - ^2D	82 359.29 - 97 492.36
K(I)	766.48	$3p^6$4s - $3p^6$4p	^2S - $^2P^0$	0 - 13 042.90
K(I)	769.92	$3p^6$4s - $3p^6$4p	^2S - $^2P^0$	0 - 12 985.19
O(I)	777.18	$2s^22p^1(^4S^2)$3s - $2s^22p^1(^4S^0)$3p	$^5S^0$ - ^5P	73 768.20 - 86 631.45
O(I)	777.49	$2s^22p^1(^4S^2)$3s - $2s^22p^1(^4S^0)$3p	$^5S^0$ - ^5P	73 768.20 - 86 627.78
O(I)	777.65	$2s^22p^1(^4S^2)$3s - $2s^22p^1(^4S^0)$3p	$^5S^0$ - ^5P	73 768.20 - 86 625.76
Cl(I)	833.35	$3s^23p^4(^3P)$4s - $3s^23p^4(^3P)$4p	^4P - $^4D^0$	72 488.57 - 84 485.31
Cl(I)	837.53	$3s^23p^4(^3P)$4s - $3s^23p^4(^3P)$4p	^4P - $^4D^0$	71 958.36 - 83 894.04
Cl(I)	842.85	$3s^23p^4(^3P)$4s - $3s^23p^4(^3P)$4p	^4P - $^4D^0$	72 827.04 - 84 688.64
O(I)	844.73	$2s^22p^1(^4S^2)$3s - $2s^22p^1(^4S^0)$3p	$^1S^0$ - ^1P	76 794.98 - 88 631.15

Table 7.2: *Selected emission lines for PCA, SIMCA and PLS-DA [Ralchenko et al., 2011].*

Principal components analysis (PCA)

PCA pressed salt samples First, a PCA was performed for the whole LIBS data set of the pressed salts. The data matrix in this case consists of 64 rows (8 salts x 8 spectra) and 32476 columns constituting the variables (corresponding to the number of bins). Before entering the PCA the spectra were rebinned, i.e. a total of 32476 bins (i.e. wavelength channels) was reduced to 6496 by averaging 5 bins each. This was done mainly for two reasons: First, the resolution of the broadband echelle spectrum was obtained with the laboratory hardware and a spectrum obtained with a spaceflight instrument would not provide this high resolution. Second, the computation time was strongly reduced for the MVA with only 6496 variables entering the analysis instead of more than 32000. A comparison showing the rebinning effect on an important region of the spectra with the most intense chlorine lines available is shown in Fig. 7.7. The chlorine lines, if present, are still resolved and, thus, provide information for the subsequent PCA. The sulfur emission lines, as stated above mostly disappear in the noise (not shown here).

In Fig. 7.8 the PCA scores of the first, second and third principal component (PC) are shown. The appropriate loadings can be seen in Fig. 7.9. Each point in these scatter plots represents one spectrum. In the space defined by the first two principal components (Fig. 7.8, top), where PC1

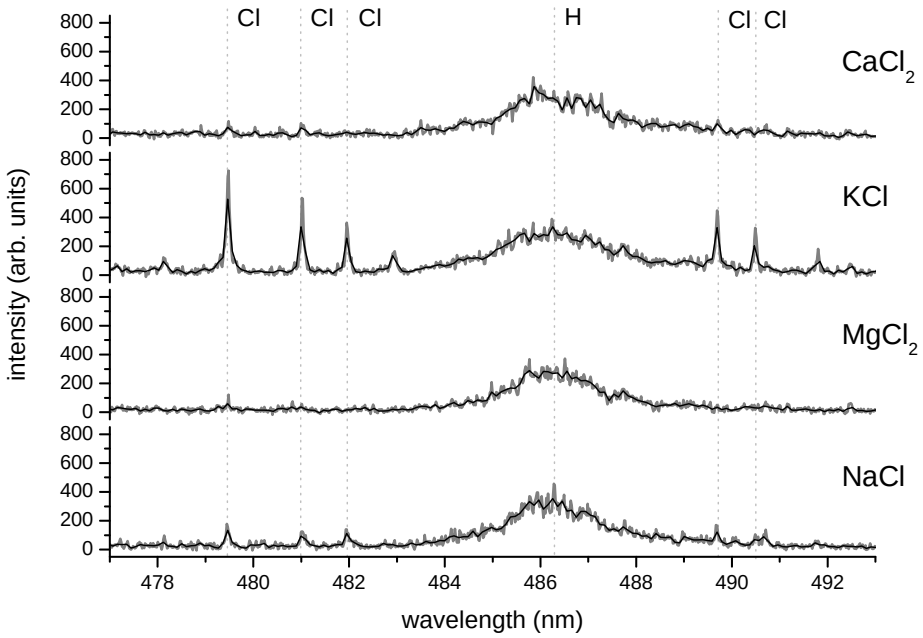

Figure 7.7: *For further analysis with chemometric methods the LIBS spectra were rebinned, i.e. five wavelength channels were averaged each, thus, reducing the resolution. For comparison the original data are depicted in grey together with the rebinned spectra in black. Shown is the region with the strongest chlorine lines available in the spectra of the frozen salt solutions. Emission lines that were detectable with higher resolution were still resolved sufficiently to enter the subsequent MVA with the rebinned data. However, several chlorine lines and most of the sulfur lines (not shown here) were not detected in the spectra of the ices.*

explains 48% of the total variation and PC2 represents 35%, separation is achieved mainly due to the metal atoms in the salts and their strong emission lines in the spectra. Four distinct clusters form on account of the emission lines of sodium, calcium, magnesium and potassium. The sodium containing salts plot in the upper right as a result of a positive loading value for PC1 along with a positive loading value for PC2 due to the sodium lines. Moreover, chlorine and sulfur weakly contribute to PC1 as shown in the enlarged extract of the loading plot in Fig. 7.10. The calcium containing salts cluster in the upper left, and the salts comprising potassium and magnesium plot in the bottom left due to the second PC that includes the magnesium lines in the spectra. In addition, hydrogen and oxygen contribute to PC2. Potassium is taken into account by PC3 (13%), clearly isolating it from the three other salts. PC3 additionally includes chlorine and sulfur, providing division of the chlorides from the sulfates in the local clusters. Hydrogen with a positive loading value and oxygen with a negative loading value support this partition. The chlorine lines and the sulfur lines are correlated in PC1 and PC3 and appear in the loadings with the same sign. An explicit anti-correlation between the chlorine lines and the sulfur lines was obtained in the PCA visible in PC4 with only 3%, providing further improved separation of all of the sulfates (clustering in the positive space defined by PC4) from the chlorides, which assemble in the bottom part of the scores plot according to negative values in PC4 (scores plot not shown here). The sulfates in this PCA study plot further out from the point of origin than the chlorides due to their higher scores along the first PCs because of the more intense metal lines in the normalized LIBS spectra. In the case of the local calcium cluster in the space defined by PC1 with PC2 and PC1 with PC3, respectively, one spectrum of $CaSO_4$ is found in between the spectra of $CaCl_2$, although only at the edge of the $CaCl_2$ group. This spectrum could be an outlier and if the PCA results were meant to be further used for a predictive model, this spectrum should be removed. Moreover, it should be carefully considered whether or not the fourth PC should be taken into account, which provides most explicitly the information of the chlorine and sulfur lines but accounts for only an additional 3%. These results show that sulfates may be distinguished in PCA from chlorides with the same cation in Martian atmospheric conditions given strong enough lines from chlorine and sulfur in the LIBS spectra.

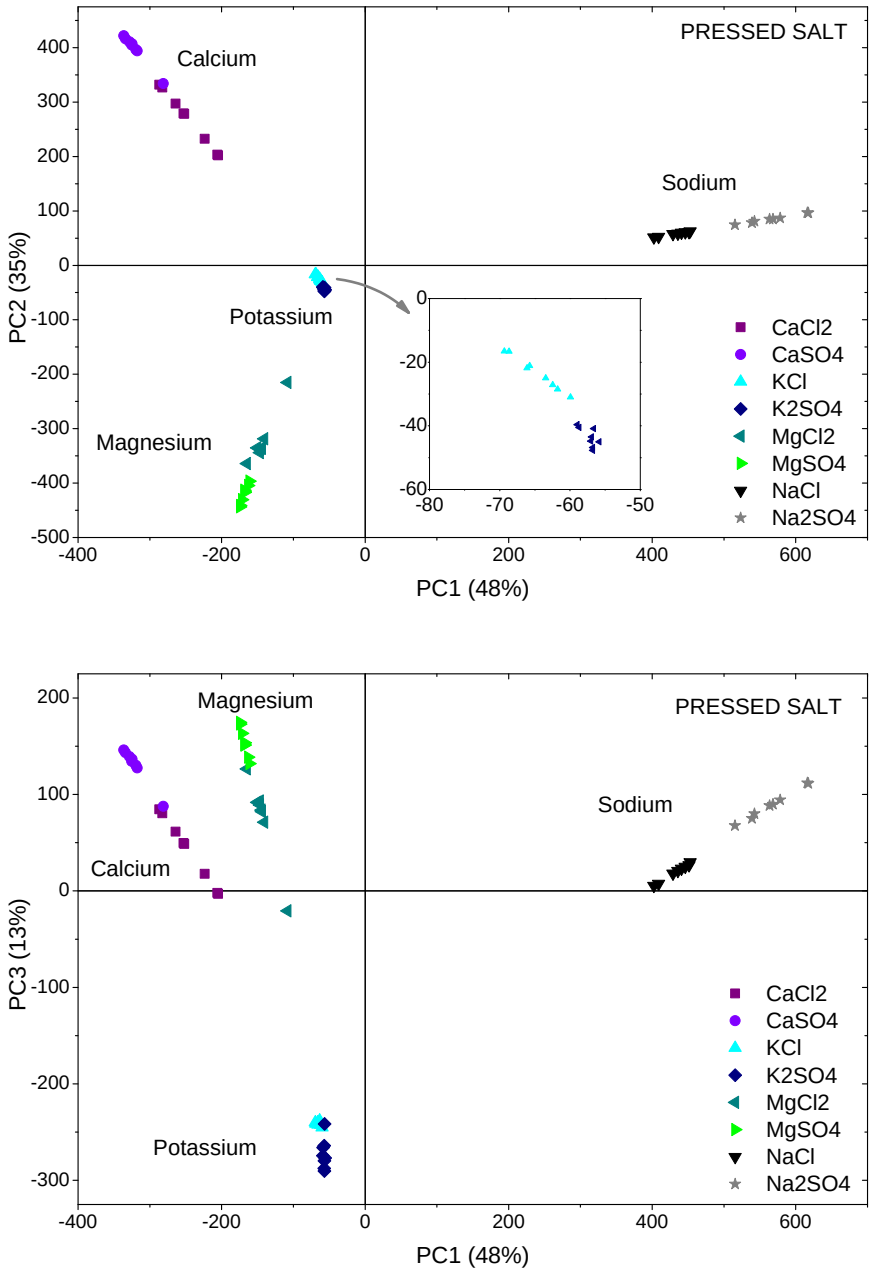

Figure 7.8: *Principal components analysis of eight salts ($CaCl_2$, $CaSO_4$, KCl, K_2SO_4, $MgCl_2$, $MgSO_4$, $NaCl$, Na_2SO_4) as pressed pellets utilizing the whole rebinned data set. One point in the scatter plots represents one LIBS spectra obtained by accumulating the plasma emission generated by 20 laser pulses each. Shown are the scores on the first and second PC (top) and first and third PC (bottom); the percentage of variance in the data explained by the appropriate component is given in brackets.*

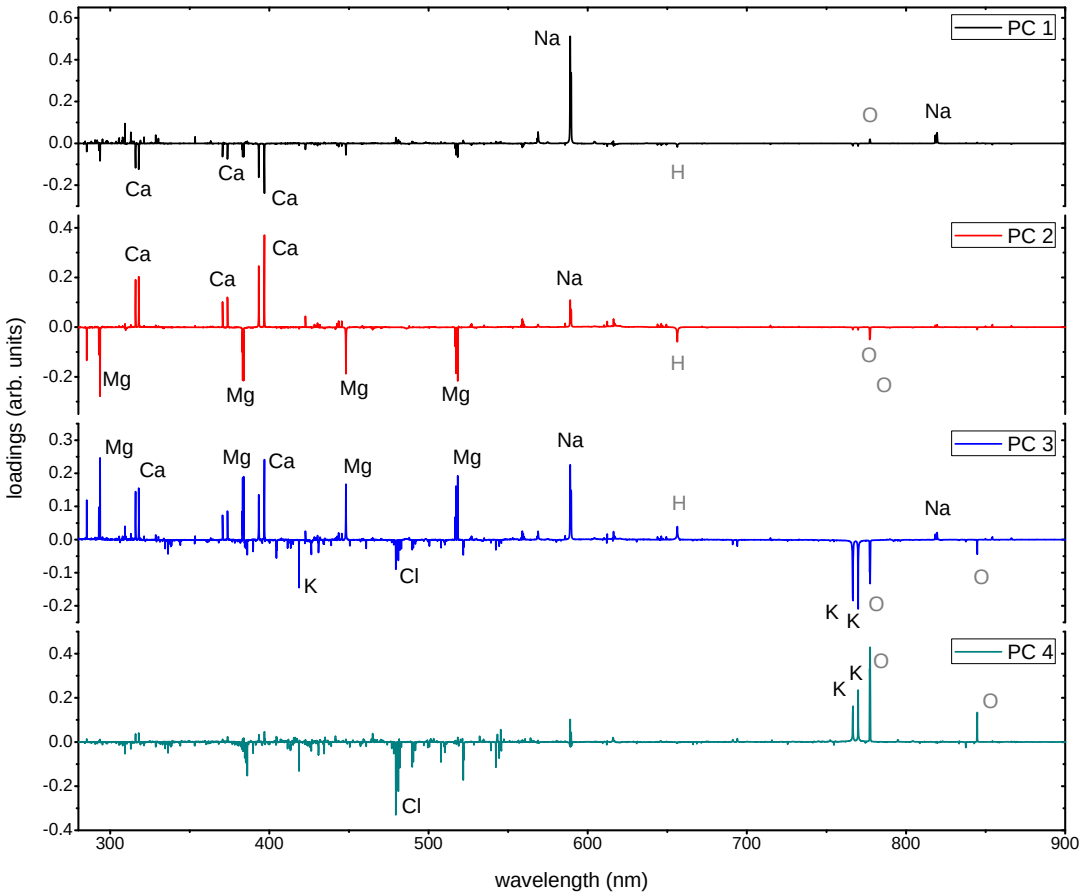

Figure 7.9: *The loadings plots of the first four PCs for the broadband LIBS spectra of the pressed salt samples demonstrate which emission lines are responsible for the variation included in the appropriate PC.*

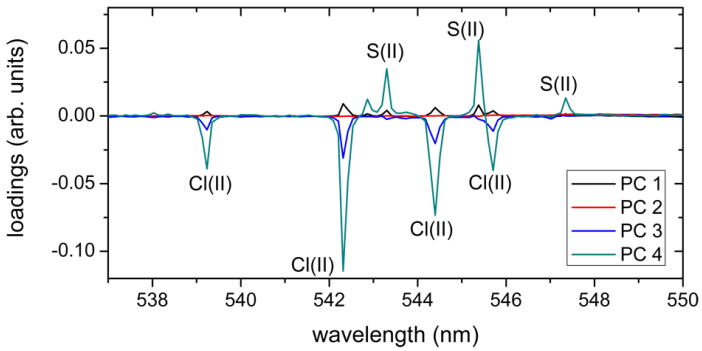

Figure 7.10: *Loadings of the first four PCs for LIBS spectra of the pressed salt samples in the wavelength range from 537 nm to 550 nm including several chlorine and sulfur lines.*

PCA frozen salt solution The PCA for the frozen salt solutions was first performed with the whole data set as done for the pressed salt pellets. Spectra of the same sample are distributed over larger areas and intermingle with adjacent groups in the scores plots due to the high variability in the LIBS spectra (scatter plots not shown here). In the space defined by the first two PCs three clusters form: one with the calcium containing salts, one with sodium, both according to PC1 and one comprising magnesium and potassium containing salts. The latter mixed cluster does not split into a magnesium and potassium group before taking into account PC4. For the first four principal components the spectral loadings are shown in Fig. 7.11.

Again, PC1 includes the information of the most intense lines, namely calcium and sodium, and explains 43% of the total variation in the data. Likewise, the much more intense hydrogen and oxygen lines of the ices, in contrast to the spectra of the pressed salts, are taken into account by PC1, but also contribute to other PCs. Magnesium contributes to PC2 (32%), potassium to PC3 (17%). The chlorine lines, however, are not considered until PC4 (3%) and have only little impact there. Sulfur lines do not contribute at all, see Fig. 7.12. The hydrogen and oxygen lines again contribute to the PC, which also includes the information of the chlorine lines (here PC4). In comparison in the PCA

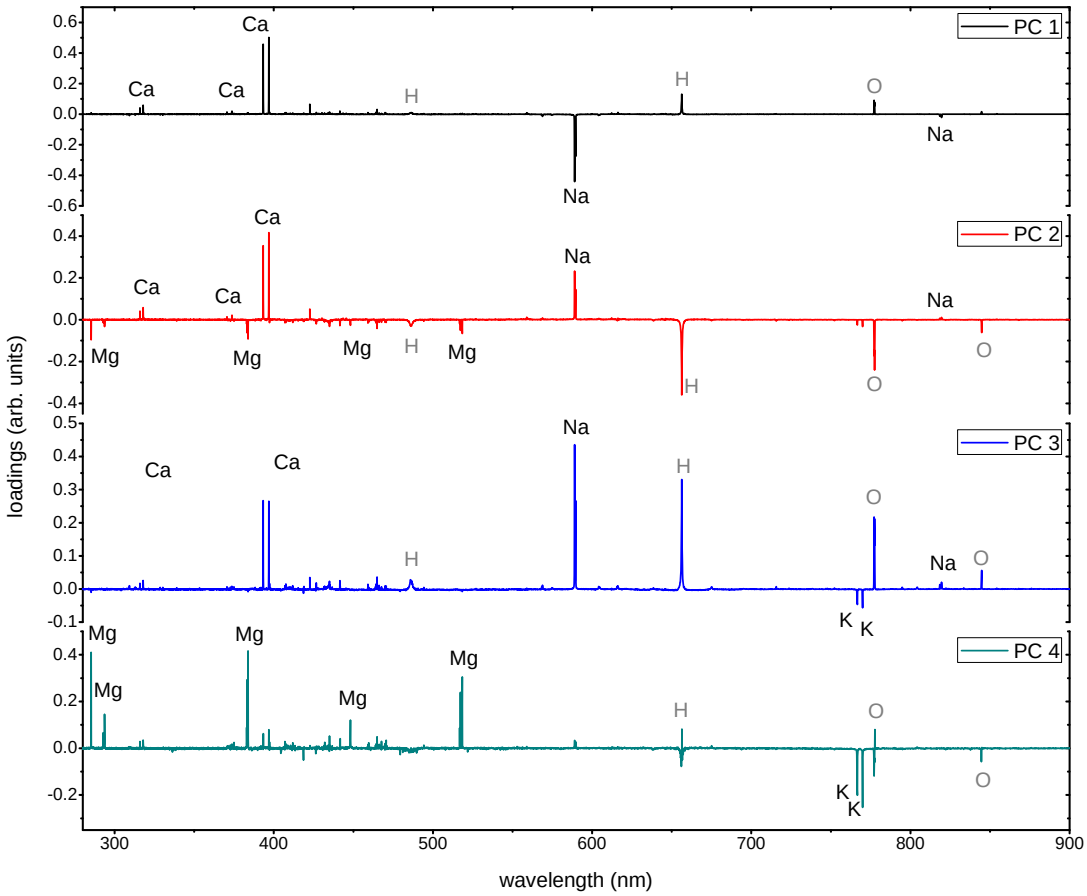

Figure 7.11: *PCA loadings plots of the principal components 1-4 for the rebinned broadband LIBS spectra of the frozen salt solutions ($CaCl_2$, $CaSO_4$, KCl, K_2SO_4, $MgCl_2$, $MgSO_4$, $NaCl$, Na_2SO_4).*

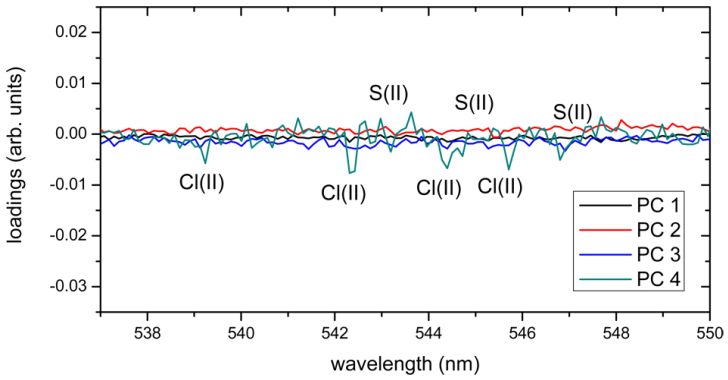

Figure 7.12: *Loadings of the first four PCs for LIBS spectra of the frozen salt solutions in the wavelength range from 537 nm to 550 nm. Marked are the positions of sulfur and chlorine lines.*

of the pressed salts the loadings of the hydrogen and oxygen lines changed the sign in PC3 (i.e. anti-correlation) and have the same sign (i.e. correlation) for the previous PCs. In the case of the frozen salt solutions, both H(I) 656.3 nm as well as the triplet at 777 nm, are found to contribute to PC4, each with positive and negative values. The hydrogen line has a positive center in the PC4 loadings while the edges of the line remain negative. This division is based on a difference in the shape of the hydrogen line in the spectra of the frozen solution with $CaCl_2$ and in the spectra of those with $CaSO_4$, but slight separation of K_2SO_4 from KCl is obtained through this reversal in the central region of the line in the loadings. In the case of the triplet the oxygen lines at 777.2 nm and 777.4 nm are found to have negative loading values as is the case for O(I) 844.6 nm, whereas O(I) 777.5 nm has a positive loading value, which is again due to differences in the shape of these lines in the spectra of $CaCl_2$ and $CaSO_4$ in the frozen salt solutions. Clear separation of the sulfates from the chlorides is achieved only in the case of the calcium salts incorporating PC4. For the Mg group, partition is obtained with no overlap but with the sulfates in close proximity to the chlorides.

In order to optimize the PCA outcome in terms of improving the discrimination ability for the frozen salt solutions, several attempts have been made. First, the most relevant lines were selected, choosing the most intense metal lines, oxygen and hydrogen and in addition all chlorine and sulfur lines available in the spectra (see Table 7.2 for further information). If available, the three bins holding the maximum values per line were chosen. In case of sulfur and chlorine, however, in consequence of the rebinning of the spectra, only 1-2 bins were utilizable for some lines. Another PCA was then performed using only the set of selected lines as input variables with the aim of forcing the PCA to focus more on the weak chlorine peaks and, in so doing, reducing the data dimensionality by two orders of magnitude. However, by this means, only a small improvement was achieved and scores plots similar to those obtained in the previous PCA with the whole data set were received with spectra of the same samples clustering only slightly closer to each other.

A more significant improvement was achieved when averaging several spectra. For the case of averaging two spectra each and additionally working with the selected lines as input variables for the PCA, the resulting scores plots are shown in Fig. 7.13. A cluster due to calcium is obtained with PC1 (50%) and PC2 (33%) in the upper right, which already splits up into two sub-clusters on account of the chloride and the sulfate; the former more widespread than the latter. Another compact cluster due to sodium plots in the upper left. Here, no separation of the chlorides from the sulfates is achieved, neither with PC2 nor with a higher PC. Potassium and magnesium containing samples

cluster in this scores plot, but split up taking into account PC4 (3%). In the space defined by PC1 with PC4 the chloride separates from the sulfate in the magnesium group mostly because of higher scores due to more intense magnesium lines in the normalized spectra of the sulfates. Additionally, in PC4 the selected oxygen and hydrogen lines facilitate the separation of the chlorides from the sulfates, whereas the selected chlorine lines hardly contribute. PC3 with 13% is neither supporting a division of Mg from K nor sulfates from chlorides in the other clusters.

As a last attempt to separate these in the analysis employing PCA for the LIBS spectra of the frozen salt solutions the data were divided on the basis of the cations of the salts and thus, four groups were obtained. A PCA was performed with the smaller sets of spectra, each containing four averaged spectra of the sulfates and the chlorides and using the selected lines as input variables only. By this means, in the case of the sodium group, a separation of the chlorides from the sulfates can be achieved with the subsequent PCA of the spectra of NaCl and Na_2SO_4 only. PC1 (77%) together with PC3 (4%) now divide both sodium containing salts due to different contributions of the intense sodium doublet around 589 nm and the oxygen triplet at 777 nm. A separate PCA for the potassium salts did not yield similar results and the cluster of sulfates and chlorides remained mixed.

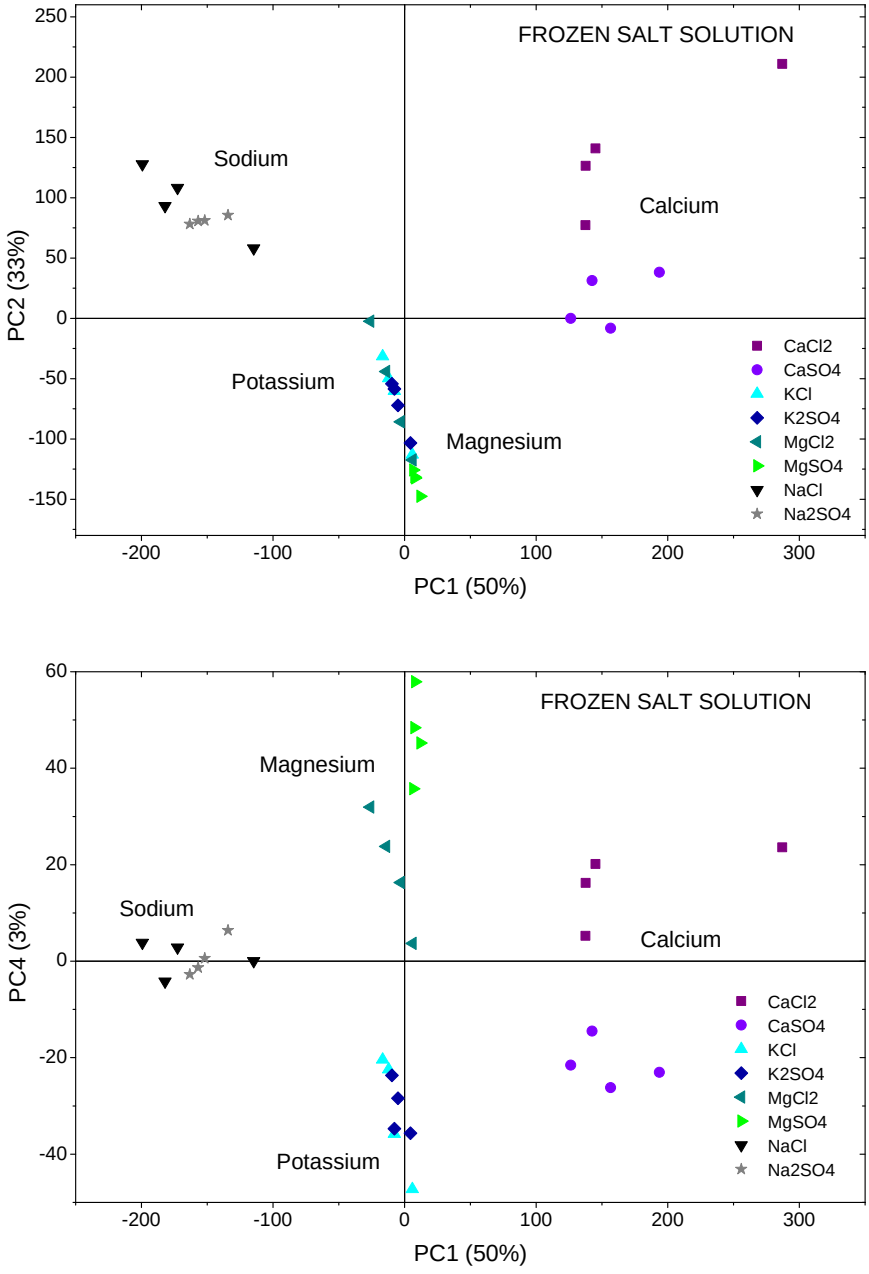

Figure 7.13: *Results of PCA with the spectra of the frozen salt solutions ($CaCl_2$, $CaSO_4$, KCl, K_2SO_4, $MgCl_2$, $MgSO_4$, $NaCl$, Na_2SO_4). Shown are the scores plots of PC1 with PC2 (top) and PC1 with PC4 (bottom). The PCA was calculated with a set of selected emission lines. One point in the scatter plots represents the average of two LIBS spectra.*

Soft independent modeling of class analogy (SIMCA)

SIMCA was applied to the spectra of the salt pellets, utilizing the whole spectra as it was done for the PCA of the pressed salts. The data set was split into a calibration set by choosing every second spectrum, while the remaining half of the spectra constituted the prediction set. A separate PCA was performed for every class i.e. type of salt, resulting in eight individual PCAs. For the prediction of the "unknown" spectra these PCA models were applied with only one PC each, except for the model of $CaCl_2$, where two PCs were used. As can be seen from the results in Table 7.3 the calcium, potassium and the sodium salts in this study could be correctly classified with no unclassified spectrum and moreover no falsely classified sample. However, SIMCA did not work in the case of the magnesium group and the number of correctly classified spectra is close to those falsely classified and thus, not adequate. The reason can be seen in Fig. 7.14 (left), where the model distances between the different classes are shown. The distance between the model of magnesium chloride and magnesium sulfate is found to be one order of magnitude smaller in comparison to the distances the other pairs of chloride and sulfate with the cation of the same kind obtained.

The number of PCs of the class models was varied in order to optimize the outcome, putting particular emphasis on the magnesium group, but no improvement was achieved with more than one PC. Using the selected lines only did not improve the separation of $MgCl_2$ and $MgSO_4$. Employing the averaged spectra for SIMCA even had a negative effect on the prediction results, yielding one unclassified spectrum for both $CaSO_4$ and Na_2SO_4, however, no false classification. With SIMCA it was not possible to distinguish between the pure pressed salts $MgCl_2$ and $MgSO_4$ when utilizing the whole data set. An improvement could be achieved for the $MgCl_2$ spectra with six out of eight correct classifications and one unclassified spectrum when using the reduced data set with selected lines only. The spectra of $MgSO_4$ could not be correctly classified with the SIMCA model of selected lines.

Sample (pressed)	**$CaCl_2$**	**$CaSO_4$**	**KCl**	**K_2SO_4**	**$MgCl_2$**	**$MgSO_4$**	**NaCl**	**Na_2SO_4**
$CaCl_2$	8	-	-	-	-	-	-	-
$CaSO_4$	-	8	-	-	-	-	-	-
KCl	-	-	8	-	-	-	-	-
K_2SO_4	-	-	-	8	-	-	-	-
$MgCl_2$	-	-	-	-	8	6	-	-
$MgSO_4$	-	-	-	-	6	8	-	-
NaCl	-	-	-	-	-	-	8	-
Na_2SO_4	-	-	-	-	-	-	-	8

Table 7.3: *SIMCA prediction results for the pressed salt samples. The salts listed in the first column are assigned to one or more of the classes listed in the top row. Stated are the total numbers of spectra assigned to the class in the top row by the SIMCA model on the basis of minimum distances between a spectrum and the individual PCA models.*

A SIMCA model was built analogously with half of the spectra of the frozen salt solutions and the remaining data were predicted subsequently. Improved SIMCA results were obtained with the reduced spectra utilizing selected lines only. However, even the improved SIMCA performance was by no means adequate since the number of false classified spectra in most cases still far exceeds the number of correctly classified spectra, making a reasonable classification of the LIBS spectra of different frozen salt solutions impossible (see Table 7.4). The SIMCA prediction model worked best with the spectra of $CaSO_4$, which were the only ones 100% correctly classified. $CaCl_2$ obtained two

times double class attributions with $CaSO_4$ and with $MgCl_2$. The sodium containing salts cannot be distinguished from each other, but can be separated from the other salts with different cations. In the case of the potassium and magnesium containing salts it was not possible to correctly classify the LIBS spectra nor to tell apart at least those two groups despite the metal lines of magnesium and potassium. The distances between the different models are shown in Fig. 7.14 (right). The maximum distance between a pair of sulfate and chloride with the same cation was obtained for the calcium containing salts. Moreover, the models of the sodium containing salts clearly separated from the other models, but were found to be too close to each other to be successfully used to distinguish the sodium chloride from the sodium sulfate.

As stated e.g. in [Gottfried et al., 2009b], SIMCA is a useful method and serves the purpose of classification well when different classes of samples are investigated and thus, their spectra vary widely. A disadvantage of SIMCA is that only maximum variance is considered for each class while no attempt is made to identify the variables that separate the classes. For this reason the application of SIMCA for the data of this study had little success. PLS-DA, which considers the variables more important for discrimination, was applied to the LIBS spectra in the third part of this chapter.

Sample (ice)	**$CaCl_2$**	**$CaSO_4$**	**KCl**	**K_2SO_4**	**$MgCl_2$**	**$MgSO_4$**	**NaCl**	**Na_2SO_4**
$CaCl_2$	8	1	-	-	1	-	-	-
$CaSO_4$	-	8	-	-	-	-	-	-
KCl	-	-	8	8	8	5	-	-
K_2SO_4	-	-	8	8	8	7	-	-
$MgCl_2$	2	-	4	3	8	4	-	-
$MgSO_4$	-	-	7	3	8	8	-	-
NaCl	-	-	-	-	-	-	8	8
Na_2SO_4	-	-	-	-	-	-	6	8

Table 7.4: *SIMCA prediction results for the frozen salt solutions. The ices with salts listed in the first column are assigned to one or more of the classes listed in the top row. Stated are the total numbers of spectra assigned to the class in the top row.*

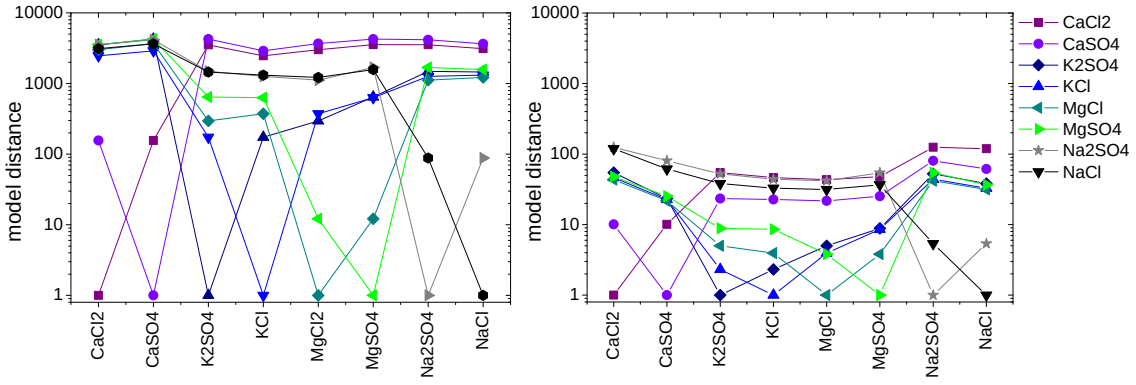

Figure 7.14: *SIMCA model distances for pressed salts (left) and for frozen salt solutions (right). The distances between PCA models are smallest for two salts with the same cation.*

Partial least squares discriminant analysis (PLS-DA)

A PLS-DA model comprising all samples was built for the unreduced LIBS spectra of the pressed salt pellets. Class affiliation for every salt was encoded and stored into a response matrix with values of "1" for members and "0" for non-members, as explained above. For the pressed salts scores and loading plots similar to those obtained in the PCA were received, but slightly improved in that the clusters appeared more close to each other. For the frozen salt solutions a similar result was achieved, again with small improvements in that the clusters appeared more concrete, which could be additionally slightly optimized using the previously selected lines as input only.

For the purpose of discriminating the sulfates from the chlorides with cations of the same kind, four data subsets were defined due to Ca, K, Mg and Na. For each of these data sets a local PLS-DA model was built to discriminate between the sulfates and the chlorides within these groups with half of the data, i.e. four spectra of both salts. The remaining half was then used as a test set, comprising the "unknown samples" that were interpreted with regard to class affiliation. All regression models obtained root mean square errors between 0.19-0.22 and were found to be convenient for the aim of discriminating the sulfates from the chlorides considering the third LV each. As a representative example the predictions of model data and the unknown samples for the potassium group are shown in Fig. 7.15. Prediction was done for the K_2SO_4 model; samples similar to this model obtain prediction values close to 1. The first four values shown (filled symbols) are those of the samples which were used to build the model. The following four symbols signify the values obtained for the test set. An unknown spectrum can be attributed to a certain group when the deviations do not overlap with those of the other group, which is not entirely fulfilled for the potassium salts with the second latent variable, but accomplished with the third. The deviation is based on an approximation of the theoretical variance of predictions under certain assumptions [CAMO, 2012] and has been improved by [De Vries and Ter Braak, 1995]. It is obtained by:

$$yDeviation = \sqrt{ResYValVar\left(\frac{ResXValSamp_{\text{pred}}}{ResXValTot} + Hi + \frac{1}{I_{\text{cal}}}\right)\left(1 - \frac{a+1}{I_{\text{cal}}}\right)}, \tag{7.2}$$

where

$yDeviation$ = deviation of Y-variable
$ResYValVar$ = y-residual variance in the validation set
$ResXValSamp$ = x-residual variance in the prediction object
$ResXValTot$ = average x-residual variance in the validation objects
Hi = leverage of the prediction object with respect to a PLS components
I_{cal} = number of calibration objects
a = number of components.

Lines of potassium ions and chlorine ions were found to be of prime importance for discriminability, along with hydrogen and oxygen emission lines.

Conclusion

A set of eight salts consisting of four chlorides and four sulfates with cations of the same kind was analyzed as pure pressed pellets and in frozen salt water solutions. MVA techniques were implemented to analyze the LIBS spectra, focusing on the aim of distinguishing the sulfate and chloride pairs. In the case of the LIBS spectra of the pressed salts, the chlorides can be distinguished from the sulfates due to their chlorine and sulfur lines by applying PCA to the whole normalized spectra. The weak

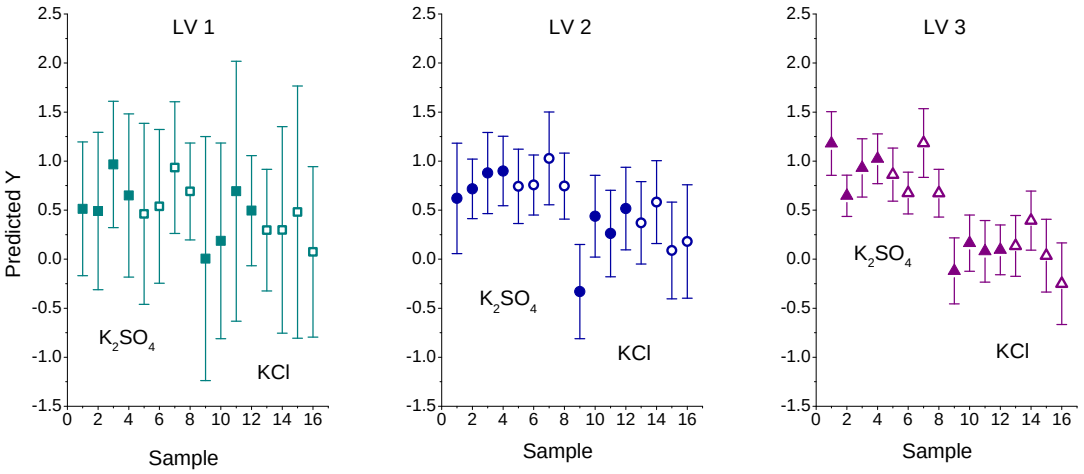

Figure 7.15: *PLS-DA prediction for K_2SO_4 and KCl frozen salt solutions. Shown are the prediction values obtained for the four spectra utilized to build the prediction model (filled symbols) and the four spectra interpreted with the model (empty symbols) for both the sulfate (left) and the chloride (right), according to the first, the second and the third latent variable (LV).*

sulfur and chlorine lines available in this spectral range are even less intense in the spectra of the frozen salt solutions and mostly disappear in the background. Relevant information to distinguish between sulfates and chlorides was found to be contained in the hydrogen and oxygen lines as well as in the particular metal lines. The PCA performed with selected lines instead of working with the whole data set merely slightly improved the results. However, averaging two spectra each already had a big impact on the PCA clusters and improved the discrimination ability. Further improvement is expected to be achieved by averaging several spectra to build more robust models; hence, more extensive data sets are necessary in order to obtain useful prediction models. Additionally, the concentration of salts in the frozen solutions should also be varied with regard to future quantitative analysis approaches. Four of eight salts in frozen salt solutions form distinct clusters and can be identified ($CaCl_2$, $CaSO_4$, $MgCl_2$, $MgSO_4$). Both sodium containing salts can be assigned with a subsequent local PCA. SIMCA was not successful for the salts in frozen solution due to the small distances between different models. With local PLS-DA of the data including only spectra of salts with the same type of cation, all chlorides can be discriminated from the appropriate sulfates. As PLS-DA performed best in this study and was generelly most successful at distinguishing sulfate and chloride salts, this MVA is recommended for distinguishing between salts and frozen salt solutions.

As a first step in this feasibility study only pure salt water frozen solutions have been investigated and tested for the potential of LIBS together with MVA to discriminate between them. A necessary next step is to consider mixtures of two or several salts and examine how they will fit into existing models and, if appropriate, expand the models.

The application of multivariate analysis methods to LIBS spectra of ices demonstrates the ability of LIBS to distinguish between different salts in frozen salt water solutions. This study confirms that LIBS is a powerful analytical technique for planetary exploration and can be utilized to determine compositional information of ice samples and identify certain salts within under Martian conditions.

ration and can be utilized to determine compositional information of ice samples and identify certain salts within under Martian conditions.

8 Studies of ferric salts in frozen solutions

In this chapter the potential of LIBS for identifying two ferric salts, iron(III) sulfate ($Fe_2(SO_4)_3$) and iron(III) chloride ($FeCl_3$), was investigated in two ways: (1) pressed into pure salt pellets and (2) in frozen salt solutions under Martian atmospheric conditions. The ferric salts have been excluded from the study described in Chapter 7 where chlorides and sulfates with the same cation have been investigated, since the strong iron lines in their spectra complicate detection of the already weak chlorine and sulfur lines. Here, most effort was made to identify chlorine and sulfur emission lines in the LIBS spectra of the ferric salts and to reveal the spectral features relevant for their discrimination both, as pressed samples and in a frozen salt water solution. For the purpose of classification the MVA method PLS-DA was employed, which was shown to be the most accurate MVA method tested for discriminating chlorides from sulfates with the same cation in the previous chapter.

Both ferric salts are considered in the context of possibly existing liquid brines on the surface of Mars [Altheide et al., 2009] and are moreover of particular interest for astrobiology in view of possible extraterrestrial life since iron is an essential component of life as we know it. Ferric sulfates such as jarosite ($KFe_3^{3+}(OH)_6(SO_4)_2$) have been found on Mars at different locations. For instance the two Martian rovers Opportunity and Spirit discovered them in Meridiani Planum [Squyres et al., 2004] and in soils in Gusev Crater with concentrations of up to 30% [Johnson et al., 2007], [Lane et al., 2008]. These salts indicate once strongly oxidizing conditions on the Martian surface and require formation from an acid-sulfate brine.

Ferric sulfate is a yellow, rhombic crystalline salt which is soluble in water at room temperature (295 K). Here, exsiccated iron(III) sulfate hydrate ($Fe_2(SO_4)_3 \cdot x\ H_2O$, M = 399.88 g/mol ($\cdot x\ H_2O$)) was used for analysis. Ferric chloride, the second ferric salt investigated, is in its anhydrous form highly deliquescent and forms hexahydrate $FeCl_3 \cdot 6\ H_2O$ when exposed to air. It is reported to have a higher eutectic temperature than its sulfate equivalent, i.e. 238 K for 28.8 wt.% [Marion et al., 2008] versus 205±1 K for 48±2 wt.% [Chevrier and Altheide, 2008]. However, a considerably higher eutectic temperature for $Fe_2(SO_4)_3$ of 247 K for 39±2 wt.% was obtained in [Möhlmann and Thomson, 2011] with a theoretical phase diagram. For sample preparation iron(III) chloride hexahydrate was used. The pressed salt samples with a diameter of 13 mm consisted of 1 g of the pure salt each and were pressed at 3760 kg/cm^2, a picture can be seen in Fig. 8.1 (left). The ice samples were prepared with the appropriate salt in a solution with salt concentrations of circa 2 wt.% as described in detail in Chapter 5.2. Pictures of both salts as a frozen salt solution can be seen in Fig. 8.1 (right). While the frozen salt solution of the ferric sulfate was solidly frozen (thus, suggesting a higher eutectic temperature with respect to the values reported in the publications above), a thin liquid layer on the frozen salt solution of the ferric chloride remained under ambient conditions in the laboratory as well as under simulated Martian conditions during the measurements.

The measurement was performed as described before: the Inlite laser was utilized with an energy attenuated to 35 mJ and the Vis/NIR wavelength range was chosen for this study to include the hydrogen and oxygen lines. The gain was set to 80 and the delay time was 500 ns with a detection time gate of 5 μs. Spectra from 20 laser-induced plasmas were accumulated each time probing a new position, collecting 20 LIBS spectra for both, the pressed sample and the frozen salt solution. All measurements were performed under simulated Martian atmospheric conditions with the appropriate gas mixture at a pressure of 700 Pa.

Figure 8.1: *Left: Pressed samples of 1) iron(III) sulfate $Fe_2(SO_4)_3$ and 2) iron(III) chloride $FeCl_3$. Middle: Frozen $Fe_2(SO_4)_3$ solution. Right: Frozen $FeCl_3$ solution. The frozen salt solutions appeared with a yellowish to white color, the color in the pictures does not resemble the real appearance very precisely. Both ices are shown after probing.*

Results - pressed salt samples

Two representative LIBS spectra of the pressed ferric hydrated salts can be seen in Fig. 8.2. They have been normalized as explained in Eq. (7.1), each divided by the average value of the spectrum and thus accomplishing an equal area under the curve for both spectra. As expected, the LIBS spectra of the pressed salts are very similar and even the strongest lines of chlorine and sulfur are weak in comparison to the strong iron lines in this spectral range. This makes a distinction of the chloride from the sulfate on the basis of these lines challenging already in the case of the pure salt pellets. If available the chlorine lines in close proximity to the hydrogen beta line at 486.1 nm are suitable for discrimination as they are still more intense and less superimposed by iron lines as the most intense sulfur lines available, which will be discussed in detail in the next paragraph. Moreover, the LIBS spectra of the pressed $Fe_2(SO_4)_3$ and $FeCl_3$ samples can be distinguished by means of

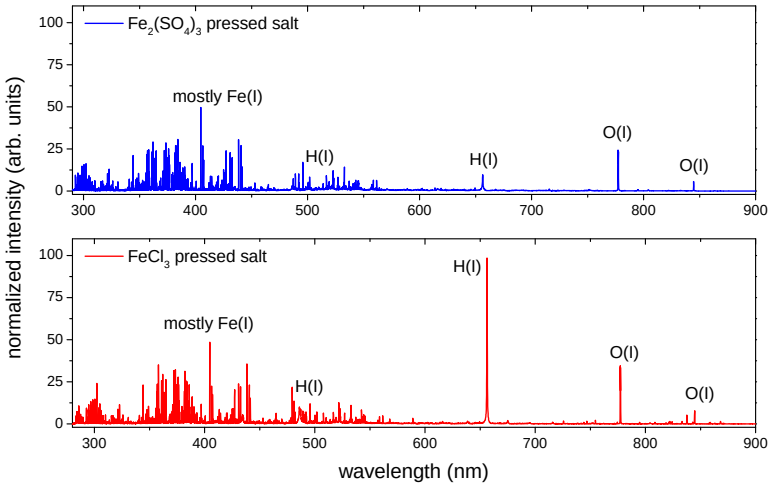

Figure 8.2: *LIBS spectra of pressed $Fe_2(SO_4)_3$ hydrate (top) and $FeCl_3$ hydrate (bottom) obtained under Martian atmospheric conditions. The spectra are dominated by the ferric lines at shorter wavelengths. In the red to infrared range the emission lines of hydrogen and oxygen are clearly visible.*

the hydrogen lines. The spectra of $FeCl_3$ feature much stronger hydrogen lines as a result of the salt's very hygroscopic behavior and the attracted and incorporated water molecules. The moisture of the salt sample also resulted in stronger background emission in the spectra of the ferric chloride. Working in the low pressure environment of a simulated Martian atmosphere did not entirely prevent this effect.

The plasma temperature was calculated for both ferric salts by means of a Boltzmann-plot (cf. Section 3.2) with the iron lines as listed in Table 8.1. For a laser-induced plasma from a pressed $Fe_2(SO_4)_3$ sample a mean temperature of 8900 $\pm$ 1500 K was obtained. In case of the pressed samples of $FeCl_3$ a lower plasma temperature was determined with a mean value of 7900 $\pm$ 1500 K, which, however, agrees with the temperature of ferric sulfate within the margin of uncertainty.

Results - frozen salt solutions

Spectral features and lines For both ferric salts in frozen salt solution LIBS spectra like those shown in Fig. 8.3 were obtained. Typical features of both are the intense hydrogen and oxygen lines in the red to infrared region. At shorter wavelengths multiple iron lines are still detectable, whereas chlorine and sulfur can hardly be distinguished from noise. For the frozen ferric salt solutions a value for the plasma temperature was also calculated with the Boltzmann-plot. The plasma temperature for both ferric salts in frozen salt solution was found to be 8000 $\pm$ 1500 K.

A spectral region ranging from 537 nm to 550 nm and including the most intense sulfur lines as well as some chlorine lines was given particular attention. It is shown in Fig. 8.4 as an averaged mean

Wavelength λ **(nm)**	**Energy levels (eV)** E_i - E_j	**Statistical weights** g_i - g_j	**Transition probability** A_{ij} **(10^8 s^{-1})**
356.5	0.95816 - 4.43461	7 - 9	0.43^{B+}
357.0	0.91460 - 4.38646	9 - 11	0.676^{A}
358.1	0.85899 - 4.32009	11 - 13	1.02^{A}
360.8	1.01106 - 4.44563	3 - 5	0.813^{A}
361.8	0.99011 - 4.41528	5 - 7	0.722^{B+}
363.1	0.95816 - 4.37135	7 - 9	0.517^{A}
364.7	0.91460 - 4.31247	9 - 11	0.291^{A}
371.9	0.0 - 3.33202	9 - 11	0.162^{A}
373.4	0.85899 - 4.17769	11 - 11	0.901^{A}
373.7	0.05156 - 3.36826	7 - 9	0.141^{A}
374.9	0.91460 - 4.22036	9 - 9	0.763^{A}
381.5	1.48486 - 4.73314	9 - 7	1.12^{A}
382.0	0.85899 - 4.10337	11 - 9	0.667^{A}
382.5	0.91460 - 4.15435	9 - 7	0.597^{A}
388.6	0.05157 - 3.24097	7 - 7	0.053^{A}
406.3	1.55736 - 4.60759	7 - 7	0.66^{B+}
430.7	1.55736 - 4.43461	7 - 9	0.338^{B+}
432.5	1.60789 - 4.47327	5 - 7	0.516^{B+}
438.3	1.48486 - 4.31247	9 - 11	0.5^{A}
440.4	1.55736 - 4.37135	7 - 9	0.275^{A}

Table 8.1: *Selected Fe(I) lines for Boltzmann-plot. The uncertainties of the transition probability A_{ij} are: $^{B+}) \leq 7\%$, $^{A}) \leq 3\%$ [Ralchenko et al., 2011].*

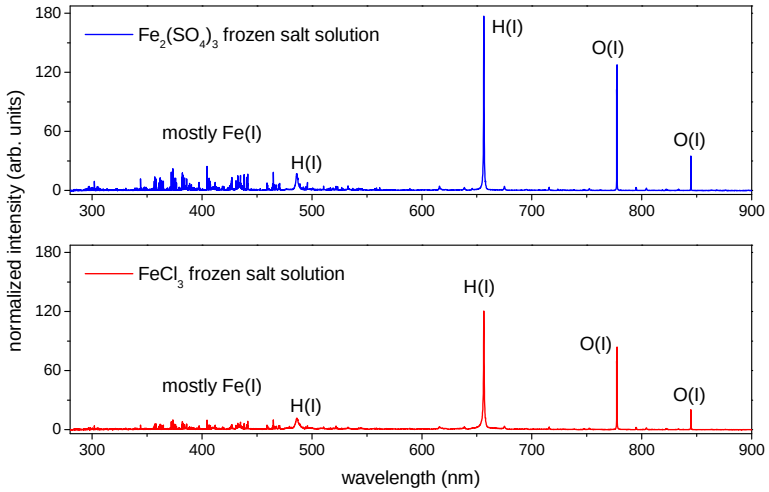

Figure 8.3: *LIBS spectra of frozen $Fe_2(SO_4)_3$ (top) and $FeCl_3$ (bottom) water solution, respectively, obtained under Martian atmospheric conditions. The spectra are dominated by hydrogen and oxygen lines in the red to infrared region with multiple ferric lines at shorter wavelengths.*

spectrum which was created from a total of eight spectra for both ferric salts and for both, the LIBS spectra of the pure pressed samples (top) and the salts in frozen salt solution (bottom). Noise is reduced in this way and even weak emission lines can become visible in the mean spectra. Additionally, the mean spectra shown were rebinned as used for the subsequent MVA, i.e. five wavelength channels were averaged as explained in the previous chapter. Iron, chlorine and sulfur lines were identified in the mean LIBS spectrum of the pressed salt sample and looked for in the mean spectrum of the frozen salt solutions. Although averaged from several spectra the lines of chlorine and sulfur in the spectra of the frozen salt solutions are hardly detectable as they are too weak and highly superimposed by the iron lines. For instance, the most intense line of S(II) at 545.4 nm is superimposed by two iron lines from a transition in a neutral atom at 545.6 nm (Fig. 8.4, top). It can be seen that, even though the number of wavelength channels was reduced by a factor of five, the merged spectral lines can still be resolved in the averaged and rebinned spectrum of the pressed $Fe_2(SO_4)_3$ as well as in the averaged and rebinned spectrum of its frozen salt solution. However, in a typically unaveraged spectrum of a frozen $Fe_2(SO_4)_3$ water solution the sulfur line is not distinguishable from noise.

A second spectral region focused on in this study was the wavelength range from 477 nm to 493 nm, which includes the intense and strongly broadened hydrogen beta line H(I) at 486.1 nm and the most intense chlorine lines, see Fig. 8.5. The hydrogen line is already quite strong in the case of the pressed sample of the strongly hygroscopic ferric chloride as mentioned above (Fig. 8.5, top). While clearly visible in the averaged spectrum of the pressed $Fe_2(SO_4)_3$ sample the chlorine lines considerably lose intensity in the averaged spectrum of the frozen salt solution and only the most intense lines Cl(II) at 478.1 nm and Cl(II) at 481.0 nm can be detected (Fig. 8.5, bottom). In an unaveraged spectrum these lines are usually not recognizable.

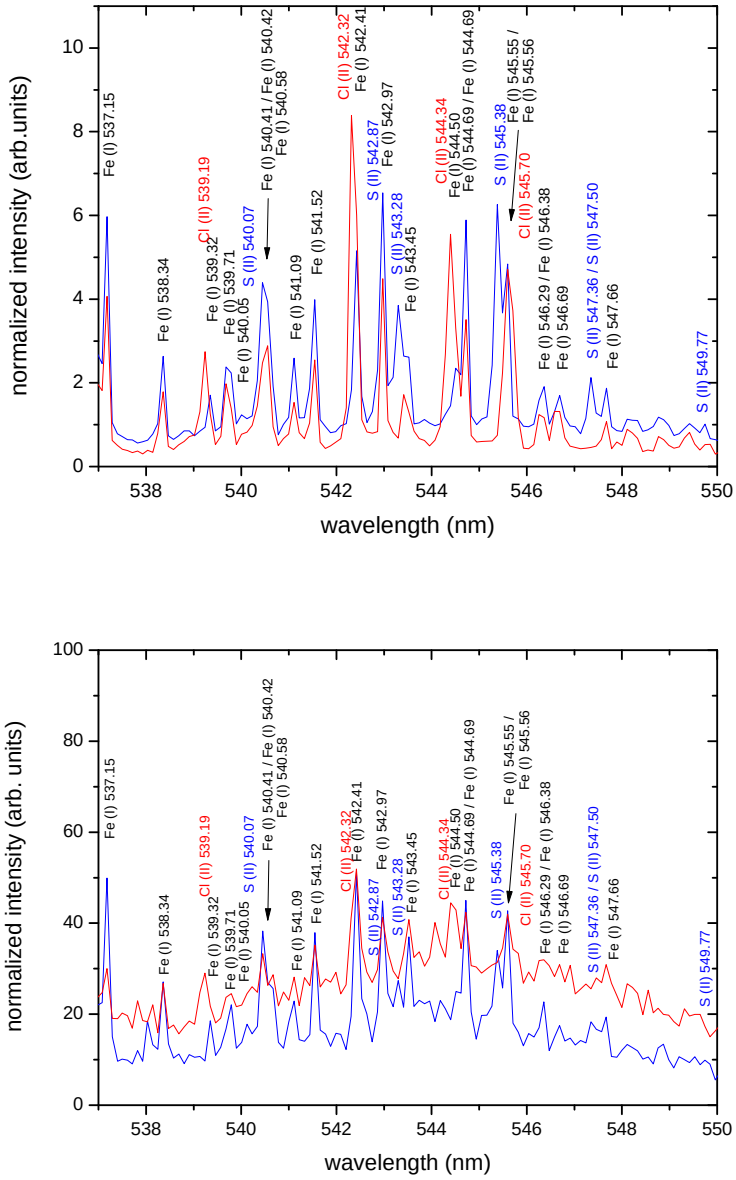

Figure 8.4: *Sulfur and chlorine lines highly superimposed by iron lines in averaged LIBS spectra of $Fe_2(SO_4)_3$ (blue) and $FeCl_3$ (red) in the case of the pressed samples (top) and for the frozen salt solutions (bottom). In the spectra of the frozen salt solutions, the lines of the non-metals are hardly distinguishable from background.*

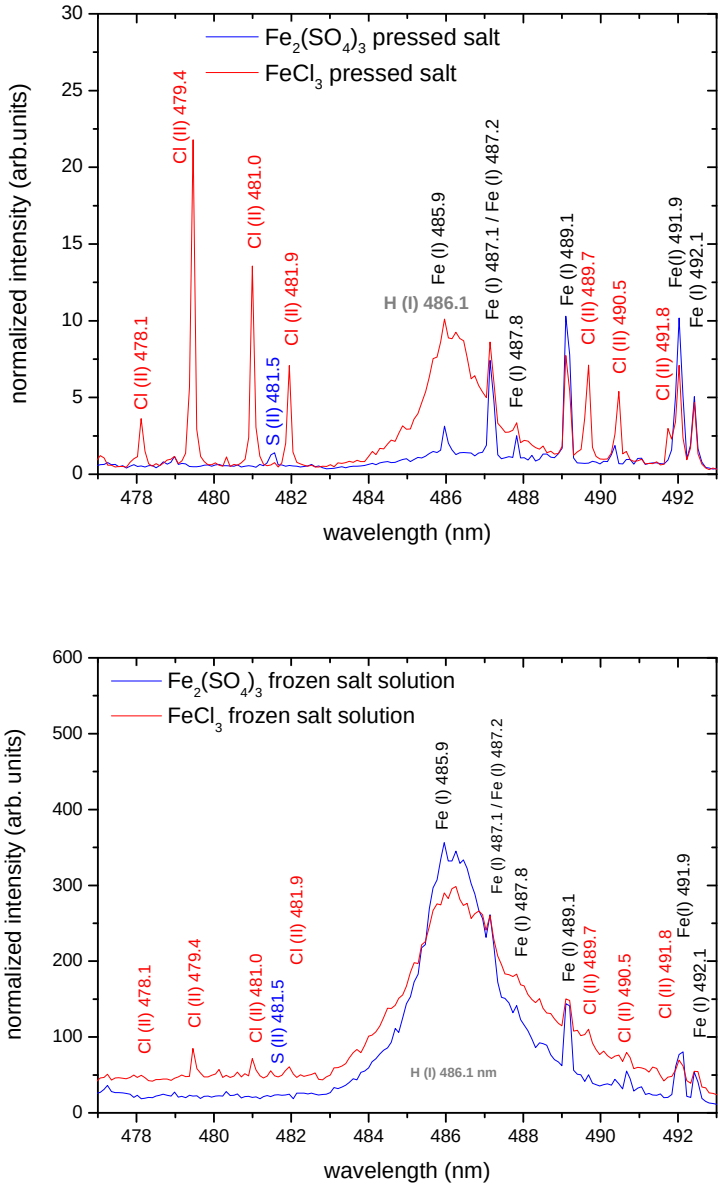

Figure 8.5: *Most intense chlorine lines in the spectra near the strongly broadened hydrogen beta line at 468.1 nm in the averaged LIBS spectra of $Fe_2(SO_4)_3$ (blue) and $FeCl_3$ (red) of the pressed samples (top) and in the LIBS spectra of the frozen salt solutions (bottom). In the spectra of the frozen salt solutions, the lines of the chlorine and sulfur are hardly distinguishable from background.*

PCA The LIBS data of the frozen salt solutions were investigated with PCA first. All spectra were rebinned before analysis, reducing the number of initial variables entering the analysis by a factor of five. As mentioned in the previous chapter this rebinning has no effect on the PCA model, but reduces computing time. In the PCA scatter plots of the scores (not shown here) the salts clustered closely to each other, the spectra of the ferric sulfate towards positive values in PC1 and spectra of the ferric chlorides towards negative values. The PCA scatter plots were improved, i.e. more distinct clusters for both salts were obtained with selected lines instead of using the whole spectra, as was already the case for the eight salts investigated in the previous study. The ten most intense iron lines were selected along with the hydrogen lines at 656.3 nm and 468.1 nm and the oxygen lines at 777 nm and 844.6 nm. For the iron lines the three bins holding the maximum values of the spectral line were chosen, for hydrogen and the oxygen triplet at 777 nm the whole range was selected. Also the wavelength channels, where the most intense sulfur and chlorine lines should appear were included, but were found to have no impact on the PCA. According to the PCA the largest differences in the spectra are due to hydrogen and oxygen for PC1 (83%) and due to iron as included in PC2 (12%). The third PC with 2% did not considerably improve the clustering of the ferric salts in the scatter plots.

SIMCA For both data sets, the ferric chloride as well as the ferric sulfate spectra, individual PCA models were calculated to test the feasibility of SIMCA to discriminate between both. However, the distance between both models was not large enough to use them for successful discrimination of the ferric chloride from the ferric sulfate.

PLS-DA model The spectra of the frozen salt solutions were then analyzed using the MVA method PLS-DA. A model was calculated with half of the spectra of each frozen salt solution, the remaining half was used as test set, comprising the unknown samples. Fig. 8.6 shows the data used for building the model with the projected test set superimposed in the space defined by the first two LVs, where each symbol represents one LIBS spectrum. Spectra of $Fe_2(SO_4)_3$ are widely spread, indicating a more heterogeneous sample in comparison to the $FeCl_3$ ice.

Similar to the PCA results, the first LV is correlated mainly with hydrogen and oxygen, for the second LV and also the third LV many iron lines are of importance. The loadings in the wavelength range from 477 nm to 493 nm are shown in Fig. 8.7 (top). The first LV includes the central part of the hydrogen beta line separated from the iron lines, which were superimposed in the LIBS spectra. The iron lines contribute to the second LV together with a broader region of the hydrogen line. This implies that the shape of the hydrogen line is of importance for discrimination and is different for the two ferric salts investigated here. The third LV is found to also include emission lines due to iron. Moreover, the chlorine lines might be correlated with LV3 to a small extent. In LV4, additional but minor contributions from some but not all iron emission lines are considered. In Fig. 8.7 (middle) the loadings between 537 nm to 550 nm are presented. Here, too, the iron lines are found to contribute to LV2 and LV3. Moreover, the chlorine lines might to a small extent be incorporated in LV3. The loadings for the strongly broadened hydrogen alpha line are shown in Fig. 8.7 (bottom).

With the objective of disentangling the contributions in the loadings and attribute them to the emission lines of the salts, the region in the loadings containing the hydrogen beta line was fitted and compared to fits obtained from the averaged spectra of the frozen salt solutions. As the hydrogen beta line in the loadings was found to be best fitted with a Lorentzian profile, the lines in the averaged spectra were fitted with Lorentzian profiles, too. Moreover, two Lorentz-lines were fitted simultaneously to account for different effects and to assign the central position and the widths to the contributions in the loadings. The hydrogen beta line in the averaged spectra of ferric chloride was best

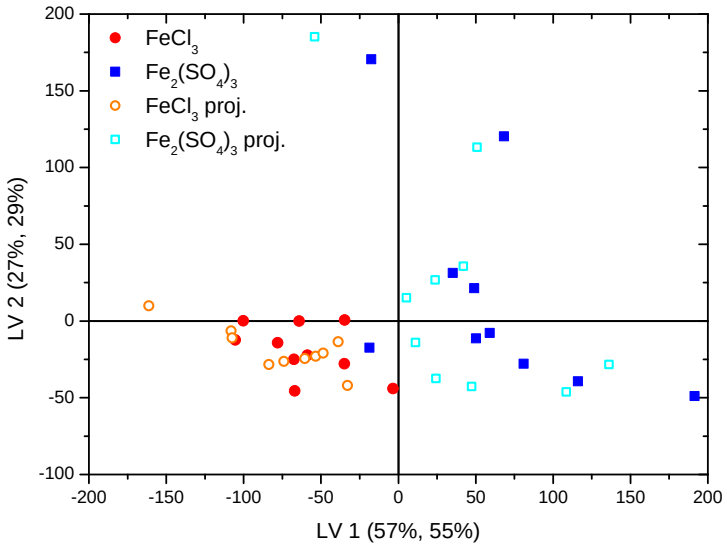

Figure 8.6: *PLS-DA scatter plots of the frozen salt solutions with projected unknown samples (empty symbols) of both, $Fe_2(SO_4)_3$ (blue) and $FeCl_3$ (red) in the space defined by the first two latent variables (LVs) of the model data (filled symbols). No outliers were removed so far.*

fitted with two Lorentzian profiles at the position $\lambda_{Chloride,a} = (486.16 \pm 0.05)$ nm and a considerably shifted position at $\lambda_{Chloride,b} = (488.14 \pm 0.57)$ nm with widths of $\omega_{Chloride,a} = (2.58 \pm 0.20)$ nm and $\omega_{Chloride,b} = (4.78 \pm 1.12)$ nm, respectively. The first line has an amplitude five times the value of the broadened second line. The fit with the two lines obtained a coefficient of determination of $R^2 = 0.99$. The shifted and broadened contribution of the hydrogen line is presumably included in the broadened but less shifted hydrogen beta line in the loadings of the LV2, which has a center at $\lambda_{LV2} = (486.31 \pm 0.13)$ nm and a width of $\omega_{LV2} = (4.36 \pm 0.93)$ nm. The central peak position of the narrower but higher line fit matches the position of the hydrogen beta line in the loadings of LV1 at $\lambda_{LV1} = (486.20 \pm 0.02)$ nm. However, the line fit of LV1 obtained a smaller width of $\omega_{LV1} = (1.78 \pm 0.09)$ nm. For the hydrogen beta line in the averaged spectra of frozen ferric sulfate two lines with the following parameters were obtained from the fit ($R^2 = 0.98$): (1) peak position at $\lambda_{Sulfate,a} = (486.61 \pm 0.21)$ nm with a width of $\omega_{Sulfate,a} = (2.46 \pm 0.18)$ nm and (2) at $\lambda_{Sulfate,b} = (485.93 \pm 0.07)$ nm with a width of $\omega_{Sulfate,b} = (1.22 \pm 0.37)$ nm. These lines cannot be attributed to a particular LV.

The hydrogen alpha line at 656.3 nm was found to be most important for the analysis in terms of discriminating between the two ferric salts. The first four loadings at the line position of hydrogen alpha were best fitted with Lorentzian profiles as was the case for the hydrogen beta line as mentioned above. Together with the loadings the Lorentzian fits are shown in Fig. 8.7 (bottom). The fits were compared to fits of the hydrogen line in the averaged spectrum of ferric chloride and ferric sulfate, respectively. Two Lorentzian profiles were superimposed, each. In the case of ferric chloride ($R^2 = 0.99$) one peak at $\lambda_{Chloride,a} = (656.33 \pm 0.00)$ nm with a width of $\omega_{Chloride,a} = (0.47 \pm 0.02)$ nm could be attributed to LV1, where the line in the loading was found to be at $\lambda_{LV1} = (656.32 \pm 0.00)$ nm, however, with a smaller width of $\omega_{LV1} = (0.34 \pm 0.02)$ nm. The second line of the fit was found to have

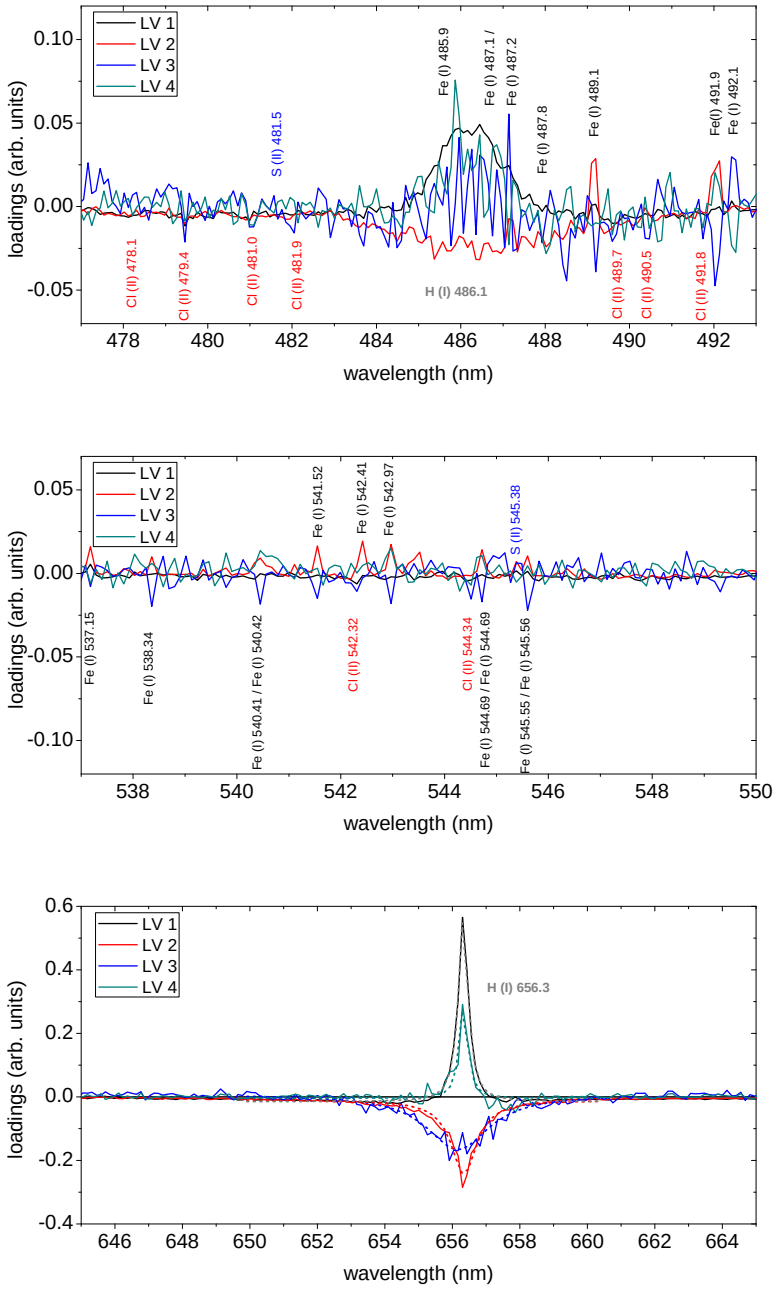

Figure 8.7: *PLS-DA loadings for LIBS spectra of $Fe_2(SO_4)_3$ and $FeCl_3$ in frozen salt solution are shown for the first four LVs in three different wavelength ranges. The main difference in the spectra is due to variations in the shape of the strongly broadened hydrogen lines (top, bottom) and the oxygen lines. The ionic sulfur and chlorine lines do not contribute significantly, little impact is due to the iron lines (middle). In the case of the hydrogen alpha line (bottom) the fits of the lines can be seen (dotted lines, bottom).*

a central position at $\lambda_{Chloride,b} = (656.19 \pm 0.03)$ nm and a width of $\omega_{Chloride,b} = (2.64 \pm 0.15)$ nm and could be incorporated in LV3 at $\lambda_{LV3} = (656.16 \pm 0.04)$ nm, however, with a smaller width of $\omega_{LV3} = (2.27 \pm 0.19)$ nm. In the case of the ferric sulfate, the narrower peak at $\lambda_{Sulfate,a} = (656.33 \pm 0.00)$ nm with a width of $\omega_{Sulfate,a} = (0.33 \pm 0.01)$ nm can be also attributed to the first LV, whereas the broader contribution at $\lambda_{Sulfate,b} = (656.29 \pm 0.01)$ nm and a width of $\omega_{Sulfate,b} = (1.18 \pm 0.06)$ nm could be incorporated in LV2 at $\lambda_{LV2} = (656.34 \pm 0.01)$ nm although with a smaller width of $\omega_{LV2} = (0.93 \pm 0.04)$ nm ($R^2 = 0.99$).

In summary, with fits of the lines and the loadings an unambiguous attribution of the different features of the loadings to a particular salt was not successful. It should be noted moreover, that these are assumptions on which contributions could come from which frozen salt solution, but are not attributed to any physical processes so far. As explained in Chapter 3, the hydrogen lines are strongly broadened by the Stark-effect, which results in a Lorentzian line profile. Moreover, the Lorentzian profile was found to be a suitable fit for the hydrogen lines in the spectra of the frozen salt solutions. However, for instance the red-shift, which can be seen in the hydrogen beta line in the spectrum of the ferric chloride but not in the hydrogen alpha line, cannot be explained by the linear Stark-effect. Properties of the frozen salt solution such as consistency and transparency and their influence on the ablation process and plasma characteristics could be possibly attributed to features in the spectra. Another explanation might be self-absorption, which leads to a reduction in the central part of an emission line. In order to disentangle the different features and the underlying physical effects, further and more extensive investigations should be done in future works.

PLS-DA prediction With the PLS-DA model obtained from the first half of the data, the test set comprising the second half of the data was interpreted with regard to class affiliation. The results allowing for the first four LVs are shown in Fig. 8.8. A value of 1 corresponds to class affiliation to $Fe_2(SO_4)_3$ while 0 corresponds to $FeCl_3$. The Unscrambler software does not include a criterion or condition for class affiliation for the PLS-DA. However, on the basis of the graph shown in Fig. 8.8 a straightforward criterion regarding minimum distance to a model can be established, i.e. prediction values < 0.5 signify class affiliation to $FeCl_3$ while prediction values > 0.5 correspond to class affiliation to $Fe_2(SO_4)_3$. In this way the test spectra can be assigned to a group. As can be seen from the plot, all spectra are assigned correctly with this criterion although three prediction values of $Fe_2(SO_4)_3$ and one of $FeCl_3$ have uncertainty intervals overlapping with the border at 0.5.

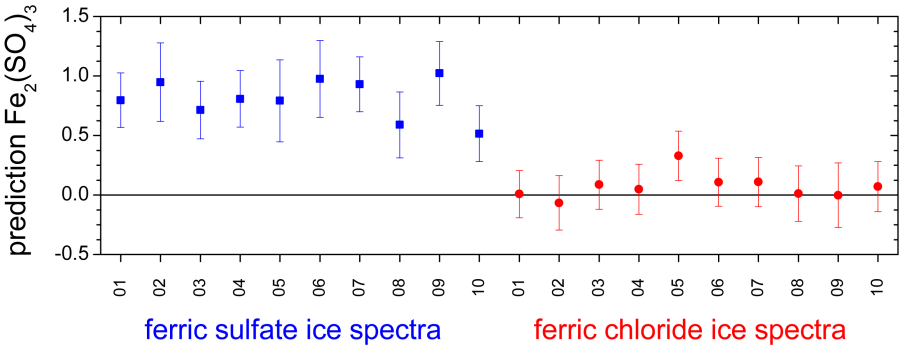

Figure 8.8: *Prediction from PLS-DA model for both ferric salts in frozen solution using four latent variables. Prediction was done for the ferric sulfate corresponding to a value of 1 while ferric chloride samples should obtain values close to 0. Clear discrimination (no overlap of the error bars) is achieved for almost all samples.*

Depth profile analysis For both frozen salt solutions a depth profile analysis was done, as described in Section 6.2. The same position at the sample surface was probed 10 times and the emission of three laser-induced plasmas was collected for one LIBS spectrum each. Thus, a total of 30 laser-induced plasmas was generated at a certain position. This was done for five different positions on the sample surface. In Fig. 8.9 the averaged emission line intensities of hydrogen, oxygen, and iron are presented for successively obtained measurements and drilling deeper into the ice. The error bars correspond to the standard deviation. Chlorine and sulfur lines were not distinguishable from noise in these spectra. Similar to the results obtained with the frozen NaCl ice sample, the emission line intensity of the cation in the salt, here Fe(I) at 372.3 nm, strongly decreases within the first measurements. The already low line intensity of iron is reduced to the level of noise after approximately five measurements. The hydrogen and oxygen lines are found to decrease, too. The effect of increasing variability in the data due to plasma confinement as seen for NaCl ice for the later obtained spectra was not observed to the same extent here. A possible explanation might be less mass ablation from the more transparent ice samples with the ferric salt and therefore less deep craters after the same number of sampling.

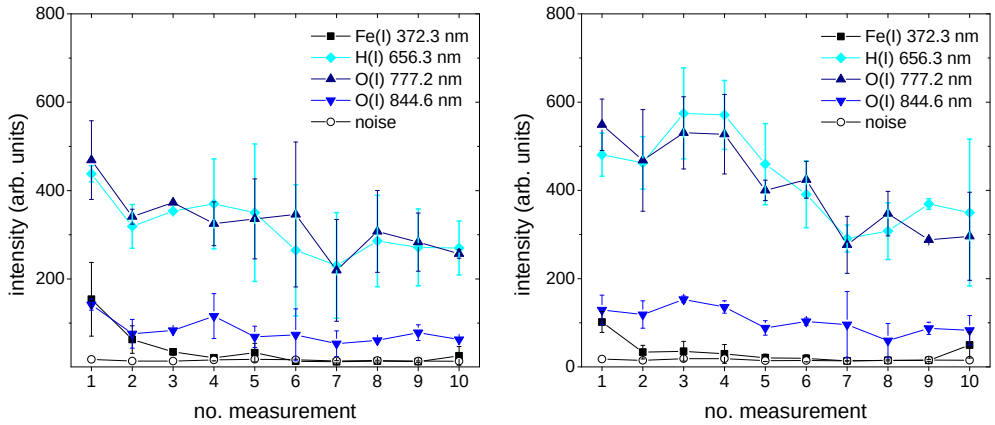

Figure 8.9: *Depths profile analysis for frozen salt solutions with $Fe_2(SO_4)_3$ (left) and $FeCl_3$ (right). The emission of three laser-induced plasmas was recorded for one LIBS spectrum, each. The same position on the sample was probed 10 times, drilling deeper into the ice with every measurement.*

Summary

In summary, LIBS is capable of investigating both ferric salts and the ferric salts in frozen salt solutions under simulated Martian atmospheric conditions. Although lines of sulfur and chlorine are generally not detectable in the LIBS spectra of the ices, the ferric chloride can be distinguished from the ferric sulfate on the basis of other lines such as hydrogen and to a minor degree oxygen and iron by applying MVA methods. It was found that essential information for the purpose of discriminating both salts is included in the shape and also shifts of the lines, in particular the strongly broadened hydrogen alpha and hydrogen beta line. Here, additional information about the sample such as consistency and transparency could be comprised, which translates into properties of the plasma and emission line characteristics. Moreover, more or less selfabsorption might alter the line profiles of the most intense emission lines, giving rise to differences in the spectra which are then revealed by MVA methods. With PLS-DA a model was built and the test set can be predicted 100% correctly with a criterion of minimum distance to a class.

9 Identifying perchlorates and chlorides in soil and in frozen salt solutions

In this chapter the focus was on the question of whether, by applying LIBS and the MVA methods, perchlorates can be distinguished from chlorides with metal atoms of the same kind (here sodium and magnesium). The focus was on PCA but also SIMCA and PLS-DA were applied to the LIBS data. Perchlorates and chlorides as well as the cations Mg^{2+} and Na^{+} among others were reported to be found in Martian soil at the Phoenix lander site [Hecht et al., 2009]. Furthermore, they could appear in the form of frozen salt solutions [Rennó et al., 2009] and are discussed in the context of liquid brines on Mars. Theoretical eutectic temperatures have been calculated to be 236 K for 52 wt.% sodium perchlorate and 206 K for 44 wt.% magnesium perchlorate [Chevrier et al., 2009], cf. Fig. 9.1.

The study presented here was twofold: the four chlorine containing salts magnesium perchlorate $Mg(ClO_4)_2$, sodium perchlorate $NaClO_4$, magnesium chloride $MgCl_2$, and sodium chloride NaCl were first investigated when mixed in Martian analogue soil and in a second step as a frozen salt solution. The identification of the cation of the salt is relatively straightforward using LIBS due to intense metal lines available in the spectra. However, discrimination of the perchlorate from the chloride is a challenging task due to LIBS being an elemental analysis method and both salts being made up of similar content except for the additional oxygen present in the perchlorates. Moreover, both perchlorates as well as magnesium chloride are hygroscopic and additional H_2O is present in these salts. Sodium perchlorate monohydrate ($NaClO_4$ x 1 H_2O), magnesium perchlorate hexahydrate ($Mg(ClO_4)_2$ x 6 H_2O), and magnesium chloride hexahydrate ($MgCl_2$ x 6 H_2O) were used in this study. Additionally, the Martian analogue soil already contains sodium, magnesium, and oxygen. In this study PCA was employed for both data sets, the salts in soil and the salts in water ice, with the objective of discriminating perchlorates from chlorides with cations of the same kind. For the purpose of prediction of unknown samples SIMCA and PLS-DA were applied.

For the first test series the perchlorate salts $Mg(ClO_4)_2$ and $NaClO_4$ were mixed with JSC Mars-1A Martian Regolith Simulant (MRS) and compressed into pellets containing about 2 wt.% of the salt. JSC Mars-1A Martian Regolith Simulant is a palagonitic tephra, i.e. volcanic ash altered at low temperatures [Orbital Technologies Corporation, 2008]. It is dominated by amorphous palagonite and the only phases detected by x-ray diffraction are plagioclase feldspar and minor magnetite. Traces of hematite, olivine, pyroxene and/or glass were detected with Mössbauer spectroscopy. In Table 9.1 the major composition is listed as provided by the distributor. 1 g of the MRS soil mixed with each perchlorate was pressed at 3760 kg/cm^2 to pellets with a diameter of 13 mm. Moreover, pellets were prepared with the same amount of $MgCl_2$ and NaCl, each, as well as a pellet consisting of pure MRS as a reference sample. The first test set thus was made up of the following samples:

(1) MRS pellet with $Mg(ClO_4)_2$ x 6 H_2O
(2) MRS pellet with $NaClO_4$ x 1 H_2O
(3) MRS pellet with $MgCl_2$ x 6 H_2O
(4) MRS pellet with NaCl
(5) MRS pellet

A picture of the five pressed samples is shown in Fig. 9.2.

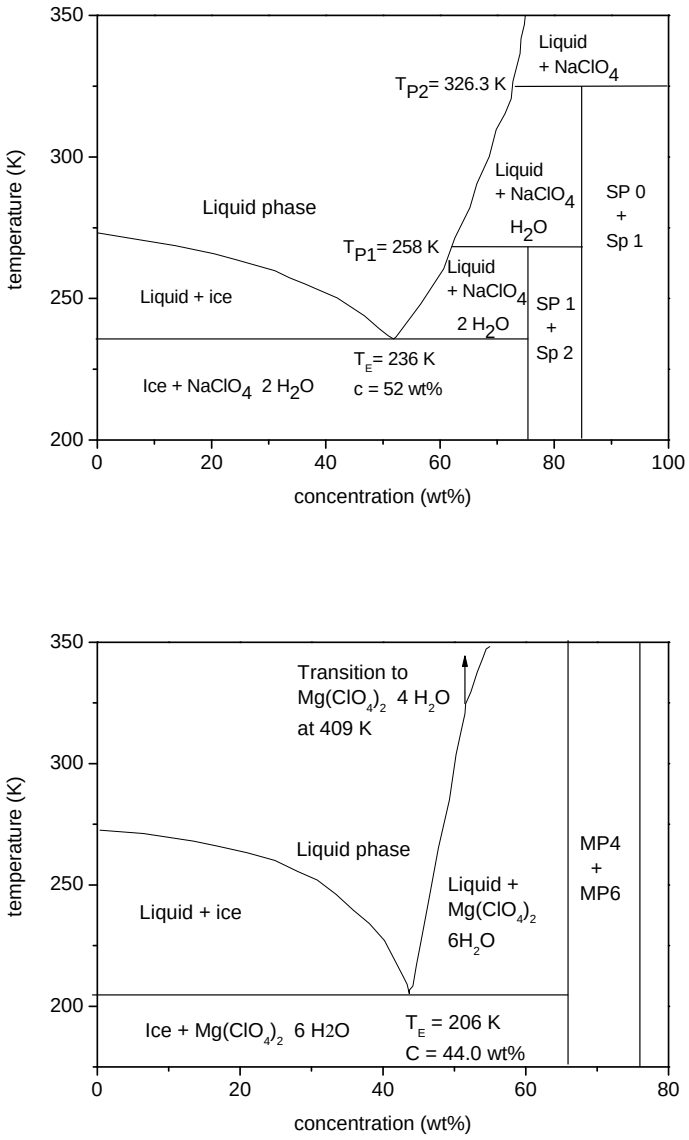

Figure 9.1: *Binary phase diagrams for sodium perchlorate (top) and magnesium perchlorate (bottom) with water. Adapted from [Chevrier et al., 2009].*

A second sample set was prepared with the perchlorates and chlorides in frozen water solutions with salt concentrations of approximately 2 wt.% as explained in detail in Chapter 5.2. Pictures of the perchlorates in frozen salt solutions after the LIBS measurement can be seen in Fig. 9.3. Both ices were solidly frozen with a white slightly transparent surface.

The measurement was performed as described before: the Inlite laser was utilized with an energy attenuated to 35 mJ by grey filters and the Vis/NIR wavelength range was chosen for this study to

Chemical composition	wt.%
Silicon Dioxide (SiO_2)	34.5 - 44
Titanium Dioxide (TiO_2)	3 - 4
Aluminum Oxide (Al_2O_3)	18.5 - 23.5
Ferric Oxide (Fe_2O_3)	9 - 12
Iron Oxide (FeO)	2.5 - 3.5
Magnesium Oxide (MgO)	2.5 - 3.5
Calcium Oxide (CaO)	5 - 6
Sodium Oxide (Na_2O)	2 - 2.5
Potassium Oxide (K_2O)	0.5 - 0.6
Manganese Oxide (MnO)	0.2 - 0.3
Diphosphorus Pentoxide (P_2O_5)	0.7 - 0.9

Table 9.1: *Composition information for JSC Mars-1A Martian Regolith Simulant (MRS). For chemical composition the normal convention for data presentation uses oxide formulae from an assumed oxidation state for each element (except for Fe) and oxygen was calculated by stoichiometry. These are representations of the chemistry and do not represent actual phases or minerals in the simulant. Adapted from [Orbital Technologies Corporation, 2008].*

Figure 9.2: *Pressed samples of MRS soil with additional Mg and Na chlorides and perchlorates, each. The fifth sample is a MRS pellet without additional salt as a reference sample.*

Figure 9.3: *Samples of sodium perchlorate (left) and magnesium perchlorate (right) in frozen salt solutions after the LIBS measurements.*

include the hydrogen and oxygen lines. The gain was set to 80 and the delay time was 500 ns with a detection time gate of 5 μs. The laser beam spot with a diameter of about 300 μm was focused at a new position for each measurement. 40 spots were probed on the pressed samples and the emission from 20 laser-induced plasmas were accumulated for one spectrum. 20 spots were probed on the frozen salt solutions. All measurements were performed under simulated Martian atmospheric conditions with the appropriate gas mixture at a pressure of 700 Pa. The measurements of the frozen

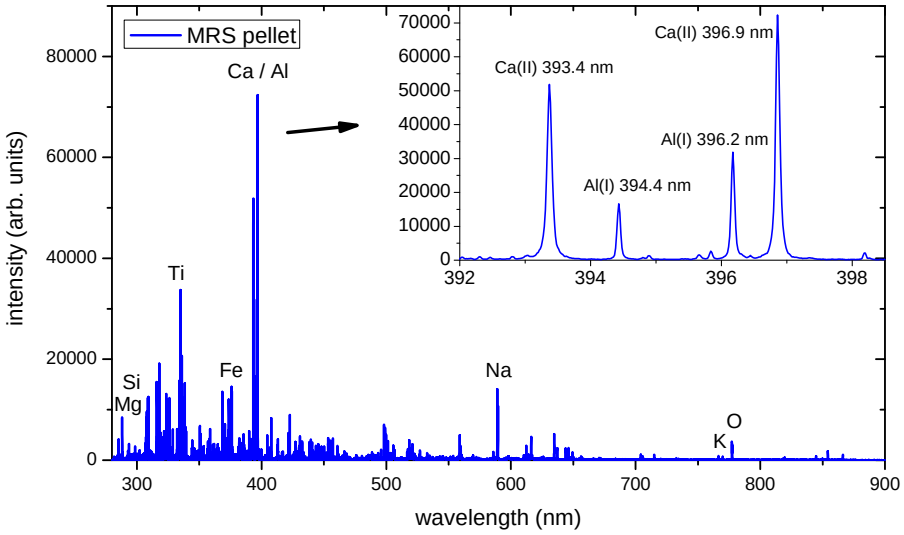

Figure 9.4: *LIBS spectrum of a pressed soil sample consisting of JSC Mars-1A Martian Regolith Simulant (MRS) obtained under simulated Martian atmospheric conditions. The spectrum is dominated by intense calcium and aluminum lines as shown in the inset. Moreover, multiple other metal lines can be detected as well as oxygen.*

salt solutions were performed at 198 K, the measurement of the pressed samples was done at room temperature (295 K).

A representative LIBS spectrum of the pressed MRS sample is shown in Fig. 9.4 and several of the most intense lines are labeled. The spectra are dominated by four intense lines between 393 nm and 397 nm due to calcium and aluminum. Moreover, intense lines due to the other metals such as titanium, iron, sodium, and magnesium can be seen in the LIBS data. The spectra of the pellets with additional salts were found to be quite similar and could not be readily discriminated from each other by visual inspection only.

All spectra were rebinned for further analysis as described in the previous chapters, reducing a total of 32476 wavelength channels to 6496. Moreover, the average of five spectra was used in the case of the pressed samples, while four spectra were averaged in the case of the frozen salt solutions.

Results - salts in Martian analogue soil

PCA The LIBS data were analyzed qualitatively first by using the MVA method PCA. For this purpose the spectra were rebinned before analysis, reducing the number of initial variables entering the analysis by a factor of five. Moreover, the spectra were normalized as explained in Eq. (7.1), each divided by the average value of the spectrum and thus accomplishing an equal area under the curve. The spectra of the pellets, which mainly consist of the Martian analogue material MRS, are dominated by the spectral lines from calcium, aluminum, titanium, and iron as mentioned above. These lines can be found in the PCA loadings, too, as shown in Fig. 9.5. For PC1 (53%), the lines of calcium,

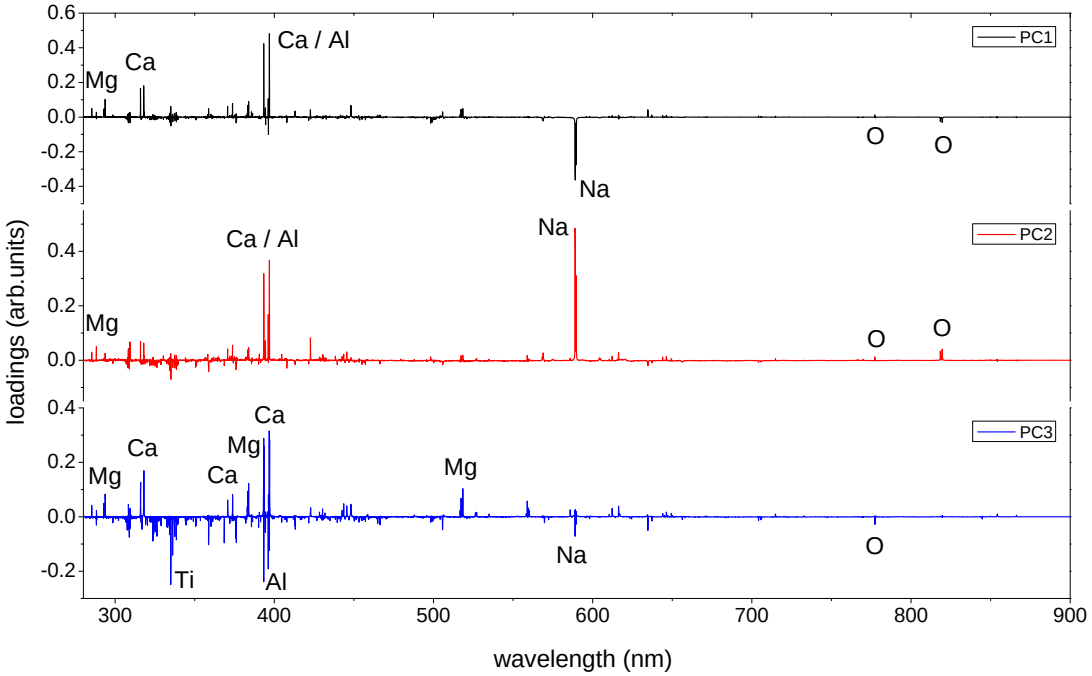

Figure 9.5: *PCA loadings for MRS with chlorides and perchlorates. The most intense line in the LIBS spectra are due to calcium, aluminum, and sodium which translates into the loadings.*

aluminum, and magnesium were found to correlate and they obtain positive loading values. They anticorrelate with sodium and to a minor degree with oxygen, which both obtain negative loading values. This leads to a separation of the samples with additional sodium, i.e. NaCl and $NaClO_4$, from the remaining samples in the scores scatter plots along the first PC (not shown here). In PC2 (18%), again sodium, calcium and aluminum correlate. Regarding PC3 (11%), the calcium lines are found to anticorrelate with aluminum and also titanium is included in this PC. In the scatter plots (not shown here) of PC1 and PC2 as well as PC1 with PC3 no distinct cluster form apart from the aforementioned separation of the samples with additional sodium.

In order to improve the PCA results a set of lines was selected, including the most intense lines of sodium (Na(I) at 589.0 nm, Na(I) at 589.6 nm), magnesium (Mg(I) at 285.2 nm, Mg(I) at 383.2 nm, Mg(I) at 383.8 nm), hydrogen (H(I) at 486.1 nm, H(I) at 656.3 nm), and oxygen (O(I) triplet at 777 nm, O(I) at 844.7 nm). Moreover, although not detectable in the spectra of the pressed MRS samples, the bins where the most intense chlorine lines have been found in previous studies, were selected, too (Cl(II) at 479.4 nm, Cl(II) at 481.0 nm, Cl(I) at 837.6 nm). The improved scatter plots with the selected lines as input variables only are shown in Fig. 9.6 for PC1 (92%) with PC2 (6%) (left) and PC1 with PC3 (1%) (right). PC1 accounted for sodium with positive loading values and magnesium with negative loading values. Thus, a cluster with the LIBS spectra of samples comprising NaCl and $NaClO_4$ can be seen in Fig. 9.6 (left) on the right. Since calcium was excluded from the spectra due to the selection of the above mentioned emission lines, now sodium with the second intense lines obtains positive loading values in PC1. Spectra of samples with $Mg(ClO_4)_2$ and $MgCl_2$ as well as the reference sample with no additional salt assemble on the left for negative loadings in PC1 due to the less intense magnesium lines. PC2 accounts for magnesium, too, but only poor clustering results are obtained along this axis. PC3 includes the oxygen lines and NaCl can be separated from

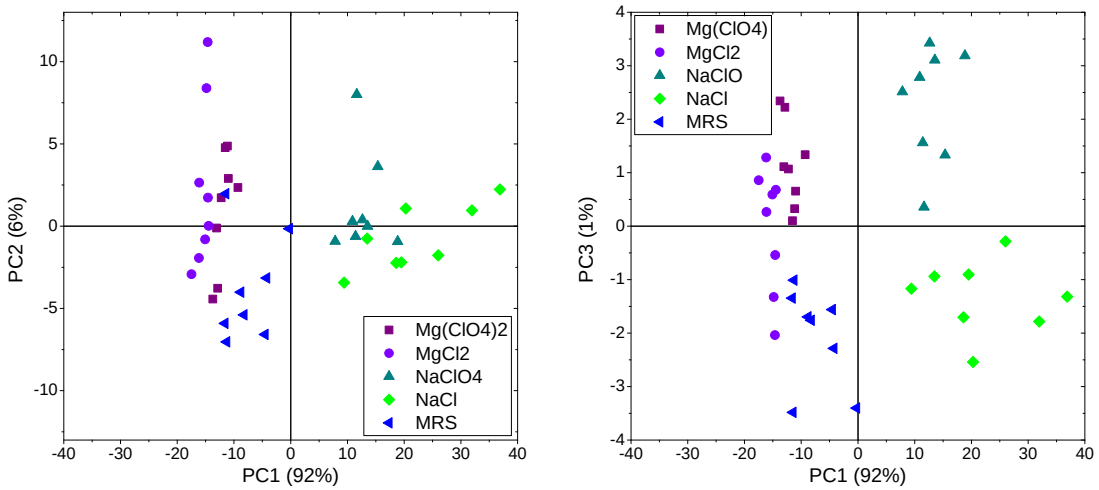

Figure 9.6: *PCA scores for pressed MRS samples mixed with chlorides and perchlorates. With PC1 the samples with additional sodium separate from the rest (left). Taking into account PC3, which includes the oxygen lines, a separation of samples with sodium chloride from those with sodium perchlorate can be obtained (right). Moreover, samples with magnesium perchlorate separate from the reference sample without additional salt along this axis.*

$NaClO_4$ with this PC. In the cluster comprising $Mg(ClO_4)_2$ and $MgCl_2$ salts and the reference sample a separation of the reference sample from the sample with additional $Mg(ClO_4)_2$ is obtained. This is no surprise as the sample with magnesium perchlorate has a much higher amount of additional oxygen due to the salt's anions and the six H_2O molecules. As can be seen, the third PC comprising the oxygen lines is most important for the purpose of separating chlorides from perchlorates when salts with the same cation are analyzed. This PC allows for the total amount of oxygen in the samples due to the anions and the hydration states of the salts. The hydrogen line was found to be less important but correlates with oxygen in the loadings. The wavelength channels where chlorine lines could appear were found to be of no importance.

In order to separate also the cluster of the $MgCl_2$ containing samples, a subsequent local PCA was calculated with the spectra of the samples with $MgCl_2$, $Mg(ClO_4)_2$, and the reference sample of MRS. The PCA scores plots are shown in Fig. 9.7. With PC1 (61%) and PC2 (34%) no separation is achieved Fig. 9.7 (left). However, three clusters due to the different salts are obtained in the PCA scores plot for PC1 with PC3 (4%), see Fig. 9.7 (right). While PC1 is due to the magnesium lines in the spectra, with PC3 the oxygen lines are considered. Arrows in Fig. 9.7 (right) indicate which emission lines are relevant for assemblage in this direction and, therefore, which lines account for the separation.

SIMCA With the LIBS spectra obtained from the five different samples individual PCA models were calculated for each group to test the feasibility of SIMCA to discriminate between all of them. However, the distance between the models was not large enough to use them for successful discrimination. SIMCA was tested for subsets due to the cations, too, but a useful prediction of the different salts in the soil was not achieved.

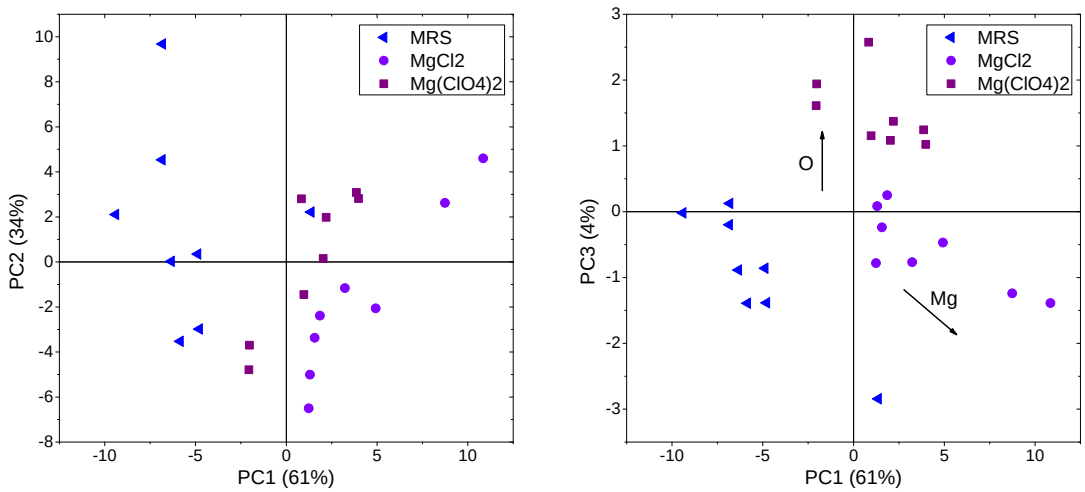

Figure 9.7: *PCA scores for the subset of samples with $MgCl_2$, $Mg(ClO_4)_2$, and the reference sample of MRS. With PC1 and PC3 (right) separation of the different samples is obtained on the basis of magnesium and oxygen lines.*

PLS-DA The LIBS data of the pressed MRS samples with chlorides and perchlorates were used to calculate a PLS-DA model. Five LVs were included in the prediction model. In a following step all LIBS spectra were interpreted on the basis of this model. In Fig. 9.8 the prediction values of all spectra for all classes are shown in a combined plot. Ideally, each spectrum should obtain a prediction value of 1 for the model of its own class. Moreover, it should obtain a prediction value equal to 0 for all of the other classes. As mentioned in Chapter 8, the Unscrambler software does not provide a criterion for assigning the spectra to a class. Again, a straightforward criterion would be regarding minimum distance to a model. However, this is not a binary model for only two types of samples as was the case for the ferric salts. Here, a suitable and easy to apply criterion would be an attribution to a certain class for spectra with prediction values > 0.5 while prediction values < 0.5 are just interpreted as "not a member of this class". Although this is a simple decision criterion, in this way a spectrum could be attributed to several classes at a time but also to none. In Table 9.2 the prediction results for this criterion are presented. By this means 37 of 40 of the spectra were attributed to the correct class. Three spectra were falsely assigned.

	$Mg(ClO_4)_2$	**$MgCl_2$**	**MRS**	**NaCl**	**$NaClO_4$**
$Mg(ClO_4)_2$	7	-	-	-	-
$MgCl_2$	1	8	-	-	-
MRS	-	-	8	-	-
NaCl	-	1	-	8	1
$NaClO_4$	-	-	-	-	6

Table 9.2: *PLS-DA prediction results for the pressed MRS samples with additional salt content. The admixed salts listed in the first column are assigned to one or more of the classes listed in the top row. Stated are the total numbers of spectra assigned to the class in the top row on the basis of a distance less than 0.5 between a spectrum and the individual PLS-DA model.*

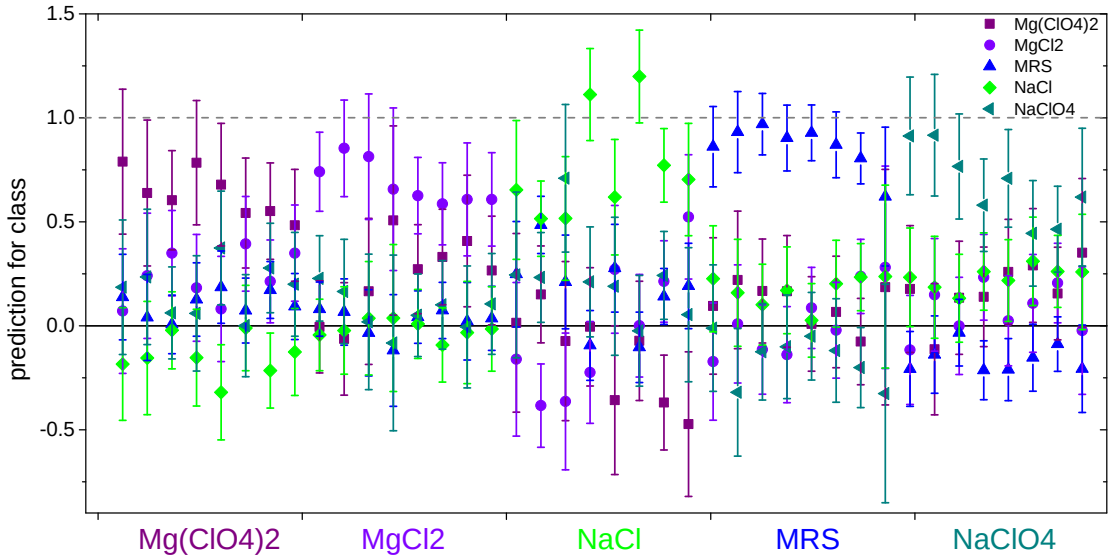

Figure 9.8: *PLS-DA prediction values for chloride and perchlorate salts in Martian analogue soil. A spectrum should ideally obtain a prediction value of 1 for its own class (salt) and a prediction value of 0 for the other classes.*

Results - frozen salt solutions

PCA For the data of the frozen salt solutions with chlorides and perchlorates a PCA was performed after rebinning (i.e. reduction of the number of initial variables by a factor of five) and normalization by dividing each spectrum by its average value as explained in Eq. (7.1). The obtained loadings are shown in Fig. 9.9. The first PC accounts for 86% and includes mainly the strong sodium lines as well as hydrogen and oxygen, which all anticorrelate with magnesium. In PC2 (12%) sodium is found to anticorrelate with hydrogen, oxygen, and magnesium. In PC3 (3%) a stronger contribution from magnesium can be seen. Moreover, both sodium lines (Na(I) at 589.0 nm, Na(I) at 589.6 nm) as well as hydrogen at 656.3 nm and oxygen (O(I) triplet at 777 nm, O(I) at 844.7 nm) now are split: the part of the line profile towards smaller wavelengths occurs with negative loadings, whereas the part of the line towards longer wavelengths is positive in the loadings. Here again, the shape of the line in the loading is found to be of importance for this PC and might indicate a (red)shift, which occurs predominantly in the spectra obtained from sodium perchlorate. As there is no shift found in the magnesium lines of magnesium perchlorate, which was sampled in the same session of data acquisition shortly before probing sodium perchlorate, a shift on account to the instrument is unlikely. The cause of the shift should be addressed in future studies, also with regard to sample properties translating into the process of ablation and plasma characteristics and, thus, possibly revealing the underlying physical processes.

Also in the case of the frozen solutions a preselection of variables, i.e. line selection was done. The same lines as in the analysis of the chlorides and perchlorates in soil were extracted for PCA: Na(I) at 589.0 nm, Na(I) at 589.6 nm, Mg(I) at 285.2 nm, Mg(I) at 383.2 nm, Mg(I) at 383.8 nm, H(I) at 486.1 nm, H(I) at 656.3 nm, O(I) triplet at 777 nm, O(I) at 844.7 nm. Moreover, although not detectable in the spectra of the frozen salt solutions the bins where the most intense chlorine lines have been found in previous studies, were selected: Cl(II) at 479.4 nm, Cl(II) at 481.0 nm, Cl(I) at 837.6 nm. The selection of this set of lines improved the PCA outcome in terms of slightly

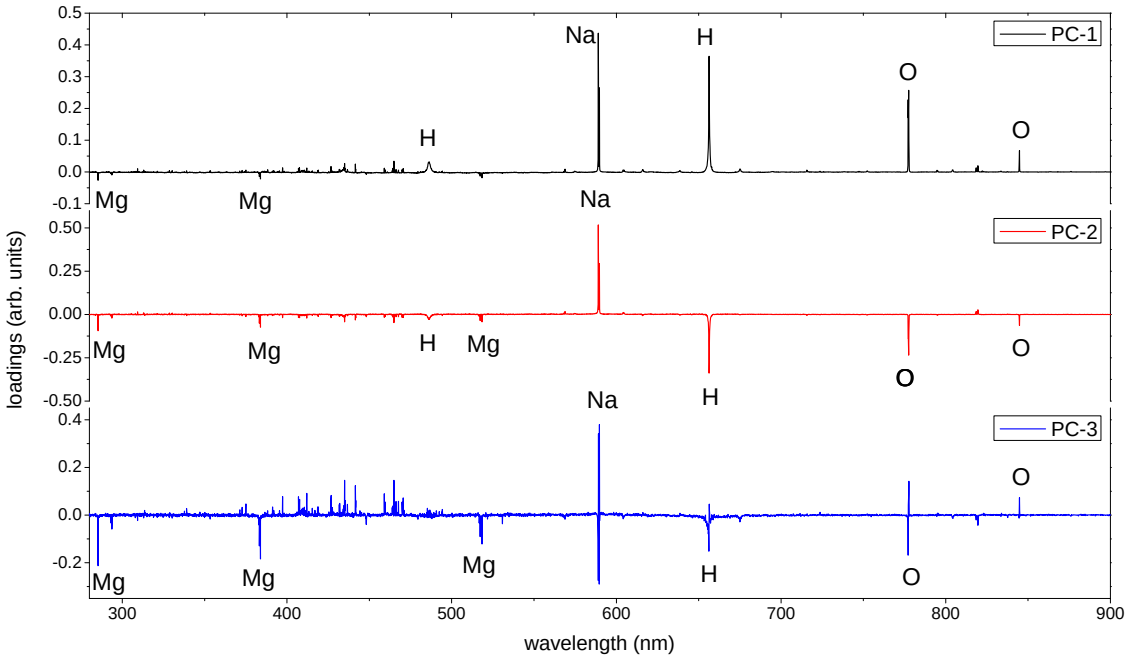

Figure 9.9: *PCA loadings for frozen solution with chlorides and perchlorates. While sodium is found to correlate with hydrogen and oxygen in the first PC (top), in the loadings of PC2 sodium and the components of water obtain different signs in the loadings (middle). In PC3 an increased influence due to magnesium can be seen. Moreover, the shape of the most intense lines of sodium, hydrogen, and oxygen are found to have influence on the PCA.*

more distinct clusters, which are shown in Fig. 9.10. Along PC1 (87%) a separation of the sodium containing salts from the magnesium containing salts is obtained on the basis of mainly sodium and magnesium lines. In the space defined by PC1 and PC2 (12%), spectra of $Mg(ClO_4)_2$ and $MgCl_2$ in ice separate on account of the hydrogen and oxygen lines in the loadings of PC2. With PC3 (1%) NaCl ice and $NaClO_4$ ice can be separated, too. This is achieved based on the line shapes of the most intense lines of sodium, hydrogen, and oxygen. Again, the wavelength channels where chlorine lines are expected, were found to have no influence on the PCA and are of no relevance for separation of the salts analyzed here.

SIMCA For the purpose of predicting unknown spectra of frozen solutions with chlorides and perchlorates with SIMCA, four individual PCAs were done for each salt. However, as was the case for the salts in soil, the models were found to be too close to each other and a successful prediction of the spectra failed.

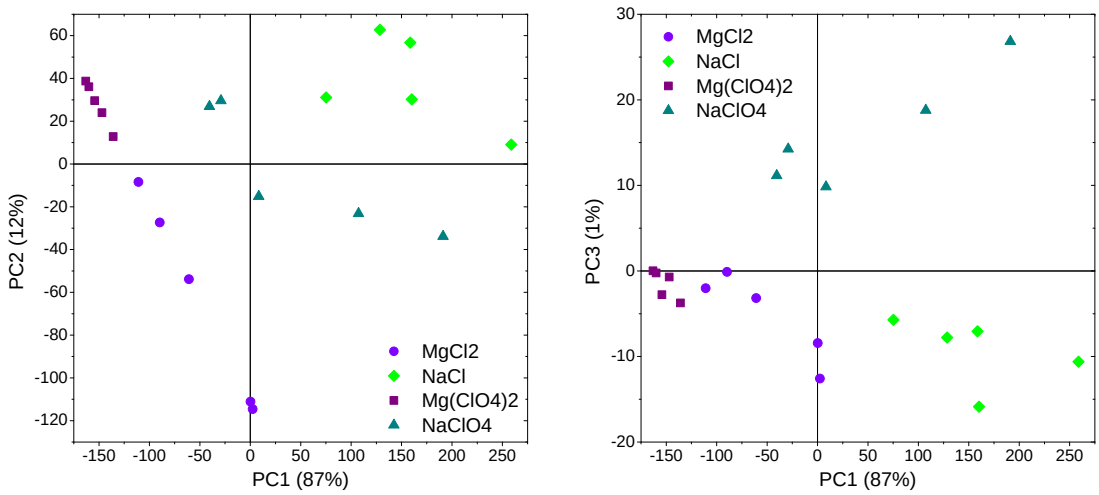

Figure 9.10: *PCA scores for frozen salt solution with chlorides and perchlorates. With PC1 the frozen solutions with sodium containing salts are separated from those with magnesium (left). Along PC2 the ice with magnesium perchlorate separates from ice with magesium chloride on account of hydrogen and oxygen lines. The ices containing sodium can be distinguish based on PC3 and the line profiles of the most intense lines of sodium, hydrogen, and oxygen.*

PLS-DA With PLS-DA a model for prediction was calculated with the data of the chlorides and perchlorates in frozen salt solutions. The PLS-DA loadings resemble the PCA loadings and LV3 to LV5 include information on the line profiles of the most intense emission lines of sodium, hydrogen, and oxygen with shift as explained above. In the PLS-DA prediction model the first five LVs were included. The prediction values for the spectra for all four classes are presented in Fig. 9.11. With the criterion as established previously for the salts in soil, i.e. spectra with prediction values > 0.5 for a certain class model are attributed to this class, all spectra of ices with chlorides and perchlorates can be predicted correctly and no samples is attributed to a false class.

Summary

For the PCA of the perchlorates and chlorides in Martian analogue soil as well as in frozen salt solutions, an improved clustering of spectra of the same kind was found when variables were preselected i.e. only certain elemental lines of the spectra were used. However, the improvement was significantly better in the case of the salts in soil. By selecting the relevant lines from the soil spectra and thus, excluding multiple other and partly very intensive lines such as calcium, the PCA was forced to focus more on the lines due to the elements that were present to a variable extent. On the other hand, in case of the chlorides and perchlorates in frozen solution, the anyway most intense lines were chosen. Thus, a minor improvement for the clusters was obtained. Main influence in the loadings was then found to be due to the emission lines of sodium, hydrogen, and oxygen as well as to a minor degree due to magnesium. The strongest chlorine lines concerning this laboratory set-up, were not strong enough to have influence on the PCA, neither in case of the pressed samples nor for the frozen solutions. Also for the PLS-DA they were of no importance for separation. However, the shape of the spectral lines of the most intense lines of sodium, hydrogen, and oxygen was found to be of importance for

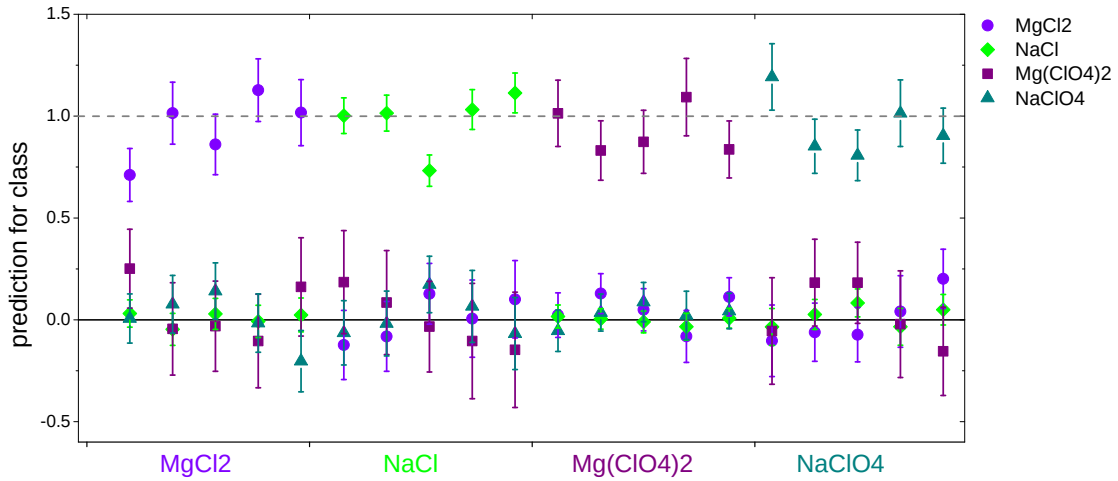

Figure 9.11: *PLS-DA prediction values for chlorides and perchlorates in ice. A spectrum should ideally obtain a prediction value of 1 for its own class (salt) and a prediction value of 0 for the other classes.*

the purpose of separation. The change of sign in the loadings of these lines indicates a shift of the lines in a subset of the spectra. As stated in the previous chapter, where the emission line profiles of hydrogen were studied in the spectra of ferric salts in frozen water solution, changes in shape and shifts of these lines might be attributed to material properties of the sample which translate into plasma characteristics and affect the emission lines. For the purpose of prediction the PLS-DA model was found to be suitable in combination with the criterion, which demands a distance less than 0.5 between a spectrum and a PLS-DA model for class affiliation. For the salts in soil 37 of 40 spectra were attributed correctly while 3 spectra were attributed to a wrong class. For the salts in ice 100% were correctly classified.

10 LIBS for astrobiology - investigation of microbiological material

Within the framework of the Helmholtz Alliance for planetary evolution and life an interdisciplinary study was carried out together with astrobiologists from the Alfred Wegener Institute for Polar and Marine Research, Research Unit Potsdam - Geomicrobiology in Periglacial Regions. The aim of the experiment described in this chapter was to test the feasibility of LIBS to distinguish between Martian analogue soil with and without microbiological material by applying MVA methods. The feasibility to investigate and classify microbiological materials such as bacteria, viruses, spores, or pollen by using LIBS has been demonstrated in multiple studies, e.g. [Multari et al., 2012], [Diedrich et al., 2007], [Rehse et al., 2012]. Here, the focus was on a possible extraterrestrial application of LIBS for the identification of biological material on Mars.

Samples of Martian analogue material (JSC Mars-1A Martian Regolith Simulant (MRS), for details see previous chapter) were prepared with different microbiological contents provided by J. Schirmack and investigated under simulated Martian atmospheric conditions. Methanogenic archaea from terrestrial permafrost regions are suitable candidates for possibly existing life on Mars. They have evolved under early Earth conditions, which are assumed to be similar to early environmental conditions on Mars, and grow lithoautotrophically under strictly anaerobic surroundings. They can tolerate low temperatures and survive the extreme environments of permafrost affected soils for several millions of years. Strains of methanogenic archaea have been isolated from the active layer of permafrost on Samoylov Island in the Lena Delta, Siberia. They were found to survive exposure to a simulated Martian diurnal profile with alternating temperatures ranging from 198 K to 293 K, humidity from 0.1 to 0.9 aw and Martian atmospheric conditions in terms of pressure and composition [Morozova et al., 2007]. Moreover, strains of methanogenic archaea from the subsurface lake of Movile Cave, Romania, were isolated. This cave contains a chemoautotrophically based ecosystem with several endemic species. One strain from the Lena Data (*Methanosarcina* strain SMA-21) and one strain from the Movile Cave (*Methanobacterium* strain MC-20) were investigated with LIBS. MC-20 are rod shaped whereas SMA-21 are irregular cocci. Both strains grew in a salt concentration from 0.02 to 0.6 M NaCl. For LIBS analysis five identical pressed samples with a diameter of 14 mm consisting of 1 g of MRS were prepared. Onto the surface of two pellets 1 ml of SMA-21 was added, once washed and cleaned from the growth medium in a salt solution of 0.15 M NaCl, once washed and cleaned from growth medium in pure H_2O. Another pair of MRS pellets was prepared analogously with MC-20. Cell concentrations of all used cultures solutions were about $1.0 \cdot 10^9 \mathrm{ml}^{-1}$. A reference pressed pellet was prepared with the same amount of pure salt solution. Thus, the test set consisted of five MRS pellets with different additional content:

1. MRS pellet with SMA-21 in salt solution
2. MRS pellet with SMA-21 washed in H_2O
3. MRS pellet with MC-20 in salt solution
4. MRS pellet with MC-20 washed in H_2O
5. MRS pellet with salt solution

For this study the Inlite laser was utilized with an energy attenuated to 35 mJ by grey filters. Spectra in both wavelength ranges, i.e. 191-372 nm (VUV/UV) and 281-900 nm (Vis/NIR) were measured and compared. A good carbon line can be found at 247.86 nm. The gain was set to 80 and the delay time was 500 ns with a detection time gate of 5 μs. The laser beam spot with a diameter of about 300 μm was focused at a new position for each measurement. 40 spots were probed on the pressed samples and spectra from 20 laser-induced plasmas were accumulated. All measurements were performed under simulated Martian atmospheric conditions with the appropriate gas mixture at a pressure of 700 Pa.

Results

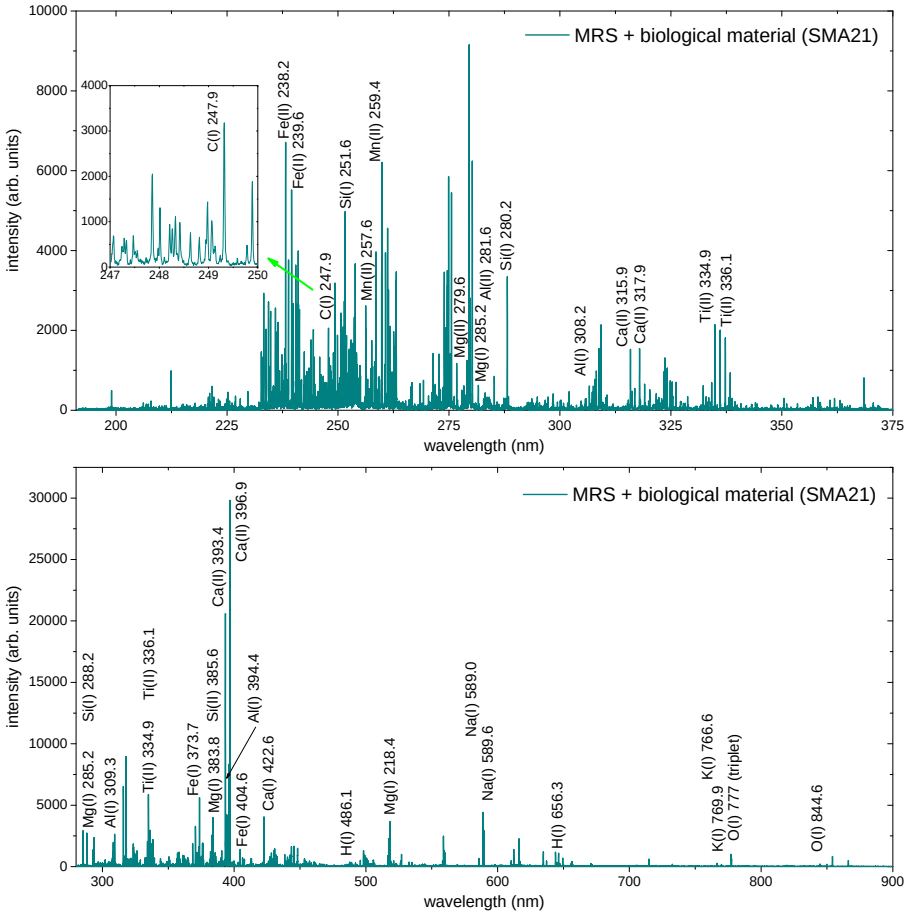

Figure 10.1: *Broadband LIBS spectra of a pressed MRS pellet with added biological material (SMA21) for the UV spectral range (top) and for the Vis/NIS spectral range (bottom).*

A representative spectrum of a MRS pellet with SMA21 in salt solution for both spectral ranges is shown in Fig. 10.1. Generally, spectra of the soil with microbiological content were not obviously different from the spectra obtained of pure soil. Characteristic features in all spectra are the strong atomic and ionic lines from inorganic elements such as calcium, magnesium, and sodium, in the Vis/NIR spectra along with hydrogen, oxygen, iron, aluminum, and potassium. In the UV spectral

range magnesium and iron were the inorganic components dominating the spectra. Moreover, emission lines due to silicon, manganese, titanium, calcium and aluminum are detectable with good SNRs. In this spectral range moreover the before mentioned carbon line at 247.86 nm can be detected as shown in the inset in Fig. 10.1.

As a first step all lines which were considered relevant for analysis were looked for in the spectra. These included the elements present in the Martian analogue soil (Al, Ca, Fe, K, Mg, Mn, Na, O, P, Si, Ti) and additionally carbon as the elemental component most important for identifying biological material, however also present in the Martian atmosphere consisting of more than 95 % CO_2. Moreover, sulfur and chlorine were looked for in the data. While in the UV spectral range a carbon line is available, emission lines from oxygen, sodium, potassium, and hydrogen were not found in the data. On the other hand, there was no carbon line detectable in the Vis/NIR range. Sulfur, chlorine, and phosphorous were neither detectable in the UV spectrum nor in the Vis/NIR spectral range.

For further analysis four spectra were averaged each to account for the biological content being heterogeneously distributed over the sample surface. For the purpose of discriminating the samples with biological content from those without a PLS-DA model was calculated for both spectral ranges, respectively. Despite the detectable carbon line in the UV range a successful analysis with regard to identifying any of the five groups on base of the PLS-DA scatter plots was not possible. For the case of the Vis/NIR spectra the obtained PLS-DA scores plots are presented in Fig. 10.2. With the first two LVs a rough separation of the samples in NaCl salt solution from the washed samples can be achieved Fig. 10.2 (left). The first LV here mostly includes information on the solution, i.e. NaCl on account of the strong sodium lines. Taking into account LV3 the samples with MC-20 in the salt solution can be separated Fig. 10.2 (right). Moreover, a rough cluster of MC-20 in H_2O but in close proximity to the reference sample of soil without biological material is obtained. The spectra of MC-20 in H_2O separate roughly and widespread from the other spectra towards more or less negative values for the third LV.

The spectra were then predicted with the PLS-DA model, including five LVs. The prediction values for the spectra are presented in Fig. 10.3. With the criterion as established previously, i.e. spectra with prediction values > 0.5 for a certain class model are attributed to this class most of the spectra can be assigned to the correct class, see Table 10.1.

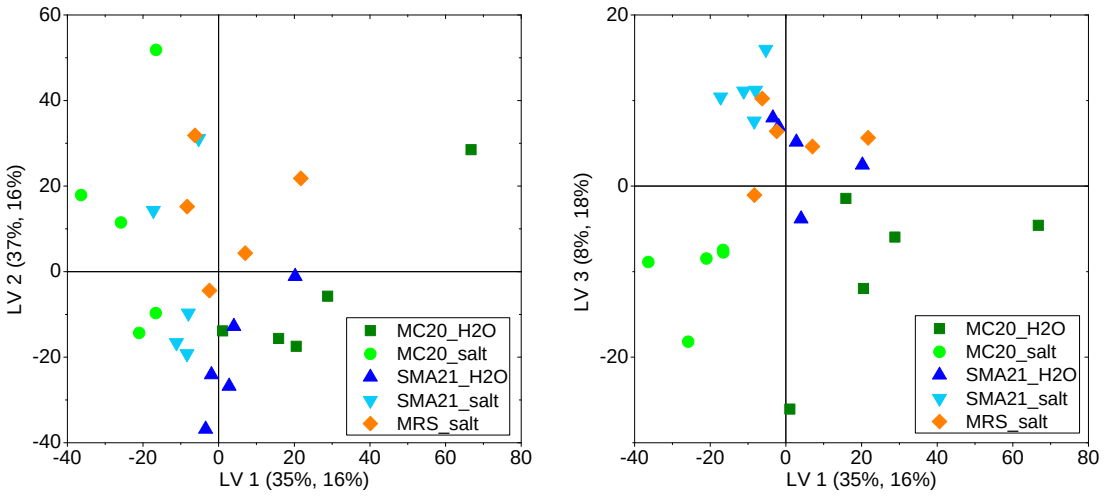

Figure 10.2: *PLS-DA scores for Martian analogue soil with biological material.*

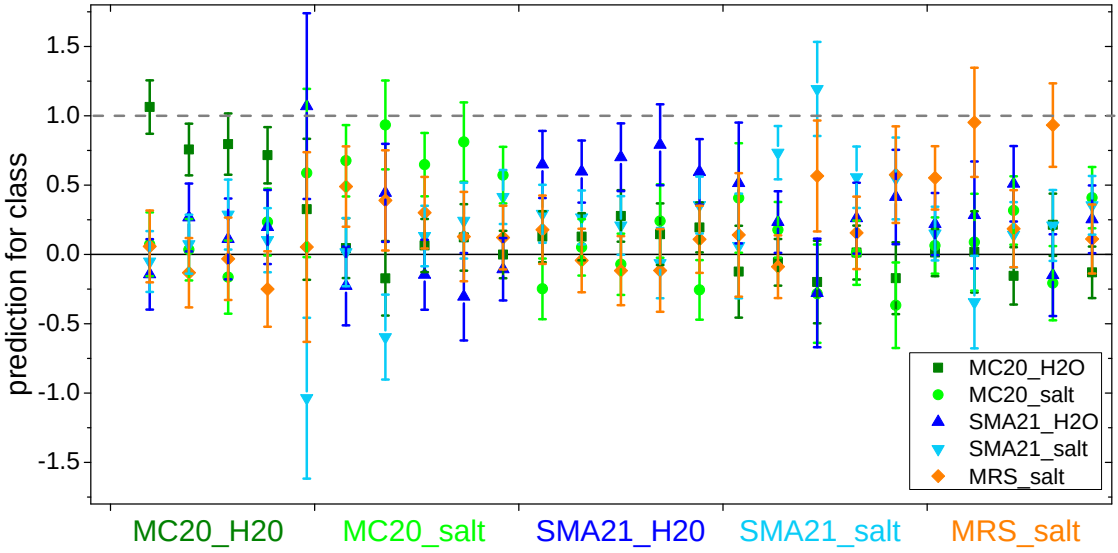

Figure 10.3: *PLS-DA prediction for biological material in Martian analogue soil*

	MC-20 H_2O	MC-20 NaCl	SMA-21 H_2O	SMA-21 NaCl	MRS NaCl
MC-20 H_2O	4	1	1	-	-
MC-20 NaCl	-	5	-	-	-
SMA-21 H_2O	-	-	5	-	-
SMA-21 NaCl	-	-	1	4	2
MRS NaCl	-	-	1	-	3

Table 10.1: *PLS-DA prediction results for the pressed MRS samples with additional biological material. The samples listed in the first column are assigned to one or more of the classes listed in the top line. Stated are the total numbers of spectra assigned to the class in the top line on the basis of the above mentioned criterion.*

Summary

In this brief study the potential of LIBS to discriminate between samples of Martian analogue soil with and without biological material was investigated under simulated Martian atmospheric conditions. The complexity of elements in the Martian analogue soil complicates the detection of biological material, which usually can be identified on the basis of the intense lines of inorganic elements [Rehse et al., 2007]. Here, the soil as well as the NaCl salt solution in which the strains grew, comprises sodium. The intense sodium emission lines in the LIBS spectra strongly control the MVA outcome which is therefore very sensitive on the growth medium.

With PLS-DA a prediction model was calculated with averaged LIBS spectra. On the basis of this model discrimination and identification seems to be feasible for the majority of spectra. However, although the PLS-DA prediction resulted in a total of 84% correct class affiliations with 4% unidentified samples and 24% false attributions, the applicability in view of identifying biological material in Martian soil with LIBS should be handled with care. This is a very preliminary result and much work needs to be done to reveal the spectral features and lines, which are really relevant for identifying the

biological material and not the growth medium or solution in which they are investigated. Moreover, for the purpose of discriminating between the samples with different biological material and the reference sample consisting of Martian analogue material a spectral range including the strong carbon line at 247.86 nm as well as the intense lines of sodium and potassium in the Vis/NIR range would be an advantage.

11 Summary and outlook

LIBS is considered a powerful analytical technique for the in-situ geochemical investigation of extraterrestrial surfaces and has been evaluated for application in planetary science in a number of studies. With the ChemCam instrument on NASA's rover MSL arriving on Mars in August 2012, the LIBS technique will be applied for the first time on a planetary mission.

The focus in this work was on the potential of LIBS to investigate and analyze salts in particular in a salt water ice matrix under Martian atmospheric conditions. It was shown that LIBS is capable of analyzing salts and of discriminating between them in pure samples. Beyond that, the feasibility of LIBS was demonstrated to probe ices and to detect components in the frozen samples given sufficient irradiance. The influence of different gating parameters for time-resolved detection of the plasma on analyzing salts and frozen salt solutions was studied. Gating parameters best suited for the LIBS analysis of ices were determined for the Inlite laser with an energy of 35 mJ and a spot diameter of approximately 300 μm at the sample surface under simulated Martian atmospheric conditions. The early phase of the plasma evolution was found to be strongly dominated by background radiation and a delay time of 500 ns significantly improved the LIBS spectra in terms of signal-to-noise ratios. The background radiation was more intensive in the case of the frozen salt solutions than for the pressed salt samples and also of a longer time duration. LIBS instruments for the use in planetary science presumably will not implement time-resolved detection due to limited mass and energy available. The effects of detection without gating on the LIBS analysis of ices should therefore be investigated in a next step. The distance of the focussing lens to the sample surface was found to have only minor influence on the intensity of the emission lines in this set-up for the studied range. However, effects of the laser drilling deeper into the ice and plasma confinement in the crater were seen in the case of the frozen sodium chloride solution. The capability of depth profile analysis with LIBS on ices was shown for this sample, too, as well as for the ferric ices. Averaging three laser-induced plasmas enabled a depth-resolved analysis where an evolving salt layer at the surface of a frozen salt solution could be detected.

In general, the emission lines of metals were found to be detectable with LIBS with good signal-to-noise ratios also in the case of the frozen salt solutions, which facilitates a relatively straightforward identification of the type of the cation in the salt. However, despite the thin atmosphere of Mars being an advantage in view of enhanced emission lines and improved ablation when compared to Earth ambient conditions, due to weak excitation of the high-energy levels required for efficient radiative transitions of both sulfur and chlorine ions, their emission lines are typically weak and hardly detectable. The lines of chlorine and sulfur were found to be detectable in the spectra of the pure salts utilizing the Inlite laser. However, in the spectra of the salts mixed in soil and also in the spectra of the frozen salt solutions, these lines are not detected, which considerably complicates differentiation between salts with the same cation.

The applied MVA methods, which were utilized to enable discrimiation between salts with the same cation in different samples, differed in suitability in terms of discriminating between the various salts. The most important emission lines for successful discrimination were identified for the LIBS spectra by means of PCA and spectral features such as line profiles, shifts, and the influence of background radiation were investigated. Successful prediction of almost all test sets with SIMCA was obtained only for the pure pressed salt samples, where the LIBS spectra of the samples are very different. PLS-DA was found to be best suited for the purpose of identification of a test set in the case of the frozen salt

solutions, but also for the other sample sets. LIBS spectra of salts with the same cation in frozen salt solution could be identified within the scope of the prediction model, although there were no chlorine and sulfur lines detectable. It was found that in order to distinguish between chloride and sulfate salts a detection of the weak sulfur and chlorine lines is not necessarily required. To a greater degree the essential information is given by other lines available in the spectra on the basis of their amplitudes, their shapes, and shifts. Presumably, additional information about the sample, such as consistency and transparency, translate into plasma characteristics and alter the line profiles, most notably for the hydrogen alpha and hydrogen beta lines. More extensive studies with ices should be done in future works in order to reveal these alterations in detail and attribute them to physical processes. As PLS-DA performed best in this study and was generally most successful at distinguishing sulfate and chloride salts, this MVA is recommended for distinguishing between salts and frozen salt solutions. In general, the application of multivariate analysis methods to LIBS spectra of ices demonstrates the ability of LIBS to distinguish between different salts in frozen salt water solutions. This work confirms that LIBS is a powerful analytical technique for planetary exploration and can be utilized to determine compositional information of ice samples. With appropriate prediction models, salts in different matrices, such as in frozen salt solutions, can be identified. As a first step in this feasibility study only pure frozen salt water solutions have been investigated and tested for the potential of LIBS together with MVA to discriminate between them. A necessary next step is to consider mixtures of two or several salts and examine how they will fit into existing models and, if appropriate, expand the models. Also, different concentrations of the salt in frozen salt solutions have to be investigated in order to determine the limits of detection for the salts in the ices with LIBS also in view of the ices becoming more transparent for decreasing salt contents. Additionally, other potentially relevant salts have to be added to the sample sets and comprehensive data bases should be build. Three MVA methods have been tested in this work. However, there are multiple other MVA methods which could prove more suitable for the analysis of salts in frozen salt solutions such as neural network models, independent component analysis or nonlinear methods [Anderson et al., 2011], [Lasue et al., 2011].

Although the generation of a suitable plasma for analysis was not achieved for most of the frozen salt water samples with the low energy laser with an energy of 2.7 mJ on the sample surface in combination with a spot diameter of 150 μm, this does not generally rule out its feasibility to investigate ice. In comparison to the Inlite laser utilized with an energy of 35 mJ and a spot diameter of approximately 300 μm a similar irradiance should be obtained on the sample surface. Improvement of the focussing optics for the low energy laser, i.e. reducing the laser spot diameter at the sample surface or reduction of the effective focal lenght might facilitate plasma generation on the ices also for a low energy laser. Moreover, this might enable the detection of sulfur and chlorine lines in the pure pressed samples, which are relevant not only for Martian geochemistry. The analysis and detection of salts and frozen salt solutions is also relevant in view of the exploration of the icy bodies in the Solar System within the scope of possible future missions to the outer planets. An interesting target is, for instance, Jupiter's Galilean satellite Europa, a moon with an apparently young surface composed of water ice with only few craters. Spectroscopic data obtained by Galileo's Near Infrared Mapping Spectrometer (NIMS) suggests that some of the optically darker regions on Europa's surface include hydrated salt minerals such as magnesium sulfates or sodium carbonates [McCord et al., 1998]. Moreover (or alternatively), sulfuric acid hydrate might be present in the water ice [Carlson et al., 2005] as well as sulfur compounds giving rise to the reddish colored surface observed [Calvin et al., 1995], [Dalton et al., 2005]. Saturn's moon Enceladus is another icy satellite which represents an interesting target for in-situ investigation of the frozen surface. More extended studies for LIBS on frozen salt solutions are required, testing laser energies between 2.7 mJ and 35 mJ under appropriate simulated conditions in terms of pressure and temperature. Moreover, detection of a spectral range in the VUV should be considered for a space flight instrument, where intense chlorine and sulfur lines are available [Radziemski et al., 2005].

List of Figures

List of Tables

List of Abbreviations

AES	Atom Emission Spectroscopy
APXS	Alpha-Particle X-ray Spectrometer
AU	Astronomical Unit
CCD	Charge-Coupled Device
CRISM	Compact Reconnaissance Imaging Spectrometer for Mars
CTE	Complete Thermodynamic Equilibrium
DLR	Deutsches Zentrum für Luft- und Raumfahrt
FWHM	Full Width at Half Maximum
ICCD	Intensified Charge-Coupled Device
LIBS	Laser-Induced Breakdown Spectroscopy
LIF	Laser-Induced Fluorescence
LTE	Local Thermodynamic Equilibrium
LV	Latent Variable
MCP	Micro Channel Plate
MERs	Mars Exploration Rovers
MET	Meteorological Station
Mini-TES	Minature Thermal Emission Spectrometer
MOLA	Mars Orbiter Laser Altimeter
MRS	Martian Regolith Simulant
MSL	Mars Science Laboratory
MVA	Multivariate Analysis
NASA	National Aeronautics and Space Administration
NIMS	Near Infrared Mapping Spectrometer
NIPALS	Non-linear Iterative Partial Least Squares
NIR	Near Infra-Red
OMEGA	Observatoire pour la Minéralogie, l'Eau, les Glaces et l'Activité
PC	Principal Component
PCA	Principal Component Analysis
PLS	Partial Least Squares
PLS-DA	Partial Least Squares - Discriminant Analysis
RAT	Rock Abrasion Tool
RSD	Relative Standard Deviation
SIMCA	Soft Independent Modeling of Class Analogy
SNC	Shergottites, Nakhlites, Chassignites
SNR	Signal-to-Noise Ratio
TECP	Thermal and Electrical Conductivity Probe
TEGA	Thermal and Evolved Gas Analyzer
THEMIS	Thermal Emission Imaging Spectrometer
VUV	Vacuum Ultra-Violet
WCL	Wet Chemistry Laboratory
XRF	X-Ray Fluorescence

Bibliography

[Altheide et al., 2009] Altheide, T., Chevier, V., Nicholson, C., and Denson, J. (2009). Experimental investigation of the stability and evaporation of sulfate and chloride brines on Mars. *Earth and Planetary Science Letters*, 282:69–78.

[Amoruso et al., 2006] Amoruso, S., Ausanio, G., Bruzzese, R., Gragnaniello, L., Lanotte, L., Vitiello, M., and Wang, X. (2006). Characterization of laser ablation of solid targets with near-infrared laser pulses of 100 fs and 1 ps duration. *Applied Surface Science*, 252(13):4863–4870.

[Anderson, 2012] Anderson, R. B. (2012). *Lasers and Landing Sites: The Geomorphology, Stratigraphy, and Composition of Mars*. PhD thesis, Cornell University.

[Anderson et al., 2011] Anderson, R. B., Morris, R. V., Clegg, S. M., Bell, J. F., Wiens, R. C., Humphries, S. D., Mertzman, S. A., Graff, T. G., and McInroy, R. (2011). The influence of multivariate analysis methods and target grain size on the accuracy of remote quantitative chemical analysis of rocks using laser induced breakdown spectroscopy. *Icarus*, 215(2):608–627.

[Angel et al., 2001] Angel, S. M., Stratis, D. N., Eland, K. L., Lai, T., Berg, M. A., and Gold, D. M. (2001). LIBS using dual- and ultra-short laser pulses. *Fresenius' Journal of Analytical Chemistry*, 369:320–327. 10.1007/s002160000656.

[Arp et al., 2004a] Arp, Z. A., Cremers, D. A., Harris, R. D., Oschwald, D. M., and Wayne, D. M. (2004a). Feasibility of generating a useful laser-induced breakdown spectroscopy plasma on rocks at high pressure: preliminary study for a Venus mission. *Spectrochimica Acta Part B: Atomic Spectroscopy*, 59:987–999.

[Arp et al., 2004b] Arp, Z. A., Cremers, D. A., Wiens, R. C., Wayne, D. M., Sallé, B., and Maurice, S. (2004b). Analysis of water ice and water ice/soil mixtures using laser-induced breakdown spectroscopy: application to Mars polar exploration. *Application Spectroscopy*, 58:897–909.

[Bandfield et al., 2000] Bandfield, J. L., Hamilton, V. E., and Christensen, P. R. (2000). A global view of Martian surface compositions from MGS-TES. *Science*, 287(5458):1626–1630.

[Barlow, 2008] Barlow, N. (2008). *Mars: An introduction to its interior, surface and atmosphere*. Cambridge University Press.

[Bell, 2008] Bell, J. (2008). *The Martian Surface. Composition, Mineralogy, and Physical Properties*. Cambridge University Press.

[Berger et al., 2009] Berger, G., Toplis, M. J., Treguier, E., D'Uston, C., and Pinet, P. (2009). Evidence in favor of small amounts of ephemeral and transient water during alteration at Meridiani Planum, Mars. *American Mineralogist*, 94:1279–1282.

[Bibring et al., 2005] Bibring, J.-P., Langevin, Y., Gendrin, A., Gondet, B., Poulet, F., Berthè, M., Soufflot, A., Arvidson, R., Mangold, N., Mustard, J., Drossart, P., and the OMEGA team (2005). Mars surface diversity as revealed by the OMEGA/Mars express observations. *Science*, 307:1576–1581.

[Bishop et al., 2009] Bishop, J. L., Parente, M., Weitz, C. M., Noe Dobrea, E. Z., Roach, L. H., Murchie, S. L., McGuire, P. C., McKoewn, N. K., Rossi, C. M., Brown, A. J., Calvin, W. M., Milliken, R., and F, M. J. (2009). Mineralogy of Juventae Chasma: Sulfates in the light-toned mounds, mafic minerals in the bedrock, and hydrated silica and hydroxylated ferric sulfate on the plateau. *Journal of Geophysical Research*, 114.

[Boynton et al., 2002] Boynton, W. V., Feldman, W. C., Squyres, S. W., Prettyman, T. H., Brückner, J., Evans, L. G., Reedy, R. C., Starr, R., Arnold, J. R., Drake, D. M., Englert, P. A. J., Metzger, A. E., Mitrofanov, I., Trombka, J. I., d'Uston, C., Wänke, H., Gasnault, O., Hamara, D. K., Janes, D. M., Marcialis, R. L., Maurice, S., Mikheeva, I., Taylor, G. J., Tokar, R., and Shinohara, C. (2002). Distribution of Hydrogen in the Near Surface of Mars: Evidence for Subsurface Ice Deposits. *Science*, 297:81–85.

[Brady, 2009] Brady, J. B. (2009). Magma in a beaker: Analog experiments with water and various salts or sugar for teaching igneous petrology. *The Canadian Mineralogist*, 47:457–471.

[Brass, 1980] Brass, G. W. (1980). Stability of brines on Mars. *Icarus*, 42:20–28.

[Brennetot et al., 2003] Brennetot, R., Lacour, J. L., Vors, E., Rivoallan, A., Vailhen, D., and Maurice, S. (2003). Mars analysis by Laser-Induced breakdown spectroscopy (MALIS): influence of Mars atmosphere on plasma emission and study of factors influencing plasma emission with the use of doehlert designs. *Applied Spectroscopy*, 57:744–752.

[Brückner et al., 2003] Brückner, J., Dreibus, G., Rieder, R., and Wänke, H. (2003). Refined data of alpha proton x-ray spectrometer analyses of soils and rocks at the Mars pathfinder site: Implications for surface chemistry. *Journal of Geophysical Research*, 108.

[Calvin et al., 1995] Calvin, W. M., Clark, R. N., Brown, R. H., and Spencer, J. R. (1995). Spectra of the icy Galilean satellites from 0.2 to 5 μm: A compilation, new observations, and a recent summary. *Journal of Geophysical Research*, 100:19041–19048.

[CAMO, 2012] CAMO (2012). The Unscrambler X.

[Campbell et al., 2008] Campbell, J. L., Gellert, R., Lee, M., Mallett, C. L., Maxwell, J. A., and O'Meara, J. M. (2008). Quantitative in situ determination of hydration of bright high-sulfate Martian soils. *Journal of Geophysical Research*, 113.

[Canadian Space Agency, 2010] Canadian Space Agency (2010). The Canadian Space Agency report to the 38th COSPAR meeting. Space science research in Canada. In *38th COSPAR meeting*, Bremen, Germany.

[Carlson et al., 2005] Carlson, R. W., Anderson, M. S., Mehlman, R., and Johnson, R. E. (2005). Distribution of hydrate on Europa: Further evidence for sulfuric acid hydrate. 177(2):461–471.

[Carr, 2006] Carr, M. H. (2006). *The Surface of Mars*. Cambridge University Press.

[Carr, 2012] Carr, M. H. (2012). The fluvial history of Mars. *Philosophical transactions. Series A, Mathematical, physical, and engineering sciences*, 370(1966):2193–215.

[Chevrier and Altheide, 2008] Chevrier, V. F. and Altheide, T. S. (2008). Low temperature aqueous ferric sulfate solutions on the surface of Mars. *Geophysical Research Letters*, 35:1–5.

[Chevrier et al., 2009] Chevrier, V. F., Hanley, J., and Altheide, T. S. (2009). Stability of perchlorate hydrates and their liquid solutions at the Phoenix landing site, Mars. *Geophysical Research Letters*, 36:10202.

[Chevrier and Mathe, 2007] Chevrier, V. F. and Mathe, P. E. (2007). Mineralogy and evolution of the surface of Mars: A review. *Planetary and Space Science*, 55:289–314.

[Chevrier et al., 2009] Chevrier, V. F., Ulrich, R., and Altheide, T. S. (2009). Viscosity of liquid ferric sulfate solutions and application to the formation of gullies on Mars. *Journal of geophysical Research*, 114:1–11.

[Clark et al., 1982] Clark, B. C., Baird, A. K., Weldon, R. J., Tsusaki, D. M., Schnabel, L., and Candelaria, M. P. (1982). Chemical composiotion of Martian fines. *Journal of Geophysical Research*, 87:10.059–10.067.

[Clark et al., 1977] Clark, III, B. C., Castro, A. J., Rowe, C. D., Baird, A. K., Rose, Jr., H. J., Toulmin, III, P., Christian, R. P., Kelliher, W. C., Keil, K., and Huss, G. R. (1977). The Viking X ray fluorescence experiment - Analytical methods and early results. *Journal of Geophysical Research*, 82:4577–4594.

[Clegg et al., 2009] Clegg, S. M., Sklute, E., Dyar, M. D., Barefield, J. E., and Wiens, R. C. (2009). Multivariate analysis of remote laser-induced breakdown spectroscopy spectra using partial least squares, principal component analysis, and related techniques. *Spectrochimica Acta Part B: Atomic Spectroscopy*, 64:79–88.

[Clifford et al., 2010] Clifford, S. M., Lasue, J., Heggy, E., Boisson, J., McGovern, P., and Max, M. D. (2010). Depth of the Martian cryosphere: Revised estimates and implications for the existence and detection of subpermafrost groundwater. *Journal of Geophysical Research*, 115.

[Colao et al., 2004] Colao, F., Fantoni, R., Lazic, V., Paolini, A., Fabbri, F., Ori, G. G., Marinangeli, L., and Baliva, A. (2004). Investigation of LIBS feasibility for in situ planetary exploration: An analysis on Martian rock analogues. *Planetary and Space Science*, 52(1-3):117–123.

[Cousin et al., 2011] Cousin, A., Forni, O., Maurice, S., Gasnault, O., Fabre, C., Sautter, V., Wiens, R. C., and Mazoyer, J. (2011). Laser induced breakdown spectroscopy library for the Martian environment. *Spectrochimica Acta Part B: Atomic Spectroscopy*, 66:805–814.

[Cousin et al., 2009] Cousin, A., Maurice, S., Berger, G., Forni, O., Gasnault, O., Wiens, R. C., and the ChemCam team (2009). Depth profiles studies using ChemCam. In *42nd Lunar and Planetary Science Conference*, page Abstract #1963, Houston. Lunar and Planetary Institute.

[Cremers, 2007] Cremers, D. A. (2007). *"Remote Analysis by LIBS: Application to Space Exploration" in Laser-Induced Breakdown Spectroscopy, eds.: Singh, J. P. and Thakur, S. N.*, volume 454.

[Cremers and Radziemski, 2006a] Cremers, D. A. and Radziemski, L. J. (2006a). *Handbook of Laser-Induced Breakdown Spectroscopy*, volume 283. John Wiley & Sons, Ltd.

[Cremers and Radziemski, 2006b] Cremers, D. A. and Radziemski, L. J. (2006b). *"History and Fundamentals of LIBS" in Laser-Induced Breakdown Spectroscopy-Fundamentals and Applications, eds.: Miziolek A. W., Palleschi V. and Schechter I.*, volume 620.

[Dalton et al., 2005] Dalton, J. B., Prieto-Ballesteros, O., Kargel, J. S., Jamieson, C. S., Jolivet, J., and Quinn, R. (2005). Spectral comparison of heavily hydrated salts with disrupted terrains on Europa. *Icarus*, 177:472–490.

[Dash et al., 2006] Dash, J. G., Rempel, A. W., and Wettlaufer, J. S. (2006). The physics of premelted ice and its geophysical consequences, reviews of modern physics. *Reviews of Modern Physics*, 78:695–741.

[Davila et al., 2010] Davila, A. F., Skidmore, M., Fairén, A. G., Cockell, C., and Schulze-Makuch, D. (2010). New Priorities in the Robotic Exploration of Mars: The Case for In Situ Search for Extant Life. *Astrobiology*, 10:705–710.

[De Lucia et al., 2008] De Lucia, F. C., Gottfried, J. L., Munson, C. a., and Miziolek, A. W. (2008). Multivariate analysis of standoff laser-induced breakdown spectroscopy spectra for classification of explosive-containing residues. *Applied Optics*, 47(31):G112–21.

[De Vries and Ter Braak, 1995] De Vries, S. and Ter Braak, C. J. F. (1995). Prediction error in partial least squares regression: a critique on the deviation used in The Unscrambler. *Chemometrics and intelligent laboratory systems*, (30):239–245.

[Del Bianco et al., 2006] Del Bianco, A., Rauschenbach, I., Lazic, V., Jessberger, E. K., and the GENTNER Team (2006). GENTNER - a miniaturised LIBS/Raman instrument for the comprehensive in-situ analysis of the Martian surface. *Proc. of 4th International Planetary Probe Workshop*, pages 116–123.

[Diedrich et al., 2007] Diedrich, J., Rehse, S. J., and Palchaudhuri, S. (2007). Pathogenic escherichia coli strain discrimination using laser-induced breakdown spectroscopy. *Journal of Applied Physics*, 102(1):014702.

[Dreyer et al., 2007] Dreyer, C. B., Mungas, G. S., Thanh, P., and Radziszewski, J. G. (2007). Study of sub-mj-excited laser-induced plasma combined with Raman spectroscopy under Mars atmosphere-simulated conditions. *Spectrochimica Acta Part B: Atomic Spectroscopy*, 62(12):1448–1459.

[Dyar et al., 2011] Dyar, M. D., Tucker, J. M., Humphries, S., Clegg, S. M., Wiens, R. C., and Lane, M. D. (2011). Strategies for Mars remote Laser-Induced breakdown spectroscopy analysis of sulfur in geological samples. *Spectrochimica Acta Part B: Atomic Spectroscopy*, 66(1):39–56.

[Esbensen, 2010] Esbensen, K. H. (2010). *Multivariate Data Analysis - in practice*. camo Software AS.

[Fabbro et al., 1982] Fabbro, R., Fabre, E., Amiranoff, F., Garban-Labaune, C., Virmont, J., Weinfeld, M., and Max, C. E. (1982). Laser-wavelength dependence of mass-ablation rate and heat-flux inhibition in laser-produced plasmas. *Physical Review A*, 26:2289–2292.

[Fabre et al., 2011] Fabre, C., Maurice, S., Cousin, A., Wiens, R. C., Forni, O., Sautter, V., and Guillaume, D. (2011). Onboard calibration igneous targets for the Mars Science Laboratory Curiosity rover and the chemistry camera laser induced breakdown spectroscopy instrument. *Spectrochimica Acta Part B: Atomic Spectroscopy*, 66(3-4):280–289.

[Feldman et al., 2002] Feldman, W. C., Boynton, W. V., Tokar, R. L., Prettyman, T. H., Gasnault, O., Squyres, S. W., Elphic, R. C., Lawrence, D. J., Lawson, S. L., Maurice, S., McKinney, G. W., Moore, K. R., and Reedy, R. C. (2002). Global Distribution of Neutrons from Mars: Results from Mars Odyssey. *Science*, 297:75–78.

[Foley et al., 2003] Foley, C. N., Economou, T., and Clayton, N. (2003). Final chemical results from the Mars pathfinder alpha proton X-ray spectrometer. *Journal of geophysical Research*, 108.

[Fußmann, 2005] Fußmann, G. (2005). Einführung in die Plasmaphysik. Skript zur Vorlesung an der Humboldt Universität zu Berlin 2005/2006.

[Gaft et al., 2009] Gaft, M., Nagli, L., Fasaki, I., Kompitsas, M., and Wilsch, G. (2009). Laser-induced breakdown spectroscopy for on-line sulfur analyses of minerals in ambient conditions. *Spectrochimica Acta Part B: Atomic Spectroscopy*, 64(10):1098–1104.

[Gendrin et al., 2005] Gendrin, A., Mangold, N., Bibring, J., Langevin, Y., Gondet, B., Poulet, F., Bonello, G., Quantin, C., Mustard, J., Arvidson, R., and LeMouélic, S. (2005). Sulfates in Martian layered terrains: the OMEGA/Mars express view. *Science (New York, N.Y.)*, 307(5715):1587–91.

[Gornushkin et al., 1999] Gornushkin, I. B., King, L. A., Smith, B. W., Omenetto, N., and Winefordner, J. D. (1999). Line broadening mechanisms in the low pressure laser-induced plasma. *Spectrochemica Acta Part B*, 54(8):1207–1217.

[Gottfried et al., 2009a] Gottfried, J. L., De Lucia Jr., F. C., and Miziolek, A. W. (2009a). Discrimination of explosive residues on organic and inorganic substrates using laser-induced breakdown spectroscopy. *Journal of Analytical Atomic Spectrometry*, 24(3):288.

[Gottfried et al., 2009b] Gottfried, J. L., Harmon, R. S., De Lucia Jr., F. C., and Miziolek, A. W. (2009b). Multivariate analysis of laser-induced breakdown spectroscopy chemical signatures for geomaterial classification. *Spectrochimica Acta Part B: Atomic Spectroscopy*, 64(10):1009–1019.

[Grant et al., 2011] Grant, J. A., Golombek, M. P., Grotzinger, J. P., Wilson, S. A., Watkins, M. M., Vasavada, A. R., Griffes, J. L., and Parker, T. J. (2011). The science process for selecting the landing site for the 2011 Mars Science Laboratory. *Planetary and Space Science*, 59:1114–1127.

[Griem, 1974] Griem, H. R. (1974). Spectral line broadening by plasmas. *Pure and Applied Physics*, 39:421.

[Griem, 1997] Griem, H. R. (1997). *Principles of Plasma Spectroscopy*. Cambridge University Press.

[Hahn and Omenetto, 2010] Hahn, D. W. and Omenetto, N. (2010). Laser-Induced breakdown spectroscopy (LIBS), part i: Review of basic diagnostics and Plasma-Particle interactions: Still-Challenging issues within the analytical plasma community. *Applied Spectroscopy*, 64:335A–366A.

[Harmon et al., 2009] Harmon, R. S., Remus, J., McMillan, N. J., McManus, C., Collins, L., Gottfried Jr., J. L., DeLucia, F. C., and Miziolek, A. W. (2009). LIBS analysis of geomaterials: Geochemical fingerprinting for the rapid analysis and discrimination of minerals. *Applied Geochemistry*, 24(6):1125–1141.

[Hecht et al., 2009] Hecht, M. H., Kounaves, S. P., Quinn, R. C., West, S. J., Young, S. M., Ming, D. W., Catling, D. C., Clark, B. C., Boynton, W. V., Hoffman, J., Deflores, L. P., Gospodinova, K., Kapit, J., and Smith, P. H. (2009). Detection of perchlorate and the soluble chemistry of Martian soil at the Phoenix lander site. *Science*, 325:64–67.

[Hilbk-Kortenbruck et al., 2001] Hilbk-Kortenbruck, F., Noll, R., Wintjens, P., Falk, H., and Becker, C. (2001). Analysis of heavy metals in soils using laser-induced breakdown spectrometry combined with laser-induced fluorescence. *Spectrochimica Acta Part B: Atomic Spectroscopy*, 56(6):933–945.

[Hoehse et al., 2009] Hoehse, M., Mory, D., Florek, S., Weritz, F., Gornushkin, I., and Panne, U. (2009). A combined laser-induced breakdown and Raman spectroscopy echelle system for elemental and molecular microanalysis. *Spectrochimica Acta Part B: Atomic Spectroscopy*, 64(11-12):1219–1227.

[Ishibashi et al., 2011] Ishibashi, K., Ohno, S., Arai, T., Wada, K., Kameda, S., Senshu, H., Namiki, N., Matsui, T., Cho, Y., and Sugita, S. (2011). Prediction of the elemental composition of olivine by laser-induced breakdown spectroscopy (LIBS). In *42nd Lunar and Planetary Science Conference*, page Abstract #1743, Houston. Lunar and Planetary Institute.

[Jakosky and Mellon, 2004] Jakosky, B. M. and Mellon, M. T. (2004). Water on Mars. *Physics Today*, 57:71–85.

[Johnson et al., 2007] Johnson, J. R., Bell III, J. F., Cloutis, E., Staid, M., Farrand, W. H., McCoy, T., Rice, M., Wang, A., and Yen, A. (2007). Mineralogic constraints on sulfur-rich soils from Pancam spectra at gusev crater, Mars. *Geophysical Research Letters*, 34.

[Kaiser et al., 2000] Kaiser, A., Rethfeld, B., Vicanek, M., and Simon, G. (2000). Microscopic processes in dielectrics under irradiation by subpicosecond laser pulses. *Physical Review B*, 61:11437–11450.

[Kargel, 1991] Kargel, J. S. (1991). Brine volcanism and the interoir structure of asteroids and icy satellites. *Icarus*, 94:368–390.

[Kessler, 2007] Kessler, W. (2007). *Multivariate Datenanalyse*. WILEY-VCH Verlag.

[Kiefer et al., 1977] Kiefer, H. H., Martin, T. Z., Peterfreund, A. R., and Jakosky, B. M. (1977). Thermal and Albedo Mapping of Mars During the Viking Primary Mission. *Journal of Geophysical Research*, 82.

[Klingelhöfer et al., 2002] Klingelhöfer, G., Bernhardt, B., Foh, J., Bonnes, U., Rodionov, D., de Souza, P., Schröder, C., Gellert, R., Kane, S., Gütlich, P., and Kankeleit, E. (2002). The Miniaturized Mössbauer Spectrometer MIMOS II for extraterrestrial and outdoor terrestrial applications: A status report. *Hyperfine Interactions*, 144-145:371–379.

[Klingelhöfer et al., 2004] Klingelhöfer, G., Morris, R. V., Bernhardt, B., Schröder, C., Rodionov, D. S., de Souza, P. A., Yen, A., Gellert, R., Evlanov, E. N., Zubkov, B., Foh, J., Bonnes, U., Kankeleit, E., Gütlich, P., Ming, D. W., Renz, F., Wdowiak, T., Squyres, S. W., and Arvidson, R. E. (2004). Jarosite and Hematite at Meridiani Planum from Opportunity's Mössbauer Spectrometer. *Science*, 306:1740–1745.

[Knauth and Burt, 2002] Knauth, L. P. and Burt, D. M. (2002). Eutectic brines on Mars: Origin and possible relation to young seepage features. *Icarus*, 158(1):267–271.

[Knight et al., 2000] Knight, A. K., Scherbarth, N. L., Cremers, D. A., and Ferris, M. J. (2000). Characterization of laser-induced breakdown spectroscopy (LIBS) for application to space exploration, appl. *Spectrosc*, 54(3):331–340.

[Kounaves et al., 2010] Kounaves, S. P., Hecht, M. H., Kapit, J., Gospodinova, K., DeFlores, L., Quinn, R. C., Boynton, W. V., Clark, B. C., Catling, D. C., Hredzak, P., Ming, D. W., Moore, Q., Shusterman, J., Stroble, S., West, S. J., and Young, S. M. M. (2010). Wet Chemistry experiments on the 2007 Phoenix Mars Scout Lander mission: Data analysis and results. *Journal of Geophysical Research*, 115:0.

[Labbé et al., 2008] Labbé, N., Swamidoss, I. M., André, N., Martin, M. Z., Young, T. M., and Rials, T. G. (2008). Extraction of information from laser-induced breakdown spectroscopy spectral data by multivariate analysis. *Applied Optics*, 47(31):G158–65.

[Lambert et al., 2010] Lambert, J. L., Morookian, J., Roberts, T., Polk, J., Smrekar, S., Clegg, S. M., Wiens, R. C., Dyar, M. D., and Treiman, A. (2010). Standoff LIBS and Raman spectroscopy under Venus conditions. In *41st Lunar and Planetary Science Conference*, page Abstract #2608, Houston. Lunar and Planetary Institute.

[Lane et al., 2008] Lane, M. D., Bishop, J. L., Dyar, M. D., King, P. L., Parente, M., and Hyde, B. C. (2008). Mineralogy of the paso robles soils on Mars. *American Mineralogist*, 93:728–739.

[Lanza et al., 2010] Lanza, N. L., Wiens, R. C., Clegg, S. M., Ollila, A. M., Humphries, S. D., Newsom, H. E., and Barefield, J. E. (2010). Calibrating the ChemCam laser-induced breakdown spectroscopy instrument for carbonate minerals on Mars. *Applied Optics*, 49:C211–C217.

[Lasue et al., 2012] Lasue, J., Wiens, R. C., Clegg, S. M., Vaniman, D. T., Joy, K. H., Humphries, S., Mezzacappa, A., Melikechi, N., McInroy, R. E., and Bender, S. (2012). Remote laser-induced breakdown spectroscopy (LIBS) for lunar exploration. 117:1–18.

[Lasue et al., 2011] Lasue, J., Wiens, R. C., Stepinski, T. F., Forni, O., and Clegg, S. M. (2011). Nonlinear mapping technique for data visualization and clustering assessment of LIBS data: application to ChemCam data. *Analytical and Bioanalytical Chemistry*, 400:3247–3260.

[Lazic et al., 2007] Lazic, V., Rauschenbach, I., Jovicevic, S., Jessberger, E. K., Fantoni, R., and Fino, M. D. (2007). Laser induced breakdown spectroscopy of soils, rocks and ice at subzero temperatures in simulated martian conditions. *Spectrochimica Acta Part B: Atomic Spectroscopy*, 62(12):1546–1556.

[Le Deit et al., 2008] Le Deit, L., Le Mouélic, S., Bourgeois, O., Combe, J.-P., Mège, D., Sotin, C., Gendrin, A., Hauber, E., Mangold, N., and Bibring, J.-P. (2008). Ferric oxides in East Candor Chasma, Valles Marineris (Mars) inferred from analysis of OMEGA/Mars express data: Identification and geological interpretation. *Journal of Geophysical Research*, 113(E7):1–18.

[Levrard et al., 2004] Levrard, B., Forget, F., Montmessin, F., and Laskar, J. (2004). Recent ice-rich deposits formed at high latitudes on Mars by sublimation of unstable equatorial ice during low obliquity. *Nature*, 431:1072–1075.

[Lucia and Gottfried, 2011] Lucia, F. C. D. and Gottfried, J. L. (2011). Rapid analysis of energetic and geo-materials using LIBS. *Review Literature And Arts Of The Americas*, 14(6):274–281.

[Marion et al., 2008] Marion, G. M., Kargel, J. S., and Catling, D. C. (2008). Modeling ferrous-ferric iron chemistry with application to Martian surface geochemistry. *Geochimica et Cosmochimica Acta*, 72:242—266.

[Massé et al., 2010] Massé, M., Bourgeois, O., Le Mouélic, S., Verpoorter, C., Le Deit, L., and Bibring, J. (2010). Martian polar and circum-polar sulfate-bearing deposits: Sublimation tills derived from the north polar cap. *Icarus*, 209(2):434–451.

[Maurice et al., 2012] Maurice, S., Wiens, R., Barraclough, B., Saccoccio, M., Barkley, W., Bell, J., Bender, S., Bernardin, J., Blaney, D., Blank, J., Bouyé, M., Bridges, N., Bultman, N., Cais, P., Clanton, R., Clark, B., Clegg, S., Cousin, A., Cremers, D., Cros, A., DeFlores, L., Delapp, D., Dingler, R., D'Uston, C., Darby Dyar, M., Elliott, T., Enemark, D., Fabre, C., Flores, M., Forni, O., Gasnault, O., Hale, T., Hays, C., Herkenhoff, K., Kan, E., Kirkland, L., Kouach, D., Landis, D., Langevin, Y., Lanza, N., LaRocca, F., Lasue, J., Latino, J., Limonadi, D., Lindensmith, C., Little, C., Mangold, N., Manhes, G., Mauchien, P., McKay, C., Miller, E., Mooney, J., Morris, R., Morrison, L., Nelson, T., Newsom, H., Ollila, A., Ott, M., Pares, L., Perez, R., Poitrasson, F., Provost, C., Reiter, J., Roberts, T., Romero, F., Sautter, V., Salazar, S., Simmonds, J., Stiglich, R., Storms, S., Striebig, N., Thocaven, J.-J., Trujillo, T., Ulibarri, M., Vaniman, D., Warner, N., Waterbury, R., Whitaker, R., Witt, J., and Wong-Swanson, B. (2012). The ChemCam instrument suite on the Mars Science Laboratory (MSL) rover: Science objectives and mast unit. *Space Science Reviews, in press*.

[McCord et al., 1998] McCord, T. B., Hansen, G. B., Fanale, F. P., Carlson, R. W., Matson, D. L., Johnson, T. V., Smythe, W. D., Crowley, J. K., Martin, P. D., Ocampo, A., Hibbitts, C. A., Granahan, J. C., and the NIMS Team (1998). Salts on Europa's surface detected by Galileo's Near Infrared Mapping Spectrometer. *Science*, 280(5367):1242–1245.

[McSween et al., 2009] McSween, H. Y., Taylor, G. J., and Wyatt, M. B. (2009). Elemental composition of the Martian crust. *Science*, 324(5928):736–739.

[McSween et al., 2003] McSween, J. H. Y., Grove, T. L., and Wyatt, M. B. (2003). Constraints on the composition and petrogenesis of the Martian crust. *Journal of Geophysical Research*, 108.

[Mezzacappa et al., 2010] Mezzacappa, A., Nortier, L., Clegg, S., Wiens, R. C., and Melikechi, N. (2010). Investigation of LIBS under low pressure for application to planetary exploration. *The Sixth International Conference on Laser-Induced Breakdown Spectroscopy. Mississippi State University, Memphis, Tennessee, 13-17.Sept*, paper P-82.

[Milliken et al., 2009] Milliken, R. E., Fischer, W. W., and Hurowitz, J. A. (2009). Missing salts on early Mars. *Geophysical Research Letters*, 36:11202.

[Milliken et al., 2007] Milliken, R. E., Mustard, J. F., Poulet, F., Jouglet, D., Bibring, J.-P., Gondet, B., and Langevin, Y. (2007). Hydration state of the Martian surface as seen by Mars Express OMEGA: 2. H_2O content of the surface. *Journal of Geophysical Research*, 112:8.

[Miziolek et al., 2007] Miziolek, A. W., Palleschi, V., and Schechter, I. (2007). *Laser-induced Breakdown Spectroscopy (LIBS): Fundamentals and Applications*. Cambridge University Press.

[Möhlmann, 2010] Möhlmann, D. T. F. (2010). Temporary liquid water in upper snow/ice sub-surfaces on Mars. *Icarus*, 207:140–148.

[Möhlmann and Thomson, 2011] Möhlmann, D. T. F. and Thomson, K. (2011). Properties of cryobrines on Mars. *Icarus*, 212:123–130.

[Moore, 2004] Moore, J. M. (2004). Blueberry fields for ever. *Nature*, 428:711–712.

[Morozova et al., 2007] Morozova, D., Möhlmann, D., and Wagner, D. (2007). Survival of methanogenic archaea from siberian permafrost under simulated Martian thermal conditions. *Origins of Life and Evolution of Biospheres*, 37(2):189–200.

[Multari et al., 2012] Multari, R. A., Cremers, D. A., and Bostian, M. L. (2012). Use of laser-induced breakdown spectroscopy for the differentiation of pathogens and viruses on substrates. *Applied Optics*, 51(7):B57–B64.

[Murchie et al., 2009] Murchie, S. L., Mustard, J. F., Ehlmann, B. L., Milliken, R. E., Bishop, J. L., McKeown, N. K., Noe Dobrea, E. Z., Seelos, F. P., Buczkowski, D. L., Wiseman, S. M., Arvidson, R. E., Wray, J. J., Swayze, G., Clark, R. N., Des Marais, D. J., McEwen, A. S., and Bibring, J. (2009). A synthesis of Martian aqueous mineralogy after 1 Mars year of observations from the Mars reconnaissance orbiter. *Journal of Geophysical Research*, 114:1576–1581.

[NASA, 2008] NASA (2008). Temperature measurements taken by phoenix spacecraft. *online available: http://www.nasa.gov/mission_pages/phoenix/images/index.html*, NASA/JPL-Caltech/University of Arizona/Canadian Space Agency.

[Neumann et al., 2004] Neumann, G. A., Zuber, M. T., Wieczorek, M. A., McGovern, P. J., Lemoine, F. G., and Smith, D. E. (2004). Crustal structure of Mars from gravity and topography. *Journal of Geophysical Research*, 109.

[Newsome et al., 2007] Newsome, G., Snead, L. L., Hinoki, T., Katoh, Y., and Peters, D. (2007). Evaluation of neutron irradiated silicon carbide and silicon carbide composites. *Journal of Nuclear Materials*, 371:76–89.

[Ollila et al., 2012] Ollila, A. M., Lasue, J., Newsom, H. E., Multari, R. A., Wiens, R. C., and Clegg, S. M. (2012). Comparison of two partial least squares-discriminant analysis algorithms for identifying geological samples with the ChemCam laser-induced breakdown spectroscopy instrument. *Applied Optics*, 51(7):B130–B142.

[Orbital Technologies Corporation, 2008] Orbital Technologies Corporation (2008). Material safety data sheet for jsc Mars-1a Martian regolith simulant.

[Osterloo et al., 2008] Osterloo, M. M., Hamilton, V. E., Bandfield, J. L., Glotch, T. D., Baldridge, A. M., Christensen, P. R., Tornabene, L. L., and Anderson, F. S. (2008). Chloride-Bearing materials in the southern highlands of Mars. *Science*, 319(5870):1651–1654.

[Palmer and Loewen, 2005] Palmer, C. and Loewen, E. (2005). *Diffraction grating handbook - sixth edition*. Newport Corporation.

[Pavlov et al., 2012] Pavlov, S. G., Schröder, S., Rauschenbach, I., Jessberger, E. K., and Hübers, H.-W. (2012). Low-energy laser induced breakdown spectroscopy for in-situ space missions to solar system bodies without atmospheres. *Planetary and Space Science*, (accepted).

[Peter and Noll, 2007] Peter, L. and Noll, R. (2007). Material ablation and plasma state for single and collinear double pulses interacting with iron samples at ambient gas pressures below 1 bar. *Applied Physics B: Lasers and Optics*, 86:159–167.

[Peter et al., 2003] Peter, L., Sturm, V., and Noll, R. (2003). Liquid steel analysis with laser-induced breakdown spectrometry in the vacuum ultraviolet. *Applied Optics*, 42(30):6199–6204.

[Poulet et al., 2005] Poulet, F., Bibring, J., Mustard, J. F., Grendrin, A., Mangold, N., Langevin, Y., Arvidson, R. E., Gondet, B., Gomez, C., and the OMEGA team (2005). Phyllosilicates on Mars and implications for early Martian climate. *Nature*, 438:623–627.

[Poulet et al., 2009] Poulet, F., Bibring, J.-P., Langevin, Y., Mustard, J. F., Mangold, N., Vincendon, M., Gondet, B., Pinet, P., Bardintzeff, J.-M., and Platevoet, B. (2009). Quantitative compositional analysis of martian mafic regions using the MEx/OMEGA reflectance data 1. Methodology, uncertainties and examples of application. *Icarus*, 201:69–83.

[Radivojevic et al., 2004] Radivojevic, I., Haisch, C., Niessner, R., Florek, S., Becker-Ross, H., and Panne, U. (2004). Microanalysis by laser-induced plasma spectroscopy in the vacuum ultraviolet. *Analytical Chemistry*, 76(6):1648–1656.

[Radziemski et al., 2005] Radziemski, L., Cremers, D. A., Benelli, K., Khoo, C., and Harris, R. D. (2005). Use of the vacuum ultraviolet spectral region for laser-induced breakdown spectroscopy-based Martian geology and exploration. *Spectrochimica Acta Part B: Atomic Spectroscopy*, 60:237–248.

[Ralchenko et al., 2011] Ralchenko, Y., Kramida, A. E., Reader, J., and the NIST ASD Team (2011). NIST atomic spectra database (ver. 4.1.0). *online available: http://physics.nist.gov/asd*, National Institute of Standards and Technology, Gaithersburg, MD.

[Rapp, 2008] Rapp, D. (2008). *Human Missions to Mars: Enabling Technologies for exploring the Red Planet*. Springer.

[Rauschenbach, 2009] Rauschenbach, I. (2009). *Laser-induzierte Breakdown Spektroskopie für die in-situ Analyse der Marsoberfläche*. PhD thesis, Westfälische Wilhelms-Universität Münster.

[Rauschenbach et al., 2010] Rauschenbach, I., Jessberger, E., Pavlov, S., and Hübers, H.-W. (2010). Miniaturized Laser-Induced breakdown spectroscopy for the in-situ analysis of the Martian surface: Calibration and quantification. *Spectrochimica Acta Part B: Atomic Spectroscopy*, 65(8):758–768.

[Rauschenbach et al., 2008] Rauschenbach, I., Lazic, V., Pavlov, S. G., Hübers, H., and Jessberger, E. K. (2008). Laser induced breakdown spectroscopy on soils and rocks influence of the sample temperature, moisture and roughness. *Spectrochimica Acta Part B: Atomic Spectroscopy*, 63(10):1205–1215.

[Rehse et al., 2012] Rehse, S., Salimnia, H., and Miziolek, A. (2012). Laser-induced breakdown spectroscopy (LIBS): an overview of recent progress and future potential for biomedical applications. *J Med Eng Technol*, 36(2):77–89.

[Rehse et al., 2007] Rehse, S. J., Diedrich, J., and Palchaudhuri, S. (2007). Identification and discrimination of pseudomonas aeruginosa bacteria grown in blood and bile by laser-induced breakdown spectroscopy. *Spectrochimica Acta Part B: Atomic Spectroscopy*, 62(10):1169–1176.

[Rennó et al., 2009] Rennó, N. O., Bos, B. J., Catling, D., Clark, B. C., Drube, L., Fisher, D., Goetz, W., Hviid, S. F., Keller, H. U., Kok, J. F., Kounaves, S. P., Leer, K., Lemmon, M., Madsen, M. B., Markiewicz, W. J., Marshall, J., McKay, C., Mehta, M., Smith, M., Zorzano, M. P., Smith, P. H., Stoker, C., and Young, S. M. M. (2009). Possible physical and thermodynamical evidence for liquid water at the Phoenix landing site. *Journal of Geophysical Research*, 114.

[Rieder et al., 2004] Rieder, R., Gellert, R., Anderson, R. C., Brückner, J., Clark, B. C., Dreibus, G., Economou, T., Klingelhöfer, G., Lugmair, G. W., Ming, D. W., Squyres, S. W., d'Uston, C., Wänke, H., Yen, A., and Zipfel, J. (2004). Chemistry of rocks and soils at Meridiani Planum from the Alpha Particle X-ray Spectrometer. *Science*, 306(5702):1746–1749.

[Russo et al., 2004] Russo, R. E., Mao, X. L., Liu, C., and Gonzalez, J. (2004). Laser assisted plasma spectrochemistry: laser ablation. *Journal of Analytical Atomic Spectrometry*, 19:1084–1089.

[Sallé et al., 2005] Sallé, B., Cremers, D. A., Maurice, S., and Wiens, R. C. (2005). Laser-induced breakdown spectroscopy for space exploration applications: Influence of the ambient pressure on the calibration curves prepared from soil and clay samples. *Spectrochimica Acta Part B: Atomic Spectroscopy*, 60(4):479–490.

[Sallé et al., 2004] Sallé, B., Lacour, J.-L., Vors, E., Fichet, P., Maurice, S., Cremers, D. A., and Wiens, R. C. (2004). Laser-induced breakdown spectroscopy for Mars surface analysis: capabilities at stand-off distances and detection of chlorine and sulfur elements. *Spectrochimica Acta Part B: Atomic Spectroscopy*, 59:1413–1422.

[Sallé et al., 2007] Sallé, B., Mauchien, P., and Maurice, S. (2007). Laser-Induced breakdown spectroscopy in open-path configuration for the analysis of distant objects. *Spectrochimica Acta Part B: Atomic Spectroscopy*, 62(8):739–768.

[Sharma et al., 2007] Sharma, S. K., Misra, A. K., Lucey, P. G., Wiens, R. C., and Clegg, S. M. (2007). Combined remote LIBS and Raman spectroscopy at 8.6 m of sulfur-containing minerals, and minerals coated with hematite or covered with basaltic dust. *Spectrochimica Acta Part A: Molecular and Biomolecular Spectroscopy*, 68(4):1036–1045.

[Shu et al., 2007] Shu, R., Qi, H., Lv, G., Ma, D., He, Z., and Xue, Y. (2007). Laser-induced breakdown spectroscopy based detection of lunar soil simulants for moon exploration. *Chin. Optical Letters*, 5(1):58–59.

[Singh and Thakur, 2007] Singh, J. P. and Thakur, S. N. (2007). *Laser-Induced Breakdown Spectroscopy*. Elsevier Science.

[Sirven et al., 2007] Sirven, J., Sallé, B., Mauchien, P., Lacour, J., Maurice, S., and Manhes, G. (2007). Feasibility study of rock identification at the surface of Mars by remote laser-induced breakdown spectroscopy and three chemometric methods. *Journal of Analytical Atomic Spectrometry*, 22(12):1471–1480.

[Sirven et al., 2009] Sirven, J.-B., Pailloux, A., M'Baye, Y., Coulon, N., Alpettaz, T., and Gossé, S. (2009). Towards the determination of the geographical origin of yellow cake samples by laser-induced breakdown spectroscopy and chemometrics. *Journal of Analytical Atomic Spectrometry*, 24(4):451.

[Smith et al., 2001] Smith, D. E., Zuber, M. T., Frey, H. V., Garvin, J. B., Head, J. W., Muhleman, D. O., Pettengill, G. H., Phillips, R. J., Solomon, S. C., Zwally, H. J., Banerdt, W. B., Duxbury, T. C., Golombek, M. P., Lemoine, F. G., Neumann, G. A., Rowlands, D. D., Aharonson, O., Ford, P. G., Ivanov, A. B., Johnson, C. L., McGovern, P. J., Abshire, J. B., Afzal, R. S., and Sun, X. (2001). Mars Orbiter Laser Altimeter: Experiment summary after the first year of global mapping of Mars. *Journal of Geophysical Research*, 106:23689–23722.

[Smith et al., 2009] Smith, P. H., Tamppari, K, L., Arvidson, R E, Bass, D., Blaney, D., Boynton, W. V., Carswell, A., Catling, D. C., Clark, B. C., Duck, T., DeJong, E., Fisher, D., Goetz, W., Gunnlaugsson, H. P., Hecht, M. H., Hipkin, V., Hoffman, J., Hviid, S. F., Keller, H. U., Kounaves, S. P., Lange, C. F., Lemmon, M. T., Madsen, M. B., Markiewicz, W. J., Marshall, J., McKay, C. P., Mellon, M. T., Ming, D. W., Morris, R. V., Pike, W. T., Renno, N., Staufer, U., Stoker, C., Taylor, P., Whiteway, J. A., and Zent, A. P. (2009). H_2O at the Phoenix Landing Site. *Science*, 325:58–61.

[Squyres et al., 2004] Squyres, S. W., Grotzinger, J. P., Arvidson, R. E., Bell III, J. F., Calvin, W., Christensen, P. R., Clark, B. C., Crisp, J. A., Farrand, W. H., Herkenhoff, K. E., Johnson, J. R., Klingelhöfer, G., Knoll, A. H., McLennan, S. M., McSween, Jr., S. M., Morris, R. V., Rice, Jr., J. W., Rieder, R., and Soderblom, L. A. (2004). In situ evidence for an ancient aqueous environment at meridiani planum, Mars. *Science*, 306(5702):1709–1714.

[Tognoni et al., 2006] Tognoni, E., Palleschi, V., Corsi, M., and Cristoforetti, G. (2006). *"From sample to signal in laser-induced breakdown spectroscopy: a complex route to quantitative analysis" in Laser-Induced Breakdown Spectroscopy-Fundamentals and Applications, eds.: Miziolek A. W., Palleschi V. and Schechter I.*, volume 620. Cambridge University Press.

[Tucker et al., 2010] Tucker, J., Dyar, M., Schaefer, M., Clegg, S., and Wiens, R. (2010). Optimization of laser-induced breakdown spectroscopy for rapid geochemical analysis. *Chemical Geology*, 277(1-2):137–148.

[Tucker et al., 2011] Tucker, J. M., Dyar, M. D., Schaefer, M. W., Clegg, S. M., and Wiens, R. C. (2011). Optimization of laser-induced breakdown spectroscopy for rapid geochemical analysis. *Chemical Geology*, (2010).

[Vadillo and Laserna, 2004] Vadillo, J. M. and Laserna, J. J. (2004). Laser-induced plasma spectrometry: truly a surface analytical tool. *Spectrochimica Acta Part B: Atomic Spectroscopy*, 59(2):147–161.

[Viskanta et al., 1997] Viskanta, R., Bianchi, M. V. A., Critser, J. K., and Gao, D. (1997). Solidification processes of solutions. *Cryobiology*, 34(4):348–362.

[Vrbka and Jungwirth, 2005] Vrbka, L. c. v. and Jungwirth, P. (2005). Brine rejection from freezing salt solutions: A molecular dynamics study. *Physical Review Letters*, 95:148501.

[Warren and Brandt, 2008] Warren, S. G. and Brandt, R. E. (2008). Optical constants of ice from the ultraviolett to the microwave: A revised compilation. *Journal of Geophysical Research*, 113.

[Wendt et al., 2011] Wendt, R. C., Gross, C., Kneissl, T., Sowe, M., Combe, J., LeDeit, L., McGuire, P. C., and Neukum, G. (2011). Sulfate and iron oxides in ophir chasma, Mars, based on OMEGA and CRISM observations. *Icarus*, 213(1):86–103.

[Weritz et al., 2005] Weritz, F., Ryahi, S., Schaurich, D., Taffe, A., and Wilsch, G. (2005). Quantitative determination of sulfur content in concrete with laser-induced breakdown spectroscopy. *Spectrochimica Acta Part B: Atomic Spectroscopy*, 60(7-8):1121–1131.

[Weritz et al., 2007] Weritz, F., Schaurich, D., and Wilsch, G. (2007). Detector comparison for sulfur and chlorine detection with laser induced breakdown spectroscopy in the near infrared-region. *Spectrochimica Acta Part B: Atomic Spectroscopy*, 62:1504–1511.

[Wieczorek and Zuber, 2004] Wieczorek, M. A. and Zuber, M. T. (2004). Thickness of the Martian crust: Improved constraints from geoid-to-topography ratios. *Journal of Geophysical Research*, 109.

[Wiens et al., 2012] Wiens, R., Maurice, S., Barraclough, B., Saccoccio, M., Barkley, W., Bell, J., Bender, S., Bernardin, J., Blaney, D., Blank, J., Bouyé, M., Bridges, N., Bultman, N., Cais, P., Clanton, R., Clark, B., Clegg, S., Cousin, A., Cremers, D., Cros, A., DeFlores, L., Delapp, D., Dingler, R., D'Uston, C., Darby Dyar, M., Elliott, T., Enemark, D., Fabre, C., Flores, M., Forni, O., Gasnault, O., Hale, T., Hays, C., Herkenhoff, K., Kan, E., Kirkland, L., Kouach, D., Landis, D., Langevin, Y., Lanza, N., LaRocca, F., Lasue, J., Latino, J., Limonadi, D., Lindensmith, C., Little, C., Mangold, N., Manhes, G., Mauchien, P., McKay, C., Miller, E., Mooney, J., Morris, R., Morrison, L., Nelson, T., Newsom, H., Ollila, A., Ott, M., Pares, L., Perez, R., Poitrasson, F., Provost, C., Reiter, J., Roberts, T., Romero, F., Sautter, V., Salazar, S., Simmonds, J., Stiglich, R., Storms, S., Striebig, N., Thocaven, J.-J., Trujillo, T., Ulibarri, M., Vaniman, D., Warner, N., Waterbury, R., Whitaker, R., Witt, J., and Wong-Swanson, B. (2012). The ChemCam instrument suite on the Mars Science Laboratory (MSL) rover: Body unit and combined system tests. *Space Science Reviews*, pages 1–61.

[Wiens et al., 2011a] Wiens, R. C., Maurice, S., Bender, S., Barraclough, B. L., Cousin, A., Forni, O., Ollila, A., Newsom, H., Vaniman, D., Clegg, S., Lasue, J. A., Blaney, D., DeFlores, L., and Morris, R. V. (2011a). Calibration of the MSL/ChemCam/LIBS remote sensing composition instrument. In *42nd Lunar and Planetary Science Conference*, page Abstract #2370, Houston. Lunar and Planetary Institute.

[Wiens et al., 2011b] Wiens, R. C., Maurice, S., and the ChemCam team (2011b). The ChemCam instrument suite on the Mars Science Laboratory rover Curiosity: Remote sensing by laser-induced plasmas. *Geochemical News*, 145.

[Williams, 2010] Williams, D. R. (2010). Mars fact sheet. *available online: http://nssdc.gsfc.nasa.gov/planetary/factsheet/Marsfact.html*, National Space Science Data Center. NASA.

[Wold, 1966] Wold, H. (1966). Estimation of principal components and related models by iterative least squares. *Multivariate Analysis, Proceedings of the International Symposium. P.R. Krishnaiah ed. Academic Press, New York*, June 1065:391–420.

[Wray et al., 2009] Wray, J. J., Murchie, S. L., Squyres, S. W., Seelos, F. P., and Tornabene, L. L. (2009). Diverse aqueous environments on ancient Mars revealed in the southern highlands. *Geology*, 37(11):1043–1046.

[Wyatt et al., 2004] Wyatt, M. B., McSween, Jr., H. Y., Tanaka, K. L., and Head, J. W. (2004). Global geologic context for rock types and surface alteration on Mars. *Boulder*, 32(8):645–648.

[Yalcin et al., 1999] Yalcin, S., Crosley, D., Smith, G., and Faris, G. (1999). Influence of ambient conditions on the laser air spark. *Applied Physics B: Lasers and Optics*, 68:121–130.

[Yatsenko and Chudotvortsev, 2002] Yatsenko, O. B. and Chudotvortsev, I. G. (2002). Ice melting and crystallization in binary water-salt systems. *Inorganic Materials*, 38(9):907–913.

[Zuber, 2001] Zuber, M. T. (2001). The crust and mantle of Mars. *Nature*, 412:220–227.